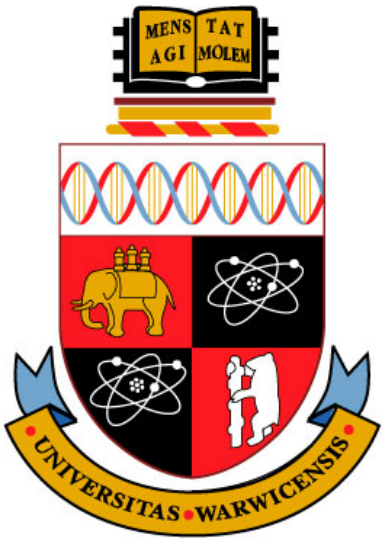

Failure prediction of spot welded boron steel

by

Neill D. Raath

Thesis

Submitted to the University of Warwick

for the degree of

Doctor of Philosophy

WMG

December 2014

THE UNIVERSITY OF WARWICK

Acknowledgments

The author would like to acknowledge the following people for help in this work.

The University of Warwick, EPSRC and Tata Steel for supporting this project. In particular my supervisors Dr. Darren Hughes, Mr. David Norman, Dr. Iain McGregor and Prof. Richard Dashwood. Their help and guidance was invaluable and much appreciated.

John Pillier, Steve Hepple, Richard Beaumont, Iain Norman, Martyn Whitwood, Holger Pfaff, Guido Hensen, Ellen van der Aa, James Kerr and Mike Keeble. Thank you all for the tremendous help you gave.

Dave Cooper, Darren Grant, Paul Johnson, Stefan Kousoulas, Carl Lobjoit and Zac Parkinson.

Sanjeev Sharma, Stefan Winkvist, James Winnett, Richard McManus, Elspeth Keating, Carlos Moreno, Craig Carnegie and Scott Taylor.

Thanks to my mum and dad for never-ending support, encouragement and snacks.

And lastly, to Esther, for all her support and putting up with me.

Declarations

This thesis is submitted in partial fulfilment of the requirements for the degree of Doctor of Philosophy and describes work carried out from July 2011 to December 2014. Unless otherwise indicated, the research described is my own and not the product of collaboration. No part of this thesis has been submitted to any other university, or as any part of any other submission to the University of Warwick.

Abstract

A methodology of material characterisation and finite element model discretisation is presented for spot welded boron steel sheets, with the aim of predicting failure during quasi-static loading. The predicted load-displacement curves from the Finite Element model are compared with experimentally measured curves for lap-shear and cross-tension weld destructive geometries, and serve as model validation.

During spot welding, the weld and surrounding material are exposed to a wide range of temperatures, from the melting point at the weld centre to room temperature in the base material. As a consequence, the weld exhibits varying microstructures with corresponding varying material properties which have a profound influence on its load bearing capacity and failure strength as a whole. In addition, boron steel spot welds exhibit unique hardness profiles, with high hardness values in the nugget and outlying base material, and a sudden drop in the area between these regions. This sudden decrease in material properties leads to further difficulties in modelling the failure of boron steel welds.

The weld process inherently produces localised residual strains which also need to be accounted for in the model simulation, together with significant plastic strain redistributions resulting from the mechanical loading of the spot weld to its ultimate failure. The initial residual strains were measured in weld samples using neutron diffraction and were subsequently input into the FEA models.

This thesis aims to quantify the varying material constitutive behaviour throughout the weld, required for the failure prediction. In particular, the following constitutive properties were extracted: the stress-strain response of certain weld regions, failure loci consisting of fracture strain versus stress state for the corresponding regions, and the residual stress distribution through the weld.

Due to the small size of the weld, cutting test specimens directly from the weld is unachievable. To overcome this problem, specific weld and heat affected zone microstructures were recreated onto practical tensile specimens through use of a Gleeble

thermo-mechanical physical simulator. These specimens were subjected to the same thermal histories as specific points in the actual weld. From these tensile specimens, stress-strain curves relating to specific weld regions could be obtained. In a similar fashion, three additional destructive specimen sets were created to obtain failure loci. These failure loci give fracture strain as a function of stress state: specifically shear, uniaxial and plane-strain states.

Due to the practical limitations in the accuracy of the Gleeble technique, deviations from the target microstructures were expected in the Gleeble samples. To gauge the extent of these deviations, a method of extracting reference material properties directly from the weld was required. Instrumented indentation offers such a solution, where the load and displacement of the indenter are measured and run through an algorithm to calculate the yield strength of the indented locations. These yield strengths are then compared with the yield from the Gleeble stress-strain curves to gauge the accuracy with which the weld microstructures were recreated. This technique serves to quantify the deviation of the Gleeble microstructures from the target material microstructures.

It is common practice to discretise the weld into a small number of bulk regions during the design process, with material constitutive behaviour assigned to these discretised parts. In the new methodology, the extracted material constitutive behaviour is modelled as a continuously varying function of the distance from the weld centre. By performing appropriate interpolation, the data may be finely or roughly discretised. The data at a certain distance from the weld centre may then be assigned to the corresponding element in the finite element model. This means one may discretise the model by choosing the level of data interpolation refinement.

The following results were observed in the thesis:

- Residual strain distributions of boron steel spot welds, which have not been measured before, were presented. Clear correlations between hardness and residual stress distributions were seen.

- A new application of instrumented indentation was attempted by verifying the accuracy of heat treated samples with respect to their target microstructures by comparing yield strengths.
- The boron steel HAZ was characterised in a finer level of detail than seen in other literature works.
- Through physical simulation, stress - strain and failure loci corresponding to certain HAZ areas were successfully extracted and used to model weld failure.
- A new method of finite element model discretisation was presented, where material properties may be input as a relatively smooth function through the length of the model.

Abbreviations

ϵ	Indenter geometrical constant
λ_{therm}	Thermal drift rate
ν	Poisson's ratio
σ_m	Mean or hydrostatic stress
σ_y	Yield stress
σ_{vm}	von Mises stress
θ	Angle between incident neutron beam and scattering planes
ε_f	Strain at fracture
c^*	Geometric constant for indentation pile-up and sink-in events
C_{eq}	Carbon equivalent number
d_0	Strain-free lattice spacing
E^*	Reduced modulus
h_c	Depth of penetration at area of contact
h_r	Residual depth of impression after indenter removal
h_s	Displacement of the surface at the perimeter of contact
h_{max}	Maximum depth of penetration
M_f	Martensite finish temperature
M_s	Martensite start temperature
p_m	Mean contact pressure
t_{sheet}	Sheet thickness

α	Ratio of principal strains
η	Stress triaxiality
λ	Wavelength
A	Projected contact area
bcc	Body centred cubic
bct	Body centred tetragonal
BM	Base Material
BP	Button pull-out
C	Constraint factor
CCT	Continuous Cooling Transformation
CGHAZ	Coarse Grained Heat Affected Zone
d	Atomic lattice plane spacing
DIC	Digital Image Correlation
DP	Dual phase
DPH	Diamond Pyramid Hardness
EDM	Electrical Discharge Machining
EDS	Energy Dispersive Spectroscopy
eV	Electron volt
F	Force
fcc	Face centred cubic
FE	Finite Element

FIF Fulll interfacial failure

FWHM Full-width at half-maximum

h Depth of penetration of indenter into material

HAZ Heat Affected Zone

HSLA High Strength Low Alloy

HV Vickers hardness

I Current

IACS International Annealed Copper Standard

IF Interfacial failure

IHAZ Intercritical Heat Affected Zone

K Strength coefficient

MFDC Medium Frequency Direct Current

n Strain hardening coefficient

P Indenter load

PIF Partial interfacial failure

Q Scattering vector

RSW Resistance Spot Welding

S Stiffness (or gradient) of unloading portion of instrumented indentation load-displacement curve

SCHAZ Subcritical Heat Affected Zone

SEM Scanning Electron Microscope

t Time

UHSS Ultra High Strength Steel

UTS Ultimate Tensile Strength

Contents

List of Figures

List of Tables

Chapter 1

Introduction

1.1 Manufacturing and processing of boron steel

1.1.1 Boron steel

Boron steel is classed as an ultra high strength steel (UHSS) consisting of a significant proportion of martensite, with an ultimate tensile strength (UTS) of up to 1500 MPa [4]. The steel has been increasingly applied in the automotive industry in structural and anti-intrusion components such as B-pillars, bumper reinforcements, roof and side rails [5, 6, 4]. The main attraction of using martensitic steels is the weight reduction and increased passenger safety it provides. This is achieved through light-weighting by gauge reduction.

1.1.2 Boron steel and processing

Due to the high strength, boron steel exhibits poor cold formability compared to other steel grades [5], hence the hot forming process is used to produce the martensitic phase transformation and desired part shape in one step. Boron steel in its as-delivered form consists of ferritic-pearlitic microstructure [7, 8]. The as-delivered steel is usually austenitised at 900°C - 950°C for 5 - 10 minutes [8, 9, 10]and then quenched and formed in a single step in a die.

1.1.3 Hot stamping

Conventional steels can achieve similar mechanical properties as hot stamped boron steel through austenitising and rapid quenching [9]. The major draw-back of using conventional low carbon steels in this fashion is that cooling rates in excess of 300 °C/s are needed for through thickness hardening [9].

In quenching boron steels from above 900 °C, a cooling rate of approximately 30 °C/s is needed to achieve maximum martensitic transformation, as illustrated in figure 1.1.1. The figure is a Continuous Cooling Transformation (CCT) diagram, representing the different phases likely to occur as the steel is cooled at different rates.

Significant amounts of substitutional alloying elements such as vanadium, molybdenum or manganese can also be used to lower the quench rates required to achieve martensite. However, these alloying elements are more expensive than boron. For example, 30 ppm of boron would replace approximately 1% Ni, 0.5% C, 0.2% Mn, 0.12% V, 0.3% Mo or 0.4% Cr [11]. The fact that smaller amounts of boron are needed and being less expensive makes it an economically attractive method to achieve high strength in steels.

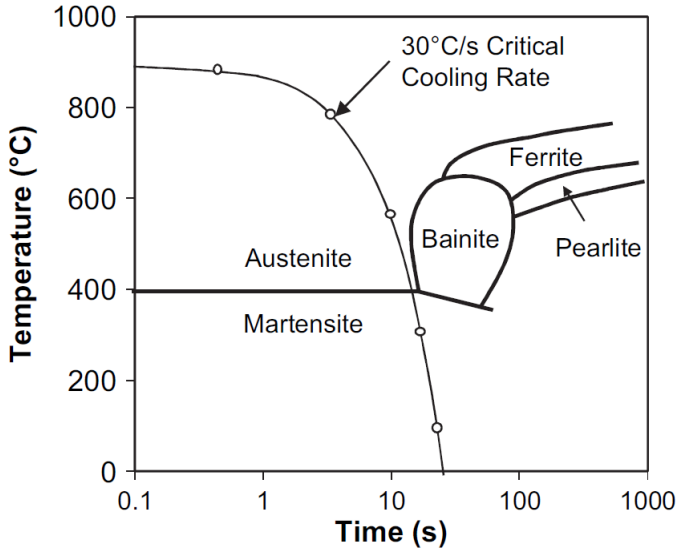

Figure 1.1.1: Schematic illustration of CCT diagram indicating critical cooling rate. Taken from [12]

1.2 Spot welding

Resistance spot welding (RSW) centres around the idea of heating a confined volume of metal above its melting point and then to resolidify it so that the final strength is sufficient to hold the parts together. The heat is generated by the resistance to the flow of current through the work-parts, which are held together under electrode pressure [13].

As shown in figure 1.2.1, the spot welding cycle consists of 4 stages : 1) *Squeeze time:* the time between the first application of the electrodes and the first application of the welding current. 2) *Weld time:* time during which current flows. 3) *Hold time:* time during which the electrode force is maintained after the current has ceases flowing. 4) *Off time:* time during which the electrodes are not in contact with the work-piece.

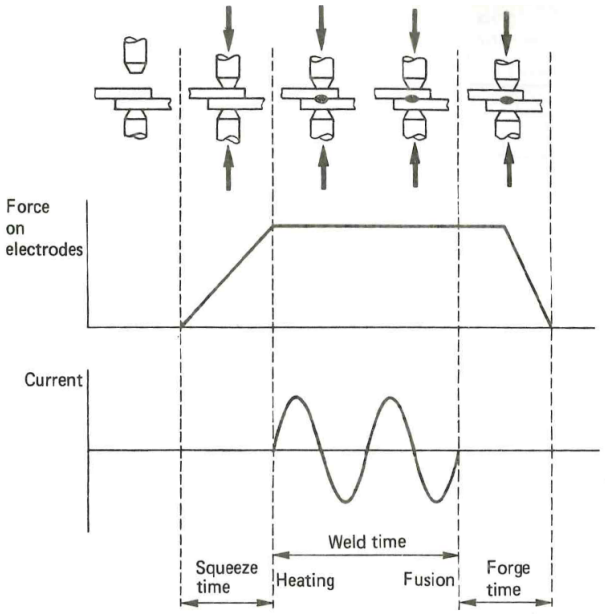

Figure 1.2.1: Spot welding cycle. Taken from [14]

The final joint is dependent on weld time, electrode force, electrode geometry and current strength. These 4 adjustable parameters will be discussed in the following subsections.

1.2.1 Current strength and heat generation

The welding current is adjusted by varying the voltage across the electrodes through Ohm's Law:

$$I = \frac{V}{R} \tag{1.2.1}$$

The resistance of the system is determined by the electrode force, work-piece surface condition and conductivity of the metal [14]. The heat (given in Watt-seconds) generated for a current flow lasting t seconds is also known as Joule heating and is given by equation 1.2.2 below:

$$Q = IVt = I^2Rt \tag{1.2.2}$$

The squared term means that the current has the greatest influence on heat generated, therefore it is the parameter which must be controlled most carefully.

By adjusting the current, heat can be generated that is sufficient to fuse the two sheets together. Producing excessive heat, however, would result in an expulsion of the molten metal from the weld zone. If the current is too low, the work-piece and electrodes conduct all the heat away from the faying surface and no weld is created. The rate of heat generated is an important consideration as well. The heating and cooling rates must be sufficient for commercial high-volume applications, but must not be so fast as to produce inconsistent welds.

The system consisting of the electrodes and work-piece is known as the *secondary circuit* of the spot welding machine, shown in figure 1.2.2. The 7 resistances connected in series are indicated by the circled numbers in the figure. The secondary circuit can be considered as a series of resistances, which can be utilised to produce heat where it is needed i.e. at the interface of the 2 sheets.

The total resistance of the sheet stack-up is attributed to the sum of the contact resistances at the electrode-sheet interface (points 2 and 6 in figure 1.2.2), the resistance at the sheet faying interface (point 4), the bulk resistances of the material (points 3

and 5) and the resistances of the electrodes (points 1 and 7). It is important to note that these resistances are not constant, with contact resistance varying strongly with temperature and pressure and the bulk resistance varying with temperature but not pressure [15]. These temperature effects will be discussed later in the chapter.

Heat will be generated at the 7 interfaces shown in figure 1.2.2 in proportion to the resistance at those points. Point 4 exhibits the greatest resistance and will therefore experience the greatest heat development. Points 2 and 6 exhibit the next greatest resistance, with peaks in temperature developing there. Water cooling in the electrodes dissipates heat away from these regions, while the heat at point 4 is trapped by the surrounding material. As the weld time progresses, the heat at point 4 rises much more rapidly than at points 2 and 6.

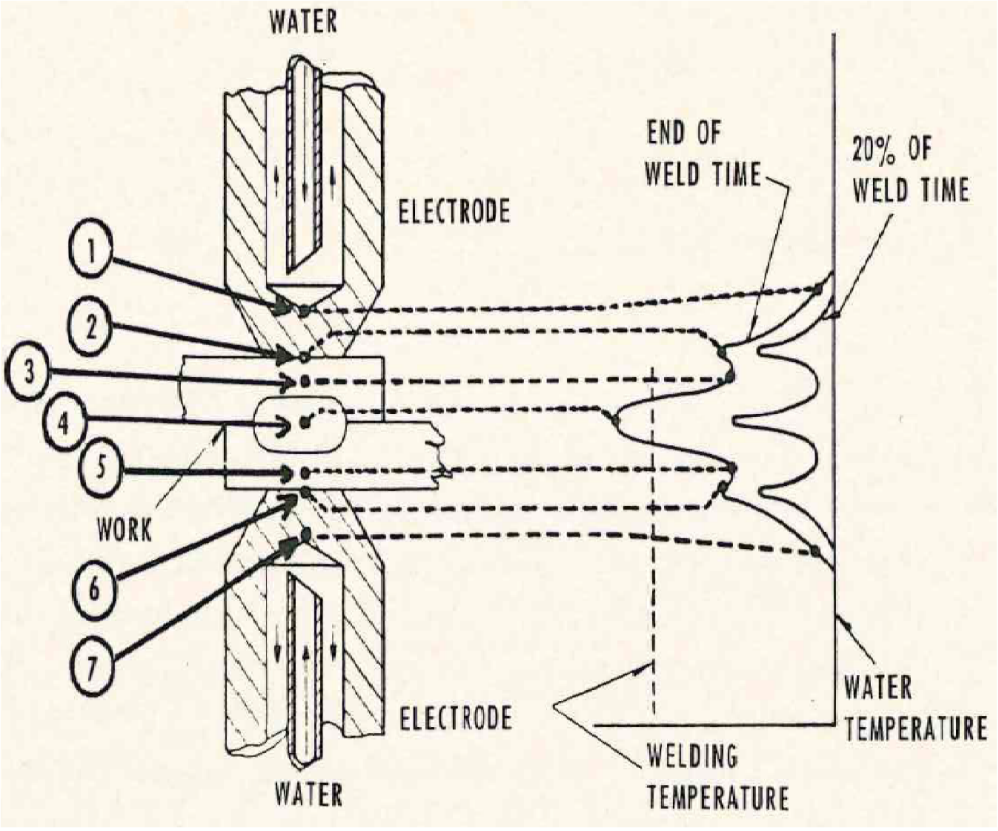

Figure 1.2.2: Temperature distribution in a spot weld and weld components. Taken from [13].

Compensation of heat losses must be taken into consideration as well. These uncontrollable losses are due to radiation from the work-piece into the air and by conduction into surrounding material and electrodes. Usually, at some point in an extended time, the radiation losses equal the heat input, thus stopping any further temperature rise.

1.2.2 Weld time

The weld times can be applied in single or multiple steps, depending on the work-piece setup. For example, a single impulse is a continuous application of current to make a single weld.

A double impulse schedule consists of 2 separate impulses. The first impulse is usually low-current and short-time, usually applied as a pre-heat step if there are coatings involved. The second impulse would be a higher-current and longer-time step for forming the weld.

If excessive welding times are used, the temperature in the weld nugget would eventually reach boiling point, leading to gas pockets being formed and a resulting expulsion of molten material [16, 15].

The amount of time required is a function of current magnitude and material thickness. That being said, heat transfer is a function of time and hence the development of the required nugget size demands a finite time length regardless of an increase in current.

The squeeze and hold times are important for ensuring inadvertent damage of the current to the work-piece. If the current is applied before the electrodes make contact with the work-piece or while they are being retracted, a high amperage arc would occur, damaging the work-piece surface and electrode tip contour.

1.2.3 Electrodes and electrode force

The electrodes serve several functions: they conduct the welding current to the work-piece, determine the current density according to the electrode geometry, dissipate the

heat from the weld zone, ensure sufficient cooling rates through a water cooling cavity and contain the molten material between the work-piece interfaces.

Due to the aforementioned functions, the electrodes must exhibit good electrical and heat conduction properties which must differ from those of the work-piece. The electrodes must remain hard at elevated temperatures to ensure a constant compressive force. To meet these requirements, alloyed copper is a common material choice for electrodes.

The electrode force ensures a closed circuit between the electrodes and the work-piece. A higher electrode force brings material surfaces into contact and reduces initial contact resistance between the material interfaces as well as those between the electrodes and outer surfaces [13].

The reduced contact resistance brought on by high electrode forces usually requires a higher current and/or a longer weld time to be used [17]. Excessive electrode forces also cause indentation, which lowers the strength of the weld [18] and reduces the aesthetic quality of the work-piece. Insufficient electrode forces would result in high contact resistances, leading to excessive heating at the interface while providing insufficient heat for fusion.

When the correct electrode force is applied, the contact resistance at the electrode-sheet interface is at such a low level that no melting occurs and the electrodes can cool the weld properly. The majority of the heat is created at the faying surfaces. In such a case, the weld is said to have a good heat balance.

1.2.4 Resistance of work-piece

As mentioned previously, the total resistance will change due to temperature variations during welding. This is known as *dynamic resistance*, which is the sum of the bulk resistance of the material and the contact resistance between the electrodes.

We will first consider the *bulk resistance* of the material being welded. The resistivity as a function of temperature for mild steel, aluminium and pure copper can be seen in figure 1.2.3. Although electrodes are usually a copper alloy, the behaviour of pure copper will give an indication of the differences in resistivity between the electrodes and material being welded.

As can be seen from the figure, there is a large difference in resistivity between steel and copper, even at room temperature. This difference in resistivity between steel and copper electrodes means that, as current begins to flow, more heat will be generated at the faying interface of the steel sheets than in the electrodes. The electrodes, being water cooled, will maintain their low resistivity. The bulk material, however, will experience an increase in resistivity as temperature increases and heat generation will further increase.

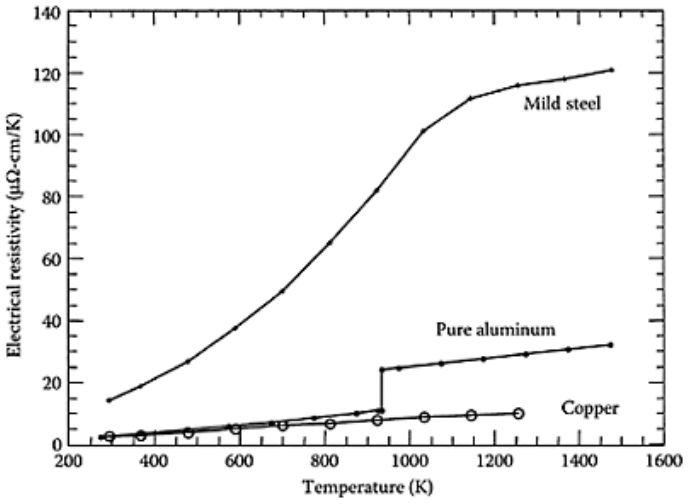

Figure 1.2.3: Bulk resistivity as function of temperature for mild steel, aluminium and copper. Taken from [15].

Next, consideration will be given to *contact resistance*. As opposed to bulk resistance, it is highly influenced by both temperature and pressure, as well as the surface conditions of the contact interfaces. For example, as indicated in figure 1.2.4, the actual contact area is small, due to the irregularities on the micro-scale. When the electrode force is increased, the contact surface is increased as surface irregularities are brought into

contact. Insufficient electrode pressure would lead to localised heating.

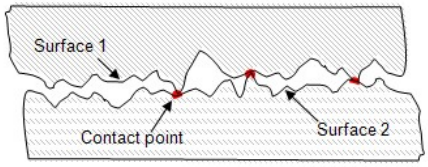

Figure 1.2.4: Surface irregularities on micro-scale. Taken from [19]

Other surface conditions that can change the contact resistance are oils, rust, oxides etc. Care should be taken in cleaning the work-pieces before welding to avoid unforeseen changes to resistance. Another surface condition to be considered is the coating, which prevents oxidation during heat treatments. While being beneficial for the steel, the coatings affect the resistivity.

An example can be seen from an experiment performed by Harlin *et al* [17] where uncoated and hot-dipped galvanised coated steels were compared (shown in table 1.2.1). It should be noted that the data presented was done on a 3-stack setup, nevertheless it gives an indication of the effect of coatings. It is evident that the coating reduces the contact resistance of the coated stacks, with increased electrode pressure causing further reductions. This means that higher currents are required for coated sheets.

	Contact resistance ($\mu\Omega$)		
	Uncoated stack (2.1 kN)	Coated stack (2.1 kN)	Coated stack (6 kN)
Electrode-sheet	305	100	32
Sheet-sheet	558	137	28

Table 1.2.1: Measured contact resistances for coated and uncoated stacks. Taken from [17]

1.2.5 Shunting

In industrial spot welding applications, several spot welds are usually produced next to each other in the same region of a part. These pre-made neighbouring welds may divert

electric current intended for producing a new weld, as shown in figure 1.2.5. This effect is known as *shunting*. The current density used to produce a weld (the shunted weld) is reduced by having a certain percentage flowing through the pre-made weld (shunt weld), hence the current density may not be sufficient to produce the required weld. Sufficient distance between welds must be accounted for when producing multiple welds on a part.

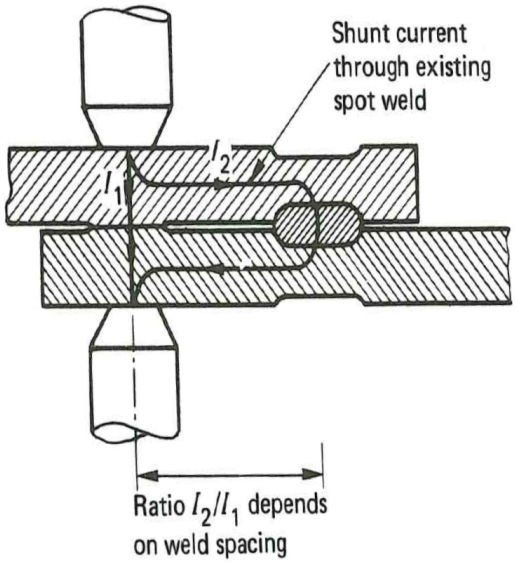

Figure 1.2.5: Shunt weld with current path. Taken from [14].

1.3 Metallurgical considerations of boron steel

1.3.1 Hardenability of steel

There are a variety of ways that steel can be strengthened; alloying, strain hardening and heat treatment. Solid solution strengthening is the process where a metal is strengthened through the addition of specific alloying elements. These alloying elements can take up either substitutional or interstitial positions in the crystalline lattice.

Interstitial elements are small enough to fit between the crystalline lattice positions, whereas substitutional elements replace locations in the crystalline lattice. In either

case, the elements cause a distortion, or strain energy, in the lattice, which creates a barrier to dislocation movement. This is the mechanism which strengthens the metal.

The addition of carbon to pure iron increases the yield strength by more than five times [20]; but carbon has a limited solubility in iron. Heat treatment and solid solution strengthening by other alloying elements are much more effective.

Steel may be divided according to carbon content as follows:

Low carbon steel	Medium carbon steel	High carbon steel
$<$ 0.3 wt% C	0.3 - 0.7 wt% C	0.7 - 1.7 wt% C

Table 1.3.1: Designation of steel types according to carbon content [21]

1.3.2 Crystal structures and phase transformations

Considering boron steel undergoes 2 main stages of metallurgical transformations, through hot-stamping and welding, it is important to consider the phase transformation that will result from these processes.

The iron - carbon equilibrium diagram (figure 1.3.1) represents the metastable equilibrium between iron and iron-carbide (also known as cementite) [1].

The standard pressure allotropes of pure iron are $\alpha - Fe$, $\gamma - Fe$ and $\delta - Fe$; where an allotrope is defined as different forms of the same chemical element. If carbon is dissolved interstitially in these allotropes, three primary solid solutions are formed; namely ferrite ($\alpha - phase$), austenite ($\gamma - phase$) and $\delta - phase$. The $\delta - phase$ is a transient high temperature phase, stable from 1400 °C to 1539 °C [22]. Since this thesis will only deal with non-transient microstructures, the $\delta - phase$ will not be discussed.

Ferrite is a soft phase with a body centred cubic (bcc) structure which remains stable from room temperature to the A_3 temperature (shown in figure 1.3.1). Upon reaching the A_3 temperature, ferrite begins the transformation into austenite. Austenite is a

high temperature phase with a face centred cubic (fcc) structure. Examples of bcc and fcc structures are shown in figure 1.3.2.

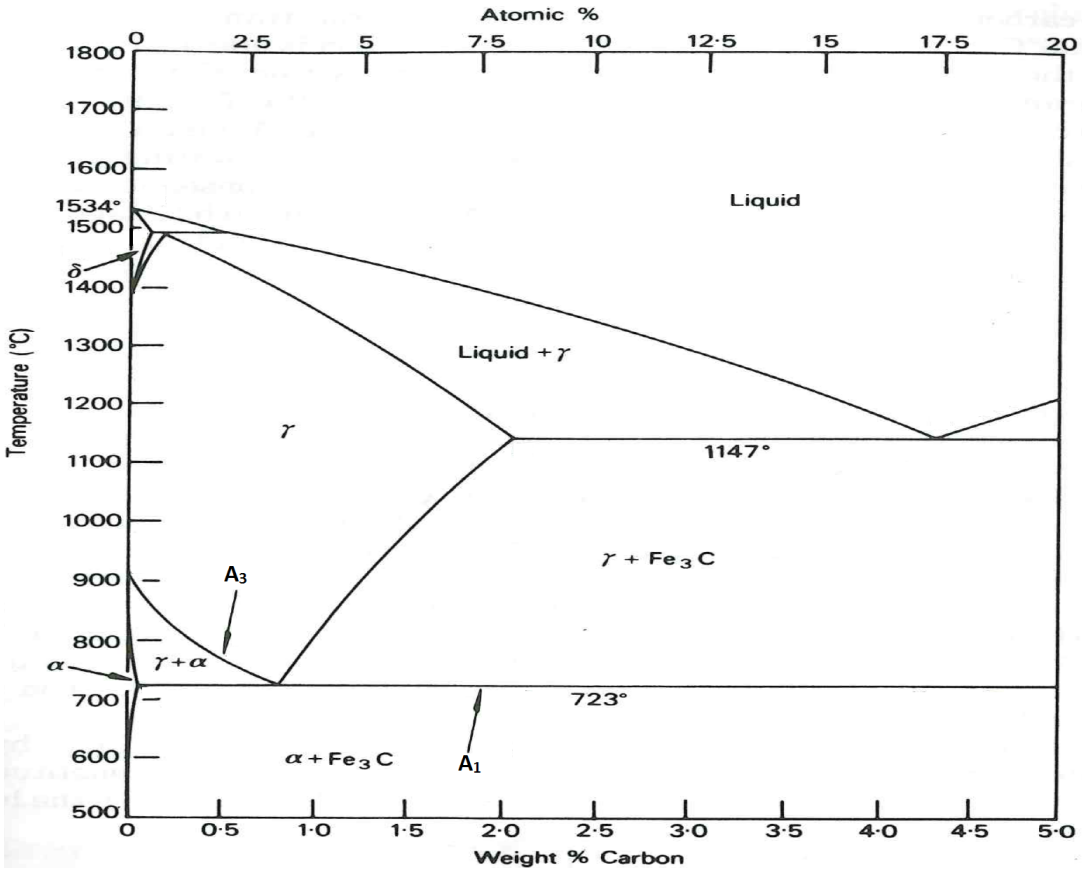

Figure 1.3.1: Iron-Carbon equilibrium Phase Diagram. Modified from [1]

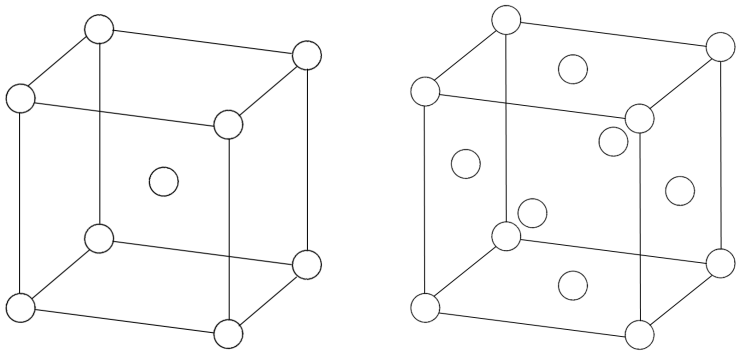

(a) Schematic diagram of a body centred cubic (bcc) structure

(b) Schematic diagram of a face centred cubic (fcc) structure

Figure 1.3.2: Illustration of bcc and fcc structures

Ferrite has maximum carbon solubility of 0.025 weight-percent (wt%) at 725 °C [21]. As can be seen in figure 1.3.1, austenite has a much larger phase field than ferrite, which reflects a higher carbon solubility; approximately 2 wt% at 1147 °C [1].

It is this higher solubility which facilitates the heat treatment of steels. For example, rapid quenching from the austenite phase leads to a hard supersaturated solution of carbon in iron, also known as martensite. Because ferrite has a restricted carbon solubility, it is usually associated with cementite.

For the iron phase, the critical transformation temperatures are assigned the letter "A", which is from the french *arrêt*, indicating the "arrest" in temperature during transformation. The eutectoid reaction occurs at the A_1 temperature (723 °C). A_3 is the transformation temperature where ferrite transforms into austenite. For pure iron, it is 910 °C, but the temperature is lowered as more carbon is added.

The A temperatures are assigned subscripts "c" and "r", depending on whether the system is heated or cooled respectively. The subscript "c" is from *chauffant*, meaning warming and "r" is from *refroidissement*, meaning cooling. It is important to note that these A_c and A_r critical temperatures are dependent on the heating/cooling rate and the amount of alloying elements.

There are two common diffusion mechanisms by which atoms move around a lattice, with the mechanism depending on the type of site occupied. Interstitial atoms migrate by forcing between larger substitutional atoms. Substitutional atoms migrate by a vacancy mechanism (as shown in figure 1.3.3).

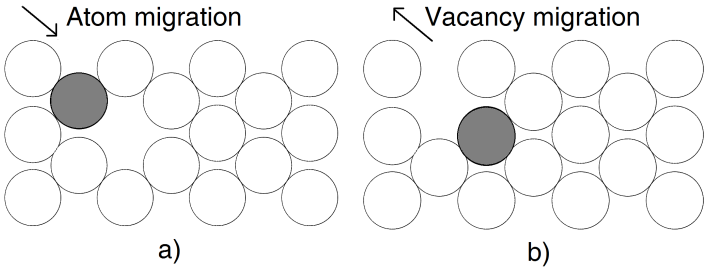

Figure 1.3.3: Illustration of the vacancy diffusion mechanism by which substitutional elements migrate.

The $\alpha \rightleftharpoons \gamma$ transformation takes place via diffusion of carbon atoms. Let us consider the formation of ferrite via cooling of austenite. Elements such as carbon and nitrogen diffuse interstitially, while iron and other substitutional elements diffuse by a vacancy mechanism [23]. Given sufficient atomic mobility (i.e. slow cooling), the fcc lattice will undergo a complete reconstruction into the bcc form via a diffusive mixing up of atoms [23]. If the fcc lattice is cooled sufficiently fast, there will not be enough time or atomic mobility for diffusional transformation. In this case, we have a diffusionless transformation, which takes place via a shear mechanism. This will be dealt with in the next section concerning martensite growth.

The majority of phase transformations in metals occur via the "*nucleation and growth*" process [24]. In this process a daughter phase initiates (nucleates) at certain sites in the metastable parent phase and grows into the surrounding matrix. During the nucleation stage, an interface is created which then migrates into the parent phase during growth.

The addition of boron to steel increases hardenability by retarding the nucleation of the relatively soft ferrite phase at the austenite grain boundaries. This effect is explained in terms of the reduction in interfacial energy when the boron particles segregate to the austenite grain boundaries, leading to an increased incubation time for ferrite formation [25, 26]. That is to say after ferrite formation has begun, its nucleation rate is lowered. Elements like manganese also improve martensite hardenability: adding ~ 0.002 wt% is adequate to have a large effect on the transformation kinetics [26].

Adding too much boron has the opposite effect. The boron leads to the formation of borides at the grain boundaries. These are known to stimulate the nucleation of ferrite [25]. It is necessary to add Al or Ti when using boron. This is because boron has a high affinity to oxygen and nitrogen, hence the titanium reacts with nitrogen and aluminium deoxidises the steel [26].

1.3.3 Martensite formation

Martensite ($\alpha^{'} - phase$) is a supersaturated solid solution of carbon in ferritic iron and is formed by a sudden shear process in the austenite lattice by the rapid quenching of austenite down to room temperature. For low carbon steels, martensite appears as lathes [27]. For medium to high carbon steels, the morphology changes to a plate [24]. The crystal structure is body centred tetragonal (bct), as shown in figure 1.3.4. As can be seen in image 1.3.5, the degree of tetragonality, measured as the ratio c/a, is affected by carbon content.

Martensite transformation activates athermally in a temperature range defined by the martensite start temperature (M_s) and the martensite finish temperature (M_f) [1], as shown in figure 1.3.6. In the figure, the circled values indicate the Vickers hardness of the quenched steel and A, F, P, B and M stand for austenite, ferrite, pearlite, bainite and martensite respectively.

The austenite has to be cooled very rapidly in order to suppress the higher-temperature diffusion controlled ferrite and pearlite reactions and to bring the metastable austenite to the M_s temperature. Once the M_s temperature is reached, martensite formation initiates. Once the temperature reaches M_f, the reaction ceases. As can be seen from figure 1.3.7, the M_s temperature is affected by the carbon content of the steel. The transformation occurs "instantaneously", at nearly the speed of sound in a solid [28].

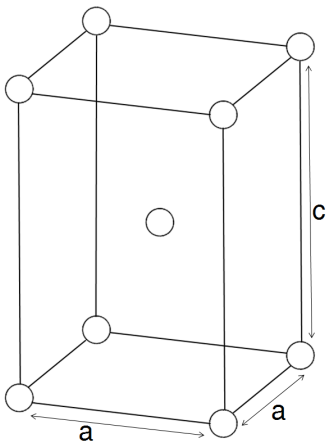

Figure 1.3.4: Body centred tetragonal (bct) crystal structure of martensite

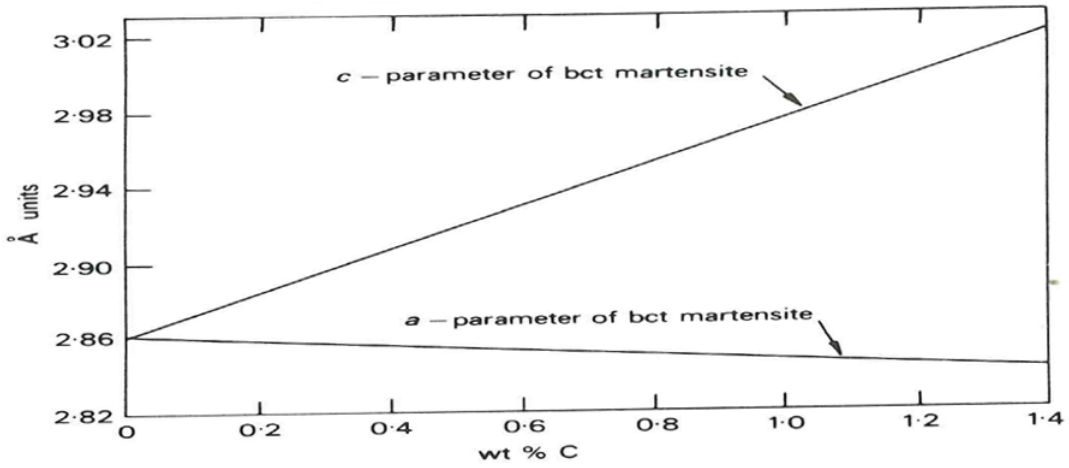

Figure 1.3.5: Effect of carbon on the lattice parameters of martensite. Taken from [1]

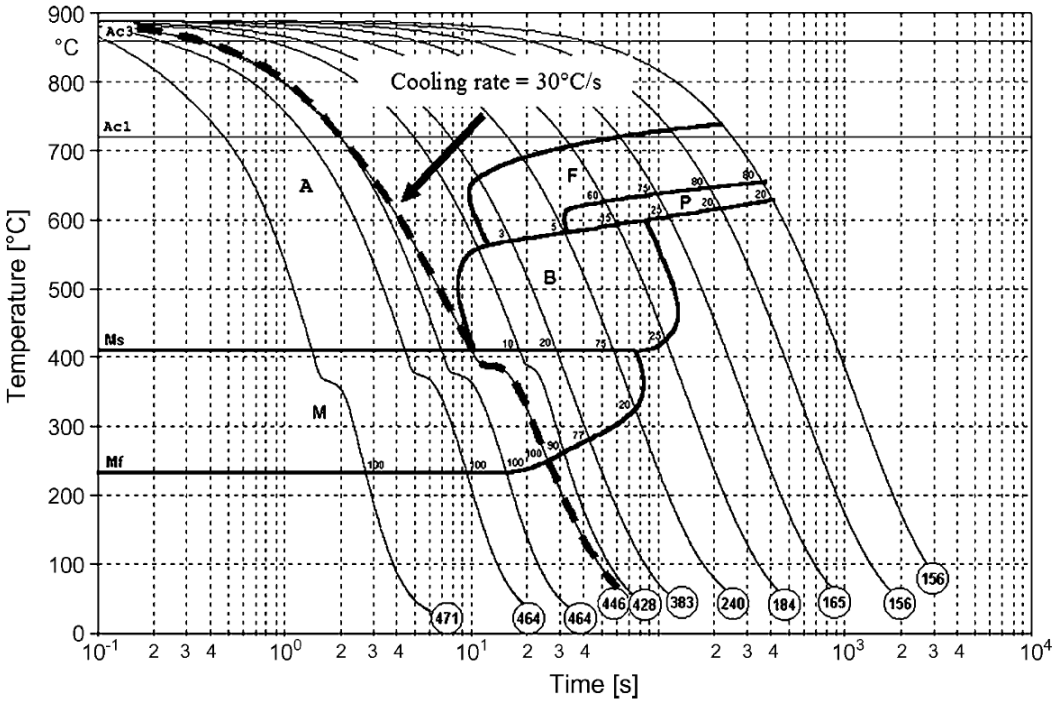

Figure 1.3.6: CCT diagram of boron steel, indicating martensite start and finish temperatures [6]

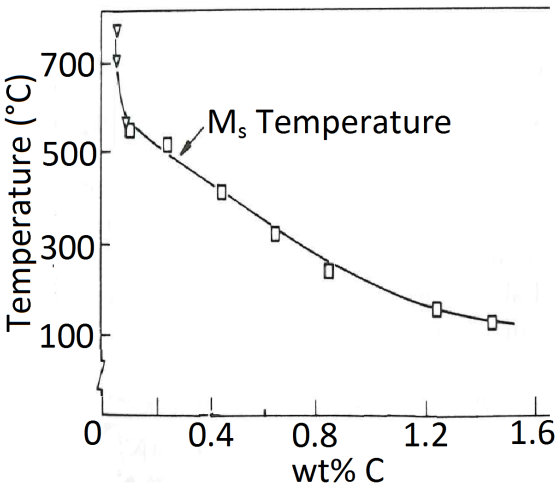

Figure 1.3.7: The effect of carbon on the M_s temperature. Modified from [1].

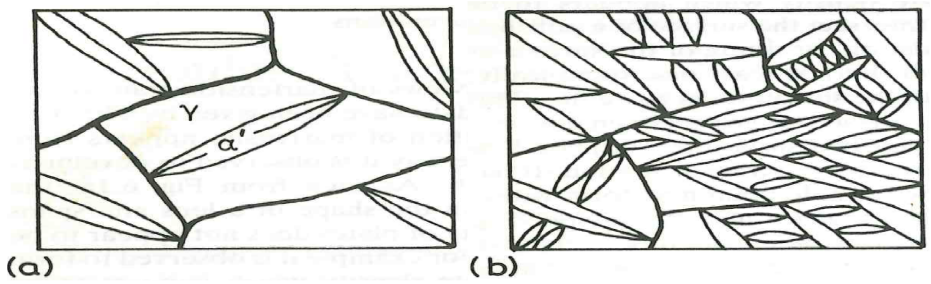

Figure 1.3.8: Schematic illustration of martensite $\left(\alpha^{'}\right)$ growth in austenite (γ) grains with increased cooling below M_s. a). Initial martensite plate formation. b). Increasing martensite fraction as cooling continues. Taken from [24]

Martensite is a product of diffusionless transformation, which is defined as "any transformation in which, from start to completion of the transformation, individual atomic movements are less than one interatomic spacing" [24, 28].

A schematic illustration of martensite growth in austenite grains is shown in figure 1.3.8. It spans the entire diameter of the austenite grains and is often lens shaped. As can be seen from the figure, the volume fraction of martensite increases by the systematic transformation of austenite remaining between the martensite plates that have already formed. It is common that not all the austenite transforms into martensite, with remaining phase known as *retained austenite*.

An interesting point to note is that martensitic transformations are not reversible [29]. Martensite is an extremely unstable phase, with the trapped carbon producing a high internal strain. Even moderate reheating would decompose the structure, a process known as tempering.

1.3.4 Tempering of martensite

Due to the thermal cycles experienced during welding, a region close to the weld will experience tempering, albeit for a very short time. Tempering involves heating the steel to below the transformation temperature, holding it for a certain amount of time, and cooling it to room temperature. This process reduces the brittleness of martensite, giving it a more ductile behaviour.

During the tempering process, martensite will precipitate carbon in the form of carbide phases and at the same time will lose some tetragonality and tend toward a bcc shape. As tempering progresses, the martensite matrix loses all tetragonality and transforms to ferrite and cementite, which nucleates at the grain boundaries [29]. The boundary sites are preferred due to the ease of diffusion at these sites.

1.4 The spot weld and heat affected zone

The area directly underneath the electrodes experiences the highest temperature; this is where the metal exceeds melting temperature and rapidly resolidifies, leaving a *weld nugget*. A decreasing temperature gradient extends outward from this area, resulting in altered microstructures; known as the Heat Affected Zone (HAZ) and can be divided into several subzones. The area beyond the HAZ is known as the base material (BM) and has not undergone microstructural transformations.

Due to the rapid nature of the thermal cycles experienced during welding, directly measuring the temperature at a certain point on the weld is very difficult. For ex-

ample, using thermocouples may interfere with the welding process and lead to inaccurate temperature measurements. The rapidity of the thermal cycles also makes using equilibrium diagrams to predict microstructures impossible [30]. However, figure 1.4.1 may be used as a starting point to interpret microstructural variations qualitatively by examining the peak temperature reached during welding [30].

The BM is defined as not having been transformed during the welding process, and hence has experienced temperatures much below the transformation point (A_1= 727 °C), although the precise temperature depends on the composition of the metal [14].

The HAZ experiences temperatures below the melting point and therefore undergoes solid-state transformations, with the result being that the HAZ exhibits different mechanical properties to the nugget and BM. The HAZ can be divided into 3 zones leading outward from the nugget; the coarse-grained HAZ (CGHAZ), the intercritical HAZ (IHAZ) and the sub-critical HAZ (SCHAZ) [15, 30].

The CGHAZ experiences temperatures above A_3 up to approximately 1495 °C and experiences austenitisation. At temperatures just above the A_3 temperature, the austenite grains are small, but as temperature increases the austenite grain size can reach a few hundred microns [30].

The intercritical zone experiences peak temperatures between A_1 and A_3. In this zone partial phase transformations may occur, depending on the duration that the metal is exposed to the peak temperature and cooling rate. Blondeau [30] defines the HAZ as starting from this point ($T > A_1$).

The SCHAZ has not undergone phase transformations, but the peak temperature is sufficient for tempering to occur. In this zone the peak temperature is usually between 600 °C and the A_1 temperature [30].

It is important to note that the metallurgical transformations discussed correspond to an equilibrium state. Due to the short length of thermal cycles during welding, the microstructural transformations sometimes occur at temperatures higher than those stated in Fe-C equilibrium diagrams.

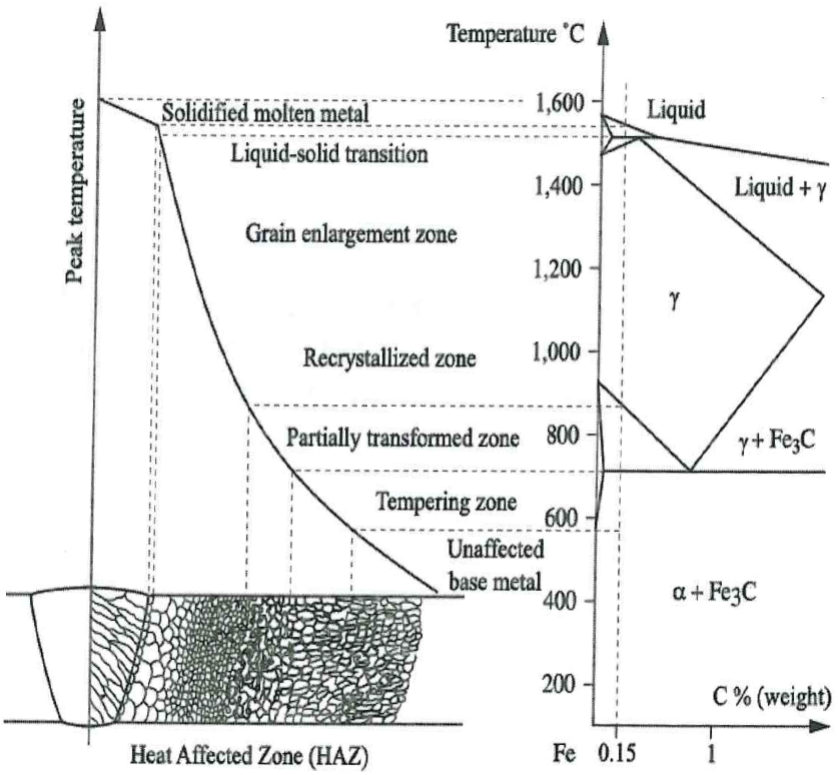

Figure 1.4.1: Constituent parts of a welded joint for a 0.15 C wt% steel. Taken from [30]

1.5 Summary and Objectives

Due to environmental considerations, there has been a need to improve fuel economy and reduce emissions in the automotive industry. A factor which contributes to this aim is reducing vehicle weight. Light-weight materials such as aluminium and carbon fibre have increasingly been utilised. However, these materials are relatively expensive compared to steel. High strength materials that are cheap to process are required in load-bearing and anti-intrusion sections to ensure passenger safety, for example B-pillar applications [5]. High strength boron steel exhibits desirable characteristics and has been utilised to reduce vehicle weight and maintain passenger safety through gauge-reduction of load-bearing parts. Unlike the majority of cold-formed sheet steel, in the application of boron steel, the high strength is achieved by hot-forming; whereby the

steel is rapidly quenched from above 900 °C to achieve a strong martensitic microstructure.

Resistance spot welding is one of the most widely used joining techniques of steel vehicle parts, with several thousand welds made on a single car. Predicting failure of welds made on martensitic boron steels presents a unique challenge. Whereas welds in non-martensitic materials show a gradual decline in hardness from the nugget to the base material (BM), martensitic welds show a sudden softening in the heat affected zone (HAZ) and a sharp increase in hardness back into the BM. It is this mechanical mismatch between the hard nugget/BM and soft HAZ which causes the HAZ to be a critical area, with reduced mechanical properties [31].

Spot welds were produced on 1.5 mm thick boron steel sheets with a zinc coating. The spot weld configuration used in this thesis was based on industrial automotive production welding schedules. The aim of the project was, therefore, to predict spot weld behaviour and load bearing capacity, under quasi-static loading, of boron steel spot welds currently used in the automotive industry.

1.5.1 Consequences of the weld process

By its very nature, the weld and surrounding material have been exposed to a wide range of temperatures. These range from above 1300 °C at the centre of the nugget, to room temperature at distances far away from the weld. As a consequence, the material is non-homogeneous and anisotropic. In particular, the following properties will vary throughout the weld:

- Stress - strain response
- Microstructure
- Residual strains/stresses

These varying material properties and process induced stresses have a profound influence on the load bearing capacity and failure strength of the weld as a whole. It may be tempting to focus on, and characterise, the weakest section of the weld to predict failure, but significant stress redistributions result during mechanical loading. As a result, all the varying material properties must be taken into account in predicting the failure load. Failure in this context is defined as the load bearing capacity of the weld.

1.5.2 Estimating the characteristics throughout the weld

The stress-strain response of a material is traditionally obtained from tensile specimens. However, due to the small dimensions, extracting tensile specimens directly from the weld is impractical. A solution is to create standard tensile specimens exposed to identical thermal histories as certain points in the weld, indicated as points "A" to "E" in figure 1.5.1. Point A, being closer to the nugget, would experience higher temperatures that point E, which is further away from the nugget. The constitutive behaviour extracted from the tensile specimens is then associated with elements at the corresponding locations in a finite element model used to predict failure.

Since the weld has such small dimensions and the electrodes obscure the weld, directly measuring the temperature history is extremely difficult. Use was made of a finite element welding simulation program called SORPAS, wherein the weld schedule was input and the thermal histories of points A - E were output, as shown in figure 1.5.1. These temperature-time profiles were fed into a thermo-mechanical physical simulator called Gleeble [32], schematically illustrated in figure 1.5.1 The Gleeble recreates these thermal histories through resistively heating the boron steel samples. An air pressurised cooling attachment helps to simulate the cooling rates experienced by the weld. From the Gleeble physical simulations, one obtains tensile specimens with microstructures corresponding to the previously defined points in the weld.

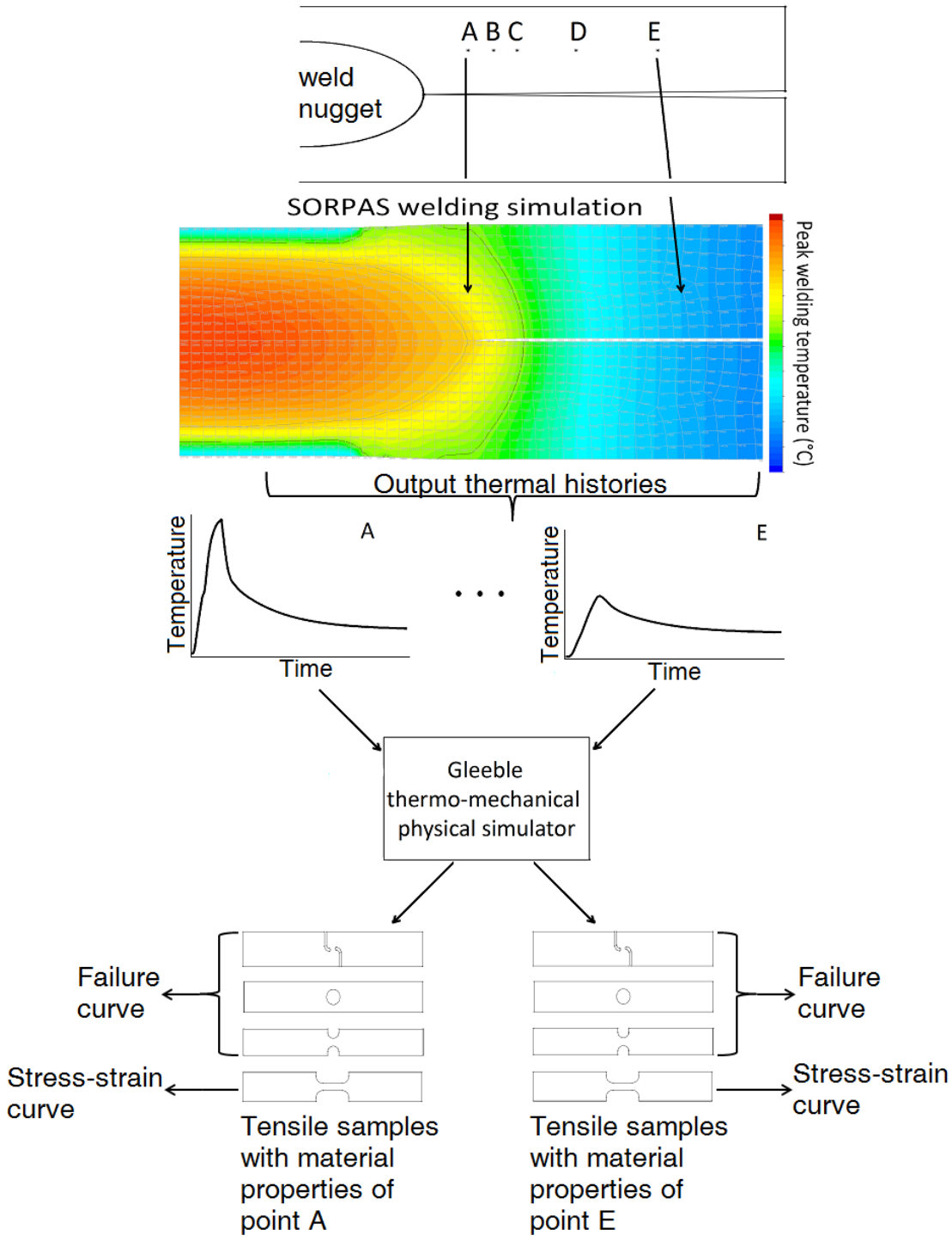

Figure 1.5.1: Selected points of interest along length of welded work-piece, indicated as points A - E. Thermal histories of these points are extracted by simulating the weld schedule in the SORPAS finite element welding simulation program. Extracted thermal histories of selected points are used to drive Gleeble physical simulations. The output of these simulations are tensile specimens with material properties of the selected points in the physical weld

The dog-bone tensile specimen gives the traditional stress-strain response of the physically simulated weld material. Three additional tensile specimen geometries are used to extract fracture loci, given as failure-strain versus stress state. The fracture loci span shear, uniaxial and plane-strain states. Due to the limitations of the Gleeble physical simulator, some deviation from the target microstructure could be expected. Therefore a method of measuring material constitutive behaviour *directly* from the weld is required. This directly measured property would then assist in verifying the degree of accuracy that the Gleeble sample microstructures were recreated.

This information comes from instrumented indentation. In this method, the load and displacement of an indenter is measured as it is indented into a section of the HAZ. The measured data is then put through an algorithm to estimate the yield strength of the indented material. From this experiment, the yield strength distribution of the weld will be calculated. These extracted yield strengths are then compared to the yield strengths from the Gleeble tensile stress-strain curves to gauge the accuracy with which the samples were recreated. This helps to verify that the constitutive behaviour extracted from, say, point "A" can indeed be allocated to the same point in the finite element model.

In summary, the experimental procedure undertaken in this work takes the following path. Points A to E are identified as points of interest. From these locations on the weld, different thermal histories are extracted, with point A experiencing the highest peak temperature and E the lowest. This gradient of thermal histories mean that the weld exhibits a gradient of microstructures and hence mechanical properties leading away from the nugget centre. This mechanical property variation at discrete points is recreated on larger tensile destructive specimens by inputting the extracted thermal histories into a Gleeble machine and recreating the microstructures of points A to E. These tensile specimens are destructively tested. From these tests, failure loci and stress - strain curves are obtained. The material property curves extracted from the samples exposed to the thermal histories of, say, point A can then be input into the corresponding location in an FE model of the weld. But before this is done, the

accuracy with which the Gleeble samples were created is verified by comparing the yield strength extracted directly from the weld through instrumented indentation, with the yield strength of the Gleeble stress - strain curves.

To this author's knowledge, the residual stress distribution in boron steel spot welds have not been measured before. An additional process induced state extracted from the weld is the residual stress distribution, obtained through neutron diffraction. Due to the expansion during heating and contraction during cooling, significant residual stresses are expected in the weld. Residual stresses are an influencing factor on spot weld failure [18]. As an external load is applied to the weld, these residual stresses would play a role in the starting stress values and subsequent stress redistribution. In other words, it is another factor influencing the way the weld fails.

As a reference material, spot welds were also produced on 1.5 mm thick DP600 steel sheets. DP600 is a dual phase steel consisting of ferrite and 15 - 20% martensite [33, 34]. The DP600 steel is well documented and provides a ready source from which to verify experimental results. For example, the known yield strength of the base material will form one of the validation parameters from which to gauge the accuracy of the instrumented indentation tests. The steel will also provide valuable insight in relation to the neutron diffraction experiments, due to its martensite content and the effect of the ferrite phase.

1.5.3 Significance and novelty of work

Sommer *et al* [31] stated that, due to the unique material property distribution of welds made from martensitic steels, there is a need to characterise the HAZ to investigate its influence on the deformation and failure behaviour of welds during loading. A similar need was expressed by Yamazaki *et al* [35]. Sommer attempted to characterise the HAZ material by creating a failure curve through Gleeble physical simulations in a similar method described in the previous section. However, it was clear there are improvements that can be made to their techniques.

Firstly, the failure loci were determined by inverse FE simulation of the heat treated Gleeble samples. This assumes that the simulations are accurate from force-displacement curves. Deviations between the simulated and experimental data was evident in their presented data. Therefore, in this work, the failure loci are directly calculated through digital image correlation of the fracture specimens, resulting in more accurate failure curves.

The second issue is the incorrect use of dog-bone specimens to extract the uniaxial failure strain data points. Lanzerath [36] reported that standard uniaxial tension specimens cannot be used in the development of a failure locus. This is due to the need to keep the stress state constant during deformation until failure occurs. This is especially true for ductile materials where, during necking, the geometry changes significantly before fracture, leading to a plane-strain state. Lanzerath suggested performing tests with a central hole in the tensile specimen.

There is a very sharp gradient of material variation in the HAZ. Sommer attempted to characterise only the softest area of the HAZ, resulting in a weld model discretised into 3 zones; the nugget, HAZ and BM. A hypothesis is made by this author that characterising the HAZ in a more finely discretised way would capture the interaction of varying microstructures in the HAZ. A significant objective of this thesis was therefore to investigate whether such discretisation would lead to higher accuracy in predicting failure.

There is also the question of how accurately the simulated Gleeble samples produced by Sommer corresponded to their target microstructures. Instrumented indentation has been used by various authors to extract material properties from welds [37, 38, 39]. However, limited amounts of material properties can be extracted using this technique. A new methodology is presented in this thesis, whereby Gleeble physical simulations and instrumented indentation are used in conjunction. As mentioned previously, deviations from the target microstructure are expected in the Gleeble samples. The yield strength distribution calculated from instrumented indentation is compared to the yield strength from the Gleeble stress-strain curves to confirm that the microstructure has

been accurately reproduced. To this authors knowledge, such a methodology has not been presented before.

For the finite element simulations, a new method of discretising the model is proposed. Weld models are typically discretised into bulk regions in the design process, with material properties associated with these bulk regions [40, 31]. The new method uses interpolated material data (residual stress, stress-strain curves, failure loci) as a function of distance from the weld centre, to discretise the model. This is achieved by making use of the fact that LS-Dyna models are written in the form of text documents, so that they may be altered by using MatLab scripts. This offers an efficient approach of altering the model as opposed to using the traditional method of employing a pre-processor and varying the properties one-by-one. By using MatLab scripts, the material data at a specific distance from the weld centre can be assigned to the corresponding element at the same distance. One may then discretise the model by choosing the degree of interpolation of measured data points.

Chapter 2

Literature Review

2.1 Effects of boron on weldability

Yu *et al* [41] investigated welding of 2 mm thick boron steel sheets. A weld growth curve, which describes the nugget diameter as a function of welding current, was created for low electrode force (4.2 kN) and high force (6 kN), as shown in figure 2.1.1. It was found the nugget diameter decreased for higher current values under low force. The authors stated that the welding window is too small under low electrode force; hence subsequent tests were performed on welds produced with high force.

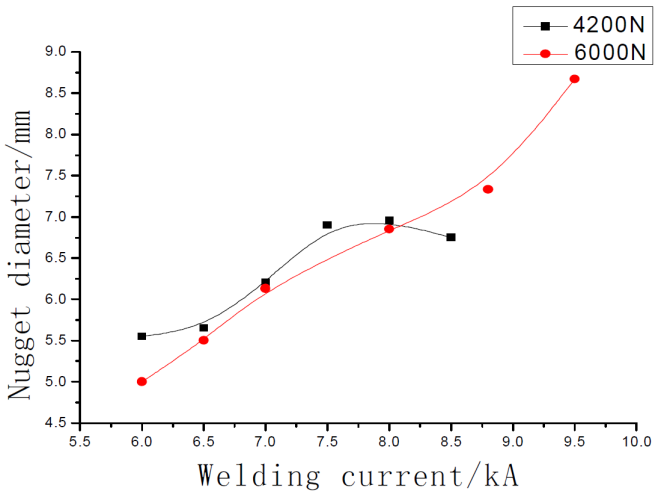

Figure 2.1.1: Weld growth curve between 2 electrode forces. Taken from [41]

The authors were able to segregate failure modes by current range, as shown in figure 2.1.2. Interfacial failure (IF) for 7 kA or less, partial interfacial failure (PIF) between

7 kA and 8.8 kA and button pull-out (BP) for 8.8 kA to 9.5 kA. No indication of the amount of samples tested was given.

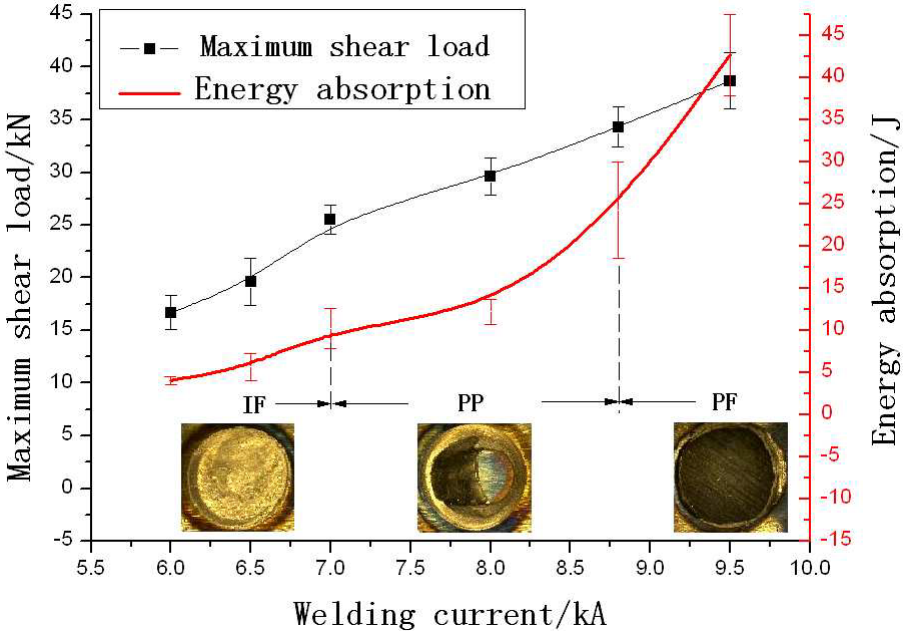

Figure 2.1.2: Relationship between current, shear load and energy absorption. Taken from [41]

The authors defined 3 HAZ areas, as shown in figure 2.1.3. Microstructural analysis was also performed on the spot welds. HAZ-1 was defined as the tempered zone where the peak temperature remained below A_{c1}[41]. Granular microstructures were identified in this zone as carbides.

Two microstructures were identified in the HAZ-2 area; martensite, and through hardness testing and elemental analysis, the other phase was inferred as ferrite. No corroborating evidence was given as to what the "ferrite" hardness was. The authors also stated that "the composition of the microstructure shows that the peak temperature is between A_{c1} and A_{c3}". No method was given as to how they arrived at this conclusion.

Fine grain martensite was identified in HAZ-3, which the authors attributed to the amount of time spent at peak temperature. This time is short, hence the austenite grains do not fully grow, causing the austenite to form fine martensite. The nugget,

which spends more time above A_{c3}, forms a "thick" [41] and brittle hard martensite.

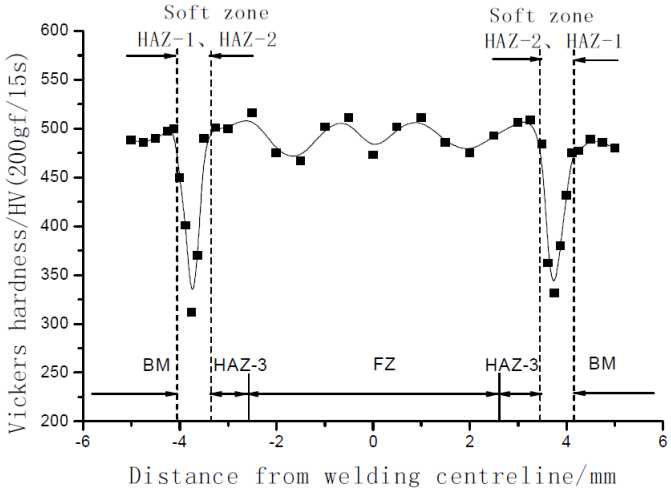

Figure 2.1.3: Boron steel spot weld hardness distribution. FZ = fusion zone (also known as the weld nugget). Taken from [41]

Choi *et al* [42] investigated welding galvanised DP780 with Aluminium (Al) coated boron steel. It might be possible that the coating was actually Aluminium-Silicon (Al-Si), however, the authors only stated Al as the coating. The authors cited the high carbon equivalent (C_{eq}) of the 2 steels as the reason for martensite formation after welding. Specifically, the authors stated that if the C_{eq} is greater than 0.24, the weld is more susceptible to crack initiation and propagation. C_{eq} is a function of alloying elements in the steel, with the aim of converting the percentage of non-carbon alloying elements to the equivalent carbon percentage [30]. This makes analysis simpler, as the iron-carbon phase diagram is better understood than other iron-alloy phases. C_{eq} is generally used to quantify the hardenability of steels [30].

The effect of current on the peak load capacity of lap-shear geometries was investigated. A drop in peak load was found to occur after 9.5 kA, as shown in figure 2.1.4. The authors reported large voids at the nugget centres for the samples which experienced expulsion. The authors reasoned that the decreased mechanical properties were due to a decrease in weld volume due to expulsions and an increase in shrinkage and solidification cracks.

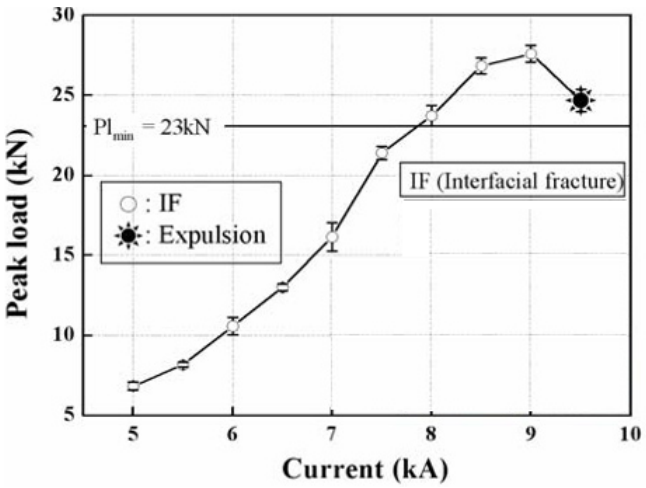

Figure 2.1.4: Peak load of weld as function of welding current (electrode force of 6 kN and 20 cycle weld time). Taken from [42].

The authors stated that the quality and strength of a weld is gauged from the size of the nugget [42]. The evidence for this can be seen in figure 2.1.4; as the weld current increases, the nugget diameter increases and the peak load increases, until expulsion, whereupon the load drops.

Microstructural analysis on the boron steel side of the weld revealed bainite in a ferrite matrix in the base material next to the HAZ and also in the HAZ. This formation of bainite was due to the slow cooling rate at the HAZ near the base material, leading to an annealing effect.

The hardness profile for the DP780 and boron steel (22MnB5) weld is shown in figure 2.1.5; with the sudden drop in hardness on the boron steel side attributed to martensite being transformed to “soft bainite in the ferrite matrix by the annealing effect” [42].

The authors did obtain a hardness distribution that has not been seen in other literature before; specifically the increase in hardness between the nugget and HAZ (between 3 and 4 mm). The authors said that the formation of carbides from the diffusion of chromium would lead to this high hardness value. This was not observed microstructurally and hence the authors cited fine martensite as the cause.

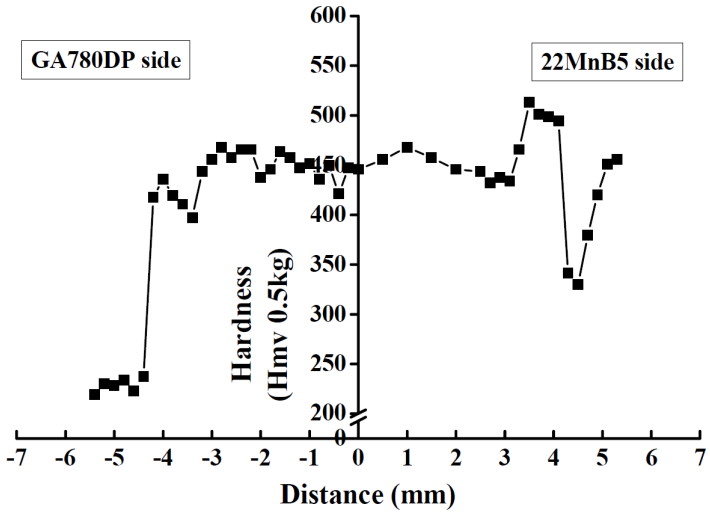

Figure 2.1.5: Hardness distribution of DP780/boron steel weld. Taken from [42]

Kong *et al* [43] performed a study on the effects of boron content and welding current on spot weld mechanical properties. 1.2 mm cold rolled complex phase (CP) steels, with boron contents ranging from 0 to 40 ppm, were used in the study. Although the initial microstructure of CP steels have a reduced martensite content, as well as additional microstructures, compared to hot-stamped boron steels, the paper does give an indication of the effects of boron content on the final weld product.

The change in resistivity of the base materials was found to be approximately 0.0011 μΩ cm/ppm over the boron composition range of 0 - 40 ppm. Hence it was suggested that such a small difference could not have an effect on the heat input. The suggestion that boron content has little effect on the nugget diameter was further evidenced in welding trials, as shown in figure 2.1.6.

In a similar fashion to welds produced from hot-stamped boron steel, the CP steel welds exhibited a softened zone in the HAZ, which was found to contain tempered martensite. It was suggested that the softening occurs due to the tempering of martensite by heating to the A_{c1} temperature. Specifically, the degree of softening depends on the amount of time spent near the A_{c1} temperature. By increasing the weld time, this retention time may be increased, leading to a higher degree of softening.

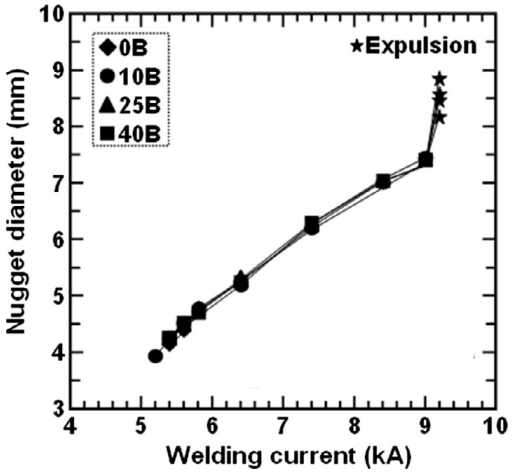

Figure 2.1.6: Nugget diameter as function of welding current and boron content. "10B" is 10 ppm, etc. Taken form [43]

2.2 Effects of coating on spot welding

Harlin *et al* [17] investigated the effect of zinc coating on welding a triple stack of low carbon steel. As seen in figure 2.2.1, it was found that the coated stack had a lower interfacial (sheet-sheet) contact resistance compared to the uncoated stack; due to the low resistivity of zinc. Increasing the electrode force reduced the contact resistance further.

An interesting point they noted was that the decrease in contact resistance at the electrode-sheet interface was proportional to the increase in electrode force. However, for the coated stacks, the contact resistance of the sheet-sheet interface at 6 kN was 5 times lower than the 2.1 kN force variant. In other words, the sheet-sheet contact resistance was reduced by 5 times, for an increase in electrode force of 3 times. From this it was concluded that using a higher electrode force would require a longer weld time to produce a nugget of given diameter.

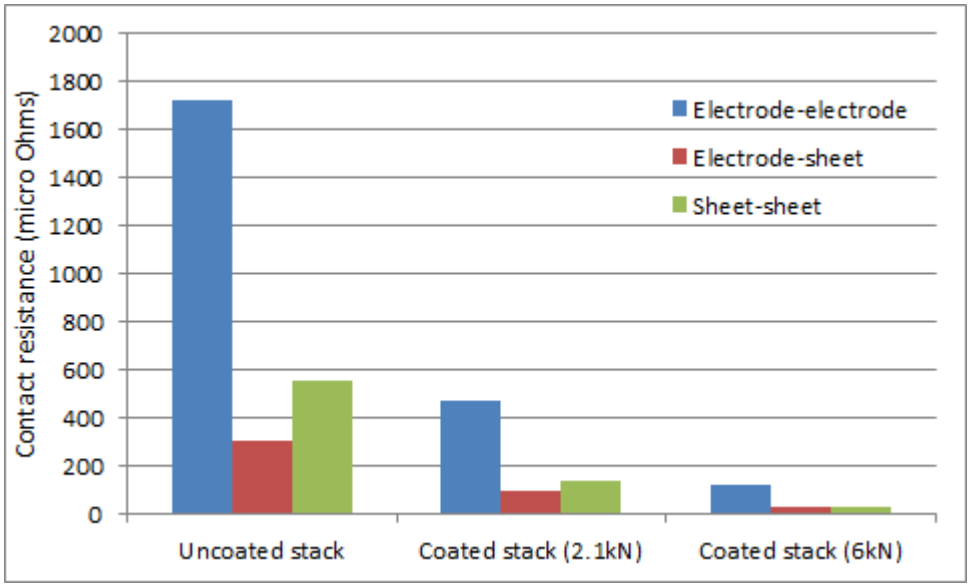

Figure 2.2.1: Contact resistances for uncoated and coated stacks. Modified from [17]

The authors defined 3 stages of nugget development; the primary stage - an incubation period where heat develops and solid bonding occurs without fusion, the secondary stage - rapid weld growth, and finally the tertiary stage - weld growth progressively decreases. Comparing the weld growth curves in figure 2.2.2 of the coated and uncoated stacks at low force, it was evident that the coated stack exhibited a longer incubation time of 1 extra cycle, due to the lower resistivity of zinc. It was concluded that, for the coated sample, either an increase in welding time or current is needed to generate the heat for weld initiation.

During the secondary stage, where the zinc is displaced from the contact areas [17], the authors expected to observe a higher rate of weld growth in the coated stack compared to the uncoated stack, due to the higher current used. This was not observed however, and it was concluded that the molten zinc segregates to the edge of the nugget, which creates a larger contact area and a low resistance path for the current.

The authors performed a metallographic study on the heat patterns developed after 4 cycles of current, which occur at temperatures greater than or equal to 750 °C [17]. The heat patterns, shown in figure 2.2.3, were observed in all 3 sheets of the uncoated

sample. For the coated sample, the patterns were only observed in the 2 outer sheets; the authors gave two reasons for the lack of heat development in the centre sheet. The first reason is zinc's low melting point (450 °C [17]), which allows it to be displaced from the centre towards the periphery of the contact area. The contact area is then increased due to the zinc segregating at the periphery; this leads to a decrease in the contact resistance which allows the heat to be dissipated more easily. The second reason is the low resistivity of zinc, where the lowest resistivity was found in the 2 contacting layers of the middle sheet and the outer sheets.

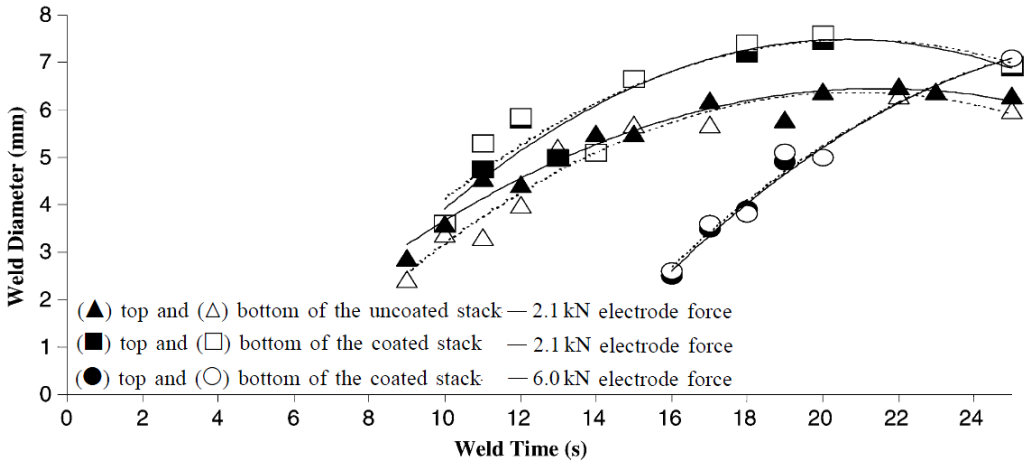

Figure 2.2.2: Weld growth curve at sheet-sheet interface at varying electrode forces. Modified from [17]

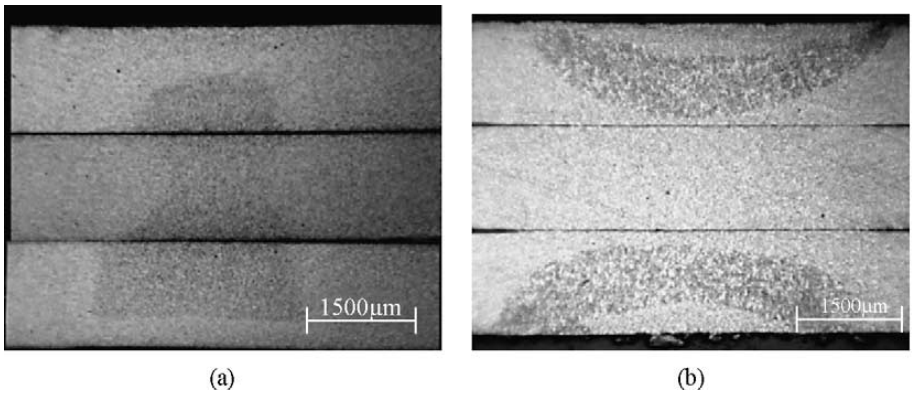

Figure 2.2.3: Initial heat development after 4 cycles of current at 2.1 kN for a) uncoated stack b) coated stack [17]

The authors used carbon imprints to investigate the contact pressure and area for low (2.1 kN) and high (6 kN) electrode forces. At the electrode-sheet interface, the contact area was consistent between low and high force. The colour intensity imprint, which indicates the contact pressure, was more consistent for the higher force. The authors concluded that the higher force improves contact and decreases contact resistance.

At the sheet-sheet interface, a similar observation was made, except the contact area was noticeably larger. From this, it was concluded that a higher force would lead to "improved cooling properties, reduced current density and interfacial resistive heating" [17], with the bulk resistance becoming the dominant heat development factor. The authors made an interesting note that the 3-stack behaves like a single thick sheet with heat developing in the geometrical centre.

By looking at the difference in shape of developed nuggets, shown in figure 2.2.4, different resistive heating mechanisms were identified for the uncoated and coated stacks. For the uncoated stack, the largest nugget diameter was observed at the sheet-sheet interface, indicating interfacial resistance as the dominant factor in forming the nugget. For the coated sample, however, the largest nugget diameter was observed in the outer sheets (with a decrease seen towards the geometric centre), indicating bulk resistance as the dominant factor. Using the higher electrode force for the coated stack required an increased weld time; limited weld growth was observed in the outer 2 sheets due to the improved cooling efficiency associated with higher electrode force. Weld growth along the sheet plane was observed however.

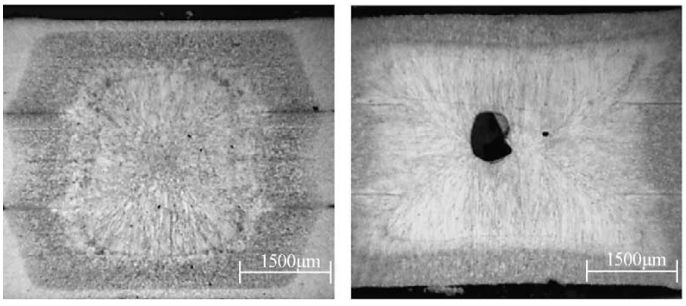

Figure 2.2.4: Locations for weld nuggets at 2.1 kN for a) uncoated stack after 9 cycles of current b) coated stack after 10 cycles of current [17]

2.3 Factors that affect fracture in spot welds

Sommer [44] cited weld diameter as the main influencing factor affecting fracture mode (BP or IF). Dancette [45] listed 3 factors that affect weld fracture; geometrical factors (weld diameter, sheet thickness etc), loading mode (normal, shear or a combination) and metallurgical factors (porosities, residual stresses, brittleness of HAZ microstructures). Specifically for martensitic steels, the HAZ is a softer zone compared to the nugget and BM, and is therefore a critical area which limits the deformation capacity of the weld [31].

Through fractography of lap-shear and cross-tension tests, Chao [18] stated that the ultimate strength is a function of sample geometry (lap-shear samples exhibit higher strengths than cross-tension samples), sheet thickness and nugget size (larger nuggets fail at higher loads). The size of the weld indentation, resulting from electrode force, was also cited as a contributing factor, with thicker sheets exhibiting a more pronounced indentation [18]. Relatively little indentation was observed for thin gauged steel (1 mm or less) and failure occurred in the BM. A deeper indentation was observed in thick gauged steel (2 mm), with failure occurring at the corner where there is a change in thickness.

Choi *et al* [42] sectioned a DP780-boron steel weld, from which all lap-shear samples failed interfacially. The sharp notch at the edge of the nugget where the sheets start to separate, was cited as a region of stress concentration during loading, from where cracks would initiate.

The boron steel investigated had an Al coating, which was also cited as a contributing factor to fracture. The authors commented that it is known that the nugget near the faying surface is weakly bonded due to the molten Al coating causing brittleness. This coated layer was also observed across the nugget where the 2 sheet's surfaces contacted, as shown in figure 2.3.1 b) and c). It was concluded that cracks initiating from the sharp notch tip would penetrate the brittle and weakly bonded region in the faying surface and subsequently travel across the fusion zone. The DP780 had a galvanitic

coating, to which no mention was made. Perhaps investigating the zinc's interaction with the aluminium could help further explain the interfacial failure.

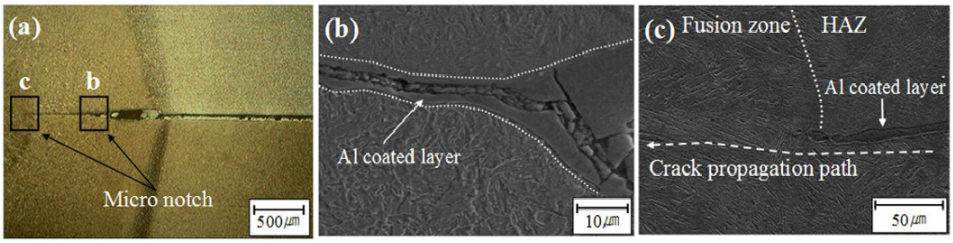

Figure 2.3.1: Optical and SEM images of 22MnB5-DP780 weld indicating aluminium coating layer. Taken from [42]

The structural differences between the HAZ and nugget/BM are an influencing factor, however, the location of the HAZ plays an important role as well [46]. As already identified, the sharp notch tip may cause a stress concentration when the weld is loaded. The difference in material properties between the HAZ and nugget/BM may *enhance* the stress concentration [46]. It was stated that an analysis was performed through FE modelling, whereby the size, yield strength, UTS and ductility of the HAZ and nugget were varied [46]. From this analysis, it was found that the ductility and ultimate load of the weld increased with nugget size, however, varying the nugget ductility and strength had little effect on weld behaviour. This behaviour was attributed to the fact that the interior of the nugget experiences relatively little stress when loaded. By increasing three parameters in the HAZ (width, ductility and strength), increases in weld elongation and ultimate load were observed [46]. From this it may be concluded that weld behaviour is sensitive to HAZ variation.

2.4 Fracture behaviour of different steel welds

Chao [47] took a theoretical approach in investigating the critical nugget diameter which separates BP and IF during cross-tension testing. The author used equations derived from fracture mechanics; relating the failure load to critical stress intensity factor. The competition between these governing equations for IF and BP failure was

investigated, with the transition between failure modes occurring where the 2 lines of the equations intersect, as indicated in figure 2.4.1. It was found that the critical nugget diameter was a function of fracture shear stress (τ_f), fracture toughness (K_c) and sheet thickness (t). In the figure, d is the nugget diameter.

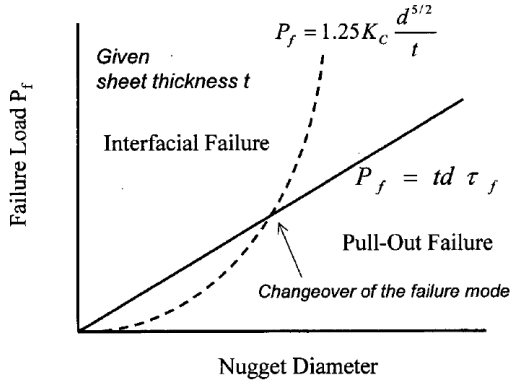

Figure 2.4.1: Competition between BP and IF [47]

The author validated his model by comparing destructive tests performed on mild steel and high strength steel; the calculated critical nugget diameter and failure load corresponded well with the separation between BP and IF. The author extended the comparison by applying the method to lap-shear samples with yield strengths varying from 206 MPa to 655 MPa.

The competition between BP and IF was able to clearly capture the critical nugget diameter which separates the 2 failure modes, as shown in figures 2.4.2 a) and b). The authors stated that the range of steels over which the model was able to capture the failure mode competition indicated the model is weakly dependent on the grade of steel. This weak dependence originates from the equation used to capture the competition between failure modes, where the ratio of the 2 material properties (fracture toughness and shear strength) leads to the elimination of the effect of material property. The author concluded that if this relation be universally applicable the ratio of τ_f/K_c must be a constant; which is approximately the case for the range of steels he used in his study. Therefore, further work would be useful to extend the range of steels to find the limits of the relationship.

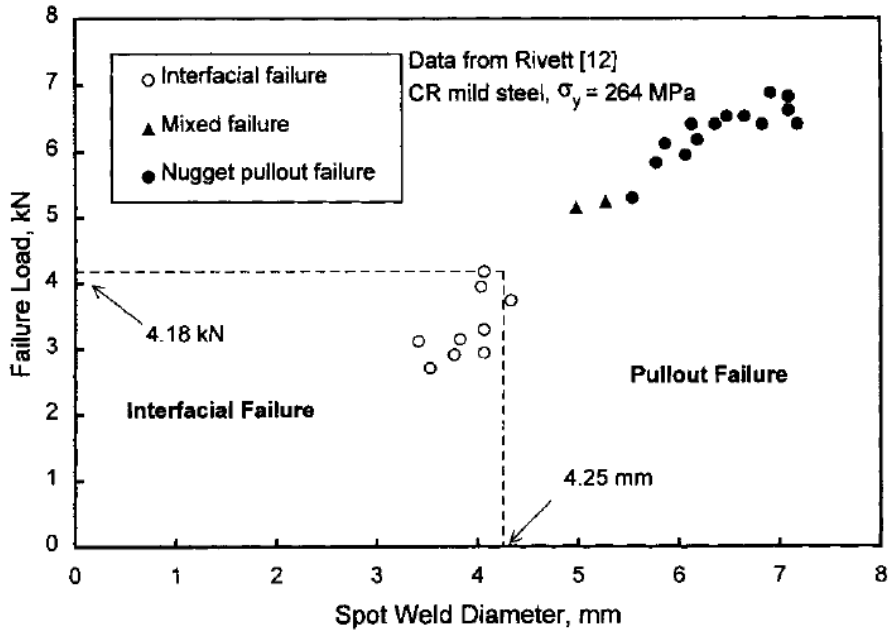

(a) Mild steel: YS = 264 MPa & UTS = 328 MPa

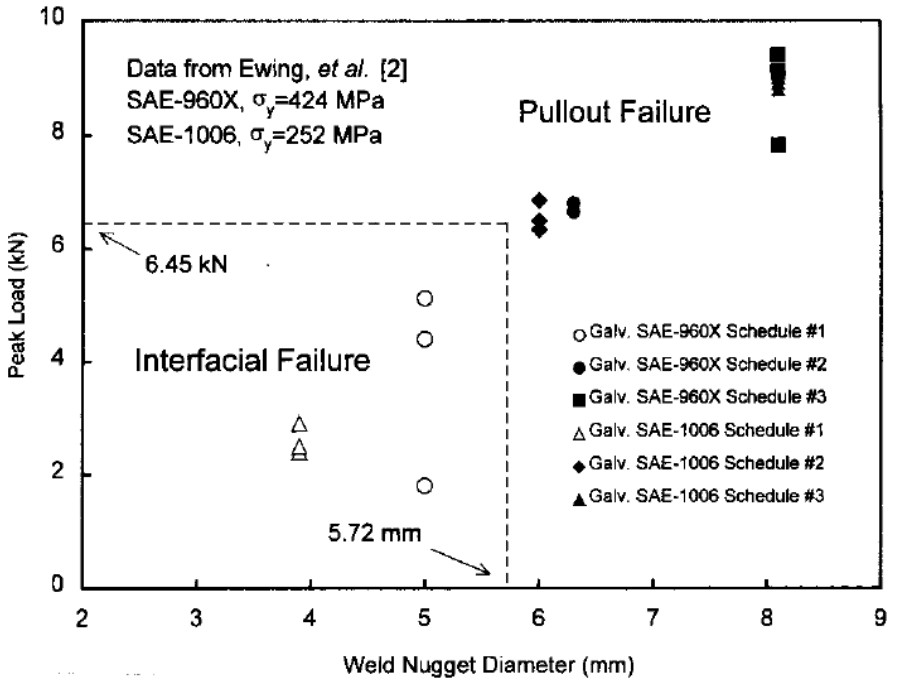

(b) SAE1006 mild steel : YS = 252 MPa & UTS = 327 MPa; SAE 960X high strength steel: YS = 424 MPa & UTS = 501 MPa

Figure 2.4.2: Test data showing IF and BP with the predicted nugget diameter separating the 2 failure modes [47]

Dancette [45] performed quasi-static cross-tension tests on small weld nuggets and large nuggets close to expulsion, with the results shown in figure 2.4.3. Five steels grades were investigated; namely IF260, DP450, DP590, DP980 and TRIP780. It was found, for large welds, the strength increased with the base metal strength, as long as the failure mode was mainly BP. The strength is defined as the maximum force normalised by sheet thickness and weld diameter ($S_{max} = F_{max}/\left(t_{sheet}.d\right)$).

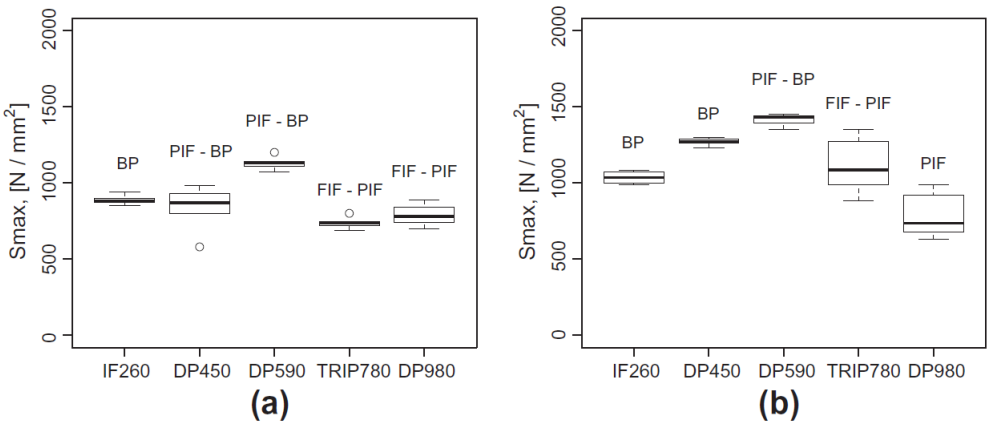

Figure 2.4.3: Normalised strength and failure type for spot welds of a) small diameter and b) large diameters. BP = button pull-out, FIF = full interfacial failure, PIF = partial interfacial failure. Taken from [45]

The steels with higher alloying levels (TRIP780 and DP980) showed a decrease in strength relative to the other steels and exhibited Partial Interfacial Failure (PIF) or Full Interfacial Failure (FIF) modes. As mentioned previously, steels with higher alloying levels exhibit a higher C_{eq}, which could be an influencing factor in crack formation. These steels show a higher level of scatter in strength as well.

It was found that smaller welds were more prone to PIF/FIF. However, there was no clear transition from BP to IF. The authors reasoned that this scatter in failure mode could be due to several reasons; the statistical nature of brittle fracture, the effect of welding process parameters on the initial notch tip sharpness, the local microstructural barriers that the crack may encounter which would lead to diverse crack paths and the effects of porosities on the crack path.

Dancette characterised the fracture behaviour of 3 zones in the weld during cross-tension testing; the BM close to the weld, the notch tip in the vicinity of the nugget and the nugget itself.

The failure mechanism in the BM close to the weld was identified as strain localisation, due to the soft BM and SCHAZ close to the hard bainitic-martensitic zone of the nugget. Ductile shear fractures were identified at the notch tip close to the nugget, leading to BP. The ductile microstructures of the nugget and HAZ (for IF260) enables notch tip blunting.

The level of shearing was less pronounced for steels with higher strength due to their harder microstructures. Semi-brittle fracture was identified as the fracture mechanism in the nugget. The semi-brittle failure leading to PIF/FIF was mainly observed for the higher strength steels (TRIP780 & DP980). Compared to DP980, the TRIP780 welds exhibited a delay in initial crack propagation from the notch tip to larger crosshead displacements.

The authors stated that this kind of behaviour can be explained by "the balance between the local energy release rate needed to propagate a crack from the notch tip and the total potential energy needed in the structure to allow unstable cracking" [45].

The authors stated that small welds were known to yield higher stress intensities at the notch tip, which favours early crack propagation. However, the total potential energy may not be sufficient to propagate the crack completely; instead the crack travels in fits and starts (stable cracking). Larger welds exhibit smoother notch tips, which experience delayed crack initiation. Hence, the elastic energy in the structure may be sufficient for unstable (sudden) cracking.

During normal loading, mild steel and High Strength Low Alloy (HSLA) spot welds showed ductile failure at the nugget boundary, which is seen as BP. The failure mode can change to brittle (PIF) failure for steels with higher amounts of alloying elements under the same loading conditions [45].

2.5 Failure prediction methods of spot welds

There are several ways to model or predict the load bearing capacity and failure behaviour of spot welds. Such methods include empirical models, limit load analysis and finite element modelling [45].

2.5.1 Empirical methods

Yamazaka *et al* [35] employed empirical methods relating the weld tensile shear strength to the tensile strength of the BM for various combinations of steels with tensile strengths ranging from 300 MPa to 1200 MPa. The empirical relations, taken from 2 different authors, gave tensile shear strength as a function of sheet thickness, tensile strength of the BM and nugget diameter. It was found that, for steels with tensile strengths above 600 MPa, the weld tensile shear strength was over-estimated by 5 to 7 kN, compared to experimental results. The authors stated that the tensile strengths of welds produced from high strength steels are reduced due to HAZ softening. The authors recommended that, for accurate estimations of failure strengths, this softening must be taken into account. This implies that further characterisation of the softened HAZ must be performed.

Lin *et al* [48] developed a "general failure criterion" for mild steel spot welds under a combined loading condition consisting of 3 resultant forces and 3 resultant moments. To develop the failure criterion, the authors performed an approximate limit load analysis; taking into account the effects of sheet thickness, nugget diameter and combination of loads. A limit load approach "is commonly used to obtain the maximum load carrying capacity of structures where plastic deformation is extensive at failure" [48]. From the limit load solution, a quadratic failure rule, employing the von Mises failure criterion, was developed.

As a starting point, the authors performed a plane-stress finite element analysis of a spot weld in a sheet. The nugget was modelled as a rigid inclusion, with the sheet

material behaviour modelled as rigid-perfectly-plastic. The reasoning behind modelling the spot weld as a rigid structure was due to the difference in hardness between the weld and sheet. The authors took the view that generally the weld exhibits higher hardness values than the BM, and hence the weld will have a higher yield strength than the sheet. This is a simplistic view and ignores any strength gradients between the sheet and weld which might affect each other. The weld was fixed in space and a displacement applied to the sheet edge. From this analysis, the authors concluded that tensile plastic deformation occurs only near a partial circumferential surface of the weld nugget. The subsequent failure criterion hence only considered plastic collapse on a partial circumferential surface.

In developing the general failure criterion, the authors found it necessary to modify the limit loads in the yield criterion to fit experimentally measured failure loads under combined loading conditions by normalising them with respect to the failure load under uniaxial opening conditions. Three correction factors, based on an assumption of material in-plane isotropy, were employed to fit the experimental results. The authors stated that the correction factors "depend upon weld nugget size, sheet thickness, sheet material and welding process" [48].

The failure criterion was validated for combined opening and shear loading, by comparing the predicted failure loads with those measured experimentally for U-shaped and square cup specimens. The authors obtained the correction factors from the experimentally measured results. For the U-shaped tests, where the specimen is subjected to uniaxial opening loading, the failure criterion over-estimated the failure loads. For the square cup tests, where the specimens are subjected to a combination of opening and shear loads, the failure criterion under-estimated the failure loads; particularly for low opening loads. The under-estimation could stem from the fact that the normalising data was not available to the authors and they subsequently estimated the normalisation factors.

A selection of the results of the analysis are shown in figure 2.5.1. For both geometries, the failure contours follow the experimental results very well, with some slight underes-

timation for the square-cup specimens. This indicates that this is a promising method for predicting spot weld failure. It is, however, difficult to apply it to boron steel spot welds. As mentioned previously, Lin's criterion stemmed from the fact that the weld was considered as a rigid inclusion in a rigid-perfectly plastic sheet, with plastic collapse only considered on a partial circumferential surface. This assumption cannot be made with a boron steel spot welds, where the weld and BM have similar strengths and the area of reduced material strength lies in-between. The shortcomings of the "rigid button inclusion" will be detailed further in this section.

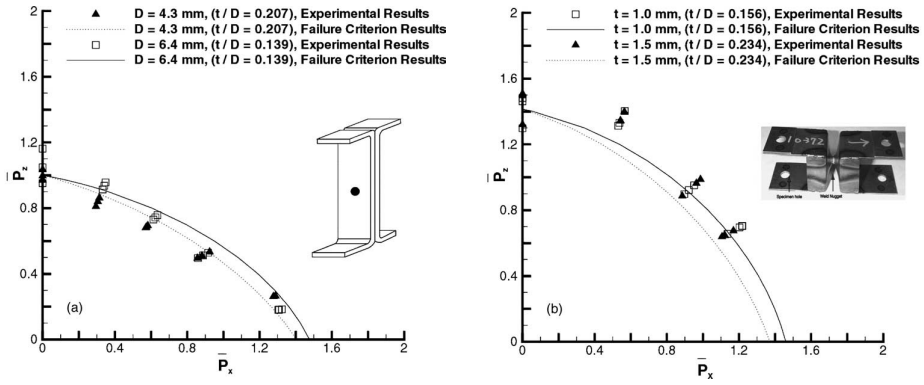

(a) U-shaped specimens (b) Square cup specimens

Figure 2.5.1: Failure loads predicted from limit load analysis for 2 spot weld geometries. $\overline{P}_{x/z}$ are the normalised loads in the x and z direction. Taken from [48]

2.5.2 Analytical methods

Chao [18] developed a mechanics based failure rule using the von Mises criterion. This criterion only considered nugget pull-out failure, hence interfacial failure was not addressed. Fracture surfaces from lap-shear and cross-tension tests were examined to identify the fracture mechanisms. Simplified stress distributions around the weld were assumed, as shown in figures 2.5.2 and 2.5.3. The steel type was not stated, although the UTS was given as 434 MPa. The predicted maximum tensile stress from the derived failure criteria compared well to finite element results, as well as comparisons to experimental results from other authors. The author also extended the failure criteria

to deal with mixed normal/shear loading. For this case, the predicted strengths were higher than the experimental results.

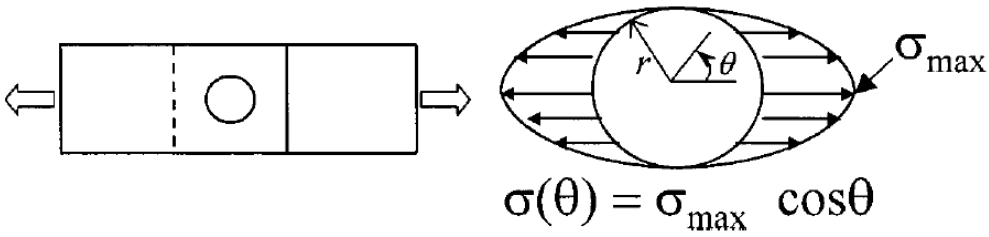

Figure 2.5.2: Assumed simplified stress distribution around weld in lap-shear test. Taken from [18]

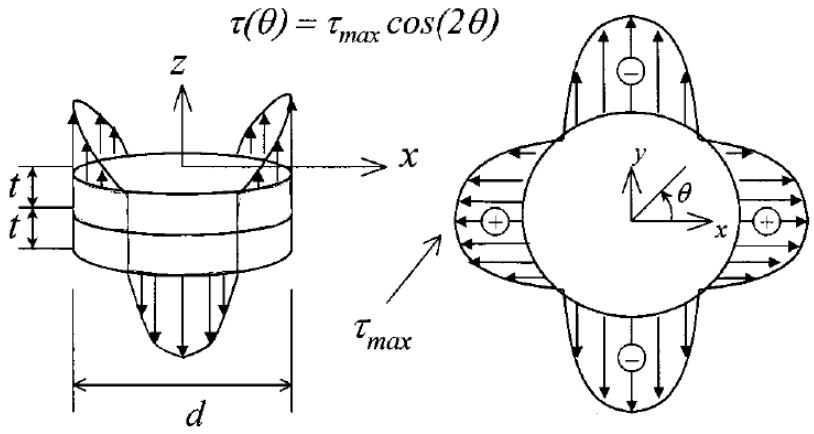

Figure 2.5.3: Assumed simplified stress distribution around weld in cross-tension test. Taken from [18]

The advantage of using such analytical techniques is obvious. As stated by the author, weld strength is related to many factors including residual stress, material inhomogeneity and welding parameters. A mechanics based model which takes all these factors into account would require significant experimental effort. The method presented by Chao would circumvent such efforts. The challenge, in applying this to martensitic boron steel welds is the main assumption that this model was based on. The author stated that "the yield stress in the nugget is generally one to three times of the base material", hence it was concluded that it is reasonable to assume a rigid button embedded in a ductile sheet. The rigid button assumption was also applied by Zhang [49]

for fracture mechanics solutions to spot welds. This assumption is not valid for a weld made from martensitic steel, where the nugget and base material have very similar microstructural properties. Again, this implies a need to investigate and characterise the HAZ zone.

2.5.3 Finite element modelling

Modelling loading of spot welds through FEA offers the chance to visualise the evolution of stresses and strains in a manner not afforded in a physical way, due to the small size of the weld and the fact that is it usually obscured by the BM.

Sommer *et al* [31] investigated fracture prediction of boron steel spot welds. The authors stated that, for an accurate simulation of UHSS spot weld fracture, failure initiation inside the soft HAZ has to be taken into account. This sentiment echoes the comments in sections 2.5.1 and 2.5.2. As will be described in section 2.6, Sommer extracted three failure-strain versus stress triaxiality ($\varepsilon_f - \eta$) failure loci through Gleeble thermo-mechanical physical simulated tensile and shear samples. These curves represent the failure strains of the nugget, HAZ and BM and were used to describe material behaviour in subsequent spot weld simulations. The stress triaxiality is a method for describing the stress state of a material and is calculated as the ratio of mean stress to von Mises stress and is written as $\eta = \frac{\sigma_m}{\sigma_{VM}}$. Simulations were performed in LS-Dyna with the material deformation and failure being modelled using von Mises plasticity in combination with ductile damage and failure criteria based on equivalent plastic strain.

An investigation was performed in how element size affects the subsequent simulations. In order to reduce the mesh size dependency of the failure initiation, the failure locus was scaled depending on the element size, with the scaling factor determined through inverse tensile test FE simulations. No indication of the accuracy of the scaling or assumptions used in the method was given. The scaled failure curves are shown in figure 2.5.4. Inverse FE simulations were used to calculate the plastic properties by

incrementally varying properties in an FE model to produce a load-displacement curve similar to an experimentally measured one.

Tensile dog-bone specimens with a spot weld in the gauge area were modelled with increasing element size (0.75 mm 1.5 mm, 3 mm), with the HAZ represented as a single row of shell elements, as shown in figure 2.5.5. It was stated that the model with the largest element size showed an underestimation in tensile strength, being due to an over-estimation of the HAZ width. To compensate for this, the authors decreased the scaling factor of the failure locus for 3 mm elements and increased the yield curve. The results can be seen as the solid black line in figure 2.5.6. The authors stressed that such a technique is purely phenomenological and should be revised for further simulations. As can be seen from figure 2.5.6, all element sizes tend to over-estimate the strain at failure.

An investigation was also performed on a simplified spot weld geometry in shear, axial and combined loading conditions, using KS2 specimens, as shown in figure 2.5.7. These welds were modelled using the *MAT_100_DA [50] material model in LS Dyna. This material model employs a single hexahedron solid element tied to shell elements making up the sheet. The weld is modelled with an isotropic hardening plasticity rule.

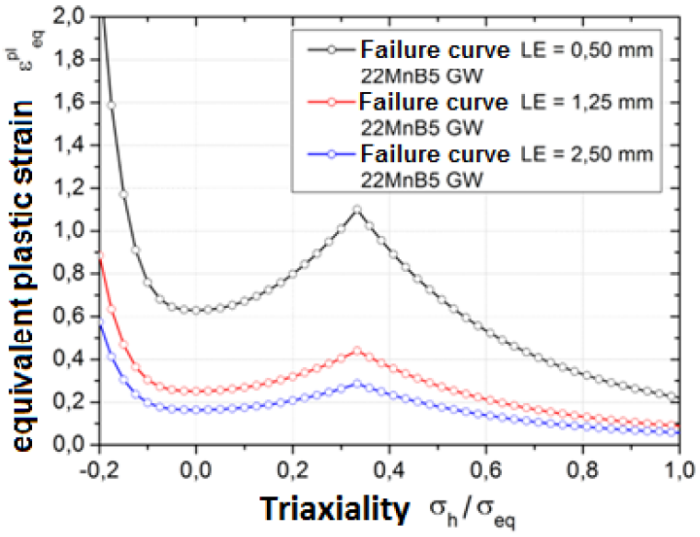

Figure 2.5.4: Scaled failure curves for element sizes of 0.5 mm, 1.25 mm and 2.5 mm. LE = element length. Taken from [31]

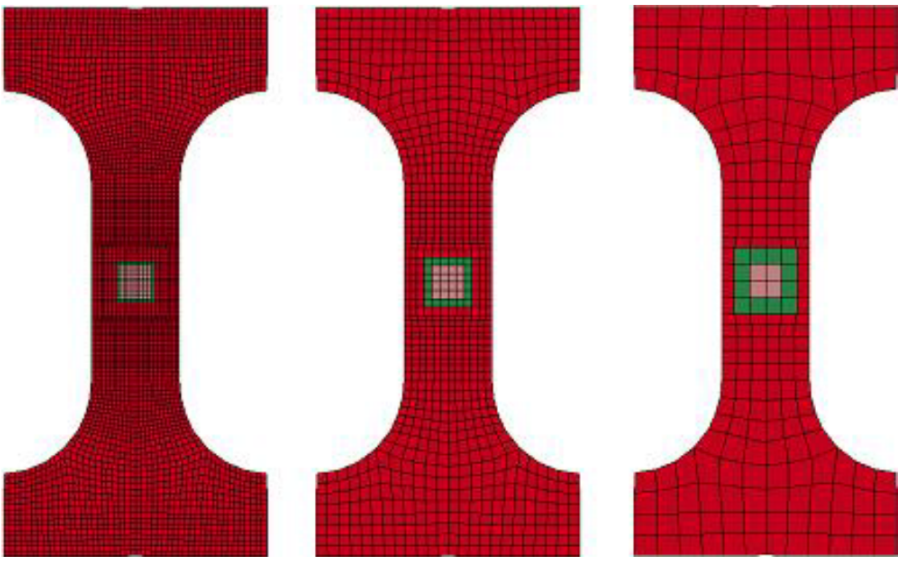

Figure 2.5.5: Tensile specimens with central spot welds. Element sizes 0.75 mm, 1.5 mm and 3 mm (l-r). Softened HAZ shown in green zone. Taken from [31]

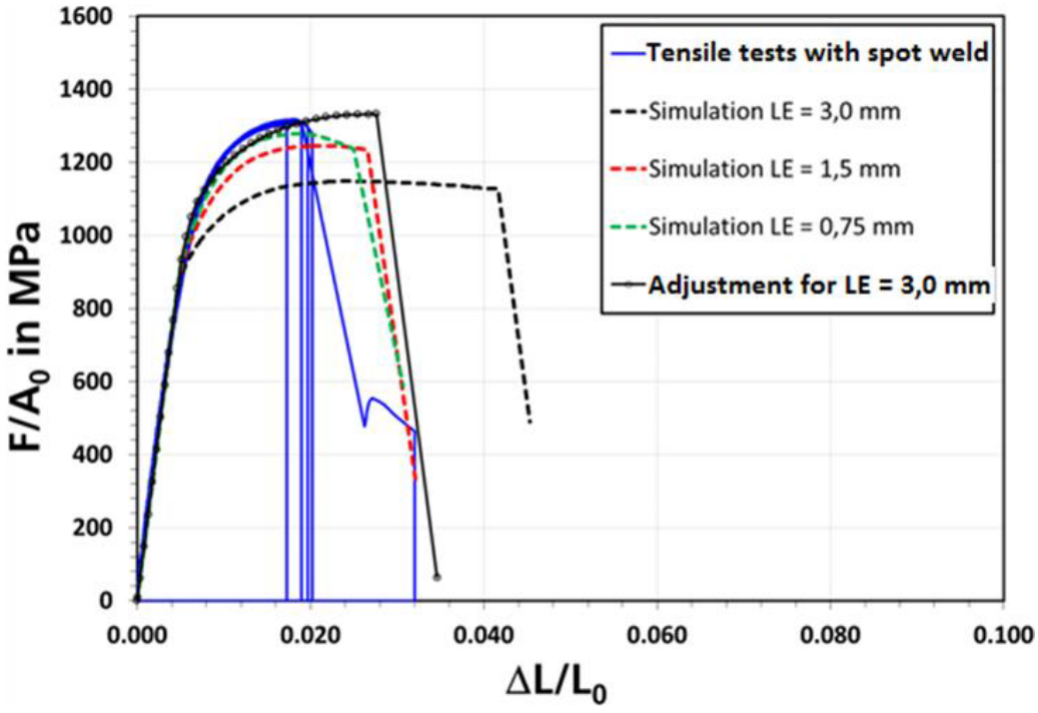

Figure 2.5.6: Experimental and simulated stress strain curves of tensile specimens with central spot welds with varying element sizes (LE = length of element). Taken from [31]

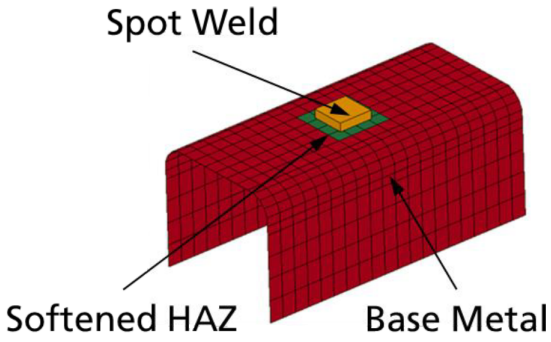

Figure 2.5.7: One half of modelled KS2 specimen. Taken from [31]

KS2 geometries were physically tested and simulated at loading angles of 0°, 30°, 60° and 90°, as shown in figure 2.5.8. A comparison between experimental and simulated results can be seen in figure 2.5.9. The figure is quite cluttered and individual results difficult to distinguish. The 0° loading angle experimental curve seems to start at 0.5 mm displacement, making a comparison with the simulation difficult. Nevertheless, the correct peak load seems to have been modelled. The 30° loading angle slightly underestimated the peak force and overestimated the displacement. The 60° loading angle achieved the correct peak load, but underestimated the displacement by approximately 1 mm. A similar case occurs for the 90° simulation.

Overall, these simplified models tend to simulate the weld behaviour quite accurately, although the load and displacement at failure results could potentially be improved. Most likely, the accuracy in modelling the load response stems from the fact that material constitutive behaviour of specific weld areas were extracted and assigned to the corresponding areas in the weld model. The inaccuracies in the final load and displacement at failure are most likely due to the weld and HAZ geometry not being properly reproduced. The authors admitted that this method of representing the spot weld as a single solid element suffers from the fact that, regardless of the failure type, failure is reproduced by elimination of the solid weld element; leaving the previously connected sheets undamaged [31]. It is therefore likely that a more detailed weld model, with the weld geometry accurately reproduced, will lead to higher accuracies in fracture behaviour.

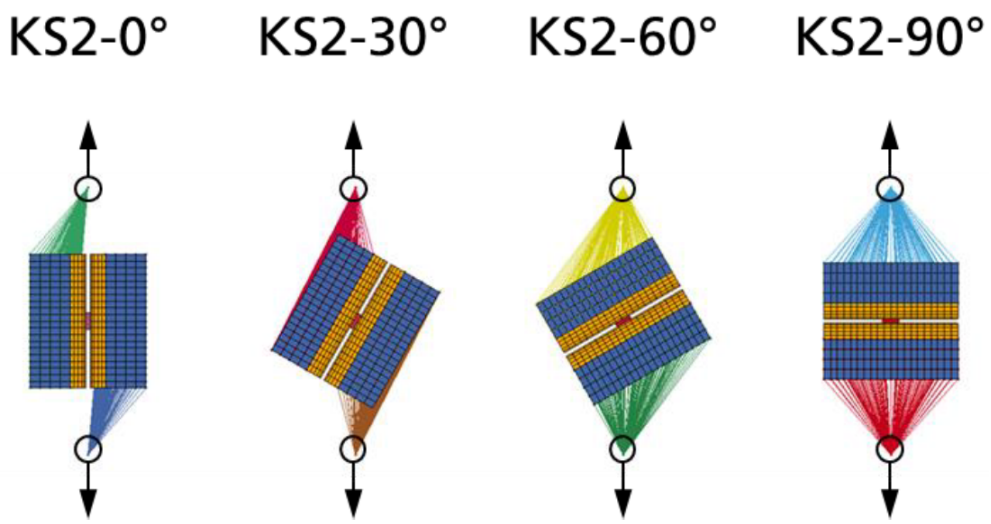

Figure 2.5.8: KS2 specimen loading angles. Taken from [31]

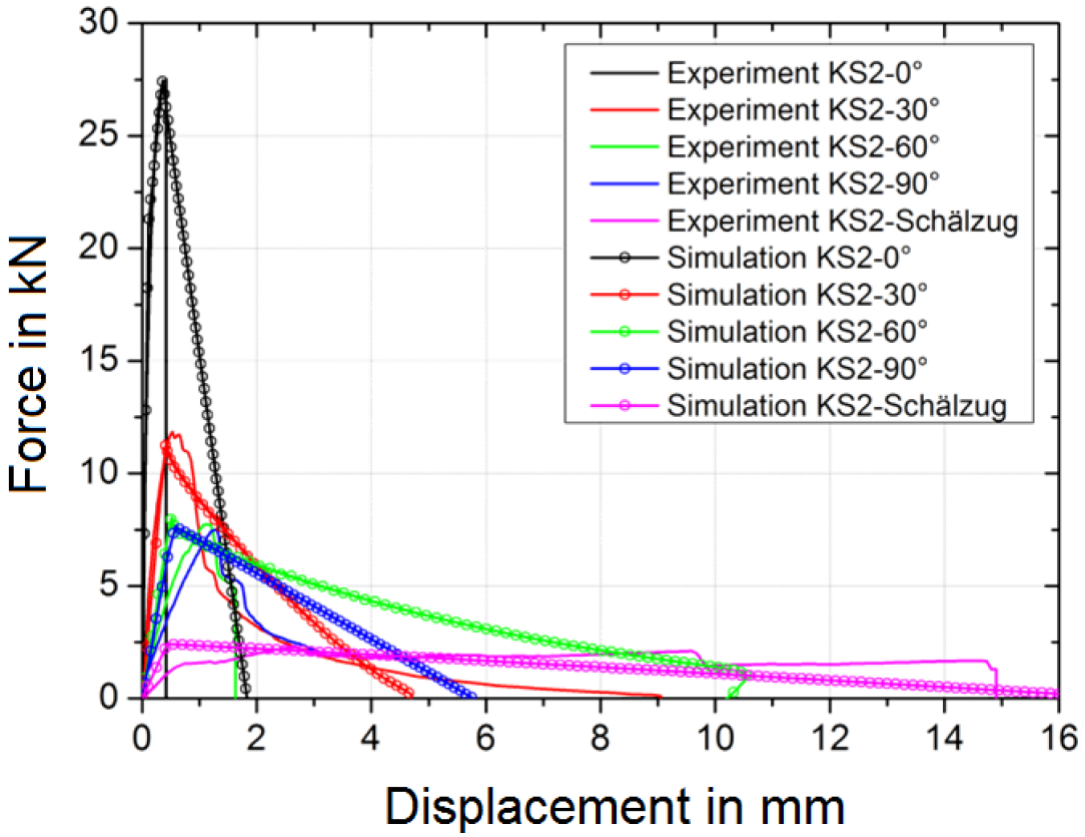

Figure 2.5.9: Experimental and simulated force - displacement results for KS2 specimens. Taken from [31]

Apart from the work of Sommer, there are relatively few published works on modelling boron steel spot welds. Therefore works and methodologies concerning the modelling of welds from other steel grades will be considered.

Dancette *et al* [45] characterised and modelled welds of Advanced High Strength Steel (AHSS). The authors characterised the HAZ constitutive behaviour through Gleeble physical simulations, as will be described in the next section. Dancette's weld model geometry was obtained from metallographic cross sections, with the model sectioned into 3 parts, as shown in figure 2.5.10. The weld nugget and CGHAZ were assumed to exhibit similar bainitic/martensitic flow properties, and were hence modelled as one structure.

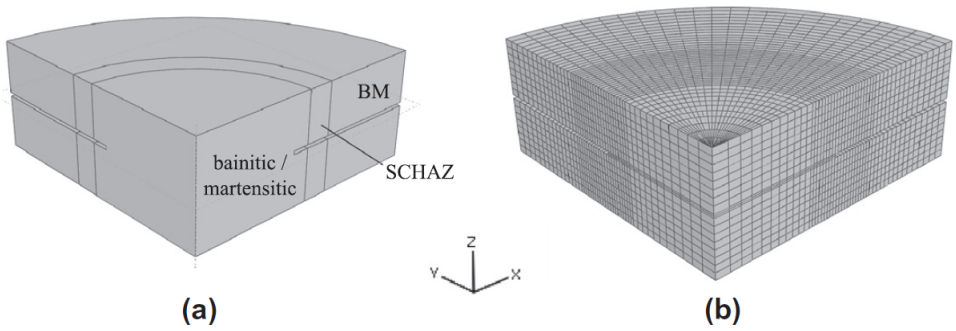

Figure 2.5.10: Cross-tension model a) discretisation of weld zones b) mesh. Taken from [45]

The von Mises yield criterion was used to describe the yield locus. The failure criterion was used in terms of local fracture strains, which were obtained from tensile tests. These tensile specimens were heat treated through a Gleeble machine to represent the HAZ microstructure of a weld. There is a problem, however, with using standard tensile specimens to obtain uniaxial fracture strains, as will be explained next.

It has been reported [36] that standard uniaxial tension specimens should not be used in the development of a failure locus. This is due to the need to keep the stress state constant during deformation until failure occurs. This is especially true for ductile materials where, during necking, the geometry changes significantly before fracture,

tending to a plane-strain state. An improvement would be to use samples with a central hole in the tensile specimen, as suggested by Lanzerath [36].

The authors acknowledged that use of such fracture strains assumes that "the levels of stress triaxiality in potential failure zones is approximately the same as ones experienced in the necking region of tensile samples" [45].

The authors also acknowledged that fracture behaviour dominated by crack propagation (i.e. IF) will not be addressed with the fracture strain failure criterion. That is to say only ductile fractures will be addressed (BP or strain localisation). The authors justified their technique by citing the fact that using experimentally measured fracture parameters avoids extensive fitting procedures required with more advanced damage models, for example in Gurson [51].

Ductile shear in the BP zone was properly reproduced for a small DP450 weld, with the load bearing capacity and extension acceptably modelled, as shown in figure 2.5.11 a). In order to simulate strain localisation in the BM and SCHAZ, the same simulations were run, but with a bigger nugget diameter. However, to properly reproduce fracture, the authors found it necessary to increase the SCHAZ fracture strain by 0.3; where the previous value resulted in a 12% underestimation of load bearing capacity. With such changes, the load-displacement curve was well reproduced, as shown in figure 2.5.11 b).

The authors admitted that their failure criterion has reached it's limit; where neither the influence of damage on the constitutive behaviour nor the effect of local stress triaxialities are accounted for. As an example,the authors stated that damage in the BP zone, for larger welds, is postponed due to smaller stress triaxialities, with strain localisation in the BM/SCHAZ leading to fracture occurring instead. Fracture initiates in the inner surfaces due to superimposed bending and tension. Further vertical displacement would tear the specimen in the BM; it is this final step which the model is unable to reproduce. FIF occurs through brittle mode I crack propagation at the faying surface [45], hence the ductile fracture strain criterion used in the previous simulations would not suffice.

Dancette's [40] next model attempted to recreate the competition between semi-brittle fracture through the faying surface leading to interfacial failure and ductile fracture leading to button pull-out for a TRIP780 steel weld. In modelling the semi-brittle interfacial failure, cohesive zones along the faying surface were introduced.

The cohesive zone elements allowed modelling of decohesion at an interface and was implemented along the expected crack path, with the elements having the constitutive behaviour shown in figure 2.5.12. Failure occurs in the elements at a critical displacement (δ_c), as shown in figure 2.5.12. The authors used a "traction-opening" profile, which accounted for a linear decay in load-bearing capacity upon reaching a maximum traction ($\hat{\sigma}$) up to a critical displacement (δ_c).

Heterogeneous and *homogeneous* weld configurations were physically tested and simulated, where "heterogeneous" means welded sheets of unequal thickness and "homogeneous" means sheets of equal thickness. Good agreement was achieved in simulating the load bearing capacity of homogeneous weld assemblies, as shown in figure 2.5.13. The failure load and displacement were slightly underestimated for the 5 mm weld diameter model, noted as "FEA d5" in the figure.

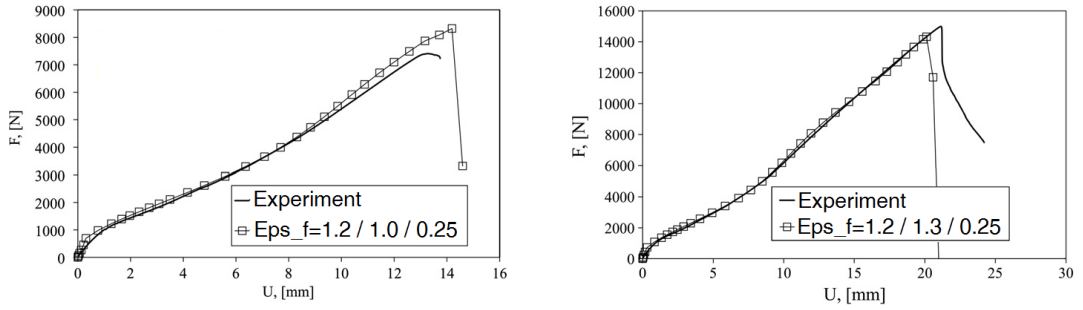

(a) Ductile shear failure of small DP450 weld

(b) Strain localisation failure of large DP450 weld

Figure 2.5.11: Load displacement curves for a) small and b) large DP450 welds. "Eps_f" is the failure strains used for BM, SCHAZ and CGHAZ respectively. Taken from [45]

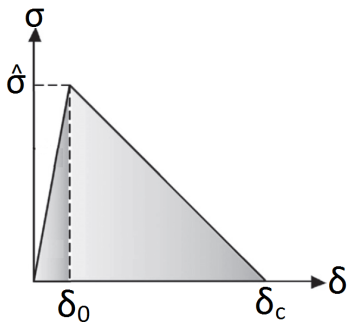

Figure 2.5.12: Cohesive zone model at faying surface. $\hat{\sigma}$ is the maximum stress and δ_c is the critical displacement. Taken from [40]

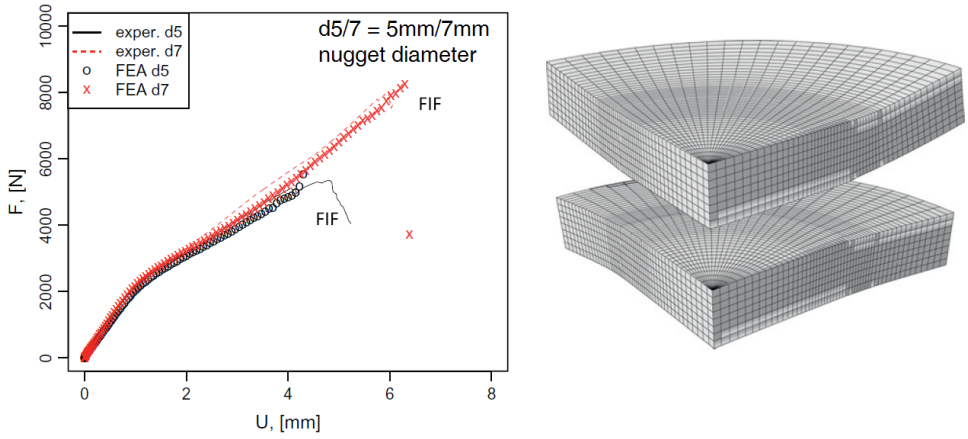

Figure 2.5.13: Predicted and experimental load - displacement curves for a homogeneous sheet assembly (both sheets 1.5 mm thick). Taken from [40]

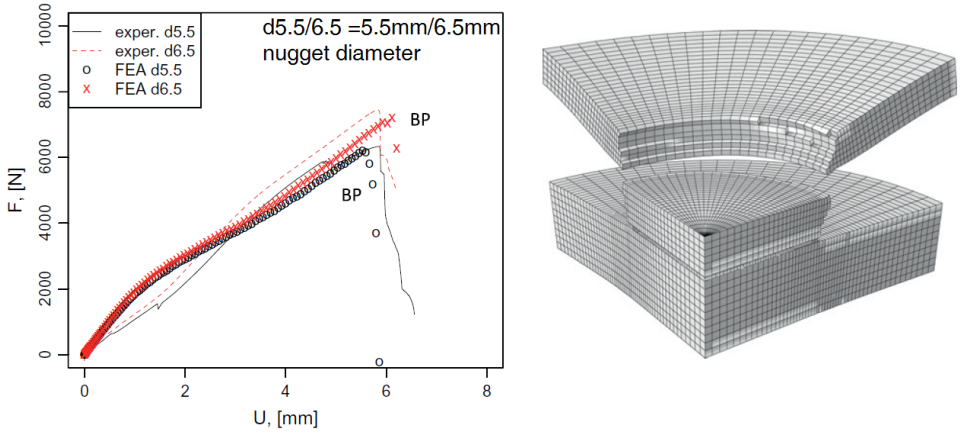

Figure 2.5.14: Predicted and experimental load - displacement curves for a heterogeneous sheet assembly (1 mm / 2 mm). Taken from [40]

A slight difference was seen in the initial response in the simulation of heterogeneous assemblies, as shown in figure 2.5.14. The authors cited difficulties in gripping the heterogeneous sheets with equal pressure, leading to sliding early in the test.

In their work, the authors reproduced the onset of crack propagations well and reproduced the failure type in all simulations. It must be noted that no indication of the amount of physical weld destructive tests was given. Therefore, one cannot say if interfacial failure and button pull-out occurred for the same weld configuration between different tests. It would be interesting to see if applying a cohesive zone model to boron steel weld simulations would achieve the same result.

In order to simulate ductile damage in a DP600 weld, Sommer *et al* [44] employed an an extension of the Gurson model; a micromechanical damage model which takes the shapes of voids into account and predicts the decrease in load bearing capacity as porosity increases. To model the brittle interfacial fracture, the maximum critical shear stress is used as a stress criterion. The Gurson model, extended to take void elongation into account, was implemented into ABAQUS with a subroutine which utilises 2 failure criteria; the Thomason formulation [52] and the Brown and Embury formulation [53].

The Thomason fracture criteria describes plastic collapse of the material between voids. The criterion fails, however, when applied to uniaxial tension; where the model calculates that the voids elongate indefinitely rather than coalesce.

The Brown and Embury criterion assumes that shear band formation between two voids causes fracture, with shear band formation occurring once the mean radius of the void reaches a critical value. The author applied the maximum shear stress criterion as the final failure criterion. All three criteria compete during simulation, with the most critical criterion initiating fracture.

During simulation, fracture was initiated for the small weld (3mm diameter) through the Embury criterion, where critical shear stress is reached and the nugget fails by IF. The load drop in this simulation was not as sudden as the one observed during experimentation. BP was initiated by the Thomason criterion. The author could accurately

reproduce the load bearing capacity; however, the stiffness was over-estimated and the displacement at fracture underestimated, as seen in figure 2.5.15. During testing the weld failed by BP and IF; whereas the model could only reproduce BP due to the ductile fracture failure criteria being employed.

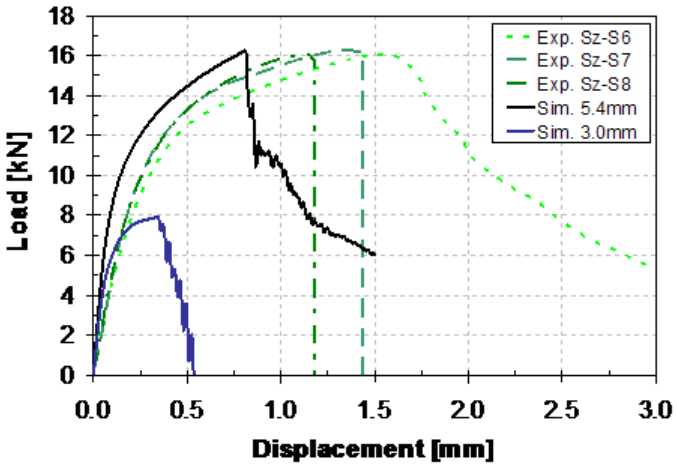

Figure 2.5.15: Experimental and simulated load - displacement curves for spot welds subjected to lap-shear loading. Taken from [44]

2.6 Extracting weld constitutive behaviour

Kong *et al* [54] presented a methodology whereby weld properties were extracted through the instrumented indentation technique, using a conventional hardness tester. No detail of the steel investigated was given, although from the BM stress-strain curve, the UTS was approximately 400 MPa. The load-depth curves were calculated by performing indents at various loads and indentation depths calculated according to the measured indent diagonals. In total, 5 weld areas were characterised (nugget, BM and 3 HAZ zones). Little detail is given in the paper as to how to calculate the indentation depths. These calculated indentation load-depth curves were used as input in an inverse FE model to calculate the stress-strain curves of HAZ zones. The calculated BM stress-strain curve was favourably compared to the experimentally measured curve, and used as validation for the rest of the HAZ curves. The stress-strain curves were

used as input in an FE simulation to model a lap-shear test, using the Gurson model for ductile failure. Close correspondence to the experimental results was obtained, as shown in figure 2.6.1.

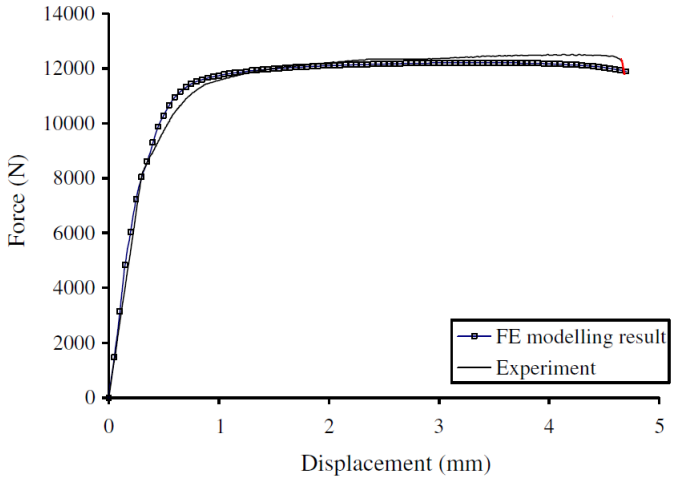

Figure 2.6.1: Force-displacement curve for lap-shear test. Taken from [54]

Dancette *et al* [55] took an experimental approach in characterising the microstructures and mechanical properties of local HAZ zones of DP590 steel welds. The weld schedule used to produce the physical welds was simulated using SORPAS. The measured distance from the physical weld centre, where hardness reached a minimum, was correlated to the thermal history experienced in the simulated weld at the same distance.

This extracted temperature history was physically simulated on a Gleeble thermo-mechanical simulator, with the purpose of producing tensile test pieces with similar mechanical properties as the point in the HAZ with lowest hardness. The water quench technique produced cooling rates approximately 2 times higher than the cooling rates predicted by SORPAS. The helium cooling device produced cooling rates between 20% - 60% of the SORPAS predicted cooling rates.

The authors found it necessary to adjust the simulated welding current in order to bring the simulated weld diameter closer to the physical diameter. This increased current could shift the location of the chosen peak temperature locations and hence lead

to discrepancies in which microstructure was actually simulated. The authors, however, verified correct simulated microstructure by comparing hardness levels in Gleeble samples with physical welds. The microstructures were also favourably compared using optical microscopy.

The authors concluded that the gradient of mechanical properties of the weld and HAZ could be captured by considering just 2 alterations of the BM constitutive behaviour; which consists of the softening of the HAZ and the increased yield strength of the martensitic zones of the weld. Tensile tests of the Gleeble samples were performed and the extracted material properties were subsequently used in the models described in the previous section.

Sommer *et al* [31] performed a novel tensile test, whereby 2 spot welded boron steel sheets were separated using electrical discharge machining (EDM) and tensile specimens machined from the sheets. Compared to the BM, the weld tensile specimen's UTS decreased by 260 MPa, shown in figure 2.6.2. The weld tensile specimens exhibited a 60% decrease in uniform elongation. It was also shown, through Digital Image Correlation (DIC), that strains localise inside the softened HAZ as elongation increased, as shown in figure 2.6.3.

To describe the damage and failure of the weld, the authors created a failure locus, defined as the failure-strain as a function of stress triaxiality. This was achieved by recreating 3 material zones (BM, softened HAZ and weld nugget) through Gleeble simulations onto tensile and shear specimens. The failure curves for the 3 material zones were calculated by inverse finite element simulation of the tensile and shear tests. Simulations were performed in LS-Dyna with the material deformation and failure being modelled using von Mises plasticity in combination with ductile damage and failure criteria based on equivalent plastic strain.

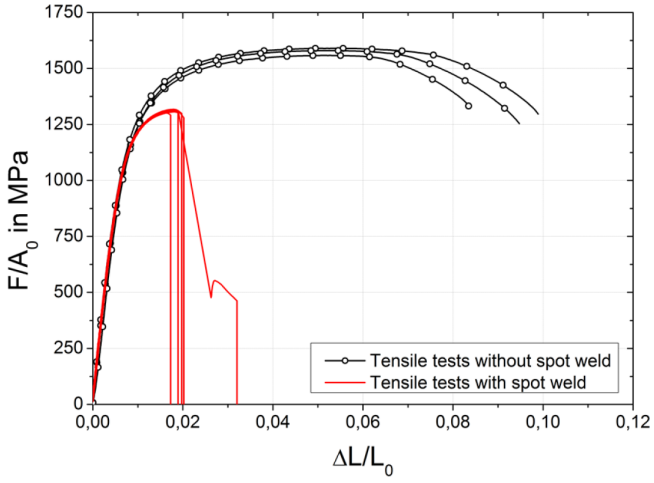

Figure 2.6.2: Tensile tests of EDM separated samples with and without spot welds [31]

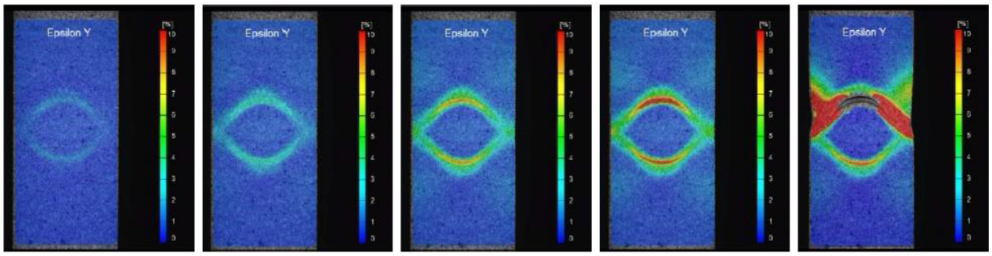

Figure 2.6.3: DIC measurements of tensile specimens with spot welds indicating strain evolution in the HAZ. Taken from [31].

Examples of the simulation results and geometries used in the creation of a failure curve are given in figure 2.6.4. From these simulations, the equivalent plastic strain and stress triaxiality were extracted. As can be seen from the figure, there are some discrepancies between the simulated and measured results, which could lead to inaccurate plastic strains. An improvement on this technique would be to use DIC to directly measure the plastic strains and stress triaxialities.

The calibrated material models were validated by simulating the tensile tests with spots welds and comparing the load-displacement output with experimental results, as shown in figure 2.6.5. The tensile test simulations overestimated stress and elongation at crack initiation. These over-estimations were likely due to the techniques used to extract the failure locus parameters.

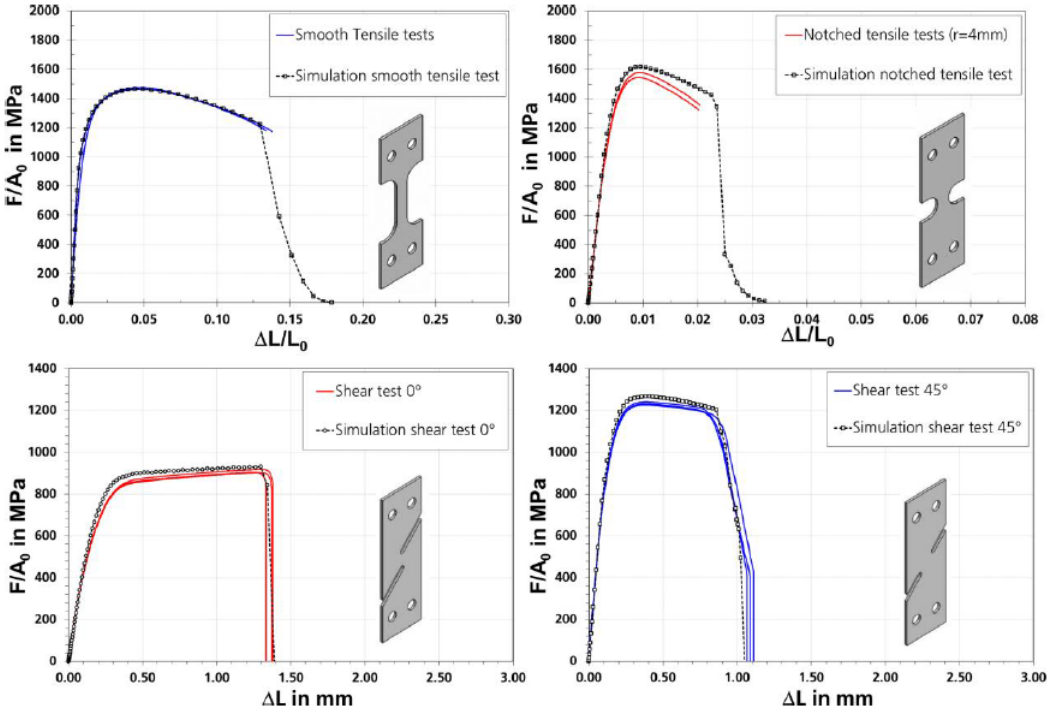

Figure 2.6.4: Comparison of experimental and simulated force-displacement curves for boron steel BM, used to create a failure curve. Taken from [31]

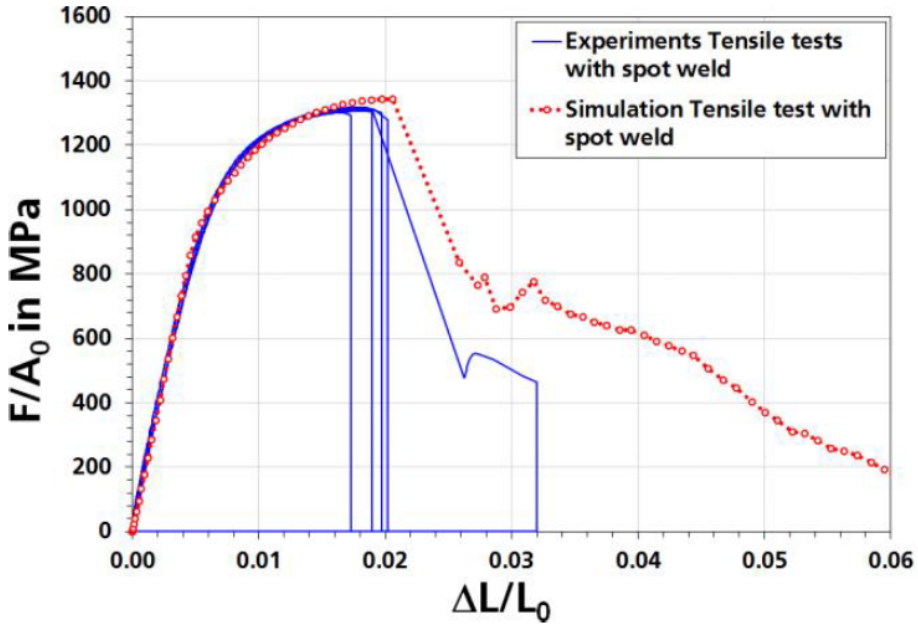

Figure 2.6.5: Comparison of experimentally measured tensile tests and simulations utilising the failure curve. Taken from [31]

2.7 Residual strain measurement

Residual strain measurement techniques can be broadly classified into destructive and non-destructive techniques, with different methods within each classification. Destructive techniques include hole drilling, where a hole is drilled into a sample, causing the stresses to relax and lead to a change in shape. The strains are measured using a rosette of strain gauges or interferometry, providing data for back-calculations of residual stresses. Although cheap, it is difficult to obtain reliable measurements beyond a depth equal to the hole diameter [56].

The deep hole drilling method can measure residual stresses up to a depth of 750 mm [57]. The basic operation is as follows: a reference hole is drilled and the internal diameter measured, then a cylinder containing the reference hole is trepanned. The change in height of the column is measured during the trepanning. The reference hole diameter is measured again after the trepanning operation and the change in diameter and height are converted to stress [58]. This technique is not applicable for components with a thickness of 6 mm or less [57], and is hence not suitable for the two 1.5 mm thick sheets welded together.

Destructively testing the spot weld is to be avoided, as the weld used in the residual stress experiments will later be used for hardness and instrumented indentation testing. Performing these tests on the same weld will give a good understanding of how the residual stress, hardness and yield strength distributions are related.

Non-destructive methods include electron, x-ray and neutron diffraction. Due to the strong interaction between electrical charges, electrons have a very small penetration depth; hence the technique is more suited for measuring very thin samples (< 100 nm) [59]. Neutrons and high-energy synchrotron x-rays have similar penetration depths, in the order of tens of millimetres [60]. With similar penetration depths, the choice between neutron and synchrotron x-ray diffraction comes down to the geometry over which measurements are made, known as the gauge volume shape. Due to the diffraction angle being ~90 ° for neutron diffraction, one obtains a near cubic gauge volume,

as seen in figure 2.7.1 a). Compared to neutron diffraction, the low scattering angles (~10 °) used in synchrotron x-ray scattering leads to a very elongated gauge volume [61], as seen in figure 2.7.1 b). In the 1.5 mm thick welded joints used in this project, the elongated gauge volume would lead to averaging of both the top and bottom layers, leading to spatial resolution deterioration.

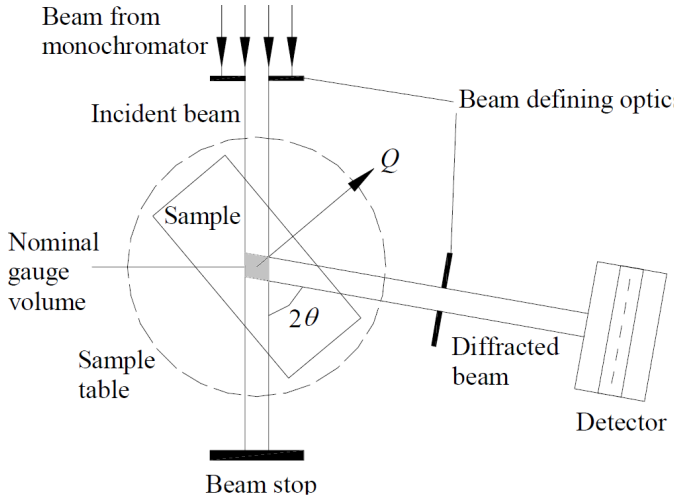

(a) Near cubical gauge volume for neutron diffraction. Taken from [62]

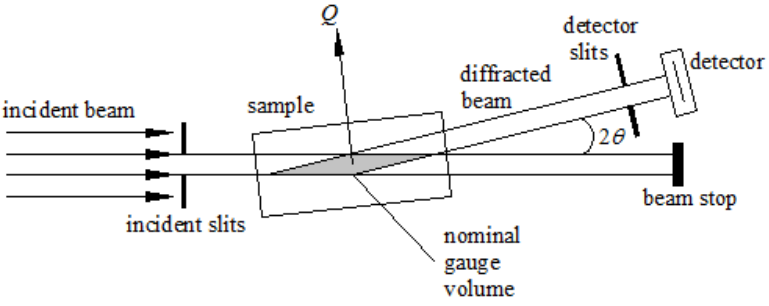

(b) Elongated gauge volume for x-ray diffraction. Taken from [63]

Figure 2.7.1: Comparison of gauge volume shapes for neutron and x-ray diffraction.

To this authors knowledge, residual strain measurements have not been performed on boron steel spot welds. The technique of measuring residual strains in welds is relatively well established [64, 65, 66] and also has an ISO standard associated with it [62]. As an indication of what to expect from the experiments, the work of Martinson [64] will be

examined. Martinson measured residual strains on spot and laser welded DC04 steel, with the results shown in figure 2.7.2. Ignoring the laser spot weld (LSW), the RSW shows significant tensile residual stresses in the weld zone, with compressive stresses in the surrounding area. Such stress magnitudes might be expected in the boron steel welds. Additionally, Ainsworth [67] stated that welded structures often exhibit residual stresses of local yield strength magnitude.

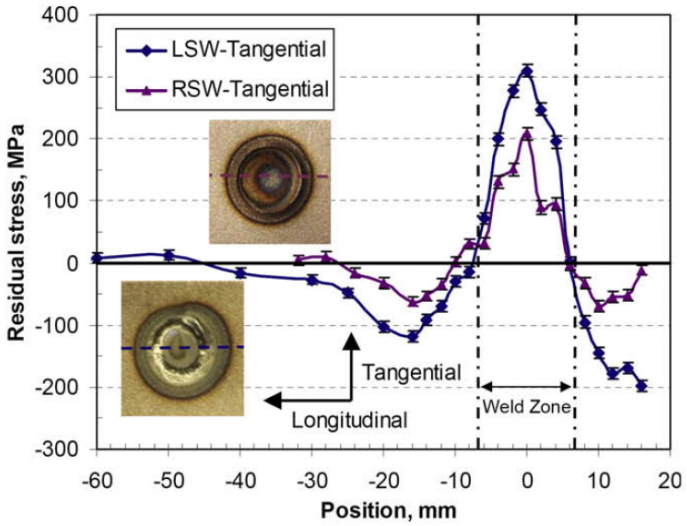

Figure 2.7.2: Tangential residual stress in Laser Spot Weld (LSW) and Resistance Spot Weld (RSW) of DC04 steel. Taken from [64]

Ainsworth *et al* [67] investigated the effect of residual stress on the failure behaviour of aluminium and steel welded plates. Machined defects were grown through fatigue loading to produce a sharp crack prior to applying an external uniaxial load. It was found that the samples without residual stress showed a load-carrying capacity 1.5 - 2 times greater than those with residual stresses.

The effects of residual stress on load-carrying capacity was found to reduce with increasing plasticity as the load approached the yield stress and no effect was seen once the load exceeded about 1.2 times the yield load. Similar observations were made for the steel specimens, with significant differences in load carrying capacity in the elastic regime and negligible differences in the plastic regime.

2.8 Instrumented Indentation

The principle behind instrumented indentation is using the experimentally measured load (P) versus displacement (h) curve of the indenter to calculate material properties of the indented material such as Young's modulus, hardness and yield strength. Methods for estimating the contact area from the indenter shape are used to provide measurements of Young's modulus and hardness; with more complex algorithms providing estimations of yield strength.

One of the first attempts at extracting material properties through indentation was performed by Bulychev *et al* [68], who analysed indentation load-displacement data according to the equation

$$S = \frac{dP}{dh} = \frac{2}{\sqrt{\pi}} E^* \sqrt{A} \tag{2.8.1}$$

where S is the experimentally measured stiffness of the upper unloading portion of the load-displacement curve (as shown in figure 2.8.1), P is the indenter load, h is the depth of penetration, E^* is the reduced modulus and A is the projected area of elastic contact. By assuming the contact area is equal to the optically measured area of the hardness indent and measuring the unloading stiffness, the reduced modulus could be derived. Oliver *et al* [69] have shown that equation 2.8.1 is valid for any indenter described as a body of revolution of a smooth function.

Bulychev's investigations employed optical methods to measure the indents. For smaller indents, where optical measurements tend to introduce errors, Doerner and Nix [70] produced a method of determining hardness and Young's modulus from the indentation load-displacement data alone. The unloading stiffness was again related to the modulus and contact area through equation 2.8.1. They proposed that the contact area be calculated by extrapolating the initial linear portion of the unloading curve to zero force, then using the extrapolated depth with the known indenter shape function. For example, the extrapolated h_c value, shown in figure 2.8.1, is used in the known area

function of a Vickers indenter; $A = 24.5h_c^2$, where h_c is the depth of penetration at the area of contact.

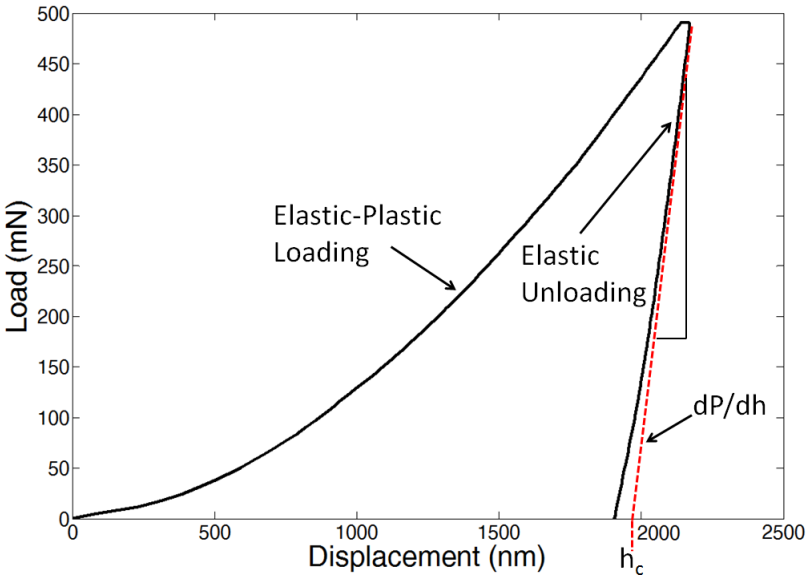

Figure 2.8.1: Linear extrapolation of the contact depth, as employed by Doerner and Nix.

The major flaw with the Doerner and Nix method is the assumption of *linear* unloading. Oliver and Pharr [69] proved that the unloading curve is in actual fact not linear. It was stated that the unloading slope changes "immediately and continuously as the indenter is unloaded" [69]. The authors investigated a wide range of materials (aluminium, tungsten, sapphire, quartz, soda lime glass and fused silica) with a pyramidal Berkovich indenter. The extent of non-linearity was shown by plotting the unloading curves on logarithmic axes, as shown in figure 2.8.2. The authors stated that the curves can be well described by a power law of the form:

$$P = \alpha h^m \tag{2.8.2}$$

Where α is a constant and the value of the exponent was found to be between 1.25 and 1.51 for the materials investigated. Equation 2.8.2 was originally developed by Sneddon

[71] as a relationship between load and displacement for various indenter geometries. Values for the exponent in equation 2.8.2 were found to be 1 for flat cylinders, 1.5 for paraboloids of revolution and 2 for cones.

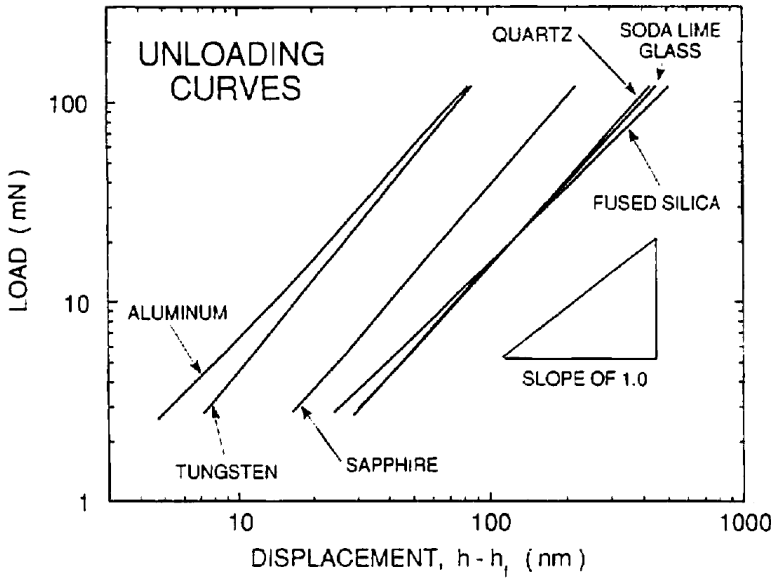

Figure 2.8.2: Investigation into non-linearity of unloading curves. [69]

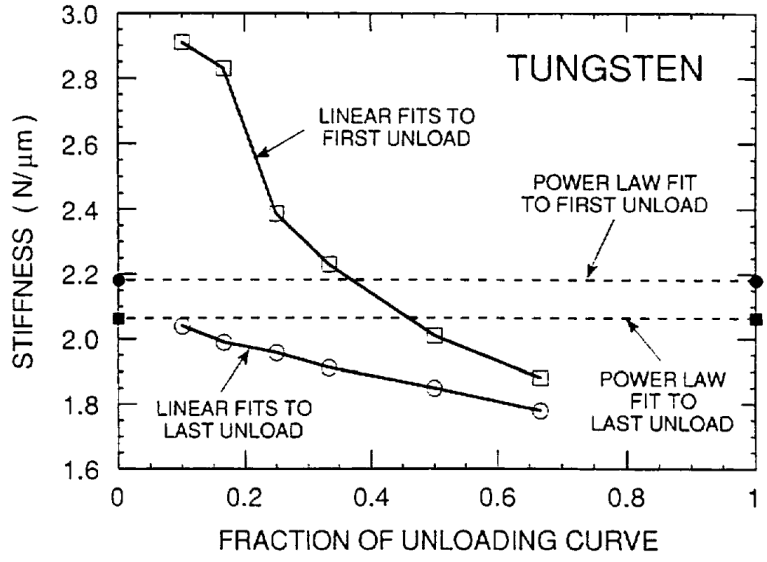

Figure 2.8.3: Stiffness calculated using linear and power law fitting techniques. Taken from [69]

Since it was found the unloading data is non-linear, the measured stiffness ($\frac{dP}{dh}$) depends on what proportion of the unloading curve is used in the fit. Oliver and Pharr [69] performed indents consisting of 3 multiple loading and unloading cycles, thereby ensuring that the unloading data was mostly elastic. A significant difference in stiffness was found between the first and last unloading data, which the authors attributed being due to creep during the first unloading, causing the slope of the upper portion of the unloading curve to be abnormally high. The authors said that this difference can be minimised by including a hold period at peak load to minimise creep effects. Putting this difference aside, for the linear fitting technique (employed by Doerner and Nix), a significant variation in stiffness was found for the final unloading data depending on how the fraction of the unloading curve was used, as shown in figure 2.8.3.

To get around this problem, Oliver and Pharr [69] noted that the unloading data is well described by a simple power law relation

$$P = A(h - h_f)^m \tag{2.8.3}$$

where the constants A, m and h_f are found by least squares fit. The unloading slope was found by differentiating equation 2.8.3 and evaluating at peak load and displacement. It was found the power law method for the first unloading gave stiffness values very similar to the last unloading (as shown in figure 2.8.3), showing that the method is less sensitive to creep.

A comparison of calculated Young's moduli and generally accepted values was made. It was found, for the materials exhibiting isotropic elastic properties (aluminium, tungsten, soda lime glass and fused quartz), the calculated moduli were within 4% of literature values. More significant deviations occurred for sapphire and quartz, which exhibits anisotropic behaviour. The authors could not account for the influence of elastic anisotropy, and suggested further work be undertaken.

Before we continue with the work involved in measuring material data from instrumented indentation, it would be worth looking at estimating properties using conven-

tional hardness testing. Pavlina *et al* [72] compiled the hardness, yield and tensile values of 150 nonaustenitic, hypoeutectoid steels and attempted to correlate the 3 properties. The steels yield and tensile strengths ranged from 300 - 1700 MPa & 450 - 2350 MPa, respectively.

The authors plotted yield strength versus hardness and tensile strength versus hardness and performed a least-squares linear regression to correlate the variables in a linear equation. Using these equations, the predicted strengths were compared with the actual strengths (obtained through tensile testing). The difference in actual and predicted yield strengths are shown in figure 2.8.4 a). As can be seen, there is a significant scatter in the results. A boron steel spot weld typically exhibits hardness values in the range of 300 HV to 500 HV; so within this range in figure 2.8.4 a), the yield strength tends to be underestimated by as much as 200 MPa.

The difference in actual versus predicted tensile strengths is shown in figure 2.8.4 b). Again, a significant scatter in actual versus predicted strengths is seen, with the highest hardness values showing the largest amount of underestimation. From this technique, it may be concluded that a rough approximation of material properties can be calculated. However, deviations from the fitted equations occur for high hardness value steels, such as boron steel. Therefore this technique might not be appropriate.

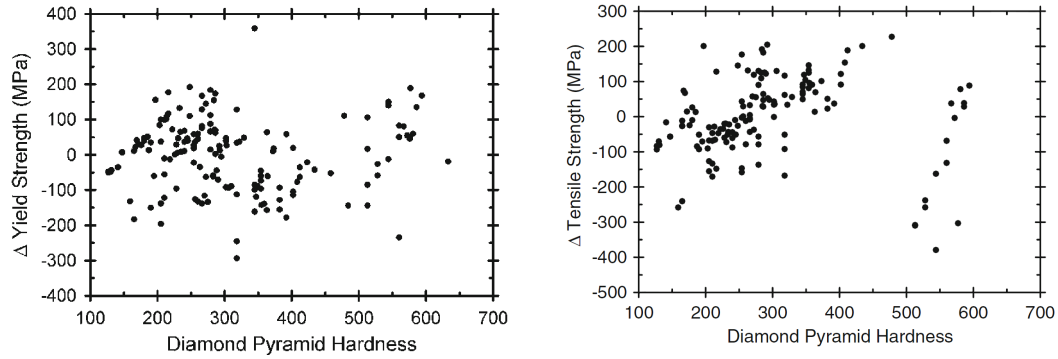

(a) Difference between actual and predicted yield strengths

(b) Difference between actual and predicted tensile strengths

Figure 2.8.4: Difference in actual and predicted yield and tensile strengths calculated from linear regression. Taken from [72]

2.8.1 Pile-up and sink-in events

An important parameter that determines an accurate extraction of material properties using the indentation technique is the projected contact area. The pile-up and sink-in events are illustrated in figure 2.8.5. The contact area for an indentation with pile-up tends to be larger than that predicted by analytical methods, leading to an overestimation of both hardness and modulus.

Pile-up tends to occur for non- or low strain hardening materials [73, 74] where, due to the incompressibility of the plastic deformation, the plastically displaced material flows up to the indenter faces. Sink-in tends to occur for high strain hardening materials [73, 74], where the material yield strength increases with increasing strain as the indenter is driven deeper, meaning the material within the plastic zone becomes "harder". The material at the outmost region of the plastic zone is "softer" and more susceptible to plastic deformation. Hence the "hard" material is driven deeper into the bulk material and the "soft" material is deformed and observed to sink in as the indenter proceeds downwards.

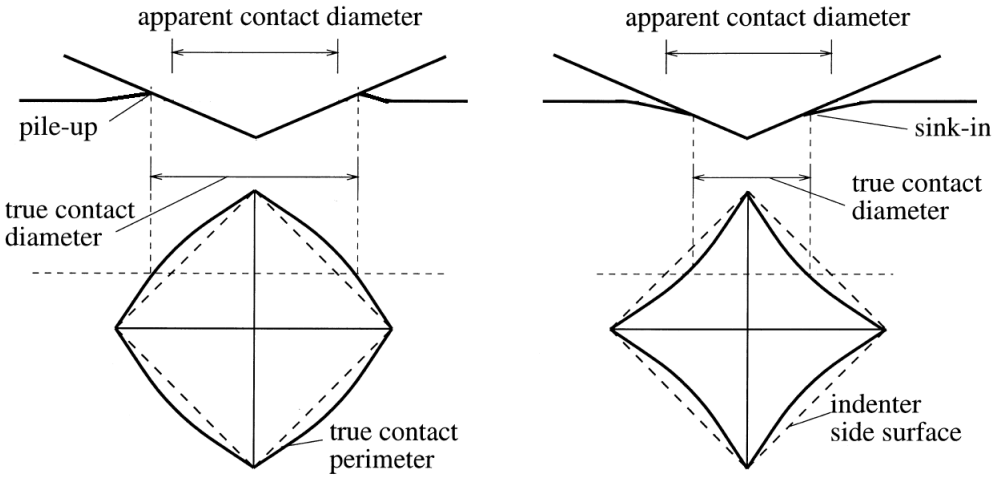

Figure 2.8.5: Illustration of pile-up and sink-in events (left and right, respectively). Taken from [73]

Oliver and Pharr [75] stated that trying to correct for pile-up has become a "holy grail" of indentation research, due to the fact that pile-up and sink-in depends on the

work hardening characteristics of the material. Without independent knowledge of the strain hardening behaviour, it is difficult to know what correction to apply. In addition, analytical methods to estimate the projected contact area have been developed from purely elastic contact solutions derived by Sneddon, and researchers are not sure how well they translate to elasto-plastic indentation [76].

Dao *et al* [77], in an attempt to take pile-up and sink-in into account, incorporated a geometric constant (c^*) using equation 2.8.1 in the rearranged form of

$$E^* = \frac{1}{c^*\sqrt{A}}S \tag{2.8.4}$$

where c^* is equal to $\frac{2}{\sqrt{\pi}}$ in equation 2.8.1. The authors stated that the true projected contact area with pile-up and sink-in taken into account can be expressed as $A = \pi a_m^2$ (in reference to figure 2.8.6).

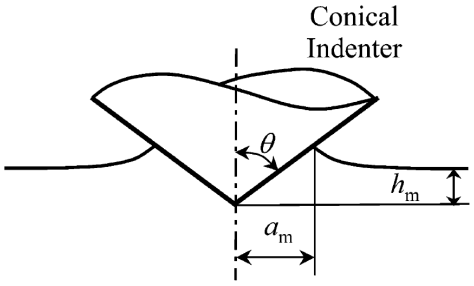

Figure 2.8.6: Schematic of conical indentation. Taken from [77]

Indentations were simulated through finite element analysis for 76 different material combinations with the following ranges; 10 < E < 210 GPa, 30 < σ_y < 3000 MPa and 0 < n < 0.5. From these simulations, values of c^* were calculated using large deformation elasto-plastic solutions for conical, Berkovich and Vickers indenters. By rearranging equation 2.8.4 and combining with $A = \pi a_m^2$, a dimensionless function was constructed that takes pile-up and sink-in into account. The method does not take strain hardening directly into account, therefore it is difficult to state the validity of their method. Unfortunately, no direct comparison between physical indentation areas and calculated areas were made.

2.8.2 Methods of extracting material properties from load - depth curves

2.8.2.1 Sharp indentation

Several methods of extracting material properties from the measured load-depth curves have been reported. The most frequently used approach is a combination of analytical methods and finite element analyses of indentations.

Suresh *et al* [78, 79] developed a theoretical framework for calculating elastic-plastic properties by fitting polynomial functions to computationally determined values of loading curves, maximum penetration values, etc. Finite element analyses were performed, simulating the loading - unloading sequence for Vickers [78] and Berkovich [79] indenter geometries. The results of these FE analyses dealt with low strain hardening materials only ($n < 0.15$). The strain hardening exponent of hot formed boron steel has been quoted as lying between 0.11 and 0.15 [80], therefore boron steel is in the outer regions of validity for their model. What the strain hardening exponent of the HAZ is, remains to be answered.

The authors compared their predicted material parameters with the known values of an ultra high strength steel (UHSS). The only extracted material parameter presented was the Young's modulus, which was estimated to 8% of the known value of the reference steel. Such an incomplete comparison makes it difficult to comment on the accuracy of predicted yield stresses.

Dao *et al* [77] developed closed-form analytical functions to estimate material properties from instrumented sharp indentation. The authors assumed a power law description for the material behaviour coupled with the von Mises yield criterion.

Finite element computations were carried out for 76 combinations of elasto-plastic material properties; namely $10 < E < 210$ GPa, $30 < \sigma_y < 3000$ MPa and $0 < n < 0.5$. It is clear that Dao's work takes into account a much wider material parameter

set than Suresh's work. The dimensionless functions and finite element computations were used to derive analytical expressions to relate the measured indentation data with elasto-plastic properties.

The authors constructed an algorithm which estimates the elasto-plastic properties from one complete load-depth (P - h) curve. The results of the algorithms were verified by analysing six indents from a 6xxx series and a 7xxx series aluminium. It was found that, in calculating E^*, the Dao algorithm gave a standard deviation of 6.5% from experimental results; whereas the same curves, when analysed with the Oliver and Pharr method, produced a standard deviation of 21.3%. The authors put this down to the fact that the effects of pile-up and sink-in effects were taken into account in their analysis, as described previously. The yield strength calculations gave a standard deviation of 30.9% however. In performing a sensitivity analysis, it was found that the yield strength displayed strong sensitivity to the measured loading and unloading curve parameters. The authors stated that the accuracy with which material parameters can be extracted depends strongly on the accuracy with which the P - h responses are measured. Therefore, it is recommended to statistically reduce the sensitivity by analysing multiple indents.

Cheng and Cheng [81] investigated whether stress-strain relationships can be determined from the loading-unloading curves alone, as opposed to using finite element methods to match the experimentally measured curves. In a similar fashion to Dao *et al* [77], dimensionless functions were developed which describe the unloading slope, relates force and indenter displacement and relates the maximum and residual impression depth.

The authors stated that a set of basic material properties (for example E, ν, σ_y and n) can be input into the derived dimensionless functions to determine features of the P - h curves such as the loading and unloading curve and the maximum and residual impression depths. Alternatively, this method can be "reversed" by using the dimensionless scaling functions to calculate the basic material properties from measured P - h curves. This is illustrated in figure 2.8.7, where Π_α is the dimensionless function describing the relation between force and indenter displacement during the loading

stage. With the known values of E and ν, the values of n and σ_y are found by drawing a line parallel to the x axis. The same loading curves are found where the values of n and σ_y correspond to the intersect of the horizontal line and Π_α. The procedure is repeated for the dimensionless functions describing the unloading curve and residual indentation depths, hence values of n and σ_y that satisfy all 3 conditions (loading curve, unloading curve and residual impression depth) are found.

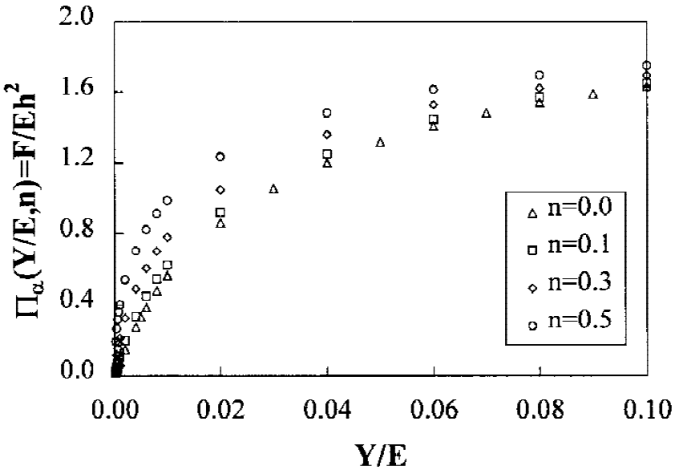

Figure 2.8.7: Dimensionless scaling relationship for the loading curve. Taken from [81]

The problem with the method becomes evident when considering the P - h curves produced by different combinations of n and σ_y, as shown in figure 2.8.8. Using a curve as depicted in the figure, multiple combinations of n and σ_y may be obtained. Dao *et al* [77] set out to address this uniqueness problem with their algorithm. The material parameters in figure 2.8.8 were used to predict three statistically unique P - h curves, with the maximum variation being an 8% change in $\frac{dP}{dh}$. The authors admitted that this does not "directly contradict" Cheng and Cheng's assertion of non-uniqueness, as they used a different cone angle in their FEA simulations and as the outputted P - h curves appear *visually* similar.

The authors stated that, even if the loading curvature were identical for 2 separate P - h responses, it was found that small variations in $\frac{dP}{dh}$ or $\frac{h_r}{h_{max}}$ were sufficient to calculate a unique value of n, and consequently σ_y. The authors concluded that such

small variations may not be visually apparent when P - h responses are plotted simultaneously. No indication of the level of variation needed to calculate unique values was given, therefore it would be advisable to use additional references to calculate the stress-strain properties from P - h curves.

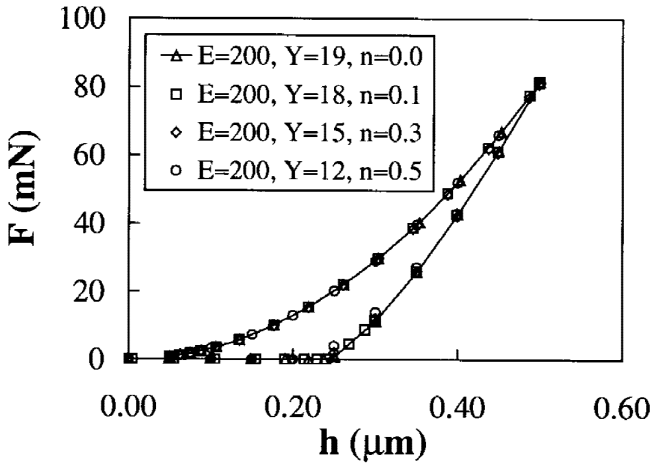

Figure 2.8.8: Example of overlapping loading and unloading curves. Y is the yield stress in GPa. Taken from [81]

2.8.2.2 Spherical Indentation

It was not possible to obtain experimental time on an instrumented indentation machine with a spherical indenter, therefore only a brief introduction will be given to spherical indentation, as it is not relevant to further work in this thesis. As opposed to sharp indenters, spherical indenters do not produce an elastic singularity at the tip, which would lead to large stresses. At small loads, the response is entirely elastic. At higher loads, a transition into the plastic regime occurs. By applying increasingly larger loads, discrete points on the indentation stress - indentation strain curve can be built up to obtain a stress-strain curve. This technique is not as commonly applied as sharp indentation though [82], for unknown reasons.

2.9 Conclusions

Information was obtained about the steel's response to variations in welding parameters. These observations will be used in choosing an appropriate weld schedule in order to produce welds for further testing. It was found that boron steel welds produced with high currents (8 kA [41] and 9.5 kA [42]) showed a reduction in mechanical properties, attributed to expulsions. A higher current will result in a larger nugget, which will exhibit higher strengths. However, caution should be exercised when welding boron steel at these high currents as expulsions and subsequent voids will reduce the strength.

It was found that a zinc coating causes the interfacial resistance to be reduced compared with uncoated sheets [17]. This is due to the low resistivity of zinc. It was found that the contact resistance decreased proportionally to the electrode force at the electrode-sheet interface. A much steeper decrease was observed at the sheet-sheet interface. Therefore, it was suggested that a higher electrode force would require a longer weld time to produce a weld of given diameter.

The microstructure of the soft HAZ in boron steel welds was found to be composed of martensite and ferrite [41]. Other authors found the soft zone to be composed of bainite in a ferrite matrix [42]. In all reviews, the authors stated that the sudden drop in hardness was caused by tempering of martensite by heating up to the A_{c1} temperature [41, 42, 43]. This information helps to narrow down the temperature range to be used in the Gleeble experiments for recreating the soft HAZ microstructure onto tensile destructive specimens. Furthermore, the cause for the HAZ softening has been identified and will be incorporated into further analysis.

There are various factors that affect failure initiation that one has to take into consideration. Identifying which factors have a greater influence will help to narrow the scope of the investigation and avoid extracting constitutive behaviour which have negligible effects on weld failure. Many authors have cited geometrical factors, such as weld diameter and sheet thickness as contributing factors to weld failure [44, 45, 18]. The notch tip was identified as a region for stress concentration during loading [42]. It has

also been stated that the structural differences between the nugget/BM and HAZ may enhance the stress concentration around the notch tip [46]. Specifically for martensitic steels, the soft HAZ was identified as a critical area which limits the deformation capacity of the weld [31]. This observation was echoed by Dancette, who stated that the interplay of soft SCHAZ microstructures next to the hard bainitic/martensitic nugget was found to promote strain localisation [45]. Therefore, characterising the HAZ is essential for predicting weld failure.

Residual stresses have also been identified as contributing to failure [45, 54, 18] and significantly affect the load carrying capacity in the elastic regime [67]. Ainsworth showed that residual stresses significantly affect the load carrying capacity of specimens, but these effects reduce with increasing plasticity as the external load approaches the yield load. It will be interesting to see if similar observations are made through FE modelling of weld destructive tests.

A review of different failure prediction methods was conducted, encompassing empirical, limit load and finite element modelling. Empirical and analytical methods proved that failure could be accurately predicted by taking material properties such as nugget diameter, sheet thickness and BM strength into account. These methods circumvent the need for significant experimental efforts in extracting material properties. The problem in applying these methods to boron steel is the assumption that the weld can be modelled as a "rigid button" embedded in a ductile sheet. This assumption stemmed from the observation that the nugget tends to have much higher hardness values than the BM. As mentioned previously, due to the hardness distribution of boron steel spot welds, this assumption may not be valid. Additionally, it was recommended to account for HAZ softening in high strength steels [35]. This sentiment was echoed by Sommer [31].

The focus was shifted to the FE methodologies of Dancette [45, 55] and Sommer [31]. Both authors extracted material constitutive behaviour of different weld zones which were used as input into FE models. The SOPRAS welding simulation program was used to extract the temperature histories of weld zones to drive Gleeble simulations,

which recreated weld material on destructive tensile specimens. From these destructive specimens, failure criteria using stress state and failure strain were developed. Potential improvements in both authors works were identified and will be outlined.

In extracting constitutive behaviour from the Gleeble tensile samples, Sommer performed inverse FE simulations where material properties were incrementally varied to match the simulated force-displacement curves to the experimentally measured ones. Slight deviations from the experimental load-displacement curves were seen, indicating that improvements can be made by directly measuring the tensile samples using DIC.

In terms of failure criteria, Dancette's work used local fracture strains obtained from the reduction in cross sectional area of uniaxial tensile samples. The use of one type of tensile geometry limits the range of triaxialities that can be applied to the failure criterion. Dancette admitted that there is an assumption that the levels of triaxiality and strain in the HAZ are the same as those experienced in the gauge length of the tensile samples. Sommer extended the range of triaxialities in the failure criterion by incorporating shear, uniaxial and plane-strain samples, thereby producing a failure curve consisting of failure strain versus stress state. An improvement in the tensile sample geometry used by Dancette and Sommer was identified. It was stated that the stress state changes from uniaxial to plane-strain as necking develops in the tensile sample. This is especially true for more ductile materials as might be found in the HAZ. Therefore, the uniaxial part of Sommer's failure curve can be improved by using tensile samples with a central hole.

Further improvements were identified in terms of how the areas of material extraction were discretised. Dancette characterised two weld zones (SCHAZ and CGHAZ) in a DP590 weld. This was because the weld showed a smooth gradient of mechanical properties leading out from the weld, and two alterations of the BM constitutive behaviour was sufficient to capture this. Sommer characterised 3 weld regions for boron steel spots welds; the nugget, HAZ and BM. A potential problem with characterising the overall HAZ would be that the behaviour of individual HAZ regions would be averaged. Therefore, an improvement to Sommer's work would be to discretise the HAZ

to a higher degree in order to capture the behaviour of the microstructural gradients through the HAZ.

An additional technique, instrumented indentation, was identified which could add value to the methodologies of Dancette and Sommer. Kong extracted constitutive weld behaviour through indentation tests using the principle of instrumented indentation. Whereas instrumented indentation machines measure the load and depth of the indenter directly, Kong approximated the indentation depths from conventional hardness impressions, likely leading to deviations from the true depth. Nevertheless, the technique showed promise in the application to spot welds. Dancette and Sommer approximated weld microstructures through Gleeble simulations. These microstructures were verified to be correct through microscopy. Extracting material behaviour directly from the weld through instrumented indentation would add a quantitative set of data from which to gauge the accuracy with which the weld microstructures were recreated.

In this thesis, instrumented indentation is used as a tool for extracting material properties from the weld. Therefore, a methodology which applies to ultra high strength steels was sought. Dao [77] presented a detailed method, which was calibrated using a wide range of steel properties. A clear improvement on the Oliver and Pharr method was presented in calculating Young's modulus, which the authors stated was due to pile-up and sink-in events being taken into account. In calculating yield strengths, deviations from accepted values were found. The authors recommended to statistically reduce such deviations by taking multiple indents. It was concluded that Dao presented the most complete, usable method to extract material properties.

Chapter 3

Welding Investigation

3.1 Introduction

The main purpose of this chapter is to finalise a weld schedule which results in an acceptable weld which can be used for extracting material constitutive behaviour. The term *acceptable* is defined here to mean that welds are consistently produced without a greatly varying nugget size, expulsions are eliminated or kept to a minimum and the nugget diameter conforms to the automotive industry standard of $4\sqrt{t_{sheet}}$ to $5\sqrt{t_{sheet}}$ [83], where t_{sheet} is the sheet thickness being welded.

It is generally accepted that welds below $4\sqrt{t_{sheet}}$ exhibit an under-developed nugget, and will hence exhibit a reduced strength. Weld nugget diameters above $5\sqrt{t_{sheet}}$ are at risk of having the molten metal reaching the sheet surface during welding, leading to expulsions.

There are a number of welding standards, including ISO 2002 [84], ISO 2004 [85] and ISO 2007 [86]. These welding standards are applicable for "the determination of the lower and upper limits of the welding current under specific welding configurations" [85]. Therefore, the standards give a range of welding parameters that are used for determining a welding window for a specific steel.

ISO standards employ specific material properties to define the range of welding parameters to be used. For example, for a given sheet thickness, the ISO 2004 standard separates the electrode force and current values by the fact if the UTS of the sheet is above or below 380 MPa. The ISO 2007 standard applies to a generic definition of

"low carbon steels", where the weld parameters are divided by the coating applied to the sheets.

As the key purpose of this project was to investigate the mechanical behaviour of welds *currently used in the automotive industry*, a weld schedule obtained from an automotive manufacturer, specifically designed for welding boron steel, was used in this study. This schedule is shown in table 3.1.1. Welding trials and simulations were performed, in which certain parameters were varied. This was performed to verify that the schedule does indeed produce the best welds possible for the given thickness of steel.

Electrode force (kN)	1st pulse		t_{pause} (ms)	2nd pulse		t_{hold} (ms)
	(kA)	(ms)		I (kA)	t (ms)	
3.5	5	250	40	7	500	250

Table 3.1.1: Automotive weld schedule

3.2 Materials

The material, supplied by Tata Steel, was 1.5 mm thick unhardened 22MnB5 steel sheets. The supplied boron steel was coated with a 20 µm thick layer of protective zinc. During press hardening, when the steel is austenitised, oxide layers form when contact is made with air [10]. A protective layer, like zinc, prevents this surface oxidation. After hot stamping, the oxide layer is usually removed by sand blasting to ensure good paint adherence [10]. For the welding trials, the zinc coating was removed from the fully hardened steel by sand blasting.

A reference steel, to be used to aid further experiments, was also used. 1.5 mm thick galvanised DP600 steel sheets were supplied by Tata Steel for this purpose.

3.3 Hot-stamping of boron steel

Before welding, boron steel required heat treatment to convert it to the fully hardened state. The steel was guillotined into strips of 40 x 400 mm, to conform to the welding jig dimensions. The strips were placed in a Nabertherm oven, preheated to 950 °C. The strips were left to austenitise for 5 minutes and then rapidly transferred to an Enefco 500 tonne press. The transfer times ranged from 9 - 12 seconds. The hot strips were placed on the bottom flat section of a top hat tool and subsequently pressed with a pressure of 4 MPa. The pressure and austenitising times were chosen according to Mohr [5].

Thermocouple tests using similar samples showed that the cooling rate was approximately 100 °C/s when full contact with the press was made [P. Chokshi, personal communication, University of Warwick, 14 September 2014]. The hardness values (shown in circled numbers) in figure 3.3.1 are used for validation of the cooling rate. An average hardness of 508 HV0.5 was found for the fully hardened strips. The high hardness from the steel strips indicates that the cooling rate was beyond the critical 30 °C/s (shown as the dashed line in the figure).

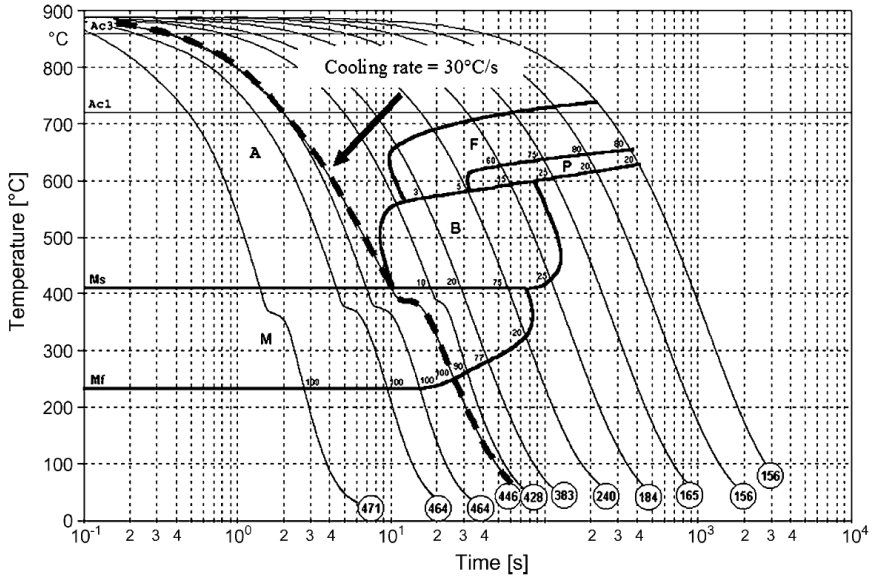

Figure 3.3.1: CCT diagram for 22MnB5 steel, indicating Vickers hardness values in circled numbers. Taken from [6]

3.4 SORPAS simulations

As a precursor to performing physical welding tests, it was deemed appropriate to simulate a basic weld schedule to investigate the effect of individual welding parameters. Simulations were performed on SORPAS welding software [87]. SORPAS contains a database of different steels, consisting of generic chemistries specific to each steel grade. Boron steel was selected from the database, and the alloy levels adjusted to correspond with the values supplied from the manufacturer.

All simulations were performed with a single pulse, to minimise the variables and simplify the analysis. Weld lobes were created by varying the weld time and current, with 2 electrode forces (3.5 kN and 7 kN). The purpose of these simulations was to investigate the effect of electrode force and electrode material. The parameter ranges held constant in all simulations in this subsection are given in table 3.4.1.

Weld time (ms)	Current (kA)	Number of pulses	Hold time (ms)	Electrode geometry
120 - 360	4 - 12	1	100	Rounded

Table 3.4.1: Constant welding parameters for weld lobes investigating electrode material and diameter

3.4.1 Effect of electrode material and force

A comparison of the weld lobes for these simulation runs is given in figure 3.4.1. A *weld lobe* indicates a range of values of a variable which results in an acceptable weld. Contours indicating “no fusion” and “expulsion” are indicated in the figures. Comparing figure 3.4.1 a) with b) (the weld lobes for the CuCrZr electrodes) and figure 3.4.1 c) with d) (the weld lobes for the CuZr electrodes), it can be seen that a higher electrode force results in a smaller welding window. Using a high electrode force results in a larger area of no fusion at low currents. On the other hand, the low electrode force results in a larger expulsion area at high currents and weld times. In all 4 figures, expulsions

start at high currents (greater than 7 kA), but a lower electrode force means welds are created at lower currents.

It can also be seen that negligible differences in final nugget diameters arise from using the two different electrode materials. These negligible differences in nugget size between the two electrode materials is attributable to the different conductivities. CuCrZr electrodes exhibit a typical conductivity of 80% IACS and CuZr electrodes exhibit a conductivity of 85% IACS. IACS is the "International Annealed Copper Standard" which is $5.8001 \times 10^7 S/m$, defined as 100% IACS at 20°C.

A comparison is performed between using electrode forces of 3.5 kN and 7 kN with the higher conducting CuZr electrode, as shown in figure 3.4.2. A clear difference in nugget diameter can be seen between 4 kA and 6 kA, with the high electrode force resulting in smaller nugget sizes. This can be explained by the reduced contact resistance due to high electrode forces. This reduced resistance is usually compensated by using higher current and/or longer weld times; however, the effect can clearly be seen at low currents. In the higher current range (more than 7 kA), the difference in nugget size becomes negligible. This is due to the higher currents compensating for the reduced contact resistance brought on by high electrode forces.

The main conclusion taken from this investigation is that the electrode material has a minor effect on the nugget diameter and weld lobe. Using a low electrode force results in nugget formation at lower currents; whereas there is a severely reduced nugget size by using high electrode forces at low currents. Finally, the expulsion window is slightly increased at higher currents when using a low electrode force. These factors will be taken into consideration when performing physical welding trials.

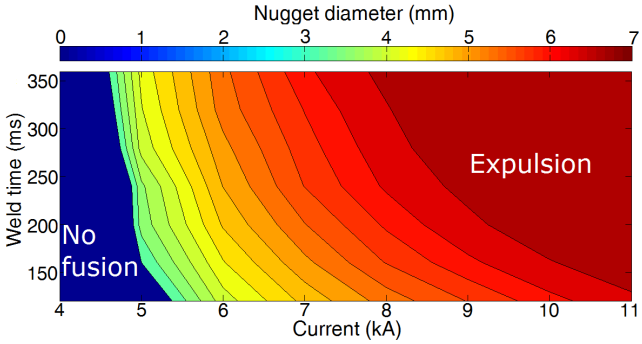

(a) CuCrZr electrode at 7 kN

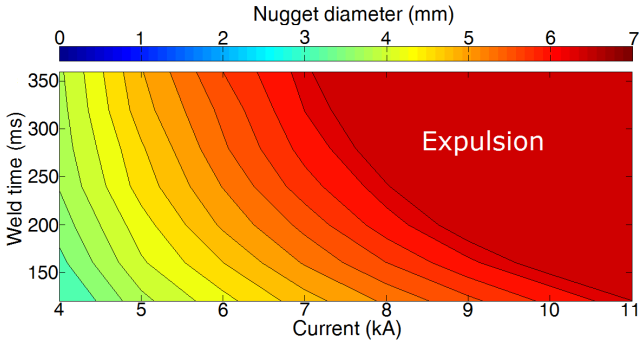

(b) CuCrZr electrode at 3.5 kN

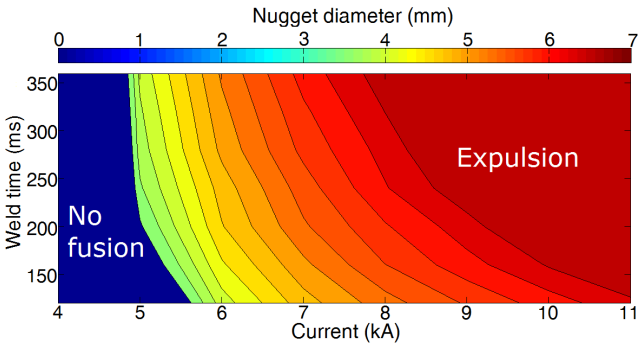

(c) CuZr electrode at 7 kN

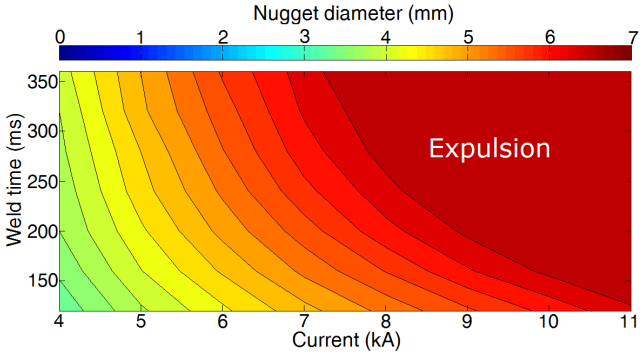

(d) CuZr electrode at 3.5 kN

Figure 3.4.1: SORPAS simulated weld lobes using either CuCrZr or CuZr electrodes at forces of 3.5 kN or 7 kN

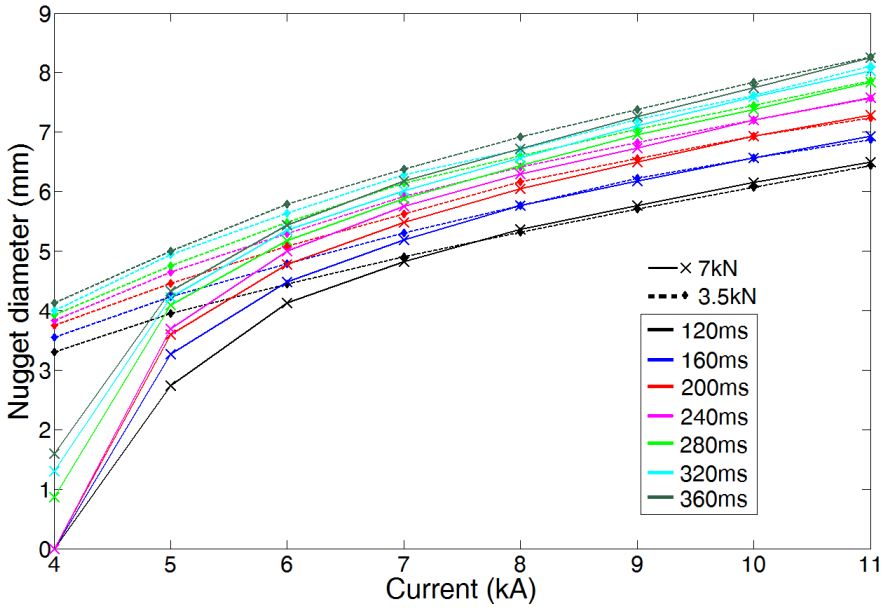

Figure 3.4.2: Comparison of final nugget diameter produced by using electrode forces of 3.5 kN and 7 kN with a CuZr electrode with diameter of 6.5 mm

3.5 Physical welding trials

The purpose of these welding trials was to ascertain that the automotive weld schedule would indeed give optimal welds for the given sheet thickness. The aim of the trial was therefore to be certain that the given weld schedule minimises expulsions and results in a nugget diameter in the range of $4\sqrt{t_{sheet}} \approx 4.9\,mm$ to $5\sqrt{t_{sheet}} \approx 6.1\,mm$, where the sheet thickness is 1.5 mm. The final weld schedule would be used to produce welds for all experimental work. Parameters from the automotive schedule were incrementally varied during these trials. These variations consisted of increasing the weld time, varying the electrode force between low (3.5 kN) and high (7 kN) values and increasing the current to find the expulsion limit.

The welds were produced with a Comau robot equipped with an ARO servo-controlled spot welding gun. The control system was a Matuschek SPATZ medium frequency direct current (MFDC) controller. The electrodes were rounded Luvata Z-Trode FA18Z01 caps, composed of CuZr, as shown in figure 3.5.1.

The sheets to be welded were 40 mm x 400 mm and 1.5 mm thick. Welds were spaced at 25 mm intervals, with 14 welds made per sheet. The welds were destructively tested through means of a peel test in accordance with the ISO 10447:2007 standard [88]. The peel test, as shown schematically in figure 3.5.2, is a fast and efficient way of determining the weld size and fracture mode.

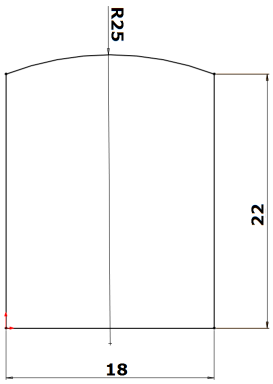

Figure 3.5.1: Schematic illustration of FA18Z01 Z-Trode electrode

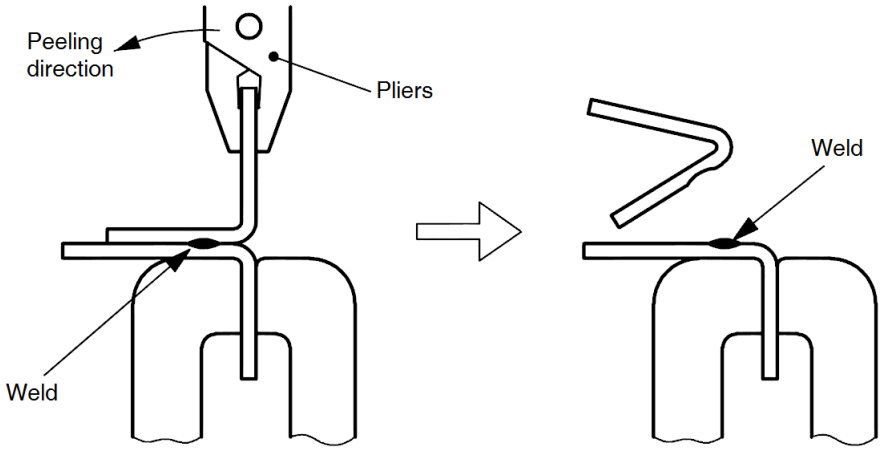

Figure 3.5.2: Schematic illustration of peel test. Taken from [86].

After peel testing, the nugget sizes were determined according to the ISO 10447:2007 standard [88], with the measurement techniques for different failure modes shown in figure 3.5.3. The mean weld diameter is defined as $d = \frac{d_1+d_2}{2}$ and the mean plug diameter as $d_p = \frac{d_2+d_3}{2}$.

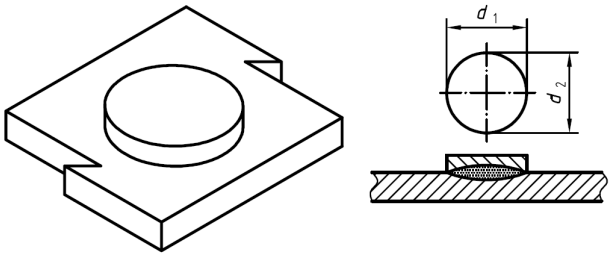

(a) Symmetrical button pull-out

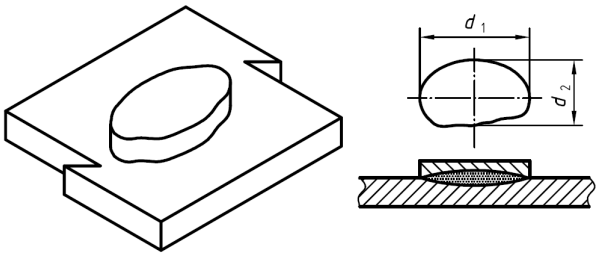

(b) Asymmetrical button pull-out

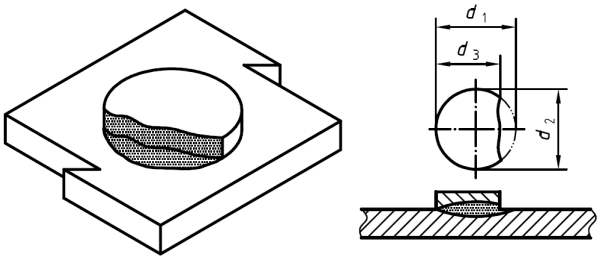

(c) Partial interfacial failure

Figure 3.5.3: Nugget measurement techniques for different failure modes. Taken from [88]

3.5.1 1st run - varying weld time

In the first welding trial, the effect of increasing the weld time (from 600 ms - 1000 ms) of the 2nd pulse was investigated. The second pulse has the greatest influence on nugget development, due to the higher current and longer weld time [M. Thornton, personal communication, 12 May 2013]; therefore, to minimise the variables, only the second pulse was varied.

As can be seen in figure 3.5.5, none of the welds showed expulsions. The average nugget size was 4.99 mm with a standard deviation of 0.17 mm. It was expected that the weld

nugget diameter would increase with increasing weld time; however, as can be seen from figures 3.5.4 and 3.5.5, no consistent nugget size variation was seen. A possible reason for this observation could be that the steel is conducting the heat away as fast as it is receiving it.

3.5.2 2nd run - varying electrode force

In the second welding trial, the effect of low (3.5 kN) and high (7 kN) electrode forces was investigated. As with the previous run, no expulsions were observed. As can be seen from figure 3.5.6 and 3.5.7, there is a general trend of bigger nugget diameters at lower electrode forces. The 7 kN force produced an average nugget diameter of 4.86 mm with a standard deviation of 0.23 mm. The 3.5 kN electrode force produced an average nugget diameter of 5.20 mm with a standard deviation of 0.28 mm.

Overall, no clear effect of varying electrode force was seen in the developed nugget sizes, as can be seen in the overlap of data points for the two forces in figure 3.5.6.

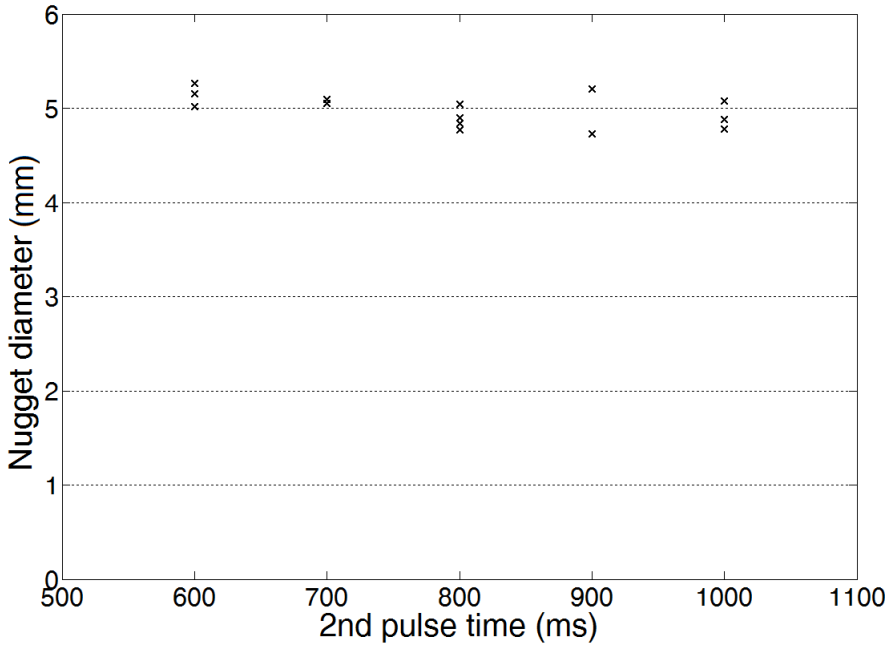

Figure 3.5.4: Weld trial run 1: Nugget diameter with increasing 2nd pulse time. Fixed parameters: Electrode force = 3.5 kN; 1st pulse = 5 kA for 250 ms; pause time = 40 ms; 2nd pulse = 7 kA for indicated times; hold time = 250 ms

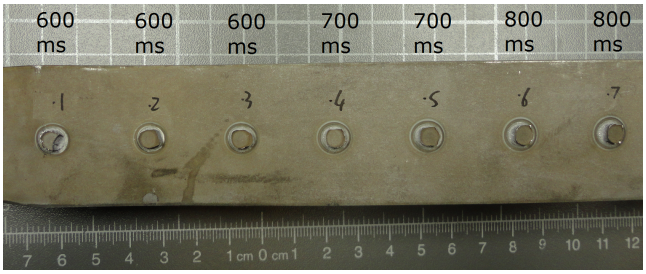

(a) Left hand side of sheet

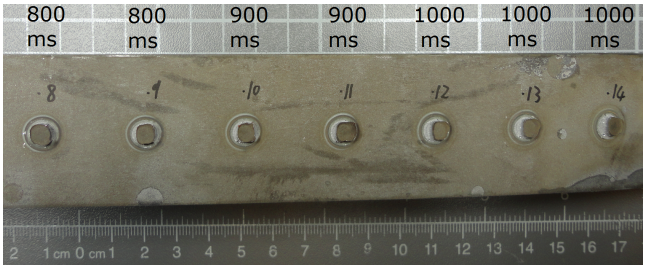

(b) Right hand side of sheet

Figure 3.5.5: Weld trial run 1: Peel tested welds from 1st run with corresponding 2nd pulse times overlaid. Weld #1 is the shunt weld i.e. the first weld created on the sheet.

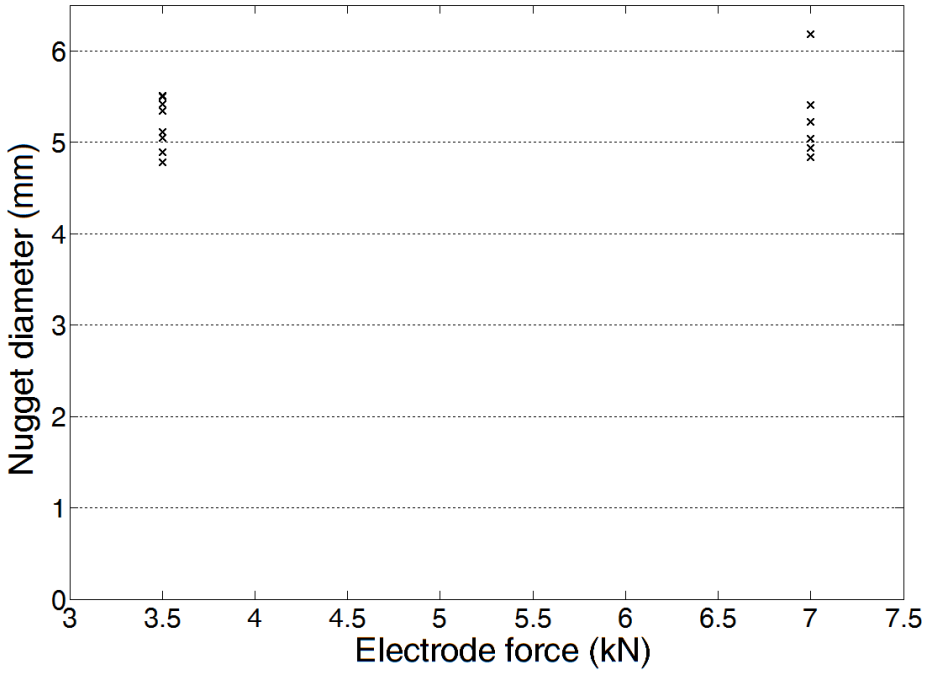

Figure 3.5.6: Weld trial run 2: Nugget diameter with low (3.5 kN) and high (7 kN) electrode force. Fixed parameters: 1st pulse = 5 kA for 250 ms; pause time = 40 ms; 2nd pulse = 7 kA for 500 ms; hold time = 250 ms

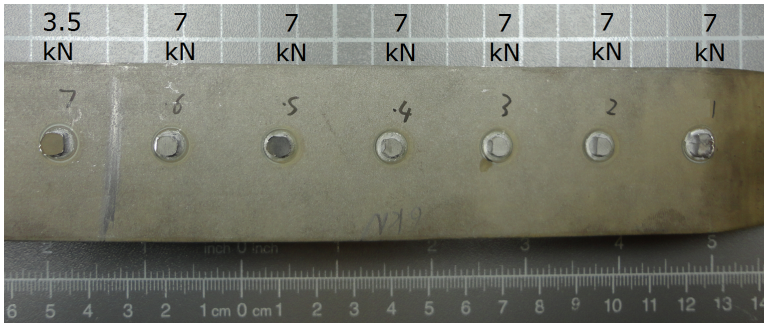

(a) Left hand side of sheet

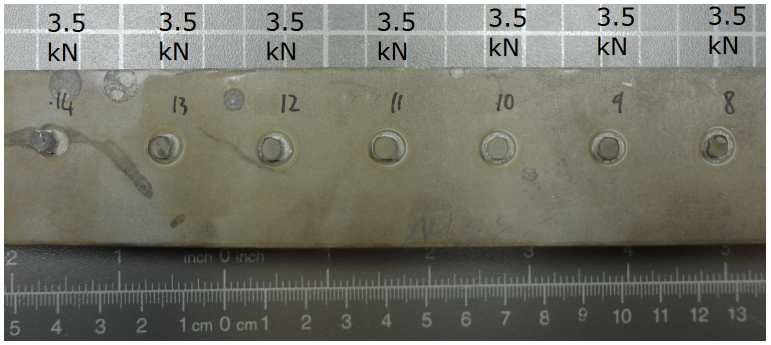

(b) Right hand side of sheet

Figure 3.5.7: Weld trial run 2: Peel tested welds from 2nd run with corresponding electrode force values overlaid. Weld #1 is the shunt weld.

3.5.3 3rd run - varying current

In the weld trials performed so far, the nugget diameters had a value corresponding to $4\sqrt{t_{sheet}}$. To increase the nugget diameter, the current of the 2nd pulse was increased. As was mentioned previously, current is a squared term in Joule's first law, and is hence expected to have the greatest contribution to heat generated and hence nugget size produced. The current for the second pulse was varied between 7.5 kA and 9.5 kA. The electrode force was maintained at 3.5 kN.

In the first part of the test, the current for the second pulse was varied between 8.5 kA and 9.5 kA. As can be seen from figures 3.5.8 and 3.5.9, the vast majority of welds exhibited expulsions.

A current of 8.5 kA produced welds with a mean diameter of 5.90 mm and standard

deviation of 0.57 mm. A current of 9.5 kA produced welds with a mean diameter of 5.80 mm and a larger standard deviation of 1.08 mm. This large deviation for the higher current welds stems from expulsions.

Comparing these results with the average weld diameter from the 3.5 kN setting of run 2, the nugget diameter has increased by 0.87 mm for the 8.5 kA setting and by 0.77 mm for the 9.5 kA setting. These higher currents have brought the weld diameter closer to the $5\sqrt{t_{sheet}}$ standard. It is clear, however, that these high currents have led the weld schedule into the expulsion zone. Therefore, the welds produced with high currents are undesirable due to the chance that expulsions have reduced the weld strength through creating voids.

The attempt at increasing nugget size through higher currents was continued, but with the currents reduced to 7.5 kA and 8.5 kA to minimise the probability of expulsions occurring. From figures 3.5.8 and 3.5.10, it can be seen that expulsions are still prominent when using a current of 8.5 kA, with weld nuggets having a mean diameter of 5.70 mm with standard deviation of 0.44 mm. Expulsions were severely reduced when using the 7.5 kA current. The one occurrence of expulsion can be viewed as an anomaly, probably being produced by factors such as dirt or grease on that section of the sheet. The 7.5 kA current produced welds with a mean diameter of 5.06 mm with a standard deviation of 0.83 mm. From these observations, it might be concluded that the edge of the expulsion zone has been identified.

From these runs, it was concluded that increasing the current increased the likelihood of expulsions occurring. It was seen that a current of 7.5 kA reduced the number of expulsions. Comparing nugget sizes for runs using a 7 kA current (from run 2) with runs using a 7.5 kA current (with both using a 3.5 kN electrode force), the latter produced diameters approximately 0.22 mm smaller than those produced by the former. Given such a small decrease in diameter, it was decided to use the 7 kA current due to the fact that this current is further away from the expulsion window, hence leading to a better chance of reducing expulsions.

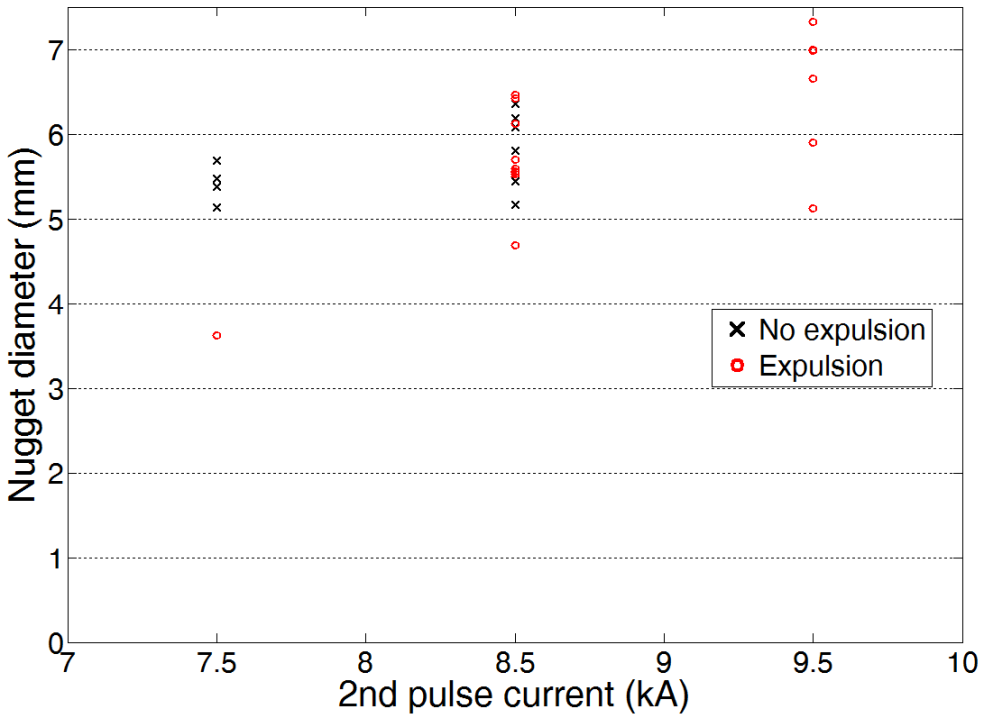

Figure 3.5.8: Weld trial run 3: Nugget size as function of 2nd pulse current. Fixed parameters: Electrode force = 7 kN; 1st pulse = 5 kA for 250 ms; pause time = 40 ms; 2nd pulse = indicated current for 500 ms; hold time = 250 ms

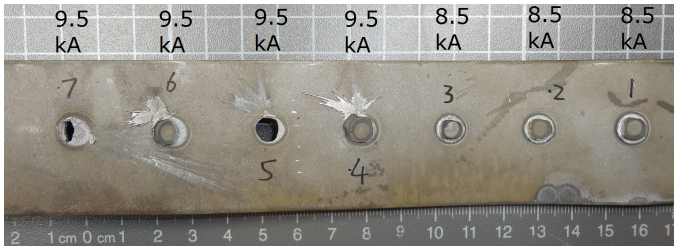

(a) Left hand side of sheet

(b) Right hand side of sheet

Figure 3.5.9: Weld trial run 3: Peel tested welds from 3rd run with current varied between 8.5 and 9.5 kA

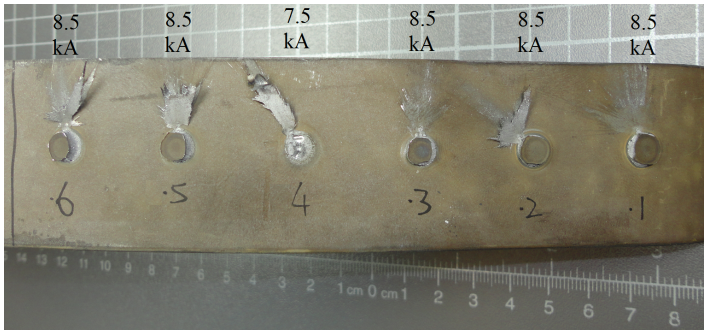

(a) Right hand side of sheet

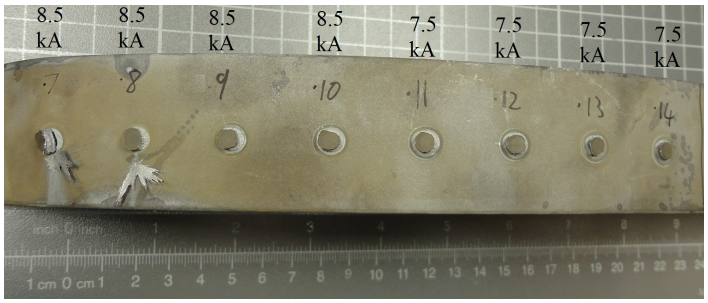

(b) Left hand side of sheet

Figure 3.5.10: Weld trial run 3: Peel tested welds from 3rd run with current varied between 7.5 and 8.5 kA

3.5.4 DP600 welding trial

As stated previously, DP600 welds are used in further experiments for benchmarking. It was decided that exposing the DP600 steel to similar welding parameters to the boron steel would aid in making comparisons between the two, as the two steel types are exposed to the same current for the same amount of time. As an initial trial, the weld schedule defined in table 3.1.1 was used, with the current in the second pulse varied between 6.5 kA and 11.5 kA. As seen in figure 3.5.11, an expulsion occurred at 11.5 kA, indicating that, in terms of current, DP600 has a larger welding window than boron steel. The average weld diameter of boron steel welds produced with the commercial schedule was 5.2 mm. From figure 3.5.11, it might be inferred that using a 7 kA current in the second pulse would bring the DP600 welds into the same nugget diameter range as the boron steel welds.

Figure 3.5.12 shows the results of the second DP600 weld trial, where the current of the second pulse was varied between 6.5 kA and 7 kA. From the figure, a current value of 7 kA produced an average weld diameter of 5.7 mm, with a standard deviation of 0.2 mm. The DP600 welds produced with the automotive weld schedule were deemed acceptable, as the weld diameter was, on average, 0.5 mm larger than the boron steel spot welds produced from the same schedule.

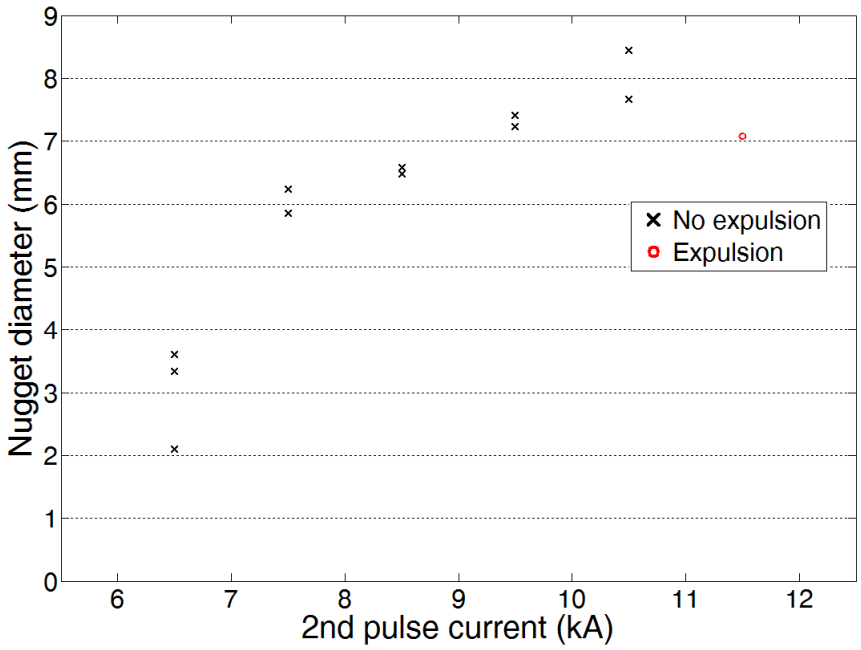

Figure 3.5.11: First DP600 weld trial: Nugget size as function of 2nd pulse current. Fixed parameters: Electrode force = 3.5 kN; 1st pulse = 5 kA for 250 ms; pause time = 40 ms; 2nd pulse = indicated current for 500 ms; hold time = 250 ms

3.5.5 Welding trial conclusions

Starting with a recommended weld schedule from an automotive company, optimisation runs were performed to establish a process window. It was seen that increasing the weld time of the second pulse had a negligible effect on the weld size. Therefore, it was decided to leave the original weld times unmodified. In the second run, an electrode force of 3.5 kN produced an average weld diameter 0.34 mm larger than an electrode force of 7 kN, although there was a large overlap in nugget diameter between the two

electrode force settings. In the third run, it was seen that employing currents higher than 7.5 kA resulted in an increase in expulsions. It was concluded that the expulsion zone starts at approximately 8.5 kN. Welds produced with a 7 kA setting had an average weld diameter of 0.22 mm smaller than welds produced with 7.5 kA. Taking a conservative approach, it was decided that the weld schedule defined in table 3.1.1 would produce welds conforming to the $4\sqrt{t_{sheet}}$ requirement while being adequately removed from the expulsion window.

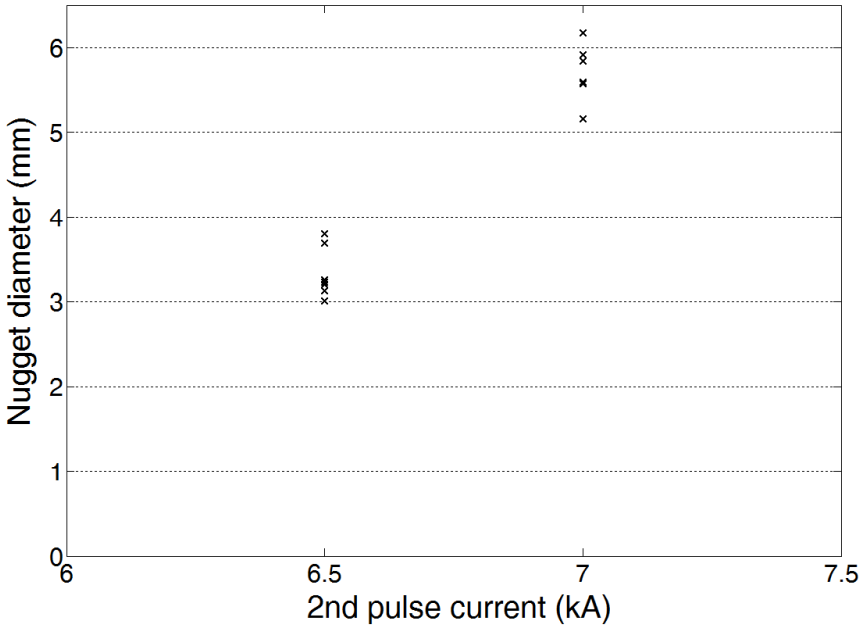

Figure 3.5.12: Second DP600 weld trial: Nugget size as function of 2nd pulse current. Fixed parameters: Electrode force = 3.5 kN; 1st pulse = 5 kA for 250 ms; pause time = 40 ms; 2nd pulse = indicated current for 500 ms; hold time = 250 ms

3.6 Weld destructive samples

Lap-shear and cross-tension samples are common methods for measuring weld strength [89]. An illustration of the test geometries and loading directions is shown in figure 3.6.1. The purpose of a cross-tension test is to determine the maximum tensile force a weld can sustain [90] and for a lap-shear test to determine the maximum shear force a weld can sustain [91].

In lap-shear tests, two steel strips are overlapped, with a spot weld made in the centre of the overlapped region. A tensile load is applied parallel to the sheet direction. In cross-tension tests, two steel strips are laid normal to each other, with a spot weld made in the centre of the overlapping region. A tensile load is applied normal to the weld.

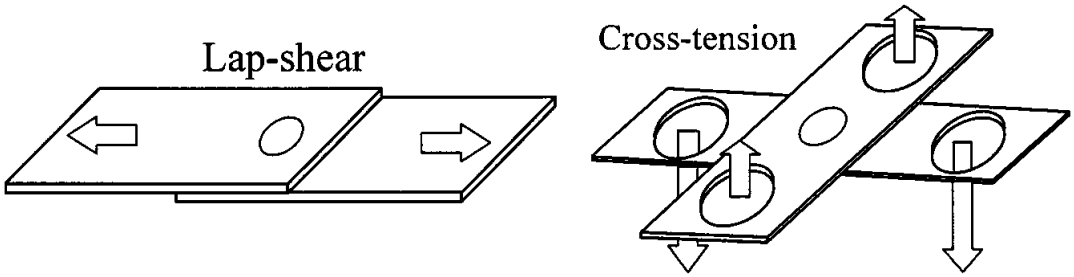

Figure 3.6.1: Lap-shear and cross-tension sample geometries (arrows indicate loading directions). Taken from [18].

3.6.1 Choice of lap-shear and cross-tension geometries

In creating the cross-tension samples, a specially built jig was available for aligning the samples during welding, as shown in figure 3.6.4. In addition, cross-tension clamps fitted to a tensile testing machine (shown in figure 3.6.7) had dimensions corresponding to those samples used in the aligning jig. Both of these testing equipment were designed to industrial automotive testing specifications [92].

There are dimensional differences between the automotive and ISO standards [90, 91], however, the main purpose of the weld destructive specimens are for validating the finite element model. Considering the finite element model will have the exact dimensions of the automotive test pieces, a direct comparison will be valid. An additional justification is that this project was supported by an industrial partner and it was for this reason that the existing equipment and standards were used.

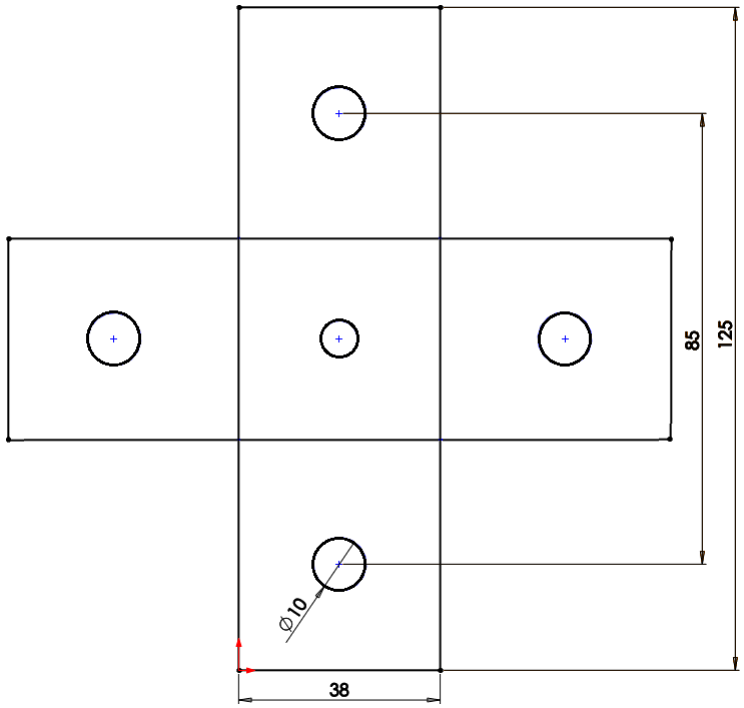

Figure 3.6.2: Cross-tension test piece. All dimensions in mm. Taken from [92]

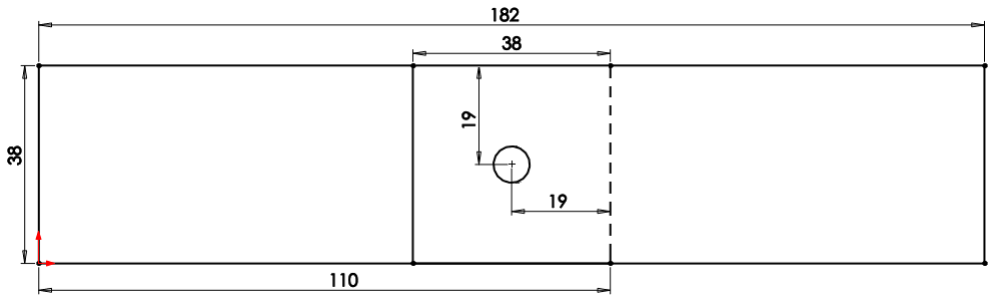

Figure 3.6.3: Lap-shear geometry. All dimensions in mm. Taken from [92]

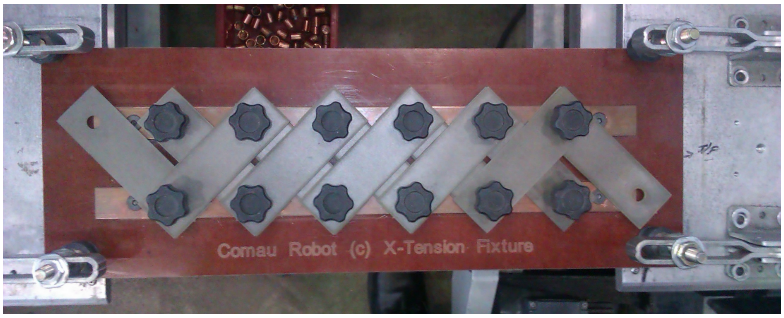

Figure 3.6.4: Cross-tension fixture

3.6.2 Creating lap-shear and cross-tension samples

The lap-shear samples were welded by taking two 110 mm x 400 mm sheets and overlapping them by 38 mm. The sheets had holes drilled in to fit onto a jig to hold them in place during welding. Individual lap-shear specimens were cut from these sheets using a water jet cutting method.

For the cross-tension samples, individual 38 mm x 125 mm sheets were overlapped in a specially designed lattice fixture, as shown in figure 3.6.4. The copper strips seen in the figure compensate for shunting, meaning all samples produced are usable.

3.6.3 Lap-shear testing

Testing was performed with a screw driven Instron 5800R tensile test machine with a 100 kN load cell, accurate to ± 25 N. The lap-shear specimens were fastened with standard tensile testing grips, with shim plates with the same thickness as the test specimen thickness to ensure the sample remained parallel to the applied force. The crosshead separation speed was 1 mm/min. A 50 mm extensometer was attached to the samples, as shown in figure 3.6.5. Using the machine displacement in the load-displacement curves would result in larger displacements than physically experienced by the test samples, as machine displacement includes the elasticity of the tensile testing machine.

The load - displacement results are shown in figure 3.6.6. The mean ultimate load at failure was 20.26 kN with a standard deviation of 1.01 kN. The mean displacement at failure was 0.40 mm with a standard deviation of 0.08 mm. Figure 3.6.6 does show some scatter between the different specimens, in terms of ultimate load but especially for the displacement at ultimate load. The reasons for this scatter will be investigated through fractography in the next section.

The measured weld diameters are shown in table 3.6.1. The average diameter is very

close to $4.5\sqrt{t_{sheet}}$. The standard deviation of the 5 weld diameters is 0.35 mm, indicating that welds of consistent sizes were created.

Figure 3.6.5: Lap-shear test setup with extensometer

Sample number	Average nugget diameter (mm)
1	5.44
2	5.69
3	5.02
4	5.44
5	5.96

Table 3.6.1: Weld measurements from fractured lap-shear samples

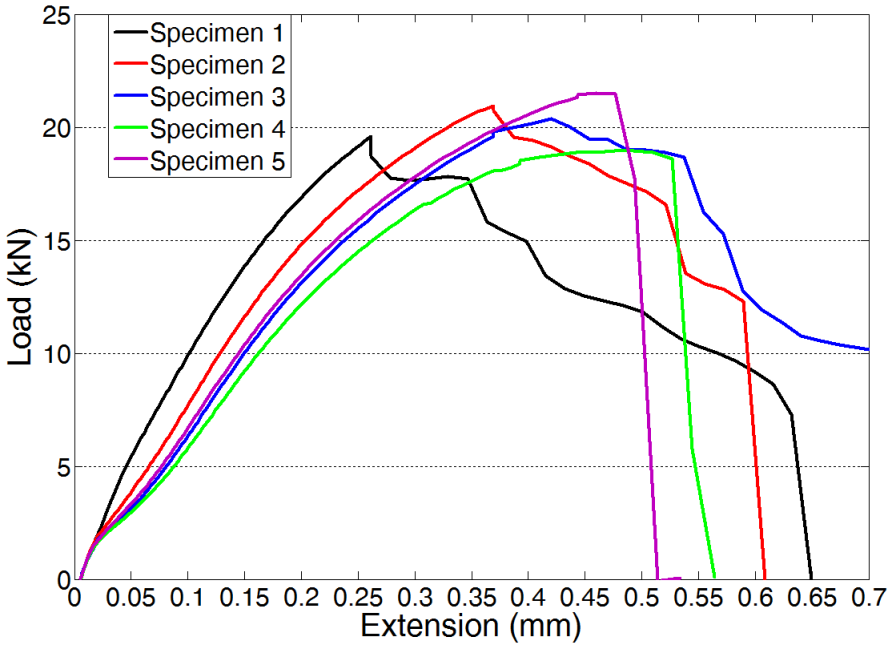

Figure 3.6.6: Load - displacement results from boron steel lap-shear tests

3.6.4 Cross-tension testing

The cross tension specimens were placed on the clamps attached to an Instron tensile testing machine, as shown in figure 3.6.7. Due to the geometry of the clamps, an extensometer could not be attached. Therefore, cross-tension results are given with the machine displacement. In comparing the results with FE analyses, only the predicted load can be reliably compared. A possible solution to measuring displacement could be to spray a speckled pattern on the cross-tension clamps and use Digital Image Correlation (DIC) to measure displacement. Insufficient time and resources were available to re-run the tests with DIC.

The crosshead separation speed was 1 mm/min. The load-displacement results are shown in figure 3.6.8. The mean ultimate load at failure was 5.91 kN with a standard deviation of 0.28 kN. The mean displacement at failure was 5.66 mm with a standard deviation of 0.31 mm. As with the lap-shear specimens, some scatter can be seen between different specimens.

The measured weld diameters are shown in table 3.6.2. All welds lie above the $4\sqrt{t_{sheet}}$ diameter criterion and on average tend towards a diameter corresponding to $4.5\sqrt{t_{sheet}}$. The standard deviation of the 5 weld diameters is 0.33 mm, indicating that welds of consistent sizes were created.

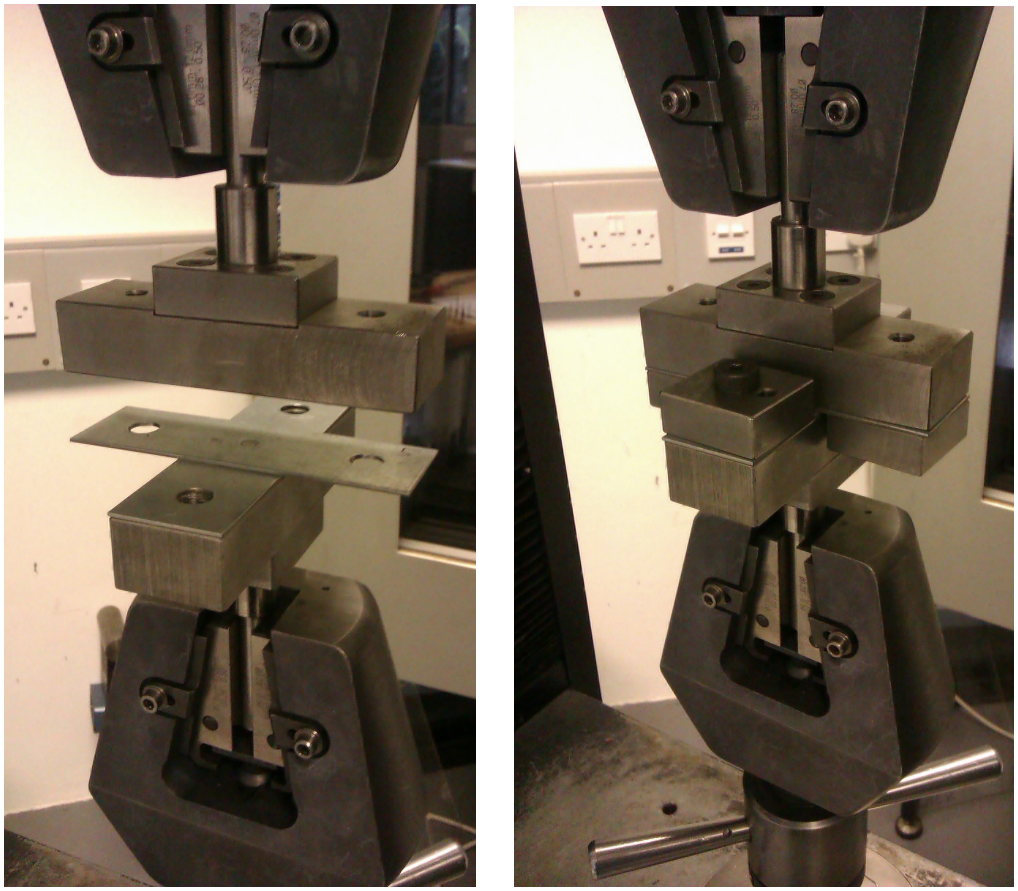

(a) Open position (b) Closed position

Figure 3.6.7: Cross-tension clamps fitted to tensile testing machine

Sample number	Average nugget diameter (mm)
1	5.56
2	5.16
3	5.02
4	5.21
5	5.82

Table 3.6.2: Weld measurements from fractured cross-tension samples

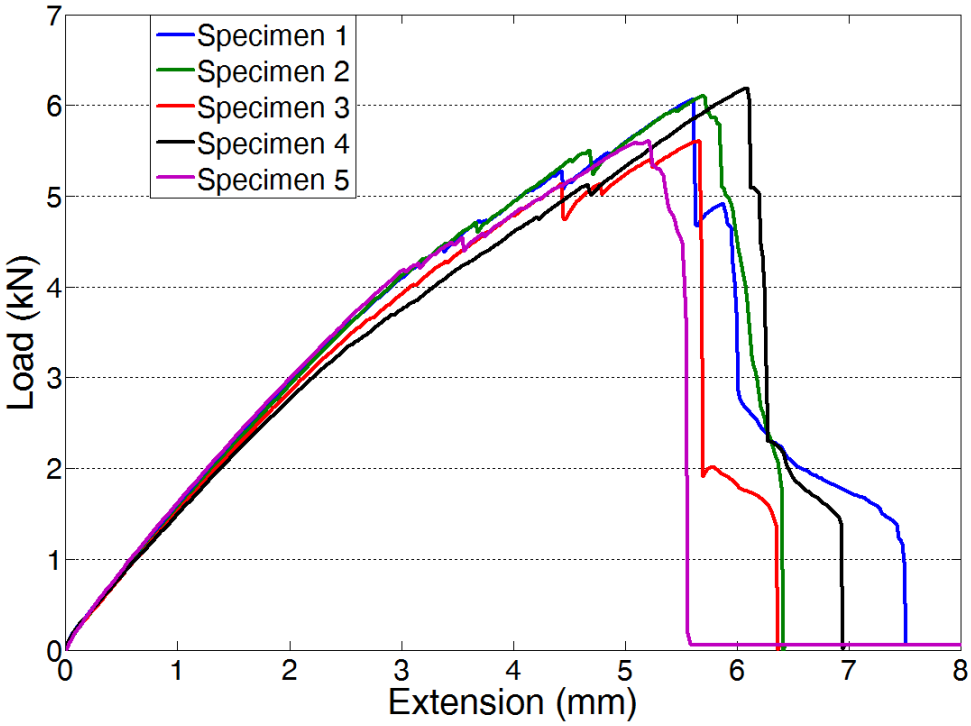

Figure 3.6.8: Load - displacement results from cross-tension tests

3.6.5 Fractography of cross-tension and lap-shear specimens

A Phillips XL30 scanning electron microscope (SEM) was used to investigate the fracture surfaces of the failed weld specimens. Additionally, Energy Dispersive Spectroscopy (EDS) was employed to analyse the elements present in inclusions. EDS works on the principle that an incident high energy electron creates a hole in an inner electron shell of the specimen atom, which is subsequently filled by an electron from a higher energy outer shell. An x-ray is generated with an energy equal to the difference in energies between the inner and outer shells. This means that the x-ray has an energy characteristic of the specimen atomic number. In this way, elements are identified.

A "standardless" analysis was performed. Such an analysis compares measured intensities with previously measured reference intensities provided with the analysis software. This is opposed to using directly measured intensities from reference materials. The EDS analysis was performed with Oxford Instruments INCA software with a materials

database to help identify various elements. For each measurement, a 20 keV beam was focused on one location on the chosen inclusion for a duration of 10 minutes. A resulting spectrum was obtained and subsequently run through the INCA analysis software. An assumption was made that if an oxygen peak is observed, the elements are present as oxides, as any free oxygen would be pumped out by the vacuum [M. Whitwood, personal communication, Tata Steel]. The software uses stoichiometry and default valencies to calculate the oxides present in the inclusions.

3.6.5.1 Fifth cross-tension specimen

Figure 3.6.11 a) shows the macrograph of the fifth cross-tension specimen, which failed by PIF. Image b) shows the centre of the weld, where a dendritic microstructure can be seen. Dendrites grow when a solid-liquid interface moves into a liquid, and the liquid temperature decreases in advance of the interface, as shown in figure 3.6.9. A requirement for dendrite formation is that the liquid be supercooled to below the equilibrium freezing temperature [22, 29]. The temperature at the solid-liquid interface rises to a higher value than both the solid or the liquid, due to the release of heat from fusion.

As one moves from the interface into the liquid, the temperature falls, because there is a flow of heat from the interface into the supercooled liquid. The resulting temperature contour shown in figure 3.6.9 is known as a temperature inversion [29]. It is this temperature inversion which causes dendrites to grow. If a small section of the interface is ahead of the surrounding surface, it will have contact with the liquid at a lower temperature. This accelerates its growth rate compared to the surrounding surface, leading to the formation of a spike. As the spike grows, latent heat of fusion is released, raising the temperature of the immediate surroundings. This retards the growth of other projections in its immediate vicinity, leading to a tree-like formation.

It is important to mention that only a few small areas of dendritic microstructures were seen. The dendrites could have formed in a shrinkage void. Another explanation could be that a cavity was created either through expulsion or from insufficient electrode force

to allow contact of the two opposite faces. Expulsion seems like a less likely cause, as there is no evidence of metal expulsion around the weld in figure 3.6.11 a). These small areas of dendrites are unlikely to have a significant effect on the load-bearing capacity of the weld, as failure usually starts from the edge of the weld near the notch tip.

Image c) shows the corona bond of the weld. The corona bond is formed at the faying surface in the HAZ region. It is formed through solid phase bonding [93], where sufficient electrode force was applied, but the temperature was insufficient to cause fusion. The highlighted area in image c) shows dimples, which follow a radial arc along the black line on the left hand edge of the corona bond zone.

Image d) shows a magnified view of the dimples with and without inclusions. The inclusion is roughly the same size as other dimples seen throughout the welds. Additionally, impressions left by the inclusions can be seen in the dimples, suggesting that the steel solidified around the inclusions [M. Whitwood, personal communication, Tata Steel]. Through EDS the inclusion in figure 3.6.11 d) was found to be mainly composed of MnO, FeO, ZnO and SiO_2, as shown in figure 3.6.10. These are the major elements present in the 22MnB5 boron steel.

The chemical composition of the BM is given in table 3.6.3, where it can be seen that manganese is a major constituent. Generally, the solubility of gases in metal decreases as temperature decreases [29]. Therefore, excess oxygen will be rejected from the cooling nugget and form gas pockets and non-metallic oxide inclusions. It is likely that not all the zinc coating was removed during sand blasting, hence the presence of zinc oxide.

The highlighted area in image d) shows a faceted structure, indicating brittle fracture [94]. Image e) is a higher magnification of the faceted structure, showing brittle intergranular fracture, which typically stems from a weak and brittle grain boundary phase [94]. A possible reason for the intergranular fracture could be from the zinc coating melting and going into the grain boundaries [M. Whitwood, personal communication, Tata Steel].

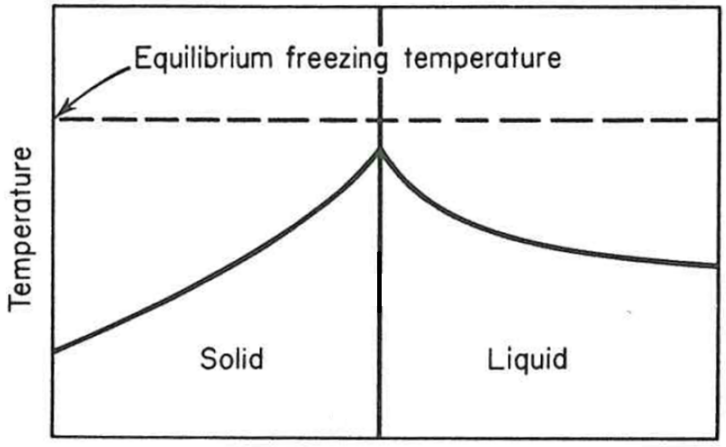

Figure 3.6.9: Temperature inversion. Taken from [29]

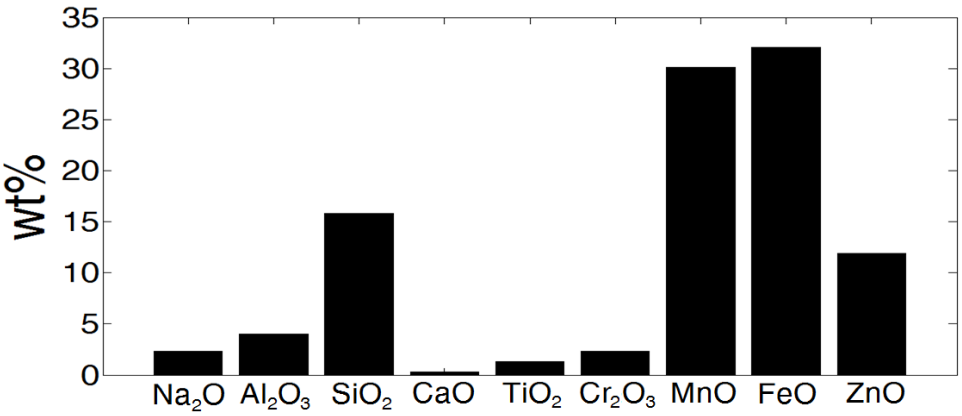

Figure 3.6.10: EDS results for inclusion in figure 3.6.11 d).

C	Mn	Si	P	S	Al	Cr	Ti	N	B
0.228	1.204	0.201	0.018	0.006	0.041	0.246	0.028	0.0044	0.0031

Table 3.6.3: Chemical composition of boron steel BM (wt%)

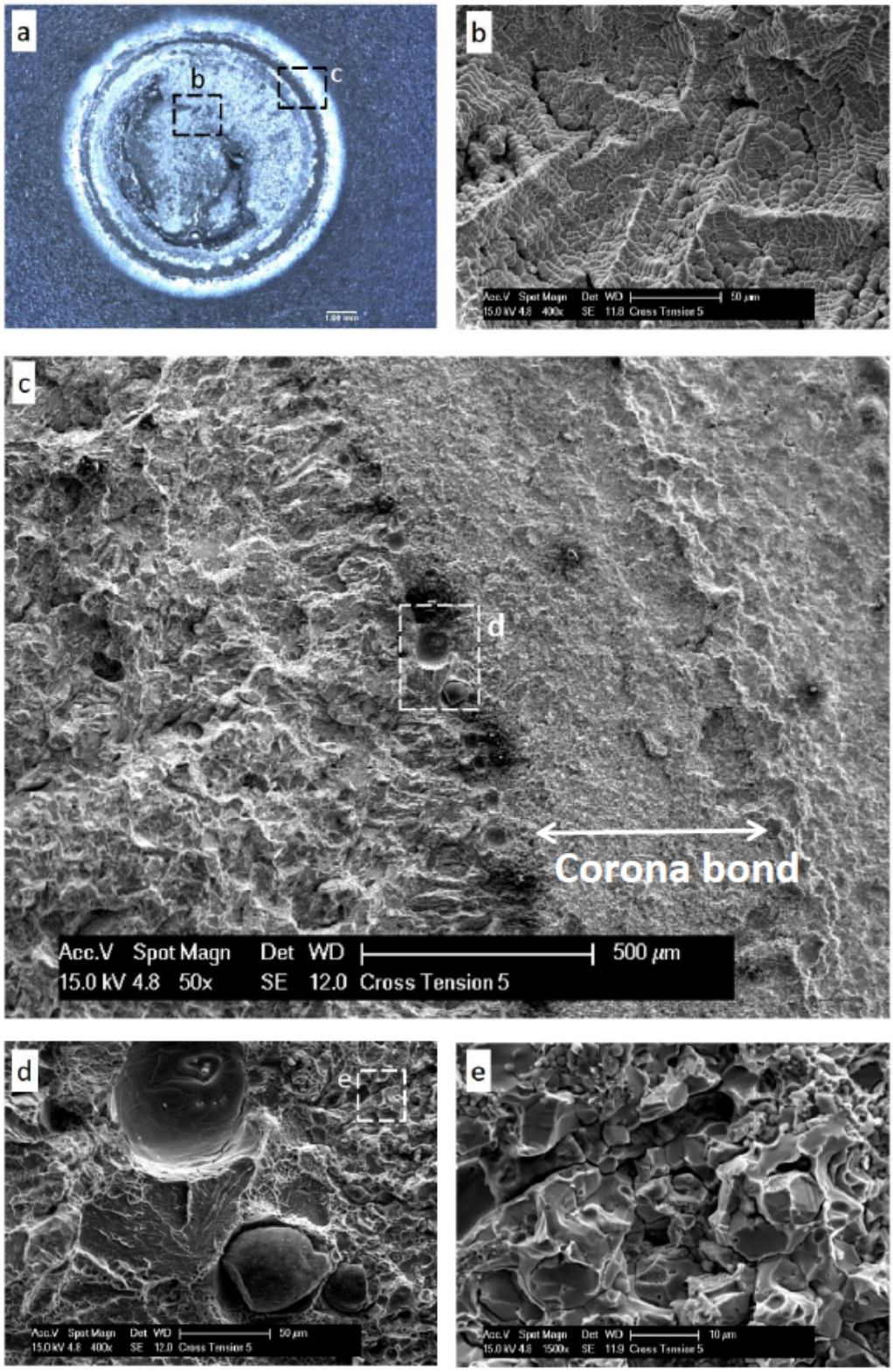

Figure 3.6.11: Macro and SEM images of fifth cross-tension specimen

3.6.5.2 First cross-tension specimen

Figure 3.6.12 a) shows a macrograph of the first cross-tension specimen, which failed by BP. In image b), two interesting features are present. Firstly, in the lower left hand corner, dimples following a radial arc can be seen. The fact that the dimples are roughly at the same radius from the weld centre suggests that the inclusions were pushed out during the welding process. Secondly, in the upper right hand corner, droplets of resolidified coating can be seen following a radial arc. These droplets suggest the two opposite sides of the steel sheets were not in contact, allowing the droplets to solidify in air. This suggests that the droplets were formed near the notch tip.

Image c) shows the lip of the pull-out zone at the 4 o'clock position, with a higher magnification of the area shown in image d). The dimpled fracture surface indicates ductile fracture [94, 42], occurring through the coalescence of microvoids which nucleate at regions of strain discontinuity, such as inclusions, grain boundaries and dislocation pile-ups. According to the ASM book of fractography [94], equiaxed dimples bounded by a rim are indicators of fracture occurring through a uniaxial tensile load, while shallow, elongated dimples are indicators of fracture occurring through shear. Therefore, the fracture surface presented in image d) is ductile shear. Image e) shows a faceted surface, with a higher magnification on image f) confirming brittle fracture.

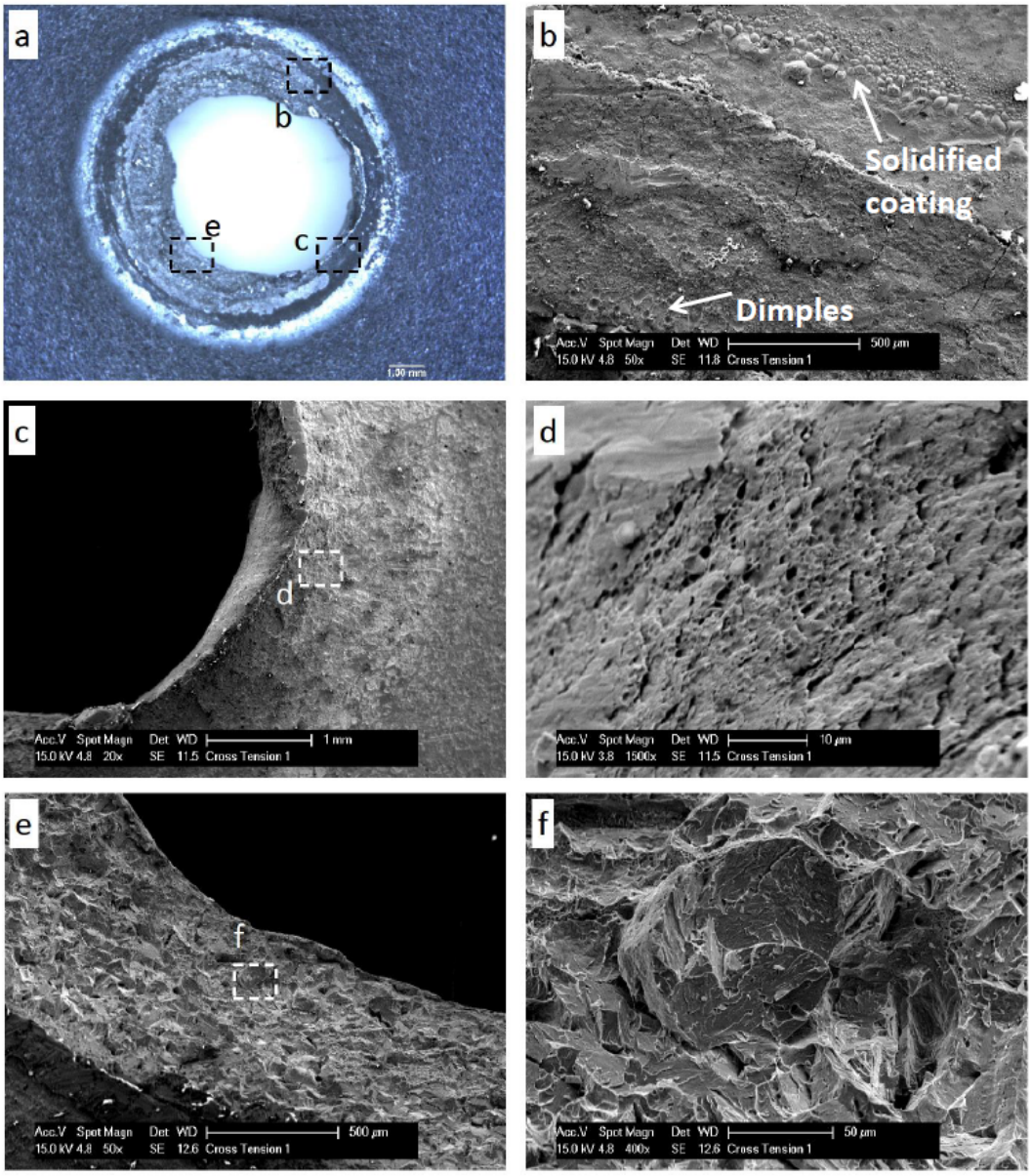

Figure 3.6.12: Macro and SEM images of first cross-tension specimen

A more thorough investigation is given to the section at 8 o'clock of the first cross-tension specimen (figure 3.6.13 a)) to illustrate the array of different fracture mechanisms present in a small area. In image b), the highlighted area indicated by "c" shows dimples, following a radial path, as previously shown in other specimens. Image c) shows a magnified view of the dimples and a surrounding area of ductile fracture. The

dimples in image d), containing small inclusions, are quite deep and appear equiaxed, confirming the uniaxial tensile load applied to the weld [94]. It is likely that the inclusions served as void-nucleating sites [94]. Image e), being further away from the weld centre, indicates brittle intergranular fracture.

From these observations, it may be inferred that the left hand side of image b) shows brittle failure and the right hand side shows ductile failure. A possible reason for this ductile - brittle separation could be due to the molten zinc segregating to the edge of the nugget, as observed by Harlin *et al* [17]. The molten zinc then travels into the grain boundaries, leading to intergranular brittle fracture.

An EDS analysis was performed on the inclusions presented previously in figure 3.6.13 d). The inclusions are numbered 1 to 4 in figure 3.6.14 a), with the corresponding weight-percent (wt%) of each identified element, calculated by the Oxford Instruments INCA software with reference material databases. Inclusions 2, 3 and 4 have similar compositions, being mainly composed of MnO, FeO, ZnO and SiO_2. The largest amount of alloying element in 22MnB5 is manganese, hence all inclusions are composed in some part of MnO. The effect of the remaining zinc coating after sand blasting is also evident, especially in inclusion 1 which is composed of 77 wt% ZnO. There are also smaller amounts of aluminium and titanium oxides present. As mentioned previously, boron has a high affinity to oxygen and nitrogen, and Al and Ti are added as alloying components to combat this.

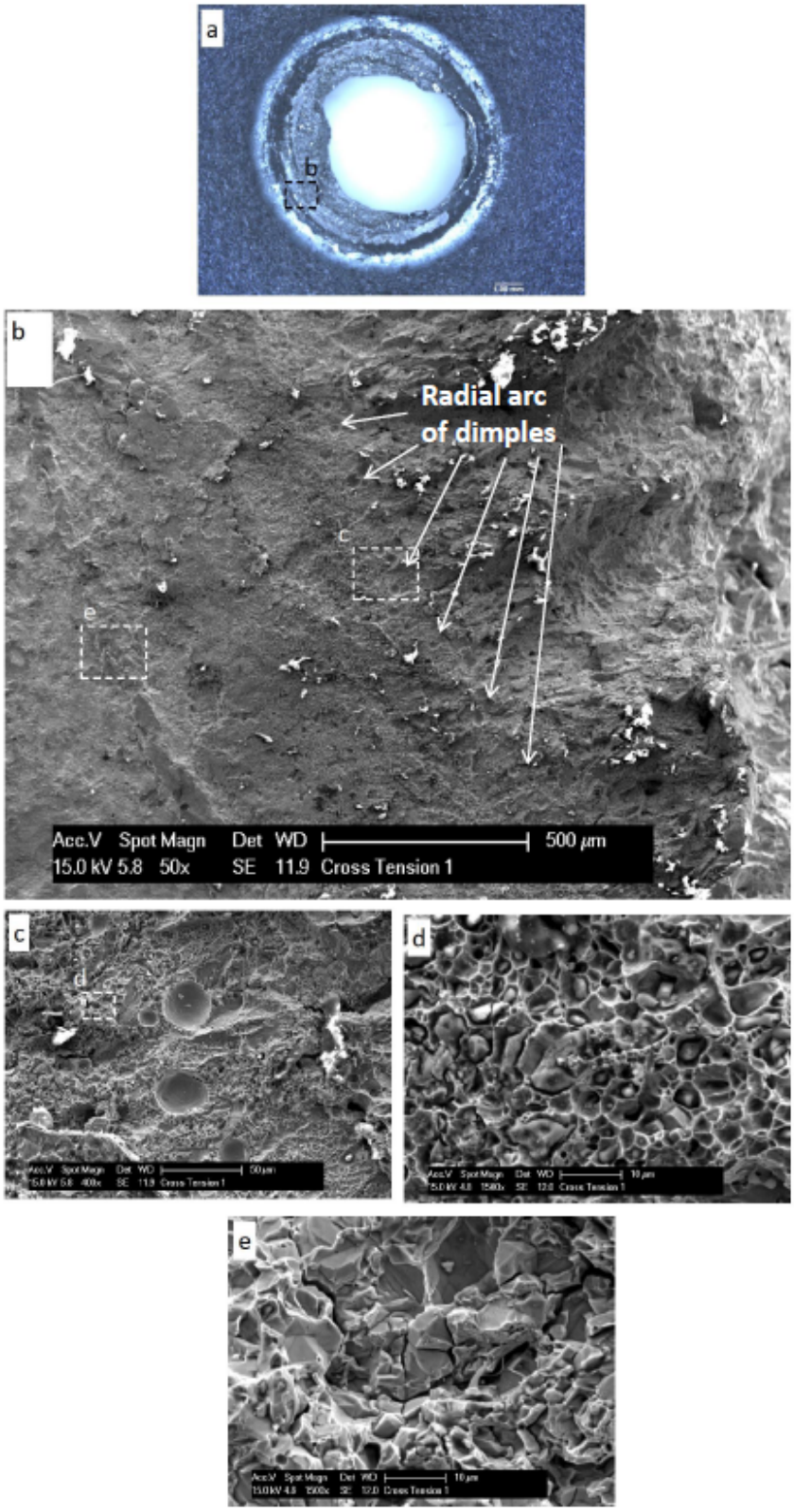

Figure 3.6.13: Macro and SEM images of first cross-tension specimen

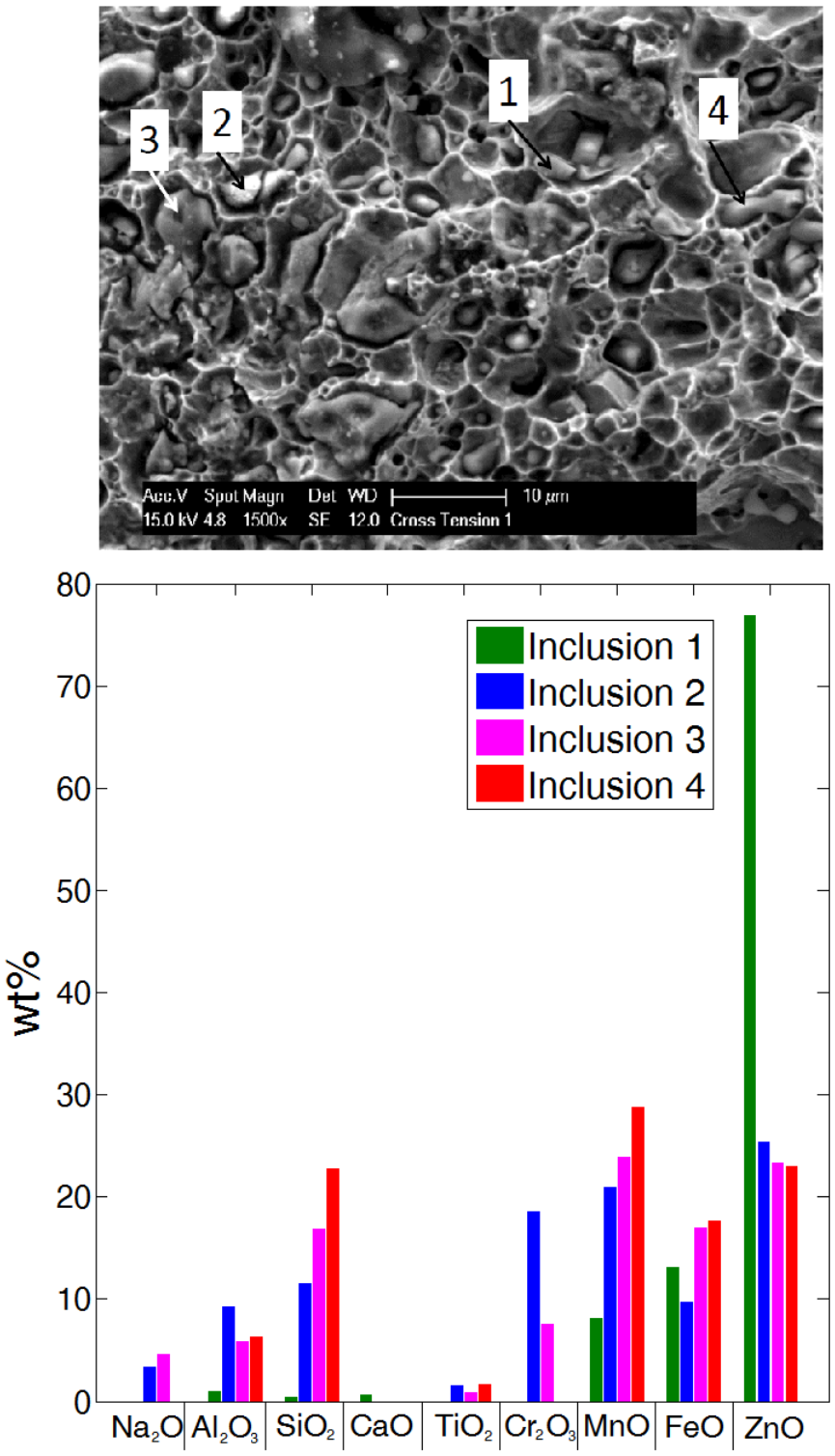

Figure 3.6.14: EDS analysis of inclusions in the first cross-tension sample

3.6.5.3 First lap-shear specimen

Figure 3.6.15 a) shows a macrograph of the first lap-shear specimen, which failed by BP. Image b) shows a backscattered image of the lip of the nugget edge, exhibiting two cross-sectioned inclusions (shown just above the highlighted area "c"). It is possible these inclusions have been smeared as the nugget pull-out occurred, causing them to appear very large [M. Whitwood, personal communication, Tata Steel]. EDS analysis showed that the inclusions were mainly composed of 52.3 wt% MnO, 23.9 wt% SiO_2, 9.9 wt% FeO.

Image c) shows elongated dimples, indicating ductile shear fracture. Image d) shows the weld at the 6 o'clock side, with what appears to be brittle fracture surfaces. Images e) and f) show the area in higher magnification. These two images indicate mixed-mode fracture occurred, with image e) showing brittle cleavage fracture and image f) showing ductile uniaxial fracture. It is interesting to note a *uniaxial* fracture surface present on a lap-*shear* sample.

Chao [18] stated that, during a lap-shear test, the nugget rotates and aligns itself with the loading direction. So even though the global load is shear, the failure mechanism on the microstructural scale was reported as uniaxial. Chao's finding stemmed from a steel with a UTS of 434 MPa, therefore of lower strength than boron steel.

Figure 3.6.16 shows images of boron steel and DP600 lap-shear samples taken with a high speed camera. The images are just before fracture. As can be seen, there is minimal rotation in the boron steel sample compared with the DP600 sample. This indicates that the boron steel weld does not align itself with the loading direction to as great a degree as lower strength steels, however some alignment occurs, leading to the ductile uniaxial fracture surfaces seen in figure 3.6.15 f).

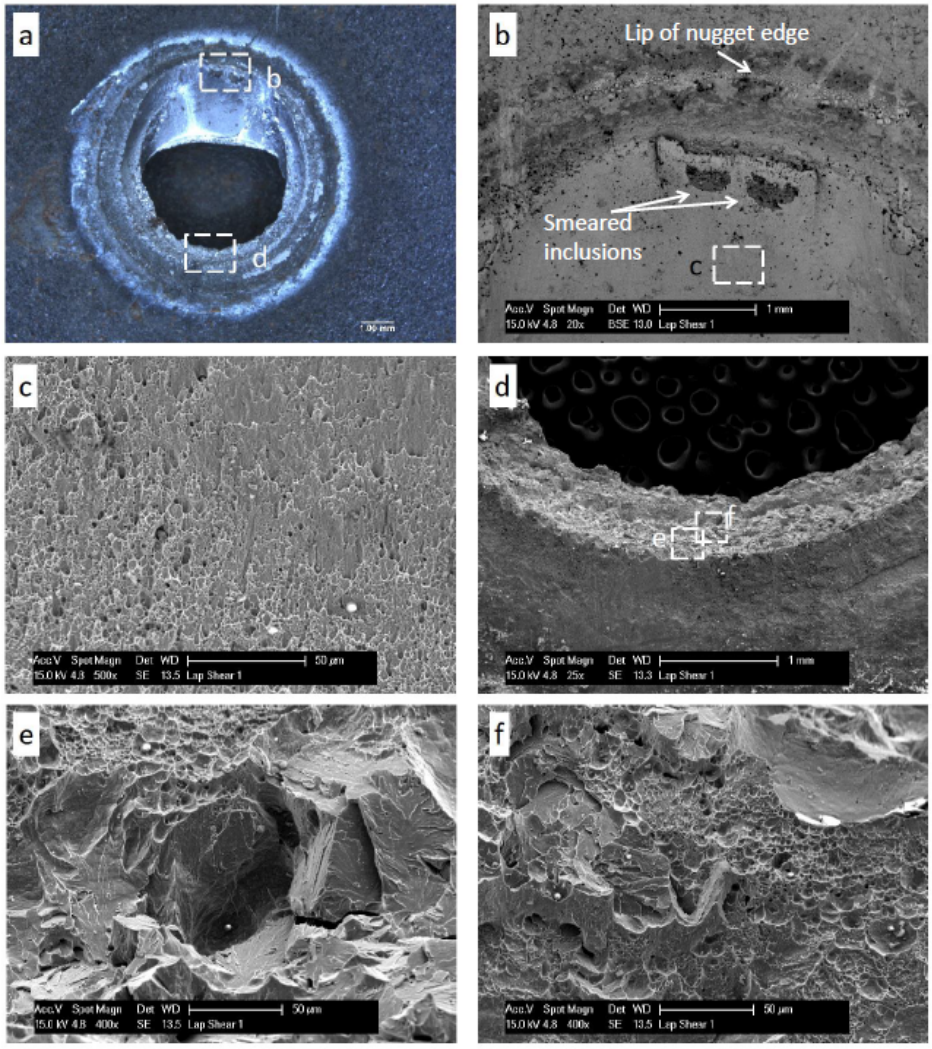

Figure 3.6.15: Macro and SEM images of first lap-shear specimen

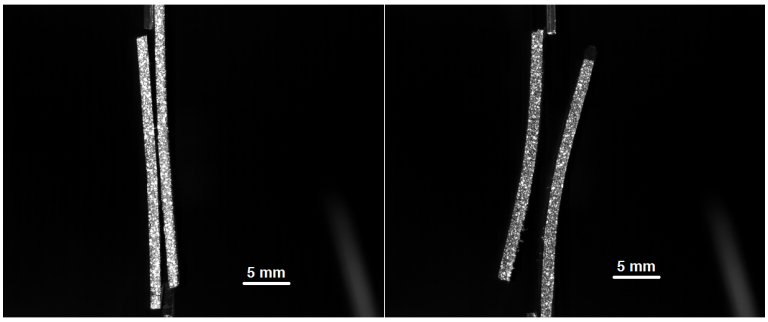

(a) Boron steel lap-shear specimen (b) DP600 lap-shear specimen

Figure 3.6.16: Rotation of lap-shear specimens

From the SEM investigations, a mix of ductile and brittle fractures were observed, regardless of the specimen geometry. The extent to which the zinc coating segregated to the edge of the nugget was found. This was evidenced by ductile fracture surfaces nearer the nugget and brittle surfaces further away. Some dendritic microstructures were observed in the nugget centres, suggesting that insufficient electrode force was used.

A noteworthy observation was the radial arc of dimples, most likely caused by large inclusions, which were found at the nugget periphery. It is likely that such defects can influence the crack paths. Ductile fracture surfaces were observed to contain small inclusions. These small inclusions were identified as potentially serving as void nucleation sites. The presence of large and small inclusions could help to explain the scatter of the load-displacement curves for the lap-shear and cross-tension tests (figures 3.6.6 and 3.6.8).

3.7 Hardness measurements

The hardness distribution of the spot weld is used extensively throughout this project. After performing the residual strain measurements described in the next chapter, the measured welds were sectioned in half using a Buehler IsoMet 4000 linear precision saw. The sectioned samples were then mounted in a thermosetting resin using a Buehler SimpliMet hot mounting press. The mounted samples were subsequently polished, using a final stage 3 μm diamond suspension polishing liquid.

All samples were etched with 2% Nital; a chemical etchant consisting of 2% nitric acid and 98% methanol. As a basic idea, the etchant selectively corrodes surfaces with different potentials. Etching occurs through an electrolytic process at structural variations resulting from physical or chemical heterogeneities, rendering some features cathodic or anodic under certain etching conditions [95]. Differences in the etchant attack rate reveals different structures. Nital etches both ferrite grain boundaries and

ferrite-cementite phase boundaries [95]. Caution should be used with Nital, as it is sensitive to grain orientation. This means that a faint etch might be produced at ferrite-carbide interfaces within certain grains. Nital is also recommended for viewing martensitic microstructures.

Hardness measurements were performed on a Wilson Hardness Tukon 1202 hardness tester with a motorised stage. Hardness tests were performed in accordance with BS EN ISO 6507-1:1998 [96]. The standard states that the distance between the centres of two adjacent indents be at least 3 times the mean diagonal length of the indents. The mean diagonals of indents in the softest part of the weld were found to be approximately 0.05 mm. Hence indents were performed at intervals of 0.2 mm. An indentation load of 0.5 kgf (or equivalently 4.9 N) was used with a dwell of 10 seconds at peak load. A Vickers indenter tip was used, shown in figure 3.7.1. The indenter is a square based pyramid with an angle of 136 ° between the opposite faces at the vertex. The hardness is proportional to the ratio obtained by dividing the force by the sloping area of the indent, as shown in equation 3.7.1

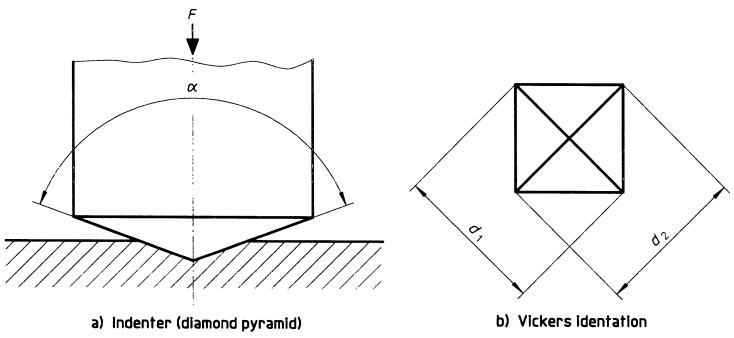

Figure 3.7.1: Schematic of Vickers indenter. Taken from [96]

$$HV = 0.102 \frac{2F sin\frac{136°}{2}}{d^2} \tag{3.7.1}$$

where HV is the Vickers hardness, F is the test force in Newtons, d is the arithmetic mean of the two diagonals in figure 3.7.1 b) and the constant 0.102 is the inverse of the acceleration due to gravity. Three line scans were performed on the upper plate, at

0.55, 0.75 and 0.95 mm from the sheet-sheet interface. The results are shown in figure 3.7.2.

The nugget and BM exhibit hardness values of approximately 500HV, with the lowest hardness in the HAZ being 325HV. This is consistent with findings of other authors [42, 41]. The similarity in hardness between the nugget and BM is most likely due to both parts containing significant amounts of martensite, which formed after rapid cooling from above the A_{c3} temperature. Severe hardness gradients in the HAZ can be seen, indicating the area of reduced mechanical properties.

There is little deviation in the hardness distribution through the thickness of the sheet. From this, an assumption is made that material properties can be approximated as being constant through the sheet thickness. This assumption is carried forward throughout other experiments in this thesis.

The hardness distribution of the DP600 spot weld is shown in figure 3.7.3. Hardness values of approximately 400HV are seen in the nugget, with a sudden drop to 200HV in the BM. This is consistent with the findings by other authors [97].

An interesting point to note is that even though both the boron steel and DP600 welds experienced cooling rates more than sufficient to form martensite, the DP600 nugget hardness is approximately 100 HV lower than the boron steel nugget. This can be understood, in part, by the carbon content of the steels. Figure 3.7.4 shows the Diamond Pyramid Hardness (DPH) versus weight percent of carbon. DPH is equivalent to HV. For the steels used in this work, the boron steel has a carbon content of 0.23 wt% and DP600 has a content of 0.1 wt%. From the figure, the cause for the difference in nugget hardness is evident. As mentioned previously, martensite is a supersaturated solution of carbon in ferritic iron, having a tetragonal structure. The degree of tetragonality increases with carbon content [1]. So from figure 3.7.4, it can be seen that as carbon content increases, so does hardness.

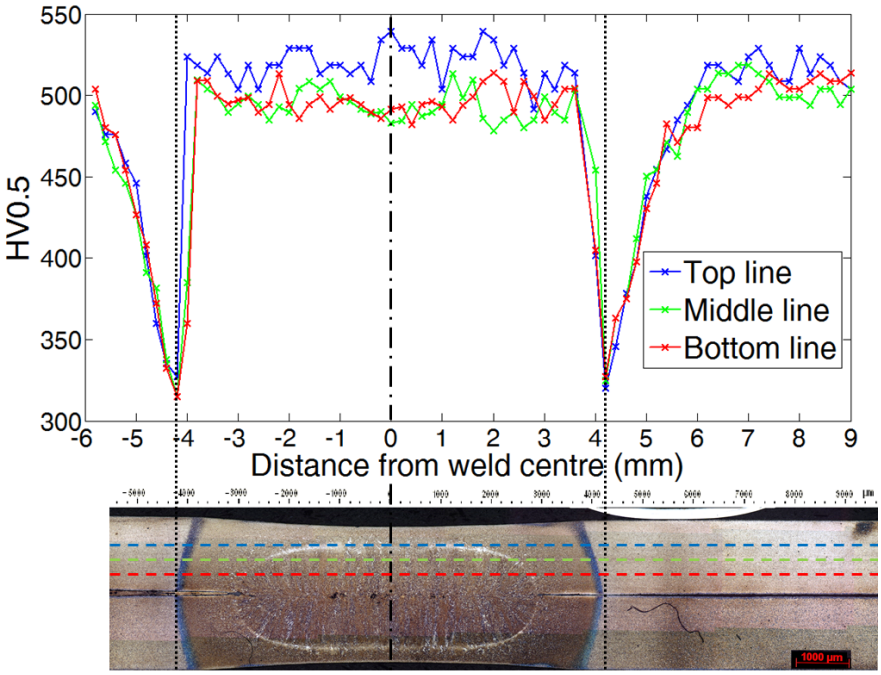

Figure 3.7.2: Hardness distribution of boron steel spot weld. Bottom, middle and top lines are 0.55 mm, 0.75 mm and 0.95 mm from interface, respectively.

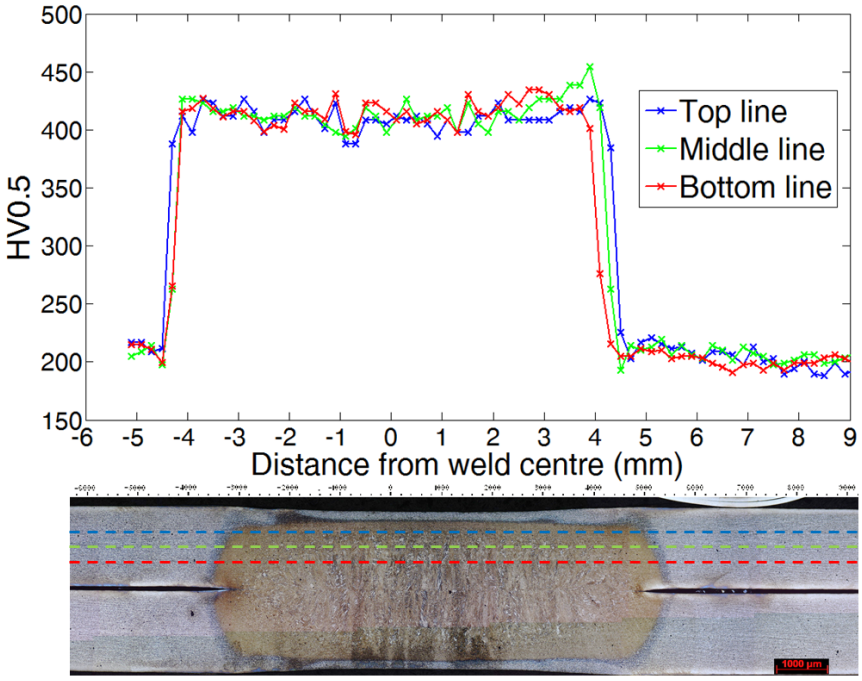

Figure 3.7.3: Hardness distribution of DP600 spot weld. Bottom, middle and top lines are 0.55 mm, 0.75 mm and 0.95 mm from interface, respectively.

Of course, different alloying elements and austenite grain size will also have an effect on the hardness, so the figure should be used as a rough guide. Hardenability increases with increasing austenite grain size [1]. As the grain size increases, the grain boundary area decreases, meaning that there are less nucleation sites for ferrite and pearlite. Alloying elements also slow down the ferrite and pearlite reaction rates. The effect of different amounts of alloying elements is beyond the scope of this thesis, and will hence only be dealt with in a qualitative manner.

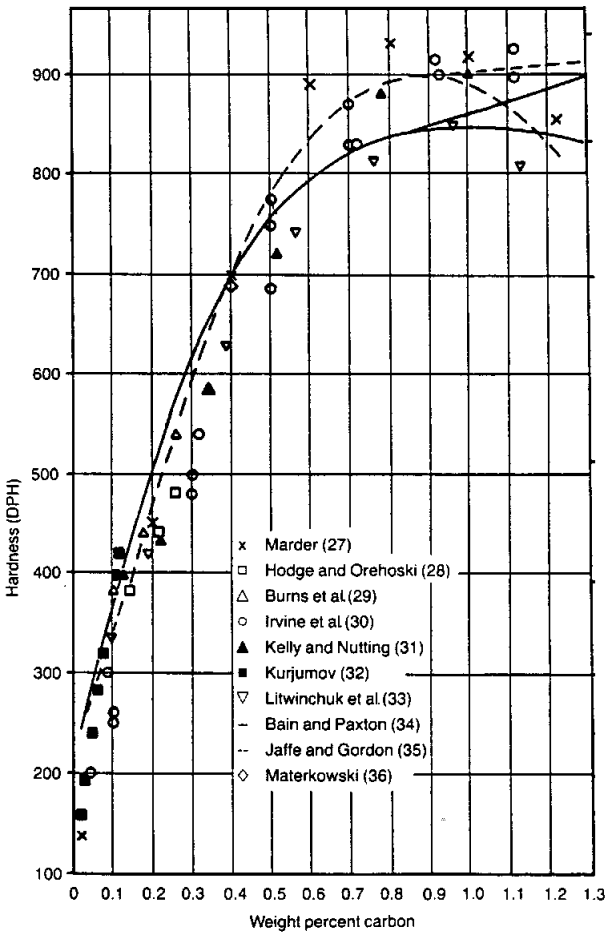

Figure 3.7.4: Martensite hardness as function of steel carbon content. Taken from [98]

3.8 Conclusions

The main aim of this section was to arrive at a weld schedule for boron steel which produced an acceptable weld for extracting material properties in further tests. Acceptability is defined as a nugget diameter between $4\sqrt{t_{sheet}}$ and $5\sqrt{t_{sheet}}$ and with minimal expulsion.

Basic weld schedules were simulated in SORPAS to gauge the effect of varying individual welding parameters, for example electrode force or current. It was found that using a high electrode force (7 kN) at low current (4 kA) severely reduced the nugget diameter compared to using a low electrode force (3.5 kN) at the same current. This was attributed to the reduced contact resistance due to high electrode forces. Negligible differences were seen in nugget diameters produced with electrodes composed of CuCrZr and CuZr. This was due to very similar conductivities between the two electrode materials. From the weld lobes, it was seen that a higher electrode force results in a smaller welding window, compared to using a lower electrode force. These observations were utilised in performing physical welding trials.

Physical welding trials were performed by varying welding parameters of the resulting welding schedule. Negligible variation in nugget diameters were observed by increasing the second pulse time from 600 ms to 1000 ms. Employing lower electrode forces resulted in larger nugget diameters. Expulsions were increased at currents beyond 7.5 kA. From these physical welding trials, the optimum weld schedule parameters were confirmed.

Lap-shear and cross-tension destructive samples were produced with the automotive weld schedule. A specially made jig was available to producing cross-tension specimens. Additionally, cross-tension clamps corresponding to the jig dimensions was available for attaching to the tensile test machine. Extensometers were used to measure specimen elongation. However, due to the dimensions of the cross-tension clamps, extensometers could not be used.

The lap-shear specimens failed at an average load of 20.26 kN and displacement of 0.40 mm. The cross-tension specimens failed at an average load of 5.91 kN and displacement of 5.66 mm.

Fracture surfaces were obtained through SEM imaging. It was found that inclusions were prevalent outside the nugget. Large dimples, most likely formed by large inclusions, were seen in a radial arc in the corona bond area. The fact that these dimples were all at approximately the same radius from the weld centre suggests that the large inclusions were pushed out during welding. Ductile fracture regions were observed, with small inclusions in the equiaxed dimples. It was suggested that these small inclusions served as void nucleating sites. The presence of inclusions are likely to affect the fracture initiation sites and it is therefore likely that they can explain the scatter in load-displacement curves seen between different weld destructive specimens.

Hardness measurements were performed on the produced welds. For the boron steel weld, it was found that the nugget and BM exhibited similar hardness values, most likely being due to significant amounts of martensite being present in both sections. Steep gradients in hardness were seen in the HAZ, indicating the area of reduced mechanical properties. Little variation in hardness distributions were seen through the workpiece thickness direction. This lead to an assumption that material properties can be approximated as being constant through the sheet thickness.

The DP600 weld nugget exhibited a hardness 100HV lower than the boron steel nugget. This is, in part, due to the difference in carbon content between the two steels.

Consistent specimens were produced using the developed weld schedule. These specimens were subsequently used for residual stress determination and local property measurements.

Chapter 4

Residual Strain Measurement by Neutron Diffraction

4.1 Introduction

As stated in the literature review, there are limited techniques to determine the internal strain profile in welded joints. From the review, it was decided to use state of the art diffraction techniques at a neutron facility.

Measuring residual strains through neutron diffraction works on the principle that the lattice spacings of crystal planes can effectively be used as internal strain gauges. For a given lattice spacing (d) the scattered waves of the incident neutron beam will interfere constructively only at certain Bragg angles, leading to peaks of the diffracted beam. The diffraction peak is observed at an angle 2θ from the incident beam, as shown in figure 4.1.1 a). As the lattice is strained, the diffraction peak shifts by $\Delta\theta$, as shown in figure 4.1.1 a) and b).

The Q-vector bisects the incident and scattered beams and represents the direction in which the strain is determined, as shown in figure 4.1.1 a). A strain-free lattice spacing (d_0) is used as a reference to evaluate modified lattice spacings due to compressive or tensile strains through Bragg's Law:

$$n\lambda = 2dsin\theta \tag{4.1.1}$$

where n is an integer, λ is the neutron wavelength, d is the spacing between the planes in the atomic lattice and θ is the angle between the incident beam and the scattering planes. The Bragg equation can be rearranged to calculate strain (ε), as shown in equation 4.1.2.

$$\varepsilon = \frac{d - d_0}{d_0} = \frac{sin\theta_0}{sin\theta} - 1 \tag{4.1.2}$$

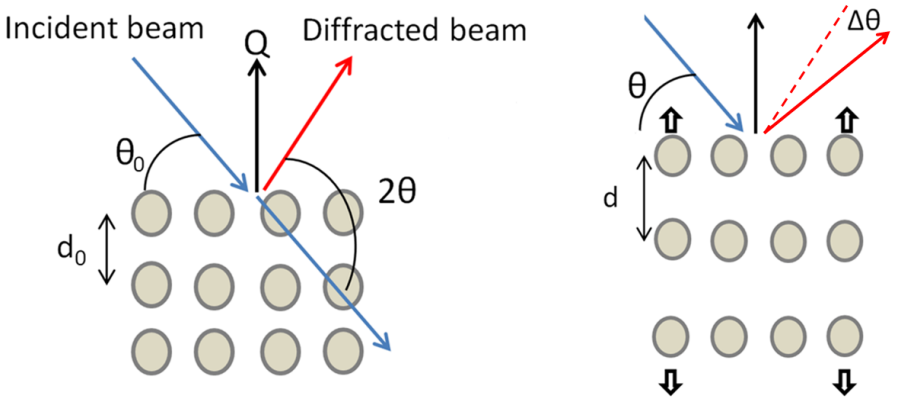

(a) Strain-free and strained lattices

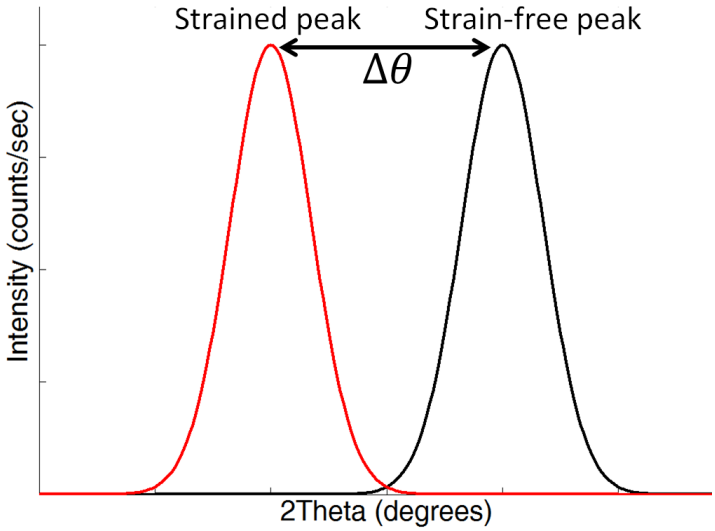

(b) Shift in diffraction peak position as result of strained lattice

Figure 4.1.1: Visual representation of principle of neutron diffraction

The peaks depicted in figure 4.1.1 b) may also broaden or contract depending on the crystal structure. For example, martensite may exhibit a broader observed peak than ferrite [99]. The degree of peak broadening can give an indication of the different metallic phases present in the weld. This will be investigated later in the chapter.

Residual stresses may be defined in terms of length scale: Type I are long range stresses which equilibrate over macroscopic dimensions, Type II stresses equilibrate over a number of grain dimensions and Type III equilibrate within a grain [56]. The residual stresses dealt with in this chapter are Type I or macro-stresses. Weld residual stresses are produced as a result of the temperature distributions and differential contractions as the weld metal cools to room temperatures.

4.1.1 Neutron diffraction technique and neutron source

The neutrons used in this chapter were produced in a nuclear reactor. The resulting neutrons have high energies (in the order of mega electron volts (MeV)), and the corresponding wavelengths are too short to investigate condensed matter. Another problem is that these high energy neutrons would damage solids by knocking atoms out of their positions, leading to vacancies. To lower the energies, the neutrons are brought into thermal equilibrium with a "moderating" material such as water or liquid hydrogen.

Thermal neutrons emerge from the moderator, with a broad spectrum of energies averaged around the moderator temperature. The average energy of a thermal neutron moderated by water is 25 meV, corresponding to a wavelength of approximately 1.8 Å, which is of the same order as typical inter-atomic distances.

After being moderated, the neutrons still have a broad energy spectrum. These neutrons are usually reduced to a *monochromatic* beam through Bragg reflection at a monochromator. The spacing of the reflecting planes of the monochromator and scattering angle are chosen so that only the neutrons satisfying the Bragg equation are reflected in the direction of the experimental area.

4.2 Experimental Method

Residual strain distributions were determined using non-destructive neutron diffraction at the SALSA (Strain Analyser for Large Scale Applications) beam line at the Institut Laue-Langevin (ILL), Grenoble [100]. The residual strains were mapped and the residual stresses were subsequently calculated as a function of position from the weld centre.

Spot welds were produced with the automotive weld schedule, as discussed in chapter 3. The residual strains were measured on spot welded 1.5 mm thick boron steel sheets and, additionally, spot welded 1.5 mm thick DP600 steel sheets, for benchmarking. The residual strain measurements were taken at 1 mm intervals at depths corresponding to the sheet mid-plane at 0.75 mm above the sheet-sheet interface in the top plate and 0.75 mm below the sheet-sheet interface in the bottom plate, shown as the dashed lines in figure 4.2.1.

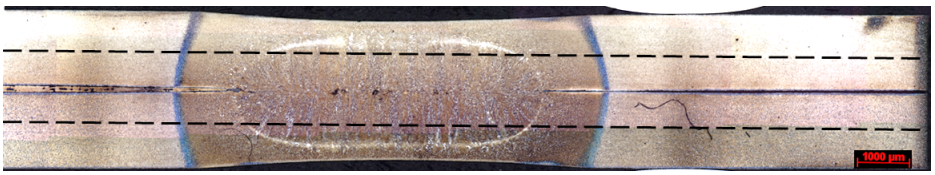

Figure 4.2.1: Neutron diffraction measurement lines

Radial collimators were used as the defining optics on both incident and diffracted beams, effectively creating an area of beam focus of 1.2 x 1.2 mm^2, with a height of 2 mm. The collimator set-up gave the beam a triangular intensity shape function with a full width at half maximum (FWHM) of approximately 0.6 mm at the point of focus [101]. The reader is referred to figure 4.3.7 for the definition of FWHM.

The determination of residual stress from the measured residual strains requires the measurement of strain in at least 6 directions, however, if the principal directions are known, then only 3 measurements are required along the principal directions. In this work, three perpendicular strain measurements were made along the radial, hoop and

axial directions. The radial and hoop directions are in the sheet plane and the axial direction is out-of-plane.

If strain measurements are made on three perpendicular directions along the principal strain directions, then it is possible to calculate the corresponding residual stresses through the generalised Hooke's Law, as shown in equations 4.2.1 to 4.2.3:

$$\sigma_x = \frac{E}{(1+\nu)(1-2\nu)}\left[(1-\nu)\varepsilon_x + \nu(\varepsilon_y + \varepsilon_z)\right] \tag{4.2.1}$$

$$\sigma_y = \frac{E}{(1+\nu)(1-2\nu)}\left[(1-\nu)\varepsilon_y + \nu(\varepsilon_x + \varepsilon_z)\right] \tag{4.2.2}$$

$$\sigma_z = \frac{E}{(1+\nu)(1-2\nu)}\left[(1-\nu)\varepsilon_z + \nu(\varepsilon_x + \varepsilon_y)\right] \tag{4.2.3}$$

where E is Young's modulus and ν is Poisson's ratio.

In order to first calculate the strains, a strain free reference (d_0) is required, as indicated previously in equation 4.1.2. Microstructural changes, as a result of welding, are known to lead to a variation in the d_0 value across the weld [60, 102]. In such cases, a global reference d_0 value cannot be assumed [60], hence it it necessary to obtain the distribution of d_0 as a function of distance from the weld centre for accurate strain calculations.

A common assumption for thin geometries, is that the normal (out-of-plane) stress is zero throughout the weld [103, 104, 102, 105]. Hence the normal strain is exclusively due to Poisson contractions stemming from the residual stresses in the other two in-plane directions. Using this plane-stress assumption, a d_0 value is applied at each measurement location to force the normal stress to zero. The in-plane stresses, calculated with the same d_0 value, are thus corrected. This will be shown in more detail in the results section.

Different hkl planes may exhibit different responses to a macroscopic stress field. It is therefore recommended to use an elasticity modulus associated with the (hkl) lattice spacing (E_{hkl}) for calculating stress. This recommendation is based on the fact that the elastic properties depend on factors such as phase volume fractions and microstructure [106, 61]. It is recommended to obtain these elastic moduli from diffraction experiments during uniaxial loading [106]. If the diffraction elastic constant are not available, then they may be determined by uniaxial loading experiment [106]. However, due to the aforementioned consequences of phase volume fractions and microstructure, care should be taken to ensure that the uniaxial specimen and diffraction specimen have comparable material characteristics [106].

Due to insufficient beamline allocation time, values of E_{hkl} could not be determined. Instead, the bulk value of Young's modulus obtained through uniaxial tensile tests of fully hardened boron steel was used in the stress calculations. The bulk modulus is thus better suited to the calculated residual stresses in the base material and nugget, but is expected to deviate in the HAZ. Additionally, the ISO TTA 3:2001(E) standard [62] recommends utilising the 211 reflection in steels, as this plane is relatively insensitive to these issues. Such a technique has been employed in previous neutron diffraction experiments on steel welds [107, 108].

The SALSA beam line has a hexapod platform capable of rotational and translational movements. The samples were clamped to the platform using an ISO TTA 3:2001(E) VAMAS [109] mounting set, as shown in figure 4.2.3.

Measurements were taken on the 211 plane, as recommended by the ISO/TTA:3:2001 standard [62]. The 211 plane peak was found at $2\theta = 89.1°$. The sample was then rotated by $\frac{180°-2\theta}{2}$ to position the longitudinal or transverse direction along the Q-vector, as shown in figure 4.2.2. The Q-vector was now 45.5° relative to the incoming beam.

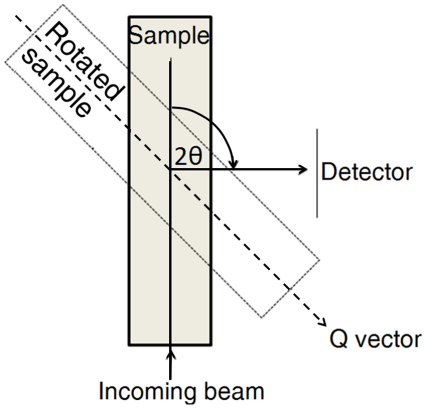

Figure 4.2.2: Rotation of sample within beam-line

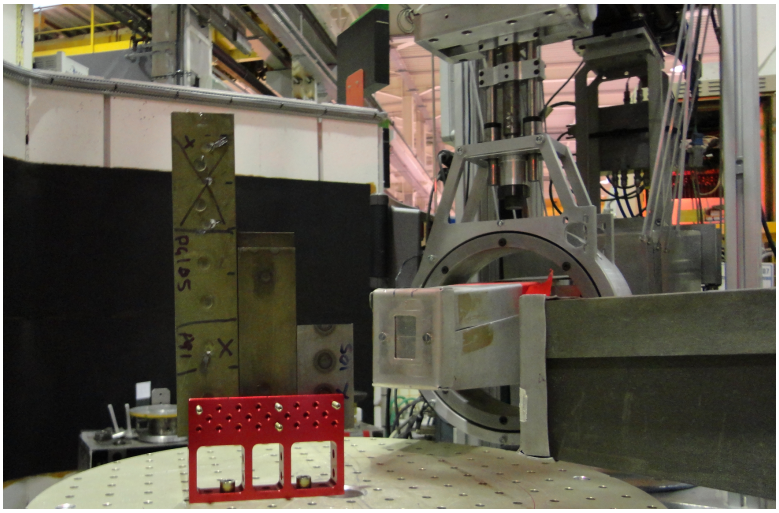

Figure 4.2.3: Mounting samples to sample stage

The sample was stepped through the beam from -2 mm to 2 mm, with respect to the weld centre, in steps of 0.2 mm to verify that the gauge volume was in the centre of the sample. It was found that the centre had an offset of 0.15 mm from where the optical systems suggested. The position was subsequently modified by 0.15 mm.

Three principal scanning directions were chosen; radial, hoop and axial. For each of the measurements, the sample was rotated to have the Q-vector coincident with the strain direction, as shown in figure 4.2.4. The samples were then scanned from -6 mm to 14 mm, with respect to the weld centre, in steps of 1 mm. This process was performed

for both the top and bottom plates of each weld configuration. Due to the allotted time on the beam line, insufficient time was available to scan from the BM, through the weld and back into the BM . Hence, measurements were initiated at the weld edge (-6 mm) and into the BM (ending at 14 mm). The measurement time was 8 minutes per measurement point.

The raw diffraction data was processed using a program developed by the ILL called LAMP (Large Area Manipulation Program) [110]. A Gaussian fit was employed to determine the angular position of the peak centre. The calculated peak centre was then used in equation 4.1.2 to calculate the strains. The θ_0 value (corresponding d_0) used in these calculations was initially a constant 89.1°. The constant θ_0 value used in the strain calculations was then modified in order to bring the axial stress to zero, to enforce plane stress.

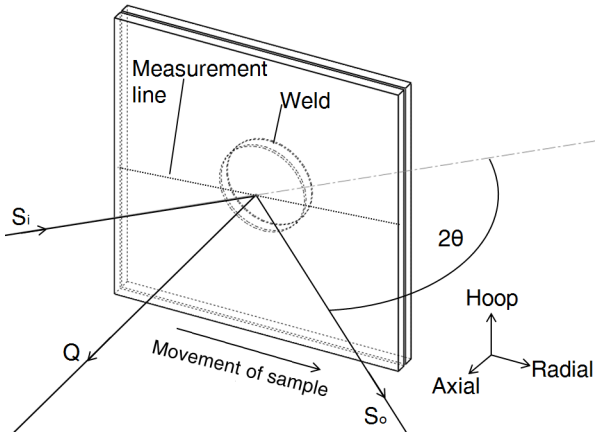

(a) Axial direction

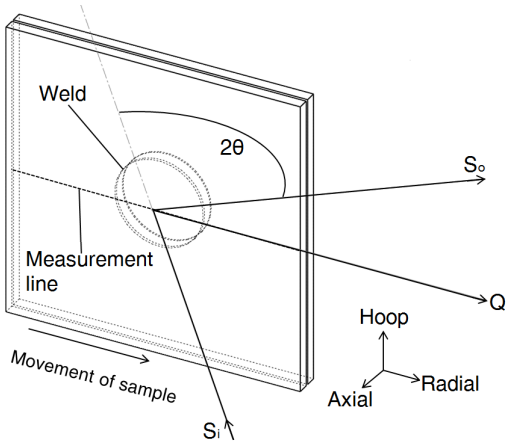

(b) Radial direction

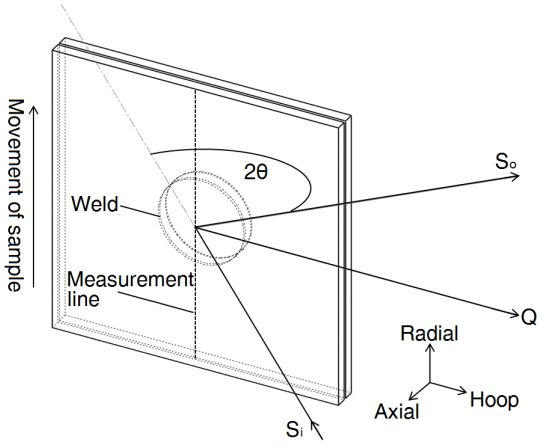

(c) Hoop direction

Figure 4.2.4: Orientation of sample for scanning the axial, radial and hoop strain directions. $S_{i,o}$ is the incoming and outgoing beam respectively. Q represents the direction in which the strain is determined.

4.3 Results and discussion

4.3.1 Strain distributions and pseudo-strain distribution for plane-stress assumption

For illustration purposes, only the results from the top sheet are included in this subsection. The differences between the top and bottom sheets will be given in the next subsection. The residual strains in figure 4.3.1 a) were calculated using a single strain-free reference parameter for all three directions. This reference parameter was taken as the average of the three directions at the furthest measurement location from the weld centre, where it was assumed the residual stresses tend to zero. It can be seen that there is some fluctuations in strains at 14 mm from the weld centre, and the strains have not yet converged to a zero value. This is, however, the first approximation to a strain-free parameter with the data available.

It can be seen that the strain in the hoop direction is the largest in tension, with peak values of 1400 με at approximately 4 mm from the weld centre. There is a significant drop to -1200 με in compression outside the weld at 8 mm. The radial and hoop strains are in tension in the nugget and HAZ (between approximately -5 mm to 5 mm from the weld centre), whereas the axial strain is completely in compression. Error bars have been included in the figure which are based on the uncertainty in the value of the peak diffraction angle. Figure 4.3.1 b) shows the residual stresses calculated using the residual strain values in figure 4.3.1 a) using equation 4.2.1. The hoop stress is dominant, with a peak value of approximately 300 MPa. In the nugget and BM, the axial stress tends around the zero value. However, it exhibits compressive stresses in the HAZ.

Figure 4.3.2 shows the pseudo-strain distribution, stemming from the application of the plane-stress assumption. The pseudo-strain is essentially a correction factor due to the microstructure variation arising from welding [102], and is subsequently applied to all measured strain data at a given distance from the weld centre. The pseudo-strain

shows the variation of the strain-free parameter as the microstructure varies across the weld. The hardness distribution of the boron steel weld is included to highlight the similar profile between the two distributions. A similar relation between hardness and pseudo-strain was found in other works [102].

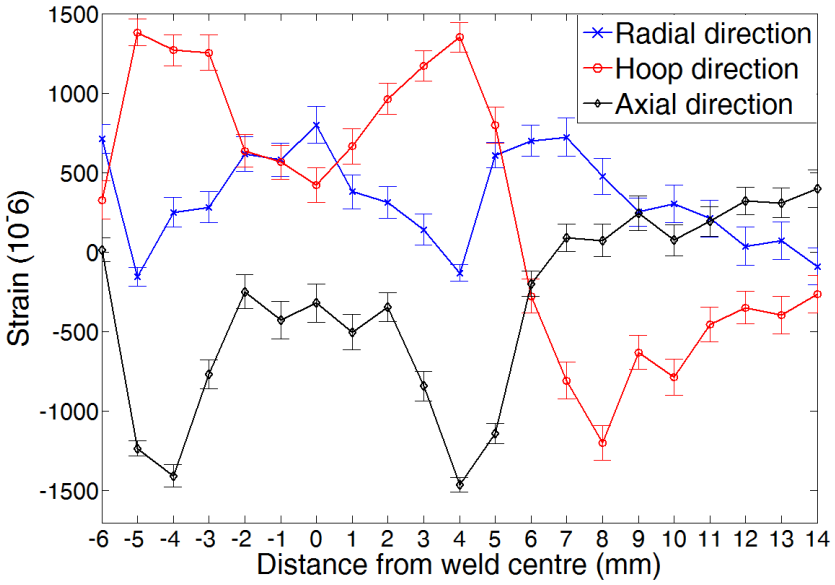

(a) Measured strain distribution in boron steel weld.

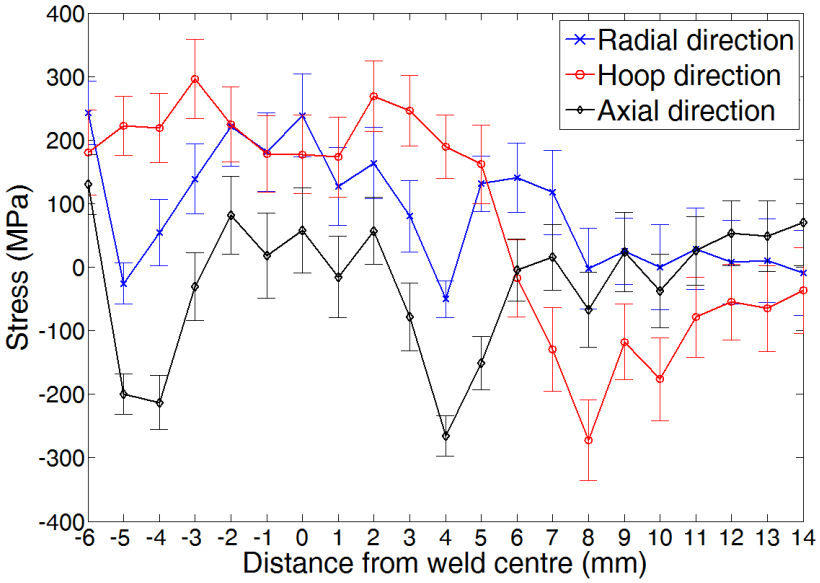

(b) Determined stress distribution using strain values in a).

Figure 4.3.1: Strain and stress distributions of boron steel weld. Values calculated using far-field reference value.

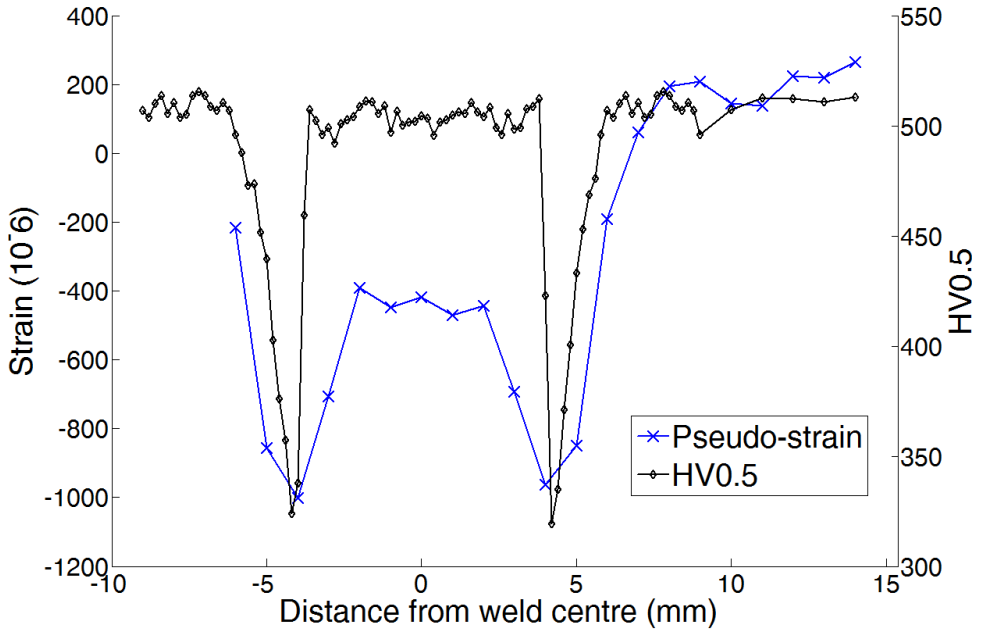

Figure 4.3.2: Pseudo-strain distribution of boron steel weld. The pseudo-strain is the variation arising due to microstructural changes across the weld.

4.3.2 Comparison of top and bottom plate strains

The measured strains for the boron steel weld, with the plane-stress assumption applied, are shown in figure 4.3.3. The hoop and axial strains show a clear symmetry about the weld centre. The top and bottom plates for these graphs exhibit approximately the same values and distributions. The radial strain distribution of the bottom plate shows a lesser degree of symmetry about the weld centre. The BM exhibits a correlation in strain between the top and bottom plates for all strain directions.

The measured strains for the DP600 spot weld are shown in figure 4.3.4. Symmetry about the weld centre is distinguishable in all three strain directions. There are differences in strain between the top and bottom plates in the weld, with a difference of approximately 600 με in the hoop direction in the weld centre. This indicates that the DP600 weld could have developed asymmetrically about the sheet-sheet interface. As with the boron steel weld, the top and bottom plate strains in the BM exhibit a close correlation.

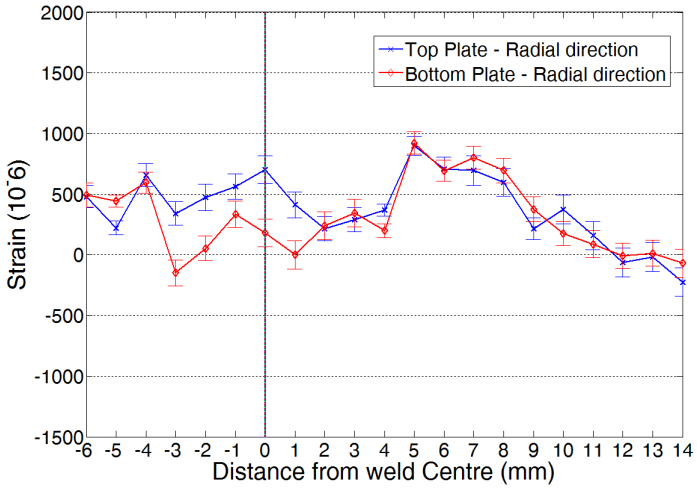

(a) Radial direction

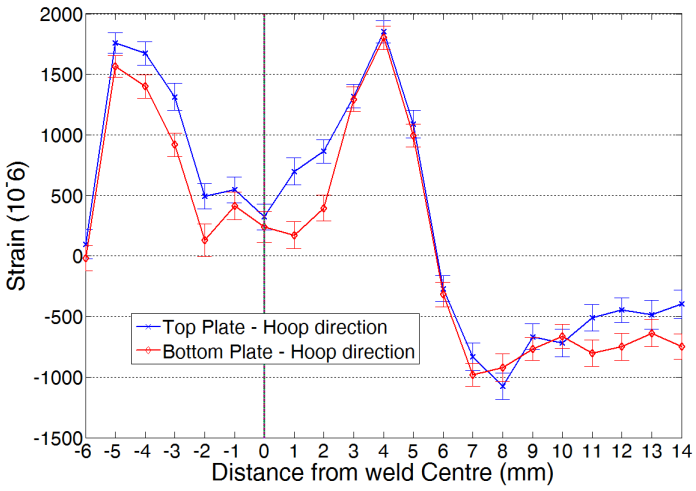

(b) Hoop direction

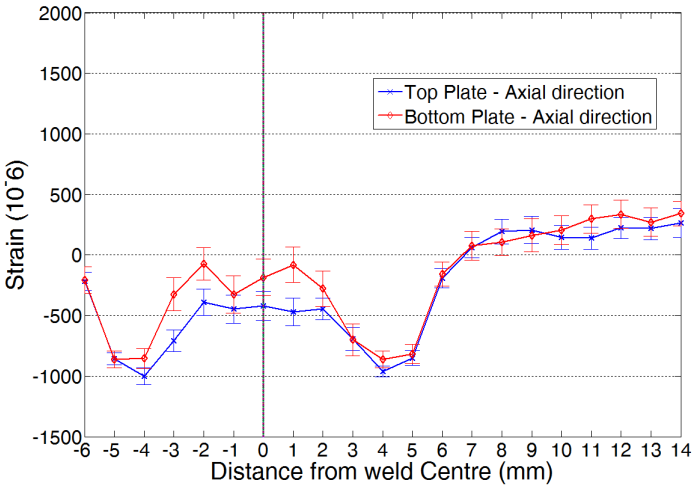

(c) Axial direction

Figure 4.3.3: Boron steel spot weld strains in top and bottom sheets

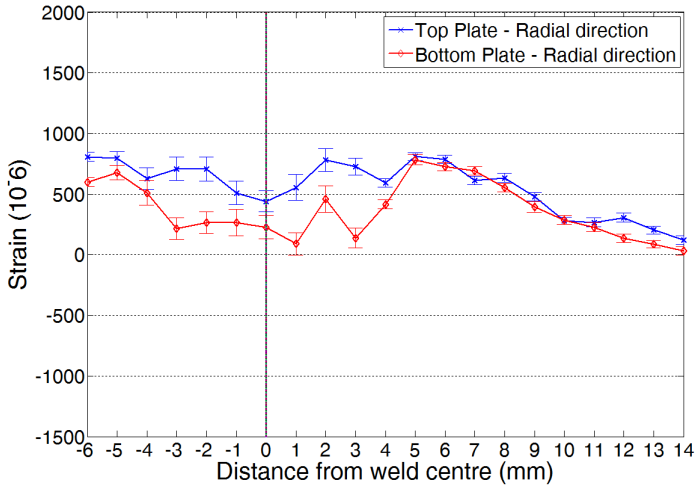

(a) Radial direction

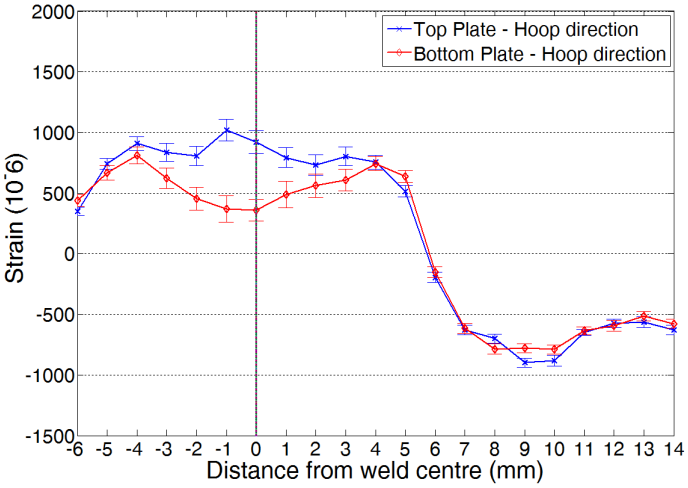

(b) Hoop direction

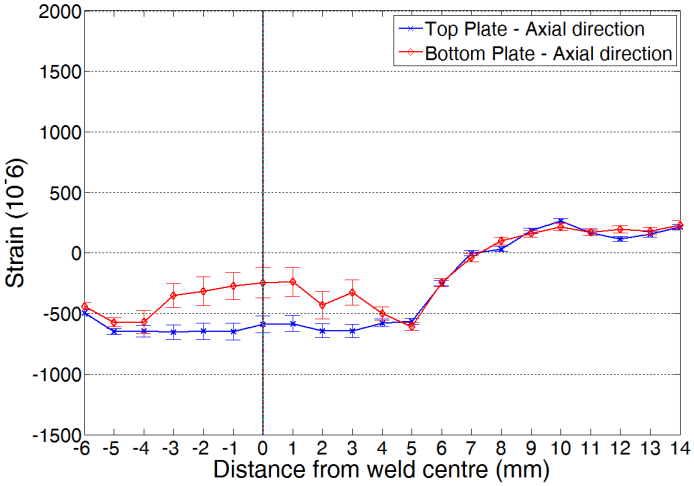

(c) Axial direction

Figure 4.3.4: DP600 spot weld strains in top and bottom sheets

4.3.3 Calculated stress

The stresses were calculated from the measured strains, using equation 4.2.1 and its variants. These calculated stresses for the boron steel weld are shown in figure 4.3.5. All stresses are calculated with a plane stress assumption. The measured hardness values are overlaid in the figure to give an indication of how the material characteristics change along the x-axis. The top sheet results are shown for clarity.

The weld and surrounding HAZ experience a tensile stress which decreases to a compressive stress in the base material. The tensile stresses are manifested due to the melted nugget contracting and cooling during welding. The HAZ area has also experienced elevated temperatures and subsequently contracted during cooling, leading to a tensile stress.

A clear symmetry can be seen about the weld centre, both in terms of residual stress and hardness. These distributions also correlate well with the pseudo-strain distribution, shown previously. A sudden drop in hardness correlated with a sudden increase in residual stress values can be seen in the HAZ (approximately 4 mm to 5 mm from the weld centre).

Stress in the hoop direction reaches a peak of 452 MPa at approximately 4 mm and decreases into negative values through the HAZ and BM. The radial direction stress reaches a peak of 283 MPa at approximately 5 mm and follows a similar path into the negative stress region as the hoop stress, although with a less steep gradient. Due to the plane stress assumption, the axial stress is not present.

The residual stress and hardness distribution of the DP600 weld can be seen in figure 4.3.6. The nugget and surrounding HAZ experience tensile stresses, leading to compressive stresses into the base material. The hoop and radial directions exhibit similar stress levels, with the hoop stresses being slightly higher.

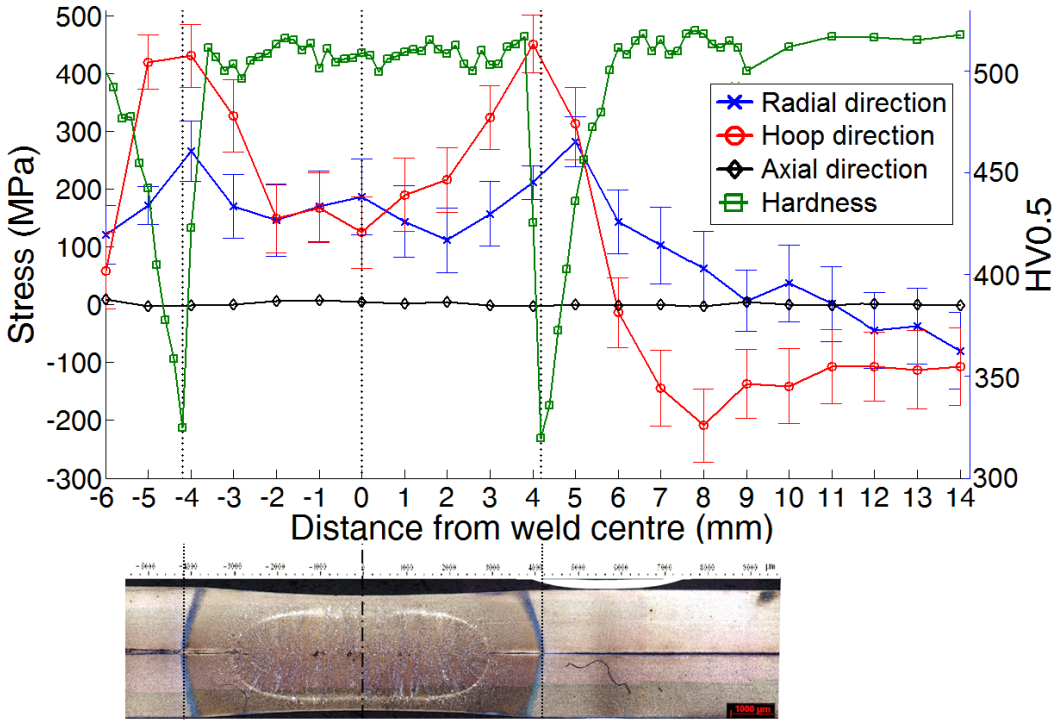

Figure 4.3.5: Calculated residual stress and hardness distributions of boron steel

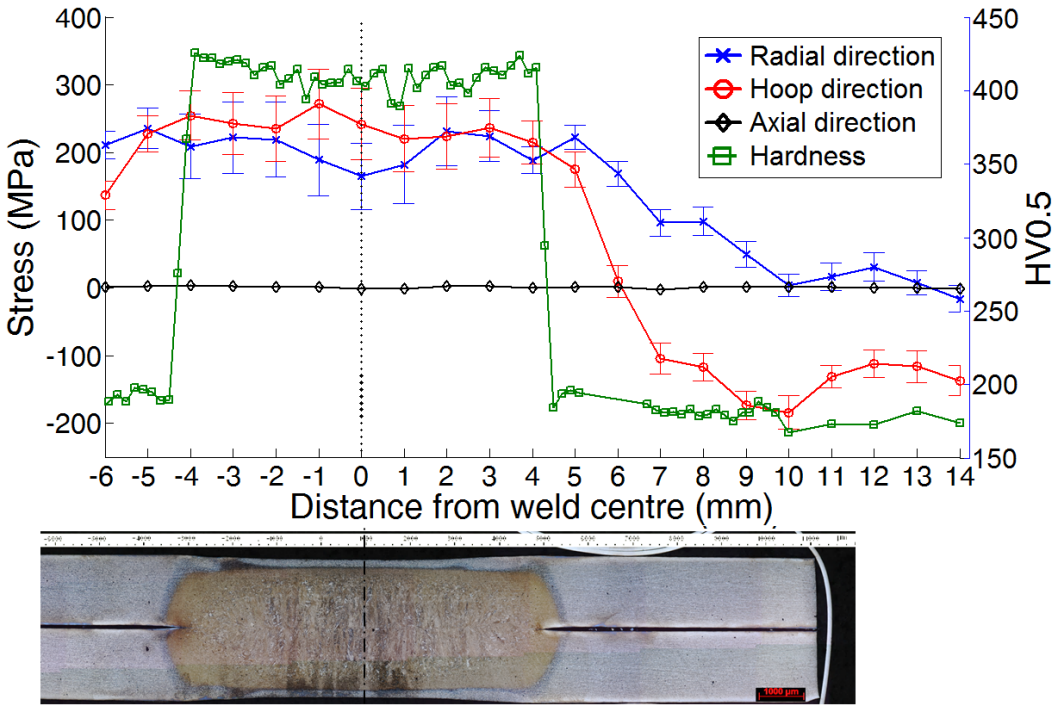

Figure 4.3.6: Calculated residual stress and hardness distributions for DP600 spot weld

4.3.4 Peak broadening

As mentioned previously, the measured peak may broaden or contract due to changes in crystal structure. This is measured by the full width at half maximum (FWHM) of the Gaussian curve, illustrated in figure 4.3.7. This definition will be used to investigate the effect that different microstructures have on the diffraction pattern, and will in turn be used to infer the microstructural variation as a function of the distance from the weld centre.

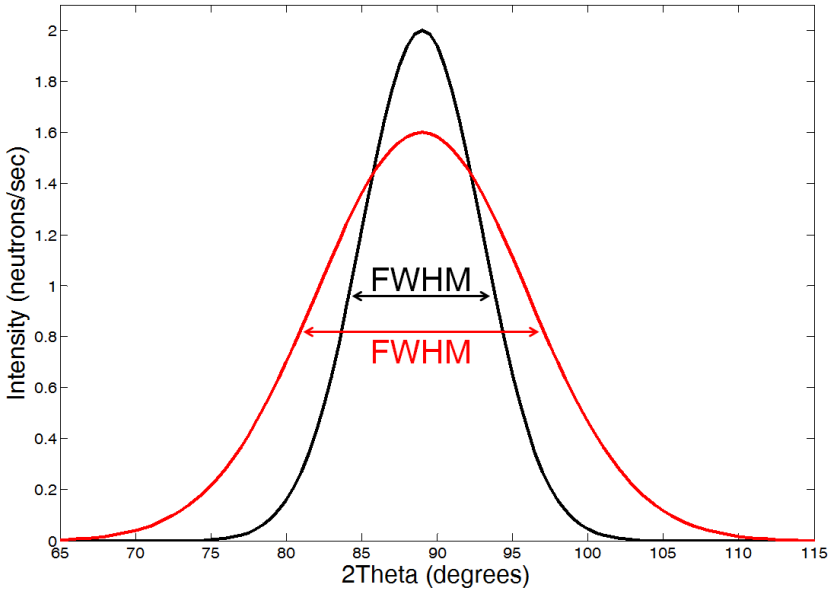

Figure 4.3.7: An illustration of FWHM

Before continuing with the results analysis, it would be useful to look at some of the investigations of dual phase (DP) steels, which consist of a mixture of ferrite and martensite. This will give an indication of the extent of peak broadening associated with each phase. Filippone [99] defined peak broadening as the calculated difference in FWHM between the DP samples and a reference martensite-free sample.

In their respective investigations of DP steels, Filippone *et al* [99] and Woo *et al* [111] stated there exists an overlap in diffraction patterns of ferrite and martensite, due to the similar crystal structures and lattice parameters of the two phases. It was also stated

that martensite has an inherently broader peak, due to the increased tetragonality of the crystal structure compared to the ferrite crystal structure [99].

As can be seen in figure 4.3.8, peak broadening increases with martensite volume fraction. It can also be seen that peak broadening levels off as the martensite volume fraction increases. The authors stated that the sharp initial rise in peak broadening was due to ferrite straining from the volumetric expansion as a result from martensite formation.

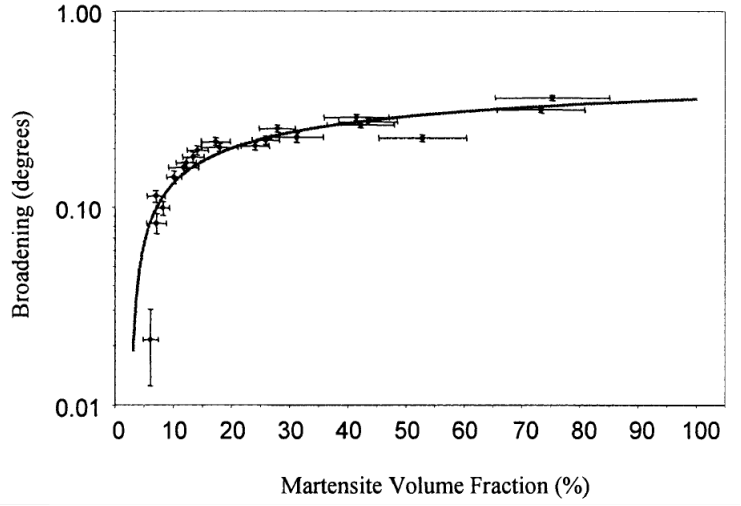

Figure 4.3.8: Peak broadening as a function of martensite volume fraction for a dual-phase steel. Taken from [99]

A clear correlation between FWHM and hardness for the boron steel weld can be seen in figure 4.3.9. From the hardness distribution, it seems that the BM starts from approximately 6.6 mm from the weld centre, where the hardness levels out to a stable value. However, the FWHM distributions reach a stable value at approximately 8 mm. Therefore, the region beyond 8mm from the weld centre can be used as a reference FWHM value for martensite. The difference between the FWHM and hardness at these distances from the weld centre may be due to the smearing effect resulting from the neutron beam area.

The weld nugget region (from -3 to 3 mm) consists mainly of martensite. However, there are microstructural changes in the thickness direction from the nugget border

to the face of the top plate. This means that the region from the nugget centre to the face of the top plate is not as homogeneous as the same region in the BM. This difference is illustrated by the greater degree of variation in FWHM observed in the weld region. Nevertheless, the effect of martensite is evident in the weld and BM, with both exhibiting similar FWHM values.

The sudden drop in FWHM (at approximately 4 mm), coupled with an equally severe drop in hardness, indicates a move away from the martensitic microstructure towards a softer phase with a reduced tetragonality, possibly tempered martensite. As discussed previously, tempering of martensite has the effect of lowering the tetragonality of the phase [1]. The reduced hardness is a strong indicator of tempering. Additionally, other authors have identified the soft HAZ microstructure in boron steel welds to be tempered martensite [41, 42, 43].

For the DP600 weld, the hardness and FWHM are well correlated again, as shown in figure 4.3.10. The DP600 base material consists of a ferrite matrix with martensitic islands (about 10 - 20%) [1, 112]. The FWHM of the DP600 base material is ~2.5 times lower than the boron steel base material, indicating a reduced martensite volume fraction. A dramatic increase in hardness and FWHM can be seen in the nugget (-3.5 to 3.5 mm). Temperatures well above austenitisation, coupled with fast cooling rates, led to the nugget consisting of a much higher percentage of martensite compared to the BM.

In the previous chapter, it was established that the DP600 nugget exhibited a hardness value of 100 HV lower than the boron steel nugget. This is due to a reduced tetragonality of the martensite phase due to a lower carbon content in the DP600 steel. The FWHM results lend further verification to this observation, where the DP600 nugget centre shows a FWHM value of 0.27° less than the boron steel weld centre.

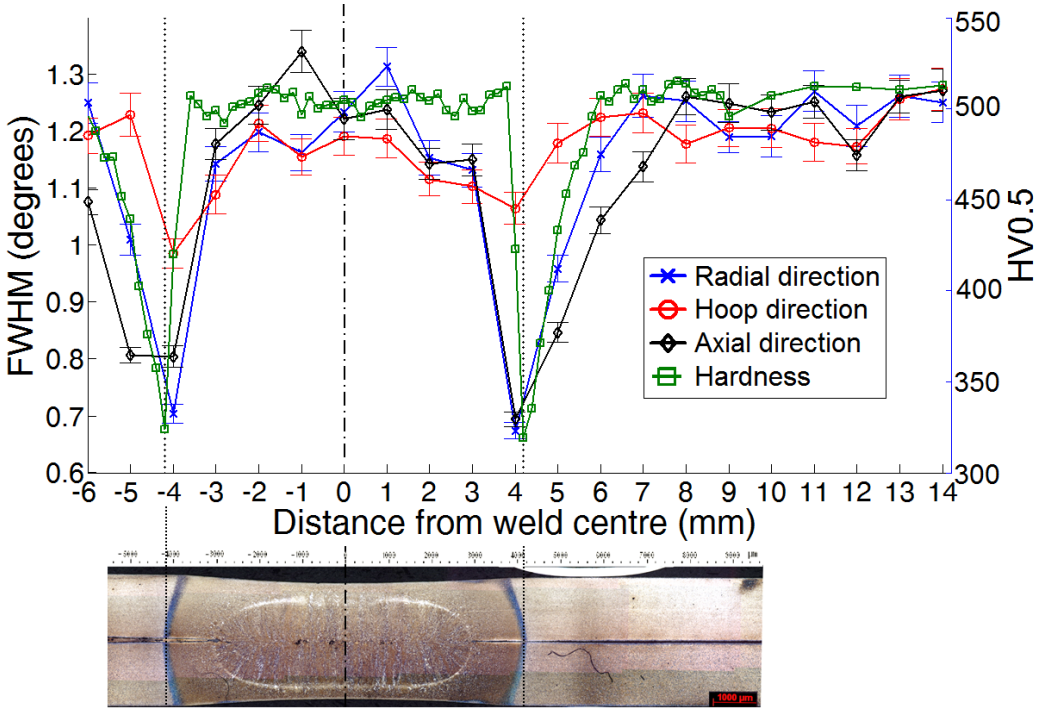

Figure 4.3.9: Boron steel Full Width Half Maximum and Hardness

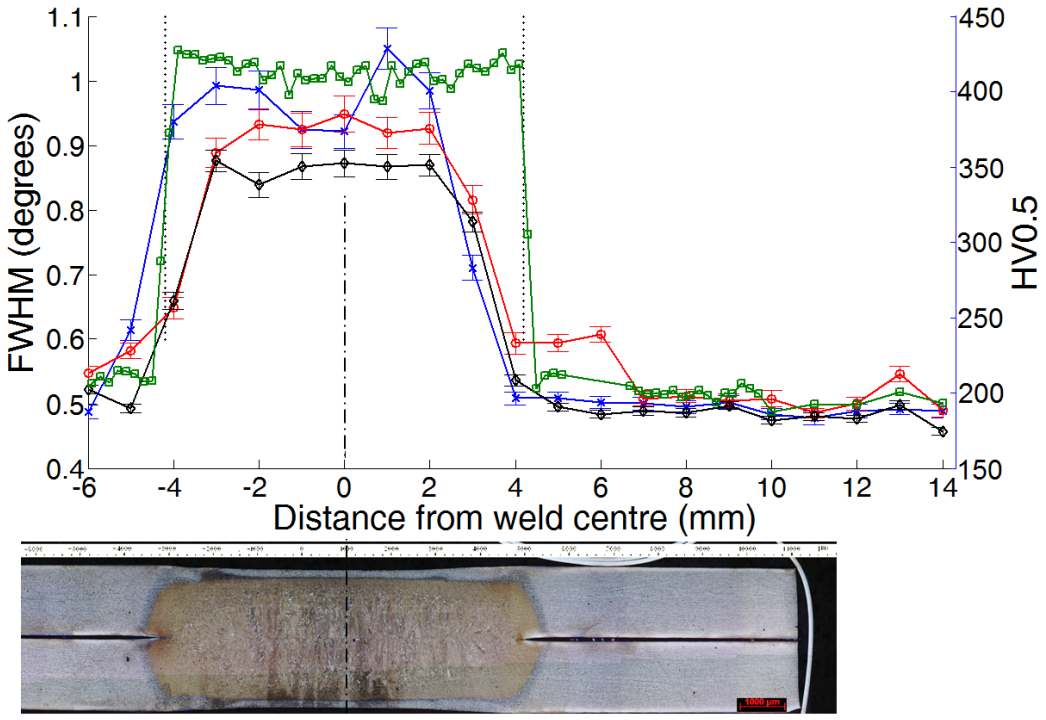

Figure 4.3.10: DP600 weld Full Width Half Maximum and Hardness

4.4 Conclusion

Residual strains were measured in two weld configurations (boron steel and DP600) and residual stress values were calculated using a plane stress assumption. Due to the neutron beam area, all measured values represent an average over a volume of approximately 2.8 mm^3. All welds exhibited a tensile stress in the weld nugget due to the molten nugget cooling and contracting at the end of the weld cycle. In all cases, the base material exhibited compressive residual stresses, so that equilibrium may be achieved in the work-piece. As the distance from the weld centre increased into the far-field, it was assumed that the stresses tend to zero. This assumption stemmed from observations from other works [102].

The boron steel and DP600 welds exhibited correlation between residual stress and hardness distributions. The DP600 weld showed a flat residual stress profile in the nugget with a smooth decline into the base material. The boron steel weld, however, showed peaks on the HAZ periphery and a lower residual stress value in the weld centre. The reduced hardness in the HAZ, in conjunction with peaks in residual stress, indicates that this is an area exhibiting extreme variation of properties and will make a significant contribution to the overall loading response of the weld.

The FWHM gave an indication of the microstructural variations through the weld. For the boron steel weld HAZ, a shift in peak breadth away from values associated with martensite corroborated evidence that the microstructure in the HAZ is a softer phase; most likely consisting of tempered martensite.

The difference in hardness between the DP600 and boron steel nuggets can be explained in terms of a reduction in tetragonality of the martensite phase (tending towards a ferritic bcc structure). This was evidenced in the FWHM values, where the DP600 nugget centre showed a FWHM value of 0.27° less than the boron steel weld centre. The reduction in tetragonality stems from the reduced carbon content of DP600 compared to boron steel. To this authors knowledge, residual stresses have not been measured in boron steel spot welds before.

Chapter 5

Instrumented Indentation

5.1 Introduction

During an instrumented indentation test, the load and indenter displacement are recorded simultaneously as the indenter is loaded and unloaded. The force and displacement can be very finely controlled, with indentations made with an applied force of a few micro Newtons, resulting in indentations depths in the nanometre range. The scale of indentations can also be applied in the micro-range, to extract bulk material properties, as has been done in this project.

The motivation for utilising instrumented indentation in this thesis is due to the scale of the spot weld. With a large volume of material, destructive test specimens can be cut directly from the material and constitutive properties extracted. However, due to the small dimensions of HAZ regions, it is not feasible to cut tensile specimens from such a small material volume. Instrumented indentation offers the opportunity to test weld sections *directly*.

5.1.1 Load - depth curves

In conventional hardness tests, the size of the residual impression is optically measured. Due to the small impressions in instrumented indentation, optically measuring the indent leads to inaccuracies. To circumvent this problem, the depth of penetration is measured as load is applied. The known geometry of the indenter then allows an

indirect measure of the size of the contact area to be determined. From this, the mean pressure and thus hardness is calculated. Utilising the elastic unloading response of the material via the slope of the unloading curve, the elastic modulus may also be calculated.

An example of a typical load-depth (P - h) curve is shown in figure 5.1.1, where load is designated as P and depth of penetration as h. The load is applied from zero up to a prescribed maximum value and then back to zero.

When the indenter is withdrawn, a residual impression is left due to plastic deformation, with some elastic recovery occurring due to relaxation of elastic strains in the material. By analysing the initial portion of the unloading curve, the elastic modulus may be calculated from the following equation:

$$E^* = \frac{1}{2}\frac{dP}{dh}\frac{\sqrt{\pi}}{\sqrt{A}} \tag{5.1.1}$$

where $\frac{dP}{dh}$ is the unloading slope, A is the *projected* contact area and E^* is known as the *reduced modulus*, which takes into account the material properties of the indenter and specimen material being indented, through the equation:

$$\frac{1}{E^*} = \frac{(1-\nu^2)}{E} + \frac{(1-\nu_{in}^2)}{E_{in}}$$

where the subscript *in* refers to the indenter and ν is Poisson's ratio. The projected contact area is calculated from the known indenter geometry and the depth of penetration at the area of contact (h_c), where h_c is illustrated in figure 5.1.2. For example, the projected contact area of a Vickers indenter is given by $A = 24.504h_c^2$ [74]. The contact areas are explained in more detail in the following sections.

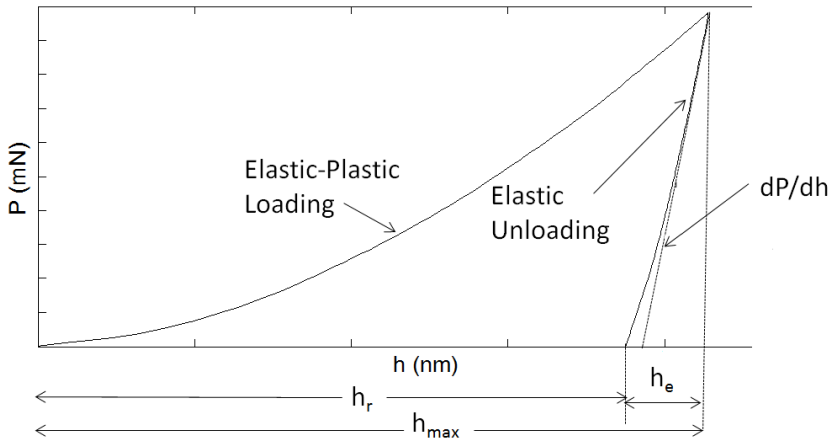

Figure 5.1.1: Example of a load-depth curve from an instrumented indentation test. h_{max} is the maximum depth at maximum load, h_r is the residual depth after load removal and h_e is the elastically recovered depth

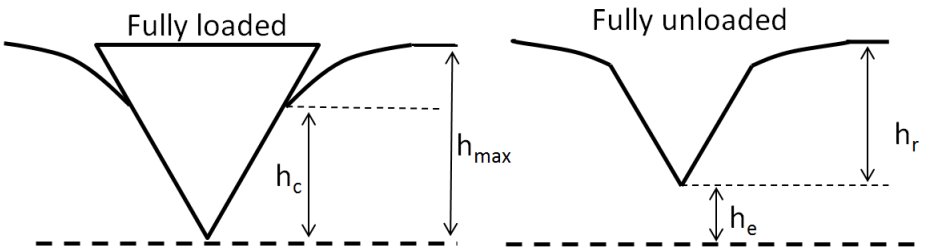

Figure 5.1.2: Schematic of the loading and unloading portions of an indentation test (h_c is the contact depth, h_{max} is the maximum depth at maximum load, h_r is the residual depth after load removal and h_e is the elastically recovered depth).

5.1.2 Contact mechanics

A pioneer in elastic contact mechanics for indentation was Hertz, who found that the radius of the circle of contact (a), the indenter load (P), spherical indenter radius (R) and the indented material's elastic properties are related by [74] :

$$a^3 = \frac{3}{4}\frac{PR}{E^*} \tag{5.1.2}$$

An illustration of spherical indentation is shown in figure 5.1.3.

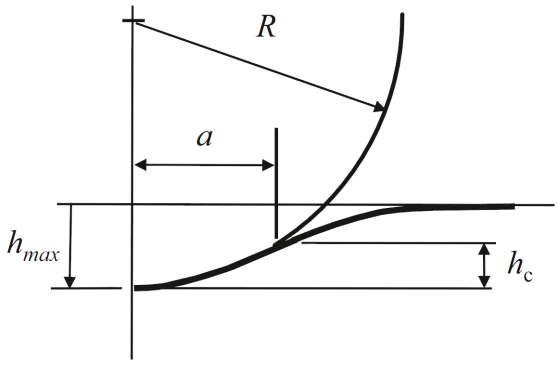

Figure 5.1.3: Indentation parameters during indentation by a spherical indenter. Taken from [74].

Relating the mean contact pressure (p_m), given by the indenter load divided by the contact area;

$$p_m = \frac{P}{\pi a^2}$$

with equation 5.1.2, one arrives at the following relation

$$p_m = \left(\frac{4E^*}{3\pi}\right)\frac{a}{R} \tag{5.1.3}$$

where p_m is often referred to as the *indentation stress* and $\frac{a}{R}$ as the *indentation strain* [74]. This stress-strain relation implies the existence of a similar stress-strain relationship found in conventional tensile or compression tests [74]. This relationship is illustrated in figure 5.1.4, in which Tabor [3] performed indentations in mild steel and copper using a spherical indenter. The overlaid stress-strain curves have been multiplied by a constant factor in order to line them up with the indentation results. It is important to note at this point that sharp indentation, as has been used in this work, does not provide such a full stress-strain relation. Such a relation can only be obtained from spherical indentation.

Hertz made major contributions to the field of elastic contact mechanics, but accounting for plasticity during indentation contact proved to be a more complex issue. This is due to the fact that in the plastic regime, the constitutive equations are non-linear and additional material parameters must be included to accurately describe the material behaviour, for example the work hardening behaviour. For this reason, analytical solutions are not easily obtained and most of the understanding of plastic behaviour in indentation has stemmed from experimental observation.

Tabor [3], and in a later collaboration with Stilwell [113] found that an impression made by a spherical indenter is still spherical, but with a slightly larger radius than that of the indenter. Similarly, indentations made by conical indenters remained conical, but with a slightly larger included tip angle. Since Hertz's equations are valid for calculating the elastic recovery when the indenters are removed, and elastic contact solutions exist for the indenter geometries, the effects of plasticity on the unloading data can be taken into account by considering the shape of the deformed surface in the elastic analysis [3, 113, 69].

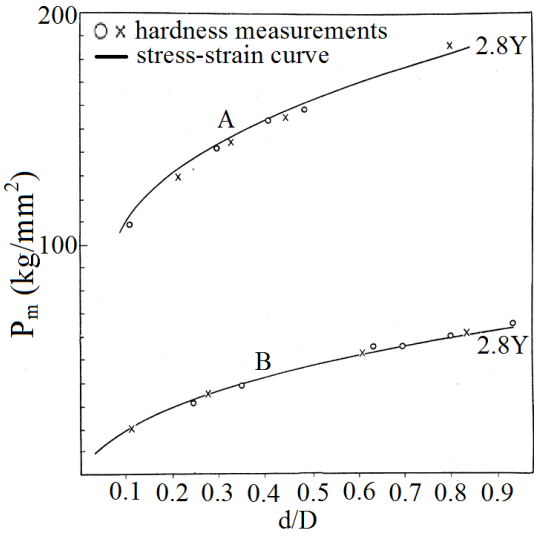

Figure 5.1.4: Hardness measurements in relation to stress-strain curves. Curve A, mild steel. Curve B, annealed copper. d is indentation diameter, D is spherical indenter diameter and Y is yield strength. Taken from [3].

5.1.3 Indenter types

Indentations are usually performed with either spherical or pyramidal indenters, with the material of choice being diamond. The four indenter tip types that will be discussed in this chapter are: spherical, conical, Vickers and Berkovich tips, illustrated in figure 5.1.5.

An advantage of the Berkovich over the Vickers tip is that it is easier to construct the 3 sides to meet up at the apex. The Berkovich indenter has a face angle which gives it the same projected area-to-depth ratio as the Vickers indenter. Of course, it is very difficult to make a perfectly sharp indenter and a new Berkovich tip has a radius of 50 - 100 nm, which increases to 200 nm after some use [74].

In analysing indentation data from pyramidal indenters, it is more convenient to treat the indent as being formed by an axially symmetric conical indenter with an equivalent cone angle, as shown in table 5.1.1. This conversion is routinely used because it allows the use of axially-symmetric elastic equations. Despite the solutions for pyramidal punch problems being available, it is generally accepted to perform the conversion to an equivalent axial-symmetric problem [74, 77, 114].

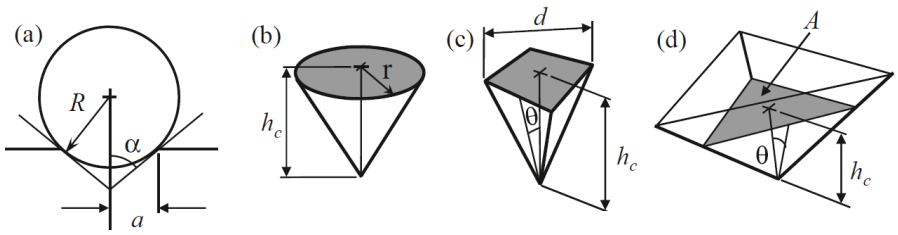

Figure 5.1.5: Indenter types and associated parameters: a) Spherical, b) Conical, c) Vickers, d) Berkovich. Taken from [74]

Indenter shape	Semi-angle	Effective cone angle	Projected area
Spherical	-	-	$A = \pi\left(2R_i h_c - h_c^2\right) \approx 2\pi R_i h_c$
Conical	θ	θ	$A = \pi h_c^2 tan^2\theta$
Vickers	68°	70.3°	$A = 4h_c^2 tan^2 68° = 24.504 h_c^2$
Berkovich	65.27°	70.3°	$A = 3\sqrt{3}h_c^2 tan^2 65.27° = 24.494 h_c^2 \approx 24.5 h_c^2$

Table 5.1.1: Angles and projected areas of the different indenter types

5.1.4 Geometric similarity

Conical and pyramidal indenters exhibit geometrically similar properties, as shown in figure 5.1.6, where the ratio $\frac{a}{h_c}$ remains constant as the indenters are driven deeper into the material. For these geometrically similar indentations, the scale of the indentation cannot be determined without some external reference. The important point to note from this is that strain is constant in the material and independent of load.

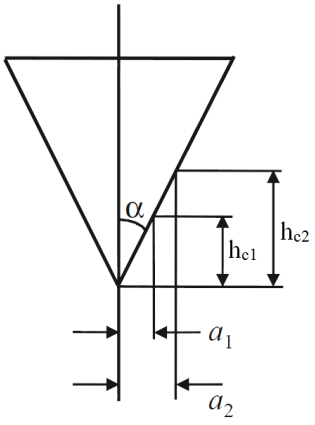

Figure 5.1.6: Illustration of geometric similarity. Modified from [74]

5.1.5 Hardness in relation to yield strength: representative strain

Representative strain is a crucial parameter used in the method to extract material properties through instrumented indentation. This section will introduce the theory behind this parameter. Tabor [3] performed experiments to find the relation between a material's hardness and its yield strength. Hardness values were obtained by indenting lead, copper and mild steel; all of which were highly work-hardened (to reduce the effect of work hardening on the results). The indentations were performed with a spherical indenter, with the yield strength (σ_y) of these materials obtained by compression tests. The ratio of p_m to σ_y was found to be approximately 3 for all materials tested, which may be expressed as:

$$p_m \approx C\sigma_y$$

where C is approximately 3 and is also known as the *constraint factor*, which will be explained later in this chapter.

Tabor made an observation, that according to the von Mises criterion, the material first exceeds the elastic limit below the surface of contact when p_m reaches a value of approximately $1.1\sigma_y$ [3]. At this stage in the indentation, the plastic region is very small.

As the load is increased, the region of plasticity increases; the size of the indentation increases slowly whilst the pressure resisting deformation increases rapidly. At this point the plastic region extends over the entire domain around the indentation and $p_m = 3\sigma_y$. Tabor stated that the "transition in the value of p_m from $1.1\sigma_y$ to $3\sigma_y$ is part of the intrinsic mechanism of plastic deformation and is distinct from the effects produced by work-hardening" [3].

The work of Tabor discussed up to now concerns perfectly-plastic behaviour, where the yield strength is approximately constant. To include the effects of work hardening, Tabor considered the stress distribution in and around the indent. For work hardening materials, the elastic limit depends on the amount of work hardening, which in turn depends on the amount the material is indented by. This means that the elastic limit will not be constant at every physical point in the indentation. Tabor postulated that there exists an average or "representative" value of the elastic limit that is related to p_m.

Tabor produced a quantitative connection between p_m and elastic limit around the indentation. Brinell impressions were made on mild steel. Vickers indents at *small loads* were subsequently made inside and outside the Brinell indentations; resulting in the determination of the elastic limit inside and outside the indentations.

The determination of the elastic limit from Vickers indents were performed in the following way. Due to geometric similarity, the hardness (or equivalently p_m) is independent of the load. A direct relation between the hardness value, the amount of deformation (or strain) and the elastic limit may be obtained by measuring the Vickers

hardness of metals compressed or elongated by various amounts. This relation can then be used to determine the elastic limit [3]. It was shown that the elastic limit rises at the edge of the indentation, as shown in figure 5.1.7. In the figure, d is the indentation diameter and D is the spherical indenter diameter.

These observations suggest that it is difficult to assign a "representative" value to the elastic limit for the whole material. Tabor performed some empirical testing to prove that the edge value of the elastic limit could be used, by comparing σ_y at the edge with p_m used in forming the indentation in copper and steel. It was found that the relation $p_m = C\sigma_y$ held over a wide range of indentation sizes. An example of some of Tabor's results are given in table 5.1.2.

The physical meaning of the constant C may be explained as follows: the mean contact pressure required to initiate yield in an indentation test is higher than that required to initiate yield in a uniaxial compression test. This is due to the fact that, in the indentation stress field, the stressed material is constrained by the surrounding matrix, leading to a substantial hydrostatic component. This is why the factor C is called the *constraint factor*. It is generally agreed that it has a value of about 3 for metals which do not strain harden appreciably [72, 115, 74].

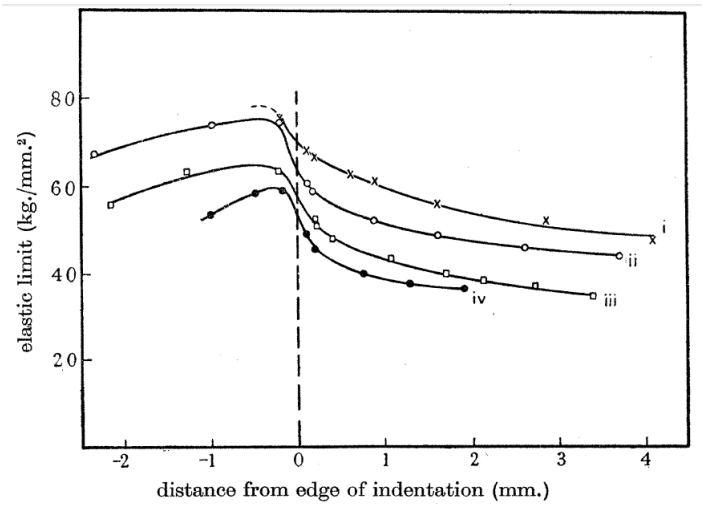

Figure 5.1.7: Vickers indents made inside and outside a Brinell impression in mild steel. Values of d/D in curve i = 0.84, curve ii = 0.69, curve iii = 0.49 and curve iv = 0.23. Taken from [3]

Metal	Size of impression (d/D)	σ_y (kg/mm^2)	p_m (kg/mm^2)	p_m/σ_y
Annealed copper	0.27	10.5	27	2.6
	0.37	14	39	2.8
	0.5	16	44	2.8
Mild steel	0.23	51	132	2.6
	0.49	57	159	2.7
	0.69	63	161	2.6
	0.84	70	190	2.7

Table 5.1.2: Indentation results for copper and mild steel showing that the ratio $p_m/\sigma_y \sim 3$. Taken from [3]

5.1.6 Dimensional analysis

Dimensional analysis has been used by some authors [81, 77] in their analysis of instrumented indentation results and offers the advantage that the number of arguments in the functions that describe the physical laws are reduced [116]. Since the end results of dimensional analyses were used as a tool in this thesis, a brief explanation of dimensional analysis will be given, without delving into too much mathematical rigour. We let there be $q_1, \ldots, q_n$ dimensional variables, which are inter-related by a homogeneous set of equations. These can then be expressed in the form:

$$F(q_1, \ldots, q_n) = 0 \; \textit{or equivalently} \; q_1 = f(q_2, \ldots, q_n)$$

If there are i fundamental dimensions (for example, distance and time) required to describe the n variables, then we have i primary variables and the remaining $j = n$ - i variables (for example velocity) are expressed as dimensionless and independent quantities. These dimensionless quantities are also known as "Pi groups", $\Pi_1, \ldots \Pi_{n-i}$. The original equations can therefore be expressed more compactly, as

$$\Phi\left(\Pi_1, \ldots, \Pi_{n-i}\right) = 0 \; \textit{or equivalently} \; \Pi_1 = \phi\left(\Pi_2, \ldots, \Pi_{n-i}\right)$$

Hence the number of variables is reduced by i.

5.1.7 Extracting material parameters

A run-through of the basic methodology and ideas behind processing instrumented indentation results follows: the method concerns extracting the indentation hardness and Young's modulus from the indented material. These parameters are necessary precursors for more complex algorithms for extracting yield strength. The method shown will be based on the method of Oliver and Pharr [69] with a Berkovich indenter, which is the most cited paper in instrumented indentation. The method is based on the analytical solutions by Sneddon [71] for punches described as conical and paraboloids of revolution. The reader is referred to figure 5.1.8 for a schematic representation of the parameters used in the analysis.

The depth of penetration during loading is written as

$$h = h_c + h_s \tag{5.1.4}$$

where h_c is the *contact depth* and h_s is the displacement of the surface at the perimeter of contact. At peak load, the load and displacement is P_{max} and h_{max} respectively, and the radius of contact circle is a. After the indenter is fully withdrawn, the residual impression has a final depth of h_r.

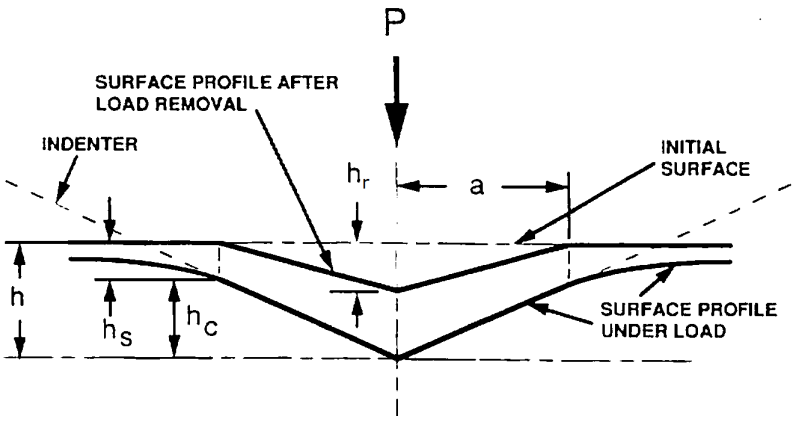

Figure 5.1.8: Schematic representation of an indentation showing various parameters used in the analysis. Taken from [69].

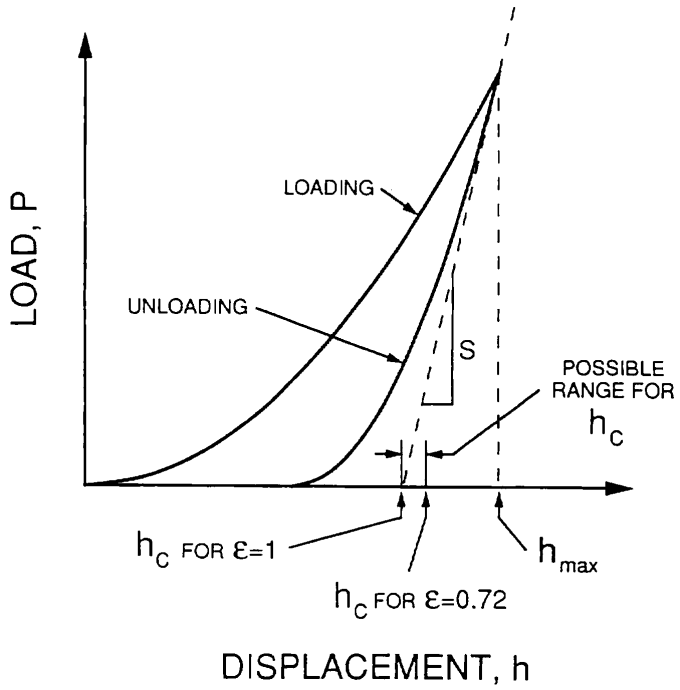

Figure 5.1.9: Schematic illustration of a force-displacement curve. Taken from [69].

The 3 experimental parameters used in the analysis are shown in figure 5.1.9; P_{max}, h_{max} and the unloading stiffness measured at peak load $\frac{dP}{dh}$ (shown as "S" in the figure). We refer back to equation 5.1.1, rewritten here for convenience

$$E^* = \frac{1}{2}\frac{dP}{dh}\frac{\sqrt{\pi}}{\sqrt{A}}$$

This relation holds for any indenter which can be described as a *body of revolution of a smooth function* [69]. As mentioned previously, it is common practice to analyse indentation problems by using an equivalent cone angle. It is clear from the equation that in order to calculate Young's modulus, the contact area at peak load must be calculated. To find the contact area, a value for h_c must be derived.

The Oliver and Pharr method assumes that the indenter geometry is described by an area function $F(h)$, which relates the cross-sectional area of the indenter with the distance from its tip (h). Since indenters are usually made of diamond, it is assumed

they do not deform significantly, hence the projected contact area at peak load can be derived from

$$A = F\left(h_c\right)$$

A more precise definition of the area function is given as

$$A = 24.5h_c^2 + C_1h_c + C_2h_c^{1/2} + C_3h_c^{1/4} + \ldots + C_8h_c^{1/128} \tag{5.1.5}$$

where the first term describes a perfect Berkovich indenter (as shown in table 5.1.1) and the other terms represent deviations from the perfect shape due to blunting of the tip, with C_{1-8} being constants. These constants are usually supplied with the indenter tips from the manufacturer, hence the procedure for calculating these coefficients will not be described.

The contact depth (h_c) can be calculated from equation 5.1.4. Since h_{max} can be experimentally measured, the key is to find h_s. For a conical indenter, the Oliver and Pharr used Sneddon's expression for the shape of the surface outside the contact area:

$$h_s = \frac{\pi - 2}{\pi}\left(h - h_r\right) \tag{5.1.6}$$

Sneddon's original expression featured h instead of $(h - h_r)$. The original expression dealt only with the elastic component of displacement and by including the final residual depth, plasticity is taken into account. The authors also made use of Sneddon's force-displacement relationship for a conical indenter, given as

$$h - h_r = 2\frac{P}{\frac{dP}{dh}} \tag{5.1.7}$$

By combining equations 5.1.6 and 5.1.7 and noting that the contact area of interest is

at P_{max}, the following relation is obtained

$$h_s = \epsilon \frac{P_{max}}{\frac{dP}{dh}} \tag{5.1.8}$$

where ϵ is the geometrical constant for a conical indenter:

$$\epsilon = \frac{2}{\pi}(\pi - 2) = 0.72 \tag{5.1.9}$$

If different indenter geometries are considered, namely a flat punch and a paraboloid of revolution, equation 5.1.8 is derived again, but with different geometrical constants, as indicated in table 5.1.3.

Indenter geometry	Conical	Flat punch	Paraboloid of revolution
ϵ	0.72	1	0.75

Table 5.1.3: Geometrical constants for different indenter geometries.

The contact depth can thus be calculated from

$$h_c = h_{max} - h_s = h_{max} - \epsilon \frac{P_{max}}{\frac{dP}{dh}}$$

where the range of h_c, for different values of ϵ, is indicated in figure 5.1.9, depending on the indenter geometry. Oliver and Pharr found that $\epsilon = 0.75$ better accounts for material behaviour. The justification for this was that the elastic singularity arising from a perfectly conical geometry is not physically possible due to tip blunting. The pressure distribution which forms around the indenter tip is more like that predicted by a parabola of revolution.

All necessary parameters are now available to calculate the modulus of elasticity according to equation 5.1.1. In addition, the projected contact area (A) is used to calculate the indentation hardness, through the following equation

$$H = \frac{P_{max}}{A}$$

It should be noted that the hardness calculated using the projected area might be different from the hardness measured using optical means. The reason for this is that a portion of the contact area under load may not have plastically deformed, meaning that the contact area measured by optical observation of the residual impression may be smaller than that at peak load.

5.1.8 Measuring the unloading curve

As mentioned in the Literature Review, Oliver and Pharr [69] discovered that unloading curves are not linear. This was proven by plotting the curves on logarithmic axes. The authors stated that because the data appears linear on a logarithmic scale, the unloading curves are well described by a power law of the form

$$P = \Omega \left(h - h_f\right)^{\Psi} \tag{5.1.10}$$

where the constants Ω and Ψ are determined by a least-squares fitting procedure. The unloading slope is then found by differentiating equation 5.1.10 and evaluating the derivative at P_{max} and h_{max}.

It should be noted that the techniques discussed so far rely on the assumption that the sides of the residual impression are flat. It has been shown that elastic recovery of the material upon unloading leads to deviations from the expected shape of the unloading portion of the P - h curve [74]. It is common practice to add a correction factor to the measured unloading slope:

$$\frac{dP}{dh} = \frac{1}{\beta}\frac{dP}{dh}_{measured}$$

where β is the correction factor. Oliver and Pharr [75] stated that a value of 1.05 should be used.

5.2 Experimental procedure

Indentations were performed on both the boron steel and DP600 spot welds, previously used in the neutron diffraction experiments. Indentations were performed on an MTS Nano Indenter XP at the Open University. A prescribed maximum load of 500 mN was used. The ISO 14577-1:2002 [117] defined the micro range test as having an applied load of less than 2 N and a depth of penetration of more than 0.2 μm. In the tests conducted, the depth of penetration was typically in the 2 μm range; therefore the instrumented indentation tests are in the micro range. Higher loads were attempted, however it was found the sample slipped from its fastener at these higher loads and was therefore deemed unreliable. Indents in the HAZ were made at 0.25 mm intervals. Due to time constraints on the indenter machine, indents in the nugget were performed in steps of 1 mm. Previous hardness tests and the residual stress distributions indicated that minimal variation occurs in the nugget, hence larger steps were deemed acceptable.

Three line scans were performed, spanning from the BM, through the weld and back into the BM. The spacing of these line scans, in the sheet thickness direction, correspond to those performed in the Vickers hardness tests. That is to say, in the middle of the top plate at 0.75 mm from the sheet-sheet interface and then at 0.15 mm above and below this mid-line. This enables easier comparisons with conventional hardness testing results. For ease of reference, the lines are presented in figure 5.2.1. The same procedure was performed for the DP600 weld.

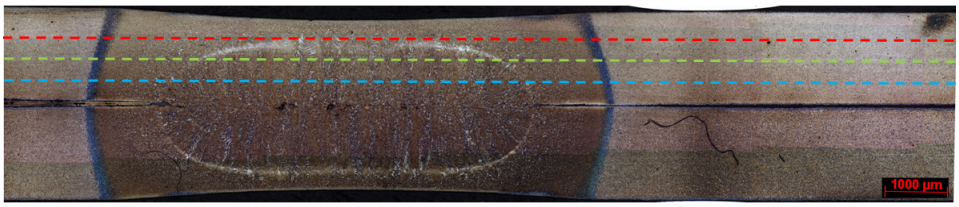

Figure 5.2.1: Three indentation line scans performed on boron steel spot weld

The recorded maximum depth of penetration is shown in figure 5.2.2. The colours of the 3 line scans correspond to the colours in figure 5.2.1. The soft HAZ region is clearly

visible from the sudden change in penetration depth.

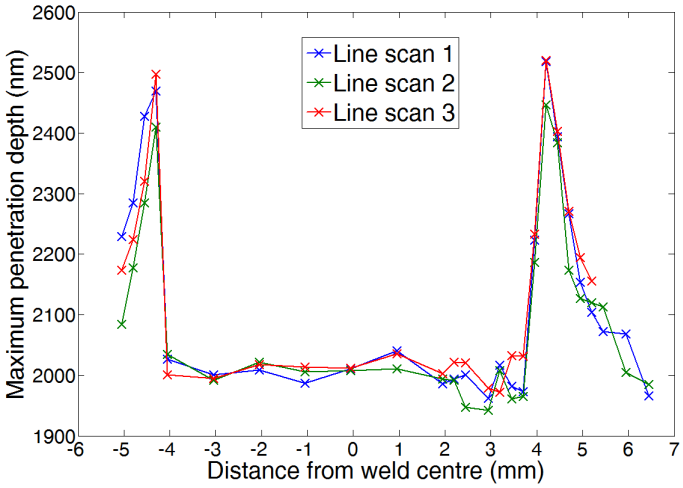

Figure 5.2.2: Maximum depth of penetration from 3 line scans of boron steel

An example of a measured P - h curve from the boron steel weld sample is shown in figure 5.2.3 a). It can be seen that the force was held constant for 2 periods during the test: at maximum load and at the end of the unloading stage. In accordance with ISO 14577-1:2002, the hold at peak load ensures time-dependent deformation (i.e. creep) is completed before load removal. Again, in accordance with ISO 14577-1:2002, a hold period is applied at 10% of maximum load at the end of the unloading stage. This hold period is used to correct for *thermal drift*; which is due to thermal expansion and contraction of the indentation apparatus, which imposes a thermal drift error onto the real depth readings. Even though the effects of thermal expansion were found to be small, any correction serves to improve the final results. By measuring the rate of change of depth with time at a constant load, the measured indentation depths are adjusted as follows:

$$h_{corrected} = h_{measured} - \lambda_{therm} t$$

where λ_{therm} is the thermal drift rate (in units of nm/s), calculated by the test software and t is the entire test time. It is common practise to extrapolate the remaining 10% of the corrected displacement to zero load to find the final residual depth [H. Pfaff, personal communication, Agilent Technologies, 3 May 2014]. Figure 5.2.3 b) shows the

detail of the thermal drift hold and the corrected displacement results, extrapolated to zero load. After these procedures, the P - h curve is ready to be used in Dao's algorithm (shown in figure 5.3.3).

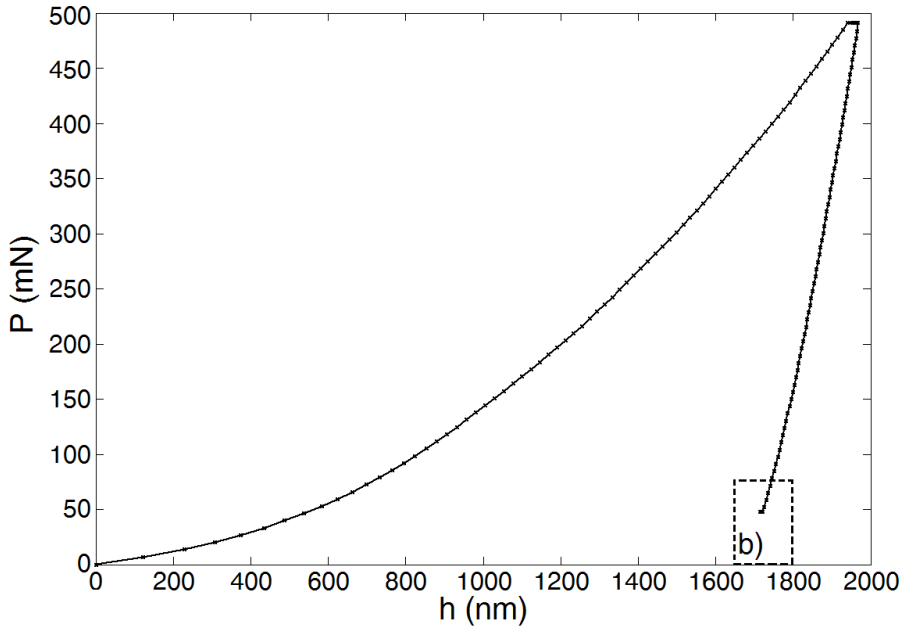

(a) Measured P-h curve from boron steel weld sample

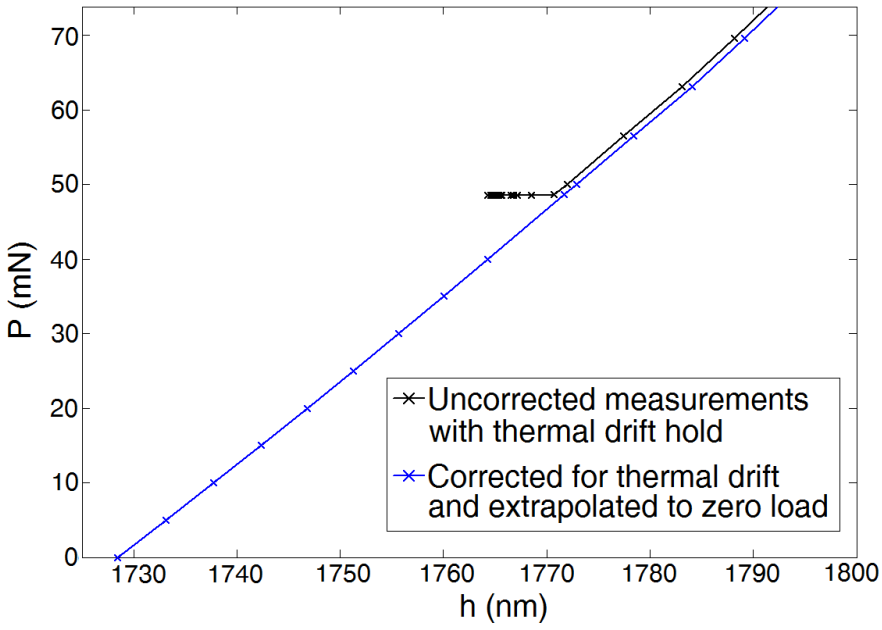

(b) Load-displacement data corrected for thermal drift and extrapolated to zero load

Figure 5.2.3: Measured load-displacement curve with thermal drift correction applied

5.3 Algorithm for material property extraction

In this thesis, instrumented indentation was used as a tool for extracting material properties from the weld. The most complete, usable algorithm was provided by Dao *et al* [77] and was hence chosen as an analysis tool.

The indented material is modelled as elastic-plastic with true stress - true strain behaviour as

$$\sigma = \begin{matrix} E\varepsilon & for\ \sigma \leq \sigma_y \\ K\varepsilon^n & for\ \sigma \geq \sigma_y \end{matrix} \tag{5.3.1}$$

where K is the strength coefficient. At the yield point, equation 5.3.1 equates as

$$\sigma_y = E\varepsilon_y = K\varepsilon_y^n \tag{5.3.2}$$

The total strain consists of elastic and plastic parts:

$$\varepsilon = \varepsilon_y + \varepsilon_p \tag{5.3.3}$$

where the subscripts y and p represent the *elastic* and *plastic* parts respectively. The plastic strain is defined as the nonlinear portion of the total effective strain accumulated beyond ε_y, as indicated in figure 5.3.1.

When $\sigma > \sigma_y$, and utilising equations 5.3.2 and 5.3.3, equation 5.3.1 becomes

$$\sigma = \sigma_y \left(1 + \frac{E}{\sigma_y}\varepsilon_p\right)^n \tag{5.3.4}$$

Dao stated that, from the above equation, the material elasto-plastic behaviour can be fully described by the parameter set (E, ν, σ_y, n). The authors also stated that the mathematical description of the plastic properties can be represented by 2 independent parameters, which was chosen to be the representative stress σ_{rep} (defined at $\varepsilon_p = \varepsilon_{rep}$, where ε_{rep} is the representative strain) and the strain hardening exponent n.

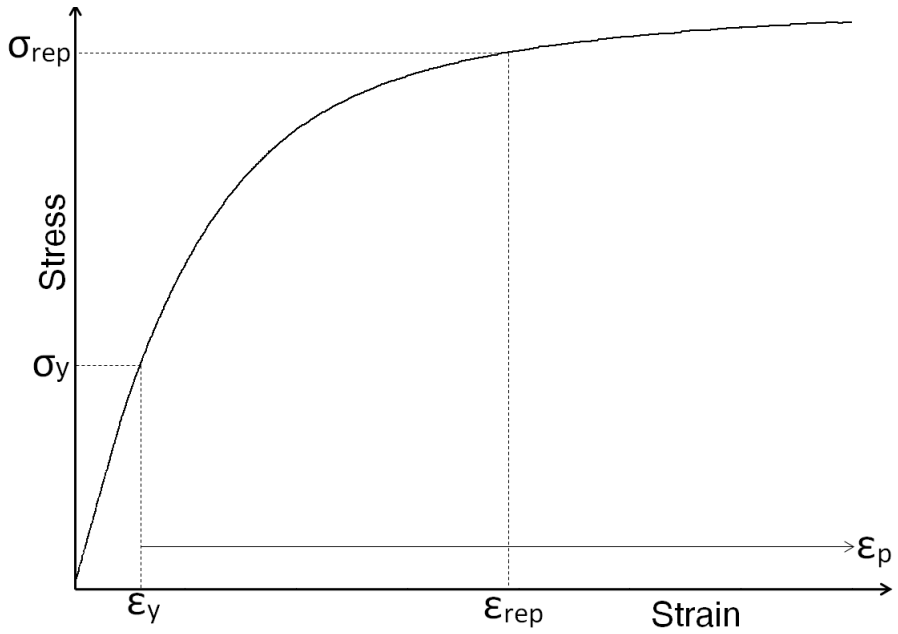

Figure 5.3.1: The power law elasto-plastic stress-strain behaviour used in the Dao algorithm.

The authors stated that, in principle, one may choose any plastic strain value to be the representative strain. However, a distinct value will be one which best normalises a particular dimensionless function with respect to strain hardening. This is best represented in figure 5.3.2, which shows the polynomial Π_1 dimensionless function plotted with various strain hardening values and at three different representative strains. It was found that when $\varepsilon_{rep} = 0.033$, the Π_1 polynomial function fitted all 76 data points to within $\pm 2.85\%$. In the Literature Review, it was mentioned that, in constructing the dimensionless functions, finite element computations were carried out for 76 combinations of elasto-plastic material properties; namely $10 < \mathrm{E} < 210$ GPa, $30 < \sigma_y < 3000$ MPa and $0 < \mathrm{n} < 0.5$.

The Π_1 function relates the loading portion of the P - h curve. A similar fitting procedure was applied to other polynomial functions. A complete list of the functions, their relations to the indentation process and fitting errors are given in table 5.3.1.

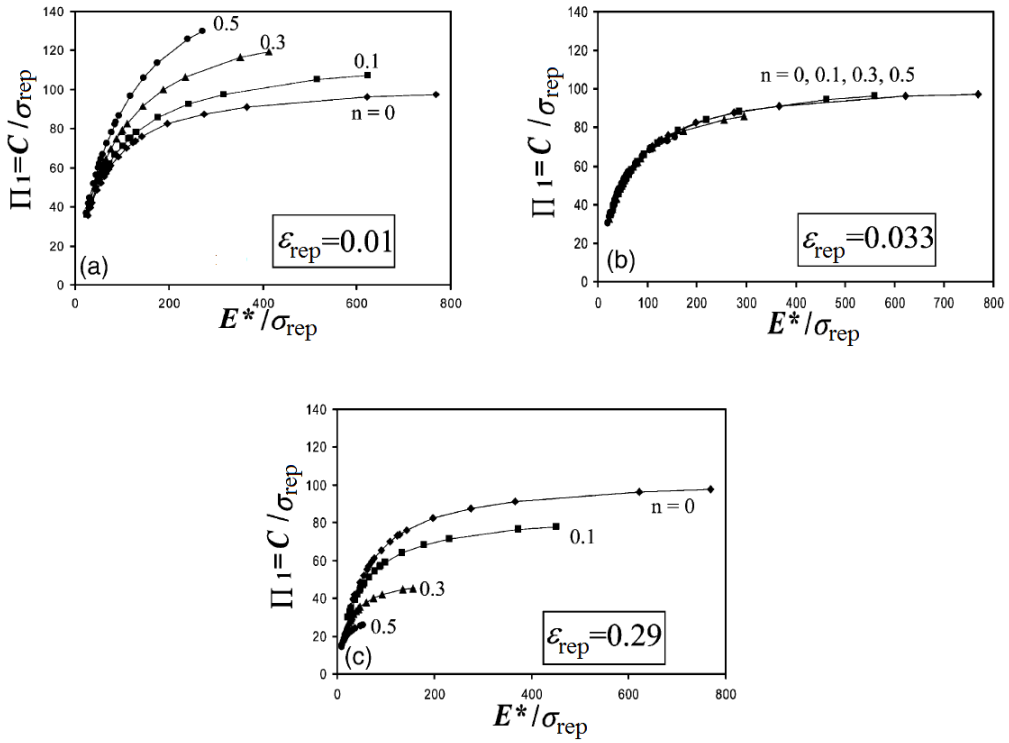

Figure 5.3.2: Dimensionless function $\Pi_1$constructed using 3 different representative strain values. Taken from [77]

Relation	Polynomial function	Fitting error
Loading portion of P - h curve	$\Pi_1\left(\frac{E^*}{\sigma_r}\right) = \frac{C}{\sigma_r}$	±2.85%
Unloading portion of P - h curve	$\Pi_2\left(\frac{E^*}{\sigma_r}, n\right) = \frac{1}{E^* h_{max}}\frac{dP}{dh}$	±2.5%
Residual and maximum penetration depths	$\Pi_3\left(\frac{\sigma_r}{E^*}, n\right) = \frac{h_r}{h_{max}}$	±0.77%
Average indentation pressure	$\Pi_4\left(\frac{h_r}{h_{max}}\right) = \frac{p_{ave}}{E^*}$	±13.85%
Projected contact area	$\Pi_6 = \frac{1}{E^*\sqrt{A}}\frac{dP}{dh} = c^*$	±0.9%

Table 5.3.1: Polynomial functions and fitting errors used by Dao *et al*

Once the P - h curve has been processed as described in section 5.2, the algorithm shown in figure 5.3.3 is followed. In the flow chart, c^* is a geometric constant which takes pile-up and sink-in into account, as described in the literature review. The C_1 constant is the indenter area correction factor shown in equation 5.1.5. This constant is supplied by the indenter manufacturing company.

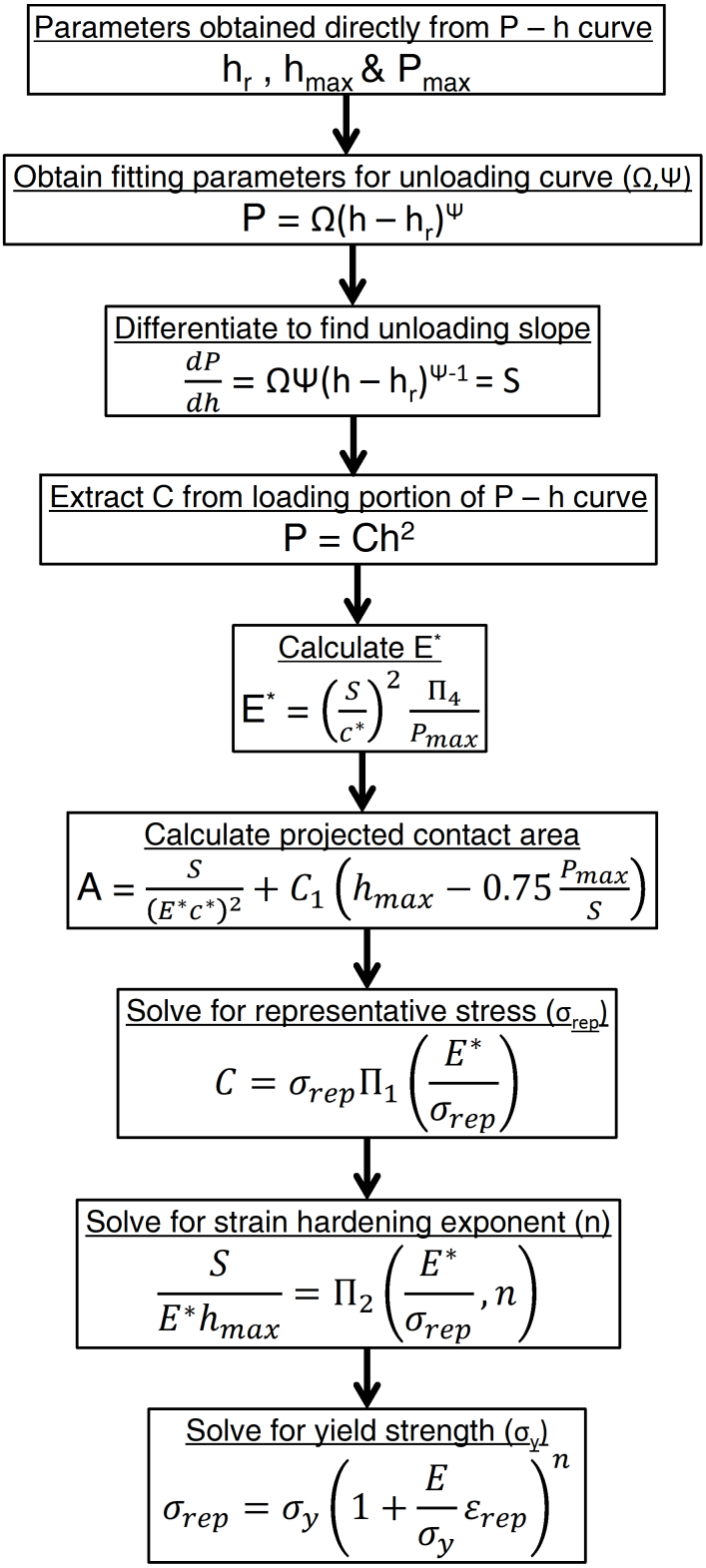

Figure 5.3.3: Algorithm for extracting material properties.

5.4 Results and discussion

Figure 5.4.1 a) shows the calculated Young's Modulus of the boron steel spot weld for each measurement and the average of 3 measurements at each specific distance. An assumption is made that Young's modulus does not change significantly through the weld, therefore the mean of the average is also presented. Although there is some scatter, the average result centres around a generally accepted value of 205 GPa, shown as the dotted line. The Young's Modulus results for DP600 in figure 5.4.1 b) show a larger scatter, but again, the data centres around the generally accepted value at 205 GPa, although there is a visible difference between the nugget and BM.

Figure 5.4.2 a) shows the calculated yield strength distribution of the boron steel spot weld. Although individual data points show scatter, the average in the nugget shows a consistent level of high yield values, with an average of 1040 MPa. The BM exhibits a yield strength value of approximately 1011 MPa. Such values are typically associated with fully hardened boron steel. Figure 5.4.2 b) shows the stress-strain curve of fully hardened boron steel with the calculated BM yield stress overlaid. The tensile test procedure to obtain the stress-strain curve is described in chapter 7. The stress-strain curve is an average of 5 uniaxial tests and has been zoomed in to the initial portion of the curve, to offer a clearer view of the yield point. The 0.2% offset yield from the experimental stress-strain curve is 1047 MPa and the calculated yield is 1011 MPa, showing a close correlation.

Due to limited allocated experimental time, indents were not made into the far-field BM, therefore, the instrumented indentation yield value presented for the BM is from the average of three data points at 6.6 mm in figure 5.4.2 a). Through hardness tests, it was shown that the BM and nugget exhibit similar hardness levels. Taking the thermal histories into account, where both the BM and nugget were austenitised and rapidly quenched, both parts are composed of significant amounts of martensite. The high level of consistent yield strengths in the nugget are used as verification that the data point at 6.6 mm is calculated to be at an acceptable value.

Figure 5.4.3 a) shows the calculated yield strength distribution of the DP600 spot weld. The yield strength in the nugget shows an average value of 925 MPa. It was previously mentioned that the DP600 nugget exhibited a hardness value of 100HV lower than the boron steel nugget. The same difference is seen here in terms of yield strength. Figure 5.4.3 b) shows the average stress-strain curve from 5 tensile tests of DP600. As with the boron steel curve, a zoomed in view is given. It is clear that the calculated yield strength gives a closer correlation to the 0% offset yield. The experimentally measured 0% offset yield is approximately 300 MPa and the calculated yield is 325 MPa.

It is interesting to note that the calculated yields of the hard boron steel BM correlated well with the 0.2% offset yield values, but the softer DP600 BM calculations correlate better with the 0% offset yield results. A possible explanation is due to the material behaviour under indentation. For harder materials, an increase in stress has relatively little impact on strain. For softer materials, a large change in strain is expected for a relatively small increase in pressure. Considering that all indents were performed under the same pressure, the difference between harder and softer behaviour under the same pressure could be a reason for the different yield strength correspondence.

The question remains, how can it be trusted that the calculated yield values in the boron steel HAZ are accurate. There are two known values that can be used for validation; the weld nugget and BM yield strengths. Both of these materials have significant amounts of martensite and are expected to exhibit a yield strength in the range of 1000 - 1100 MPa, which is evident in figures 5.4.2 a) and b). Therefore, it can be concluded that the calculated yield strengths in these areas compare well with experimentally measured yield strengths from fully hardened boron steel BM tensile tests.

However, these high strength areas of the weld are likely to exhibit different responses to indentation than the softer, more ductile HAZ areas. The results from the DP600 BM can be used as verification that the algorithm works for softer metals. As mentioned, the calculated yield strengths in the DP600 BM are approximately 25 MPa below the generally accepted value. It is likely, therefore that the boron steel HAZ results could

have a similar small underestimation, although the exact figure cannot be given.

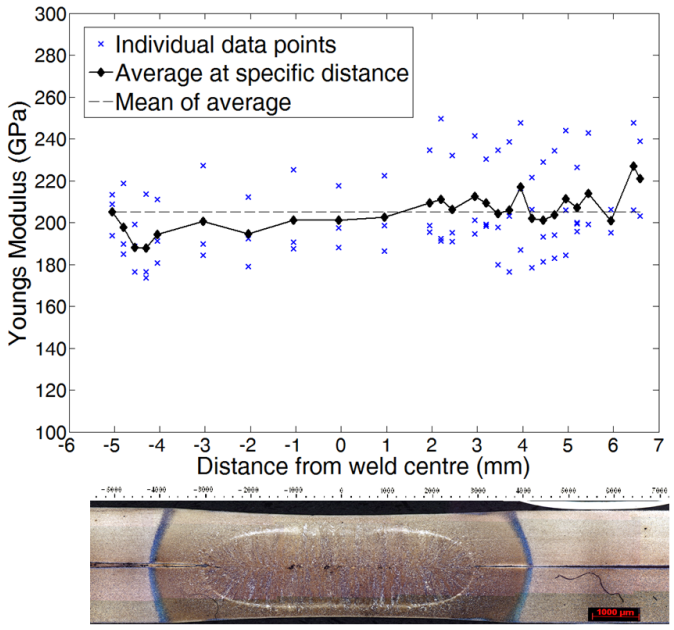

(a) Boron steel spot weld

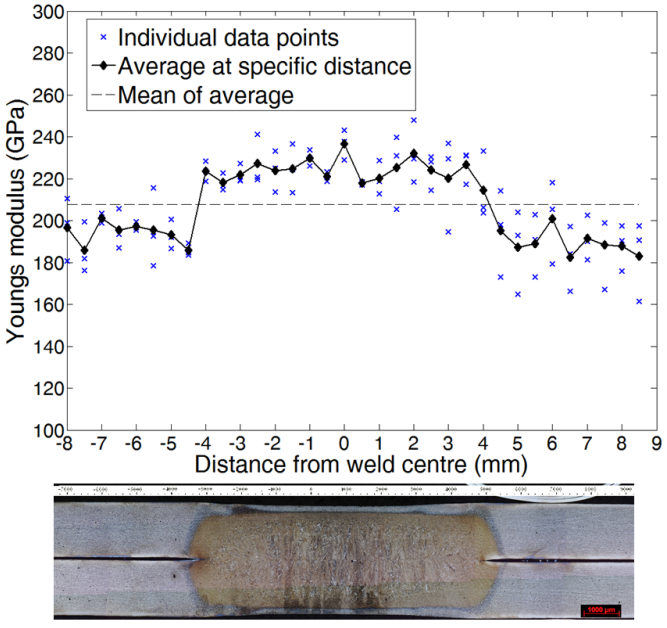

(b) DP600 spot weld

Figure 5.4.1: Calculated Young's modulus results from instrumented indentation

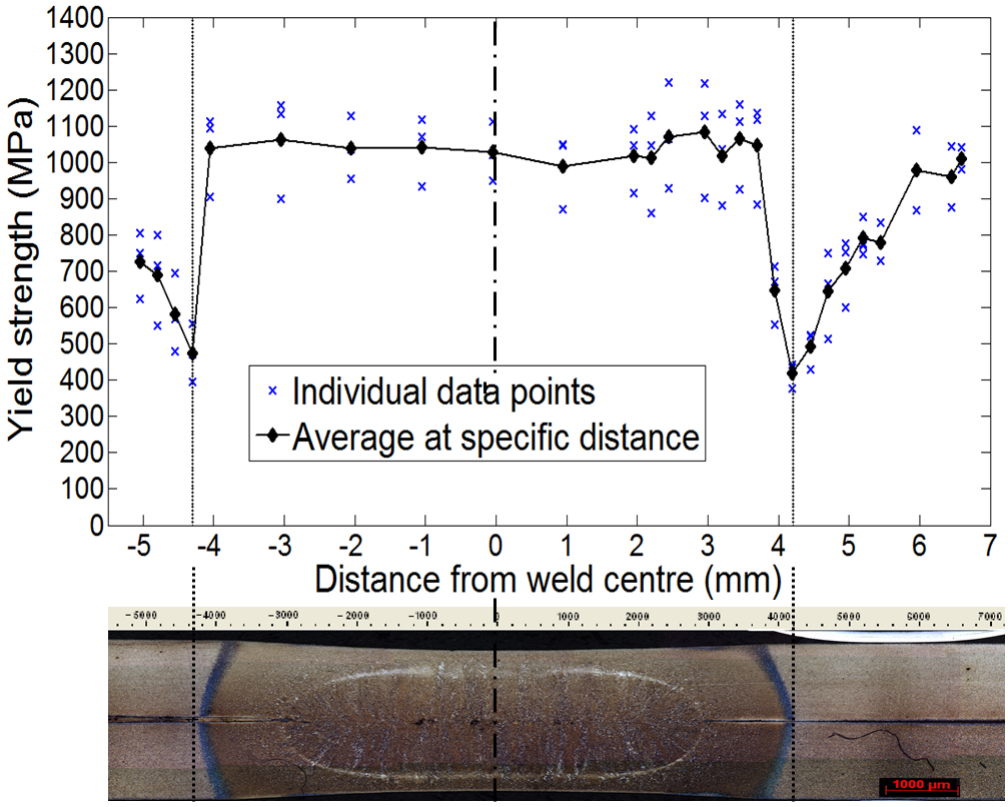

(a) Calculated yield strength distribution of boron steel weld from indentation results

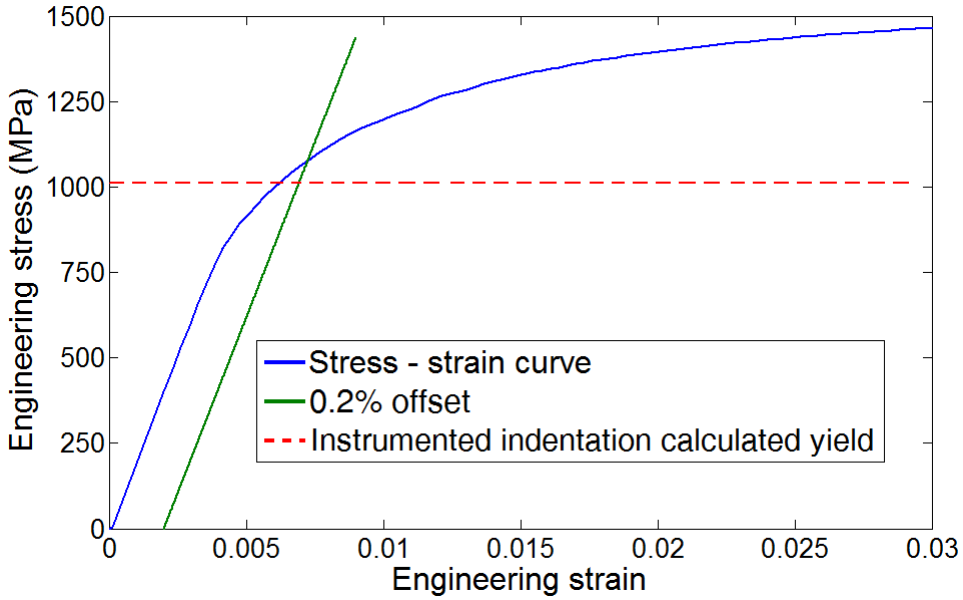

(b) Boron steel base material stress-strain curve with instrumented indentation calculated yield strength of the base material

Figure 5.4.2: Calculated boron steel weld yield strength distribution and validation with BM stress-strain curve

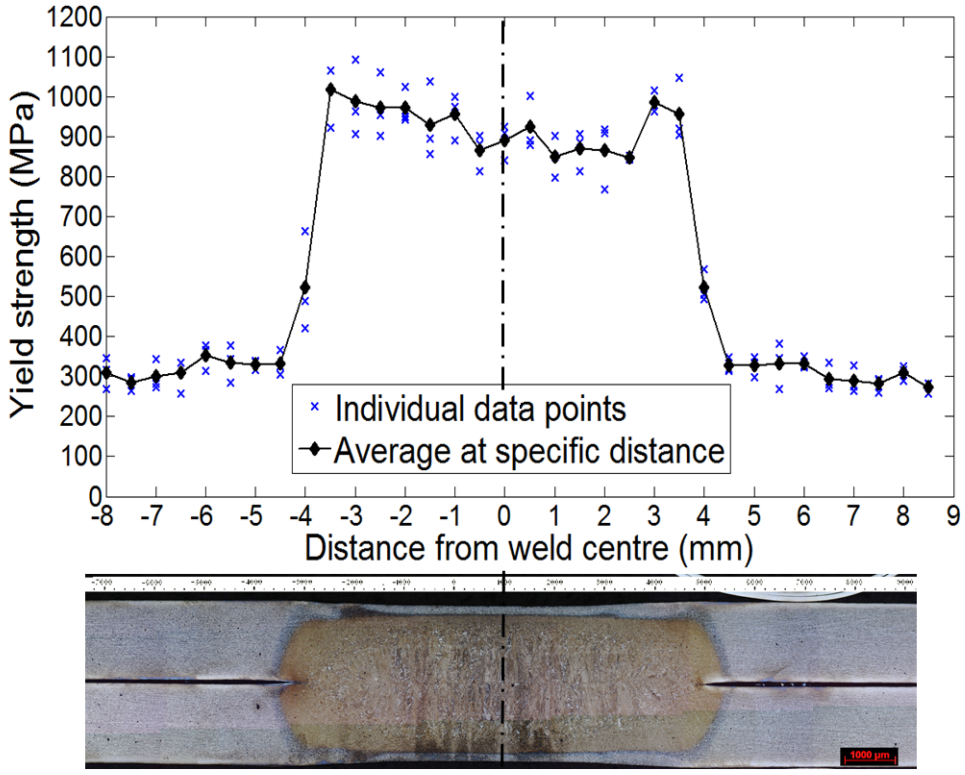

(a) Calculated yield strength distribution of DP600 steel weld from indentation results

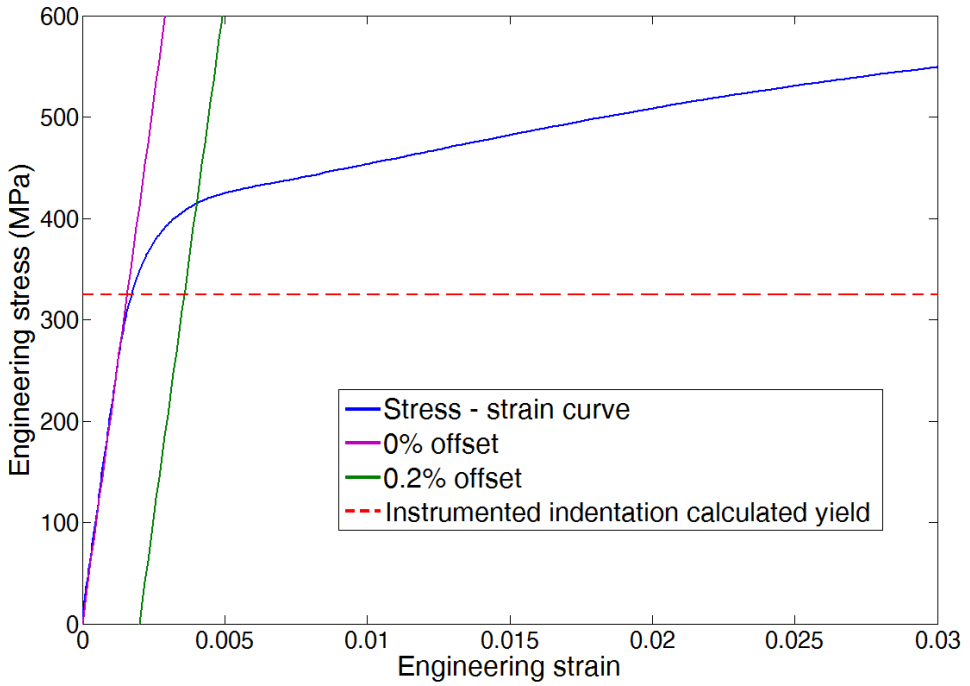

(b) DP600 steel base material stress-strain curve with instrumented indentation calculated yield strength

Figure 5.4.3: Calculated DP600 steel weld yield strength distribution and validation with BM stress-strain curve

5.5 Conclusions

Instrumented indentations were performed on boron steel and DP600 spot welds. These were the same welds as used in the neutron diffraction experiments. Three scan lines were performed on each weld at depths of 0.6 mm, 0.75 mm and 0.9 mm from the sheet-sheet interface. An algorithm developed by Dao *et al* [77] was used as a tool to calculate the modulus of elasticity and yield strength distributions of the welds.

Generally, individual data points showed scatter at a specific distance from the weld centre. In presenting the algorithm, Dao recommended to use multiple indents to reduce this scatter. It was seen that taking an average of 3 data points per location brought the results to acceptable values.

The Young's modulus results showed some scatter for both welds, but centred around commonly accepted values for steel of 205 GPa. After taking an average of the individual data points at specific distances, the yield strength distribution of the boron steel weld nugget showed a consistent high yield level, with an average value of 1040 MPa. Comparing the BM yield strength result to tensile tests performed on the boron steel BM, this showed a 36 MPa underestimation in yield strength. The HAZ showed lower yield strengths compared with the BM and nugget. The yield strength of the DP600 BM was underestimated by 25 MPa, compared to experimentally measured yield strengths from DP600 BM tensile tests.

An interesting observation was made that the yield strengths calculated for the harder materials of the boron steel correlated well to the 0.2% offset yield on the stress - strain curve and the softer material of the DP600 correlated well with the 0% offset yield. It was suggested that the higher strength materials exhibit different responses to indentation than the softer materials.

In the next section, HAZ microstructures are approximated through Gleeble heat treatment and some deviations from the target microstructure are expected. The information gathered through instrumented indentation is used to gauge the accuracy with which the Gleeble samples were created.

Chapter 6

Recreating weld microstructure

6.1 Introduction

A spot weld exhibits a symmetric geometry and when subjected to an external load, certain sections of the weld will undergo specific stress states or combinations thereof. Therefore, a curve describing the fracture strains as a function of stress state is essential for failure prediction. This function is known as a fracture locus, and is typically represented as strain at failure (ε_f) against a variable denoting the stress state. This variable is either the stress triaxiality (η) or ratio of principal strains (α). The considerations of using these two values will be discussed below.

The challenge presented in this chapter is firstly to employ a method of extracting such a locus. This is achieved through the use of Gleeble physical simulation. Such a method is somewhat novel and has been performed by relatively few authors to extract fracture loci for welds [40, 31]. In the Gleeble method, specific weld microstructures are recreated onto rectangular sheet specimens. From these rectangular sheet specimens, destructive specimens are cut out into several geometries. These different geometries will fail at different stress states. Local failure strains will be extracted through the use of Digital Image Correlation (DIC). The difficulty in the method is in recreating the high heating and cooling rates experienced by a certain part of the physical weld. Additionally, obtaining a large enough area of homogeneous microstructure on the destructive specimens is difficult to achieve.

The second challenge is to extend the concept of a fracture locus for a single material and to create loci as a function of the distance from the weld centre. As stated

previously, the spot weld consists of different microstructures due to different peak temperatures and cooling rates achieved as one moves outward from the weld centre. These different microstructures will exhibit different loading responses and fracture strains to one another. Therefore, in order to capture this material variation, it is essential to acquire fracture loci corresponding to different regions of the weld. Whereas Sommer [31] defined the boron steel HAZ as one structure, and assigned failure criteria as such, the current work discretises the HAZ more finely in order to capture the sharp material gradients present in the HAZ. Therefore, to fully capture these gradients, material constitutive behaviour was obtained at an increased number of locations in the HAZ.

The material property obtained so far is the yield strength distribution and process induced state of residual stress. Both of these data sets were obtained at a relatively fine resolution; at intervals of between 1 mm for the residual stress and 0.2 mm for the instrumented indentation tests. Due to the time consuming nature of the Gleeble experiments, fracture loci will be obtained at discrete points, and the results interpolated to obtain material properties at a higher resolution. The main objective is therefore to obtain local material properties in the form of fracture loci as a function of the distance from the weld centre. These loci will be used as input to the FE models to predict weld failure.

6.1.1 Representations of fracture loci

Stress triaxiality gives a single number describing the stress state of a material by comparing the deviatoric and hydrostatic components of stress and is represented as

$$\eta = \frac{\sigma_m}{\sigma_{vm}}$$

where σ_m is the mean or hydrostatic stress and is given by:

$$\sigma_m = \frac{\sigma_1 + \sigma_2 + \sigma_3}{3}.$$

σ_{vm} is the von Mises or deviatoric stress component and is given by:

$$\sigma_{vm} = \frac{1}{\sqrt{2}}\left[(\sigma_1 - \sigma_2)^2 + (\sigma_2 - \sigma_3)^2 + (\sigma_3 - \sigma_1)^2\right]^{1/2}$$

Figure 6.1.1 a) shows a typical plot of fracture strain versus stress triaxiality. From the graph it can be seen that shear, uniaxial tension and plane-strain stress states are found at $\eta = 0,\ \frac{1}{3}\ and\ \frac{\sqrt{3}}{3}$ respectively.

Another common representation of a fracture locus is the use of the ratio of principal strains, defined as

$$\alpha = \frac{\varepsilon_2}{\varepsilon_1}$$

As shown in figure 6.1.1 b), the shear, uniaxial tension and plane-strain states are found at $\alpha = -1,\ -\frac{1}{2}\ and\ 0$ respectively.

In performing measurements, the preferred representation of the fracture locus will be $\varepsilon_f - \alpha$. This is because the principal strains are native outputs from the strain measurement techniques, which will be described later in this chapter. However, the FE model requires failure curves to be in the form of $\varepsilon_f - \eta$. Hence the curves will be converted before inputting into the FE model.

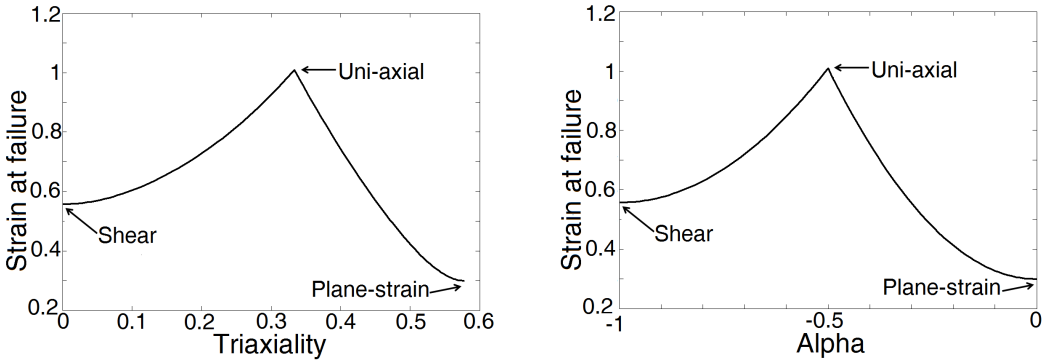

(a) Strain at failure vs stress triaxiality fracture locus

(b) Strain at failure vs alpha fracture locus

Figure 6.1.1: Schematic illustrations of triaxiality and alpha fracture loci

6.1.2 Determining fracture locus

As can be seen from figures 6.1.1 a) and b), shear and plane-strain are local minima and uniaxial tension is a local maximum. Bao and Wierzbicki [118] performed 11 tests consisting of uniaxial compression, shear, combined shear and tension, uniaxial tension and plane-strain tension. The authors found that simple parabolic curves in the ranges of $-1 \leq \alpha \leq -\frac{1}{2}$ and $-\frac{1}{2} \leq \alpha \leq 0$ were found to be in good agreement with experimental data. Therefore, to construct a fracture locus, only the minimum and maximum points need to be measured and parabolic curves fitted between them. Such a method was successfully employed by Beaumont [119] and is adopted in this work.

6.2 Physical simulation of weld microstructures to obtain failure curves for discrete weld regions

6.2.1 Gleeble thermo-mechanical simulator

The method of creating fracture loci corresponding to specific weld regions consists of recreating the microstructure of the specific weld region on a larger, practical destructive specimen i.e. shear, plane-strain and uniaxial tensile specimens. This is achieved by simulating the temperature history of the specific weld or HAZ region on a larger specimen through use of a Gleeble thermo-mechanical simulator. In reality, this is difficult to achieve due to the high heating and cooling rates involved. Additionally, due to the thermal mass of the specimen, a trial-and-error method is necessary to achieve the closest approximation to the heating times and cooling rates experienced during welding. This can be a time consuming process in which multiple variables can be adjusted to fine-tune the rates required.

As shown in figure 6.2.1, a rectangular specimen is clamped by 2 stainless steel grips, and the sample is heated through resistance heating. The thermocouples provide signals for feedback control of the specimen temperatures. Temperature-time curves are used

as input to drive the thermal cycles. An air-quench system approximates the cooling rates achieved during welding. The servo-hydraulic system is capable of exerting 10 tonnes of force and has a maximum displacement rate of 1000 mm/s, although this functionality was not utilised.

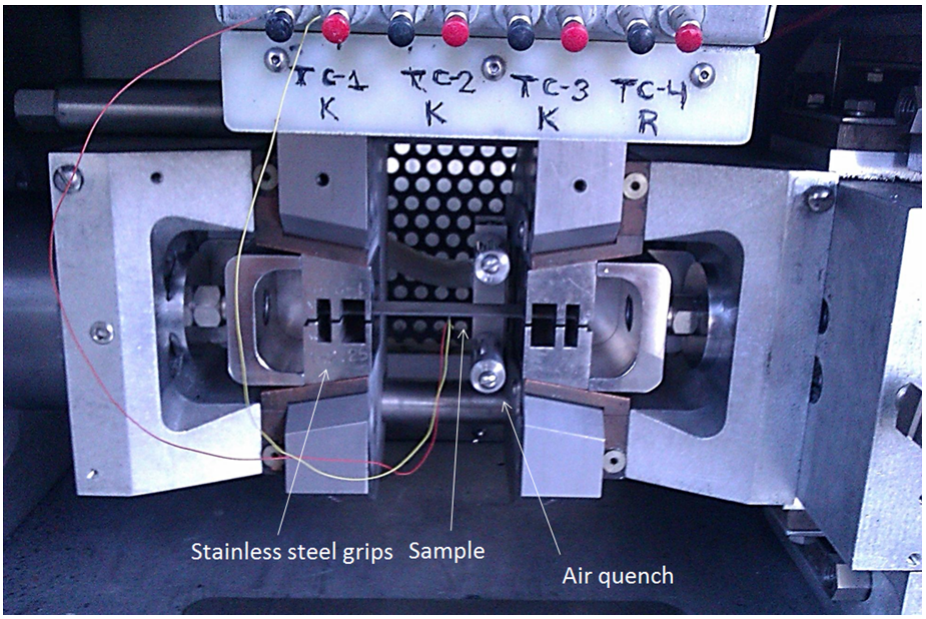

Figure 6.2.1: Specimen clamping section of Gleeble 3500 system.

6.2.2 Obtaining temperature-time curves to drive Gleeble simulations

6.2.2.1 SORPAS simulation

The automotive weld schedule, used to produce the weld that was measured in the residual stress and instrumented indentation experiments, was simulated using SORPAS welding simulation software. SORPAS is a dedicated resistance welding simulation program and is widely used in industry. The weld schedule was input into the software with the outputs of interest being the final nugget size and the temperature history. The final simulated nugget size was validated against that of the physical weld. As shown in figure 6.2.2, the final simulated nugget has a diameter of 6.029 mm. This corresponds well to the physical weld diameter of 6 mm.

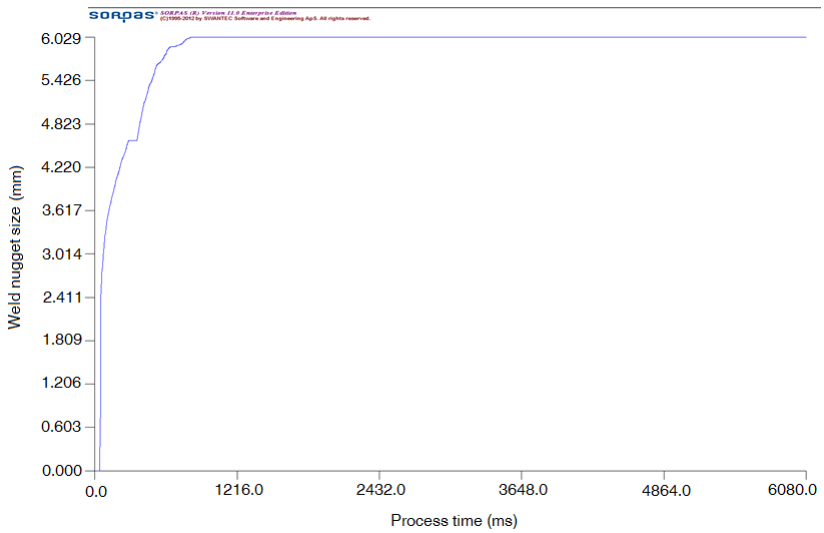

Figure 6.2.2: Weld nugget evolution for the industrial weld schedule.

6.2.2.2 Establishing points of interest

A plot of the hardness distribution of the physical weld was used to determine the locations from which the temperature histories were obtained, as shown in figure 6.2.3. For ease of reference, the points of interest are referred to as A to E, as indicated in table 6.2.1.

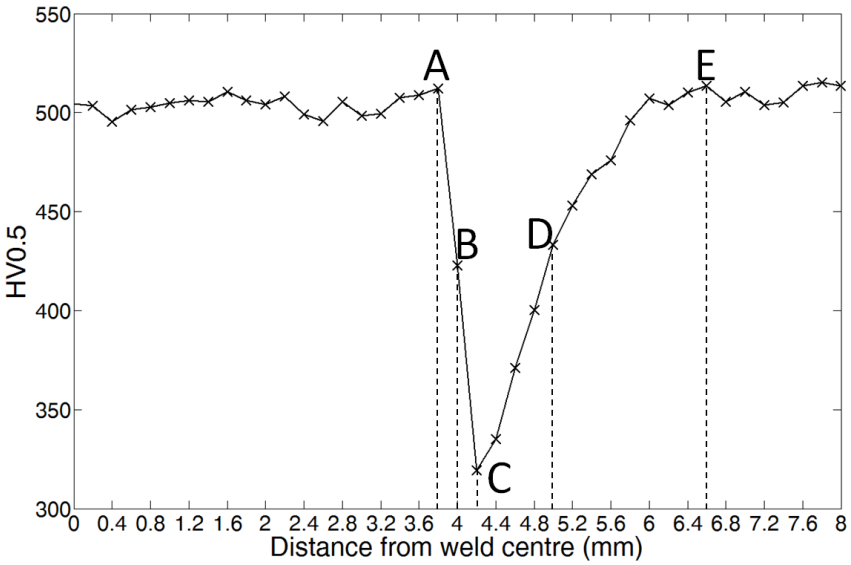

Figure 6.2.3: Hardness distribution of commercial boron steel spot weld.

The reasoning behind choosing these points was that the region between 3.8 mm and 6 mm was previously determined as the area of reduced mechanical properties. Obtaining data at these discretised points would aid in the subsequent fine interpolation of material properties. Tensile destructive specimens are also produced from the hot stamped BM. The BM is conservatively defined to start at 6.6 mm from the weld centre and is referred to as point E.

Figure 6.2.4 shows the peak temperature distribution of the weld obtained through the SORPAS simulation. Points A to D are shown in the figure. The temperature-time histories were extracted from elements at the mid-point of the top plate, giving an average of the thermal history experienced at that particular distance from the weld centre. The extracted thermal histories are shown in figure 6.2.5.

	Peak temperature (°C)	Distance from weld centre (mm)
A	1100	3.8
B	925	4.0
C	725	4.2
D	575	5.0
E	Hot stamped	6.6

Table 6.2.1: Points of interest in boron steel weld

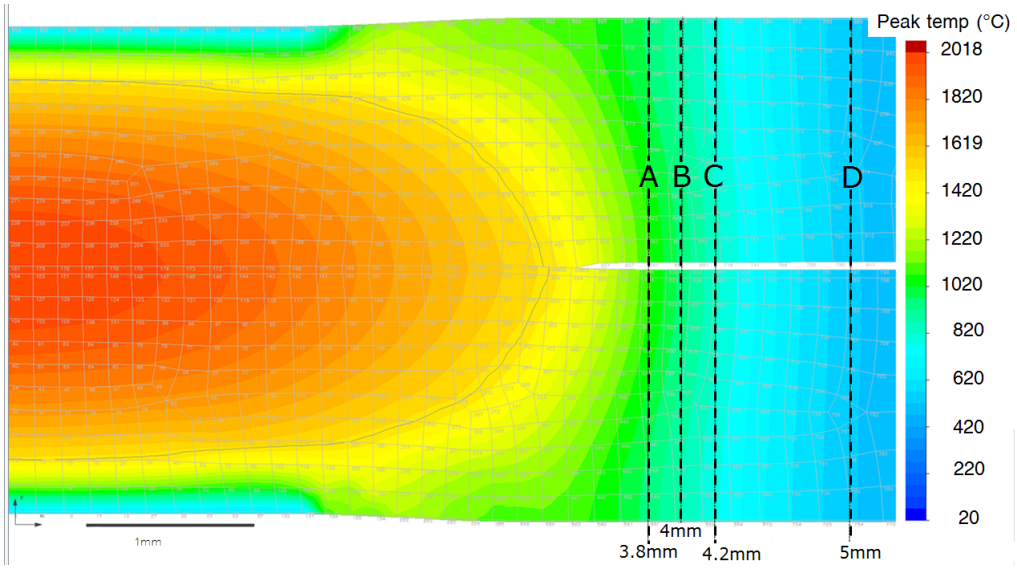

Figure 6.2.4: SORPAS simulation showing peak temperature distribution and coordinates correlating to the chosen points of investigation in reference to figure 6.2.3.

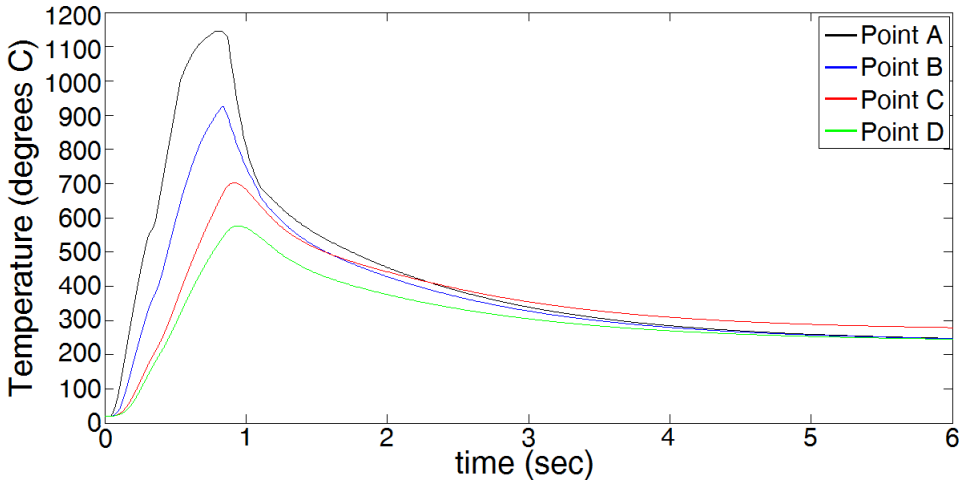

Figure 6.2.5: Temperature-time curves extracted from elements in the SORPAS weld simulation.

Sayles [120] performed dilatometry tests on a similar steel composition as used in this thesis. Sayles found that the A_{c1} temperature is 733 °C and the A_{c3} temperature is 858 °C. From these findings, it is reasonable to expect that the samples produced by the heating runs with 575 °C and 725 °C will produce tempered martensite, as they are below the transformation temperatures.

6.2.3 Grip selection for Gleeble machine

The thermal profile that develops along the sample length during Gleeble physical simulation is strongly controlled by 2 factors of the Gleeble machine; the type of grips and the *free-span* of the sample, with the free-span being the distance between the grips. In perfect Joule heating, the temperature is only related to the sample cross-section, however, the water cooled grips cause localised cooling. Thus a temperature gradient develops along the sample length with the centre portion of the sample experiencing the highest temperature.

The most common grips used in a Gleeble machine are water cooled copper, and as can be seen from figure 6.2.6 they give a highly parabolic temperature profile. This is due to the high thermal conductivity of copper in addition to being water cooled.

The stainless steel half-contact grips were available and were recommended by Dynamic Systems [D. Jacon, personal communication, Dynamic Systems Inc., 16 February 2014]. The low thermal conductivity of stainless steel results in a flatter thermal profile by drawing less heat away from the sample ends. The reduced contact area also aids in reducing the amount of heat drawn from the sample.

The 2 types of grips have different behaviours at fast heating rates. The stainless steel grips are by design built to maintain a flatter thermal profile. Applying fast heating rates will result in electrical arcing and localised hotspots within the grips [D. Jacon, personal communication, Dynamic Systems Inc., 16 February 2014]. In contrast, the copper grips allow for very fast heating rates, with a parabolic thermal profile. Preliminary tests were performed using both grip systems, however, the samples produced from the copper grip system showed unsatisfactory hardness distributions along the sample length.

As the destructive tensile coupons would be extracted from the Gleeble rectangular samples, it was deemed more important to achieve a homogeneous microstructure in the gauge area than to achieve fast heating rates. If the copper grips were used, it is likely that the tensile samples would exhibit a gradient of constitutive properties throughout its length. The interplay of varying properties would then invalidate the test results. Therefore, the half-contact stainless steel grips were selected for use, as this would maximise the volume of homogenised microstructure in the centre of the sample.

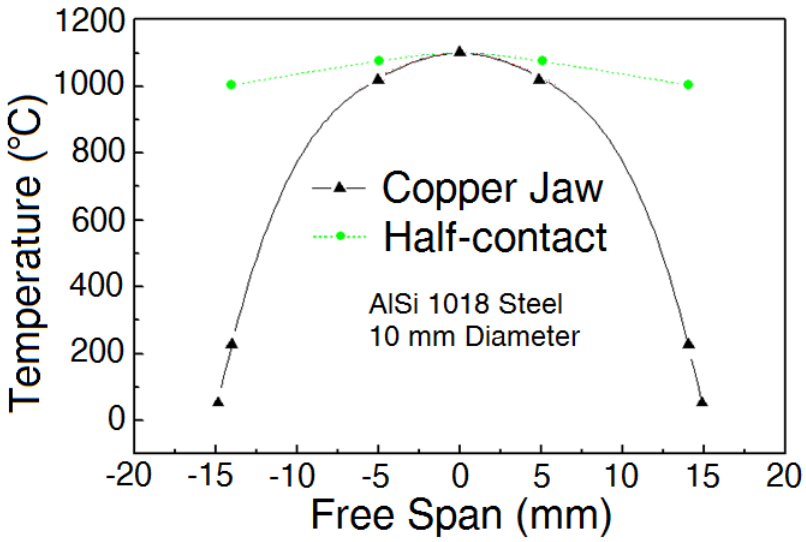

Figure 6.2.6: Thermal profile in the free span of the sample, given by various grips used in Gleeble machine. Image courtesy of Dynamic Systems Inc.

6.2.4 Sample geometry considerations

6.2.4.1 Geometry width

The samples used during the physical simulation trials in the Gleeble machine were rectangular in shape. The rectangular shapes were chosen because performing the heat treatments with the tensile and shear geometries already machined would have resulted in distortion of the samples, invalidating any further tests performed on them. One of the key challenges was to choose the dimensions of the rectangular samples to achieve a sufficiently homogenised microstructural zone and for the machined samples to be sufficiently large to be used in a conventional tensile testing machine.

A problem of having wide samples is achieving consistent peak temperatures and hitting the correct heating rates. In initial tests, the samples were 40 x 130 mm. In these initial tests and all subsequent tests described, the samples were 1.5 mm thick. As can be seen from figure 6.2.7, having such a large width resulted in a large scatter in peak temperatures between samples. From this experience, it was decided to reduce the

sample width. Due to the need for gripping length during tensile testing, the length of the sample cannot be shortened significantly. Therefore a compromise was made between reducing the sample width and having a sample with sufficient physical size to be used in a conventional tensile testing machine.

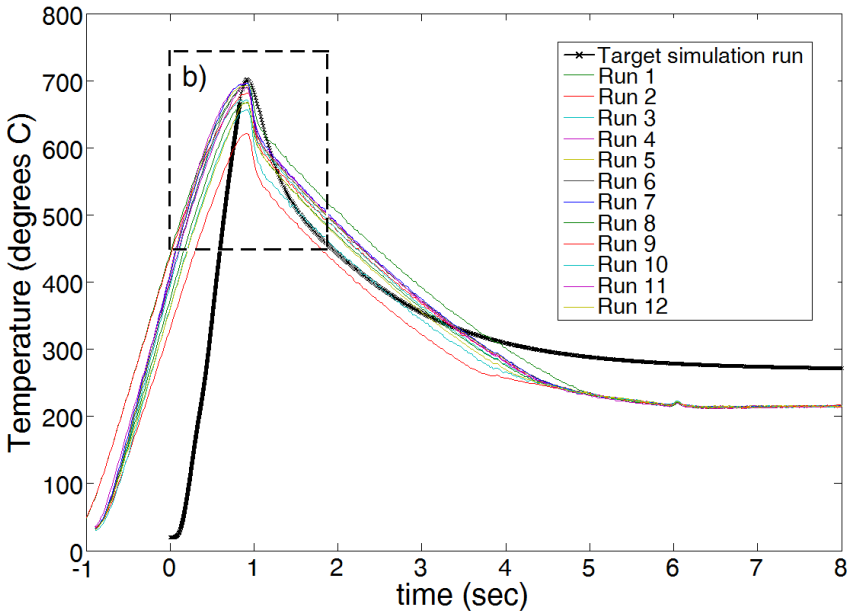

(a) Entire set of Gleeble runs for point C (725 °C peak temperature)

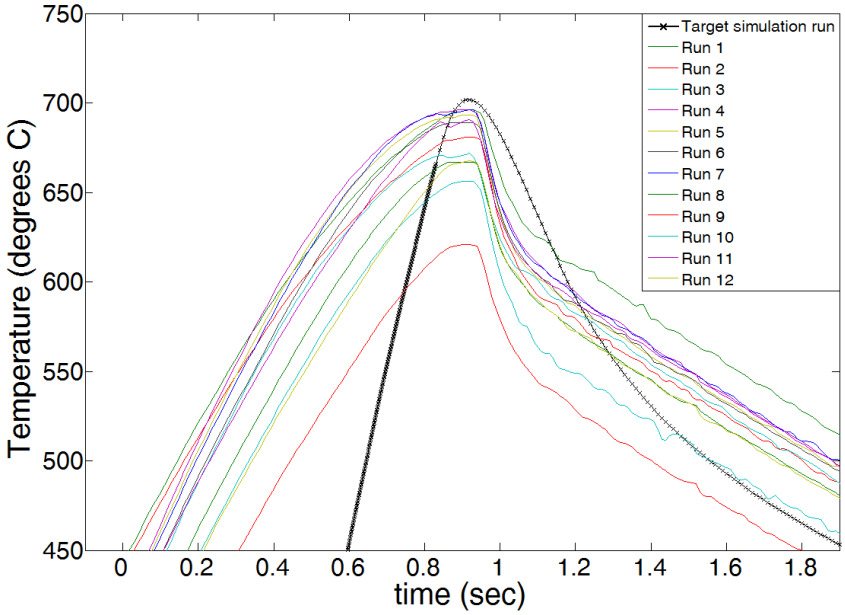

(b) Close-up view of peak temperature region

Figure 6.2.7: Inconsistent peak temperatures for 12 repeats from initial Gleeble runs.

6.2.4.2 A note on destructive tensile geometry selection

The size restrictions imposed by the Gleeble machine means that the tensile and shear geometries, to be prepared after the heat treatment runs, will not conform to ISO standards [121]. Sommer *et al* [31] performed a similar experiment to the one described in this chapter. Therefore, it was decided to utilise their tensile and shear geometries and improve upon them. Figure 6.2.8 shows the geometries used by Sommer.

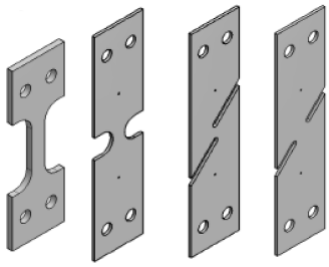

Figure 6.2.8: Tensile, plane-strain, 0° shear and 45° shear specimens used by Sommer *et al*. Taken from [31].

The plane-strain stress state is relatively easy to approximate. The sample exhibits a transverse dimension larger than the axial dimension, leading to an increased transverse stiffness and a minimised axial contraction. That is to say $\varepsilon_2 = 0$ and $\alpha = 0$. A common geometry to achieve plane-strain is a notched sample. The sample geometry used by Sommer *et al* was deemed sufficient and hence modifications were not necessary.

Standard uniaxial tensile tests pieces, also known as *dog-bones*, are routinely used to extract material properties such as yield strength, tensile strength and modulus of elasticity. Lanzerath [36] reported that standard uniaxial tension specimens cannot be used in the development of a failure locus. This is due to the need to keep the stress state constant during deformation until failure occurs. This is especially true for ductile materials where, during necking, the geometry changes significantly before fracture, tending towards a plane-strain state. Lanzerath suggested performing tests with a central hole in the tensile specimen. The reasoning behind this suggestion is as follows: the free edge of a material under tension is assumed to be under uniaxial

tension, therefore, to ensure the specimen fails under uniaxial tension, a stress raiser such as a hole is needed. The first proposed improvement of Sommer's experiment is thus the introduction of a central hole sample.

Sommer *et al* give no indication of the source of their fracture samples; however, their shear specimens seem to be based on the Scherzug geometry [122]. It was found that the Scherzug geometry actually gave a triaxiality value indicative of mixed-mode shear [119]. In a review of different shear specimens, Beaumont [119] stated that the Peirs shear geometry [123] gave the most consistently low triaxiality. The Scherzug and Peirs geometries are shown in figure 6.2.9. A finite element simulation was performed, comparing both shear geometries. It can be seen that the Peirs geometry gives an alpha value closer to the theoretical value associated with pure shear, as shown in figure 6.2.10.

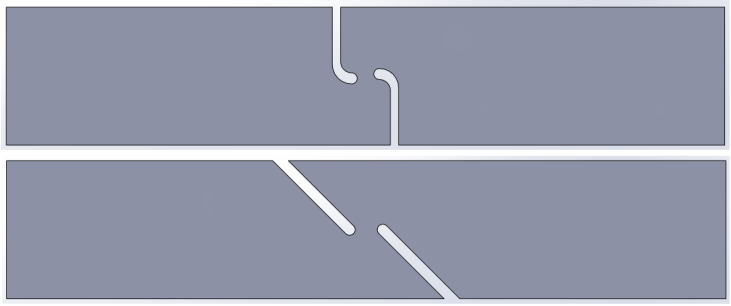

Figure 6.2.9: Peirs (top) and Scherzug (bottom) shear geometries.

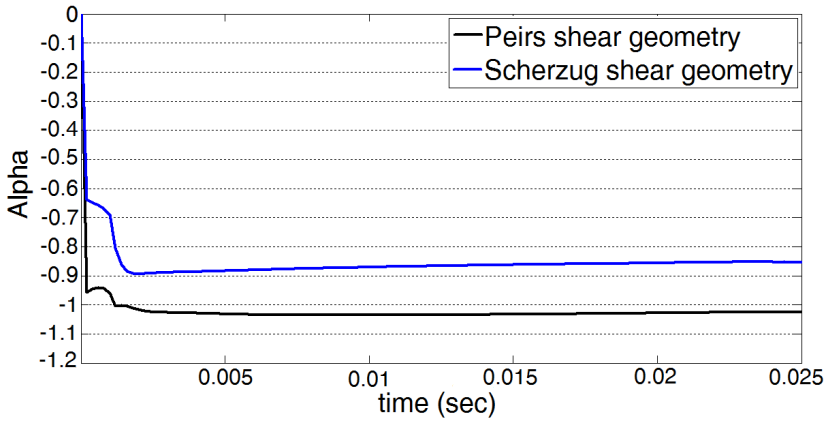

Figure 6.2.10: LS-Dyna simulation of evolution of alpha for shear specimens with material properties of boron steel base material.

Finally, a dog-bone specimen was also included in the collection of geometries. This will enable the extraction of stress-strain curves of the specific weld regions. The dimensions of the dog-bone were kept to Sommer's specifications.

In conclusion, to allow the tensile destructive specimens to be created and to meet the heating/cooling rate requirements for Gleeble physical simulation, the final rectangular geometries used to perform the Gleeble physical simulations were 20 x 130 mm for the tensile, central hole and plane-strain samples and 25 x 130 mm for the shear samples. The samples to be used in the Gleeble simulations were first heat treated in accordance to the hot stamping regime previously defined. This means any simulated microstructure originates from the same physical BM microstructure.

6.2.5 Establishing heating regimes

The collection of temperature histories obtained through the SORPAS simulation (previously shown in figure 6.2.5) is defined as the "target heating regime". In performing the physical simulation experiments, this target heating regime was scaled into a "slow heating regime" and a "fast heating regime". An example of the 925 °C temperature-time curves are shown in figure 6.2.11 to illustrate the difference between the heating regimes. The reasons for the scaling operations are explained as follows.

The significant difference between the welding process and the Gleeble physical simulation is the mass and volume of the two materials being heat treated. A subsection of the HAZ targeted for simulation is significantly smaller than the rectangular specimen clamped in the Gleeble machine. This difference in mass/volume leads to a discrepancy between the heating rates required to achieve the same temperature and subsequent microstructure in the large physical simulation sample as in the weld sample. Due to the limited access time to the Gleeble machine, a thorough investigation of the effects of heating rate could not be conducted. Instead, two extreme versions of the heating rate were used to tackle this issue.

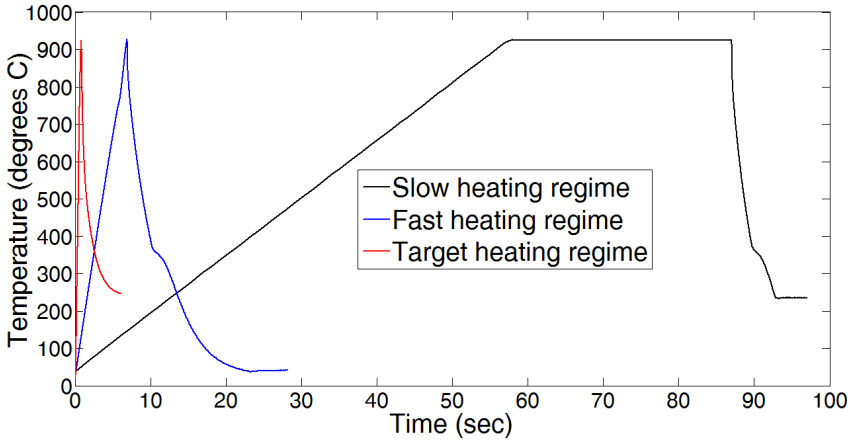

Figure 6.2.11: Heating and cooling curves for the 2 experimental Gleeble runs (925 °C peak temperature) with the target curve

6.2.5.1 Slow heating regime

The slow heating regime consists of using both a controlled heat and a dwell time at peak temperature. As stated previously, preliminary tests showed that the main challenge was to consistently achieve the peak temperature. The conservative slow heating rate was thus chosen to ensure consistent peak temperatures between samples. The dwell time was incorporated to ensure the development of a homogeneous microstructural zone in the gauge area of the destructive samples. The scaling for the slow heating regime was performed on the basis that the target temperatures are reached within 60 seconds, thus ensuring a stable, controlled heat to peak temperature. The final scaled slow regime is shown in figure 6.2.13 c).

6.2.5.2 Fast heating regime

The fast heating regime was a direct simulation of the fastest heating time that is possible to achieve with the chosen Gleeble set up. As will be shown in the results section, after obtaining satisfactory results from the more conservative slow heating runs, in terms of consistent peak temperatures, a second experimental attempt was made to obtain a closer approximation to the actual welding temperature-time curve.

This was achieved by including rapid heating and discarding the dwell at peak temperature. The challenge presented with this heating regime is to obtain not only the fastest heating rate possible, but to consistently hit the correct peak temperature. Test runs were performed to find the fastest time to reach peak temperature which results in the correct peak temperature. The investigation into finding the fastest heating time is illustrated in figure 6.2.12, which shows 3 heating times applied to each of the 4 peak temperatures.

As the target temperature increases, the fastest heating time (5 seconds) results in the greatest undershoot. The 7 second heating time reached the target temperatures in all regimes except the 1100 °C regime, with an undershoot of approximately 30 °C. Given that 1100 °C is far above the A_{c3} temperature, such a small undershoot would have a minimal effect on the final microstructure. It was decided, therefore, as a compromise between heating rate and peak temperature accuracy, to scale the target heating regime to achieve peak temperature within 7 seconds. The final scaled fast regime is shown in figure 6.2.13 b).

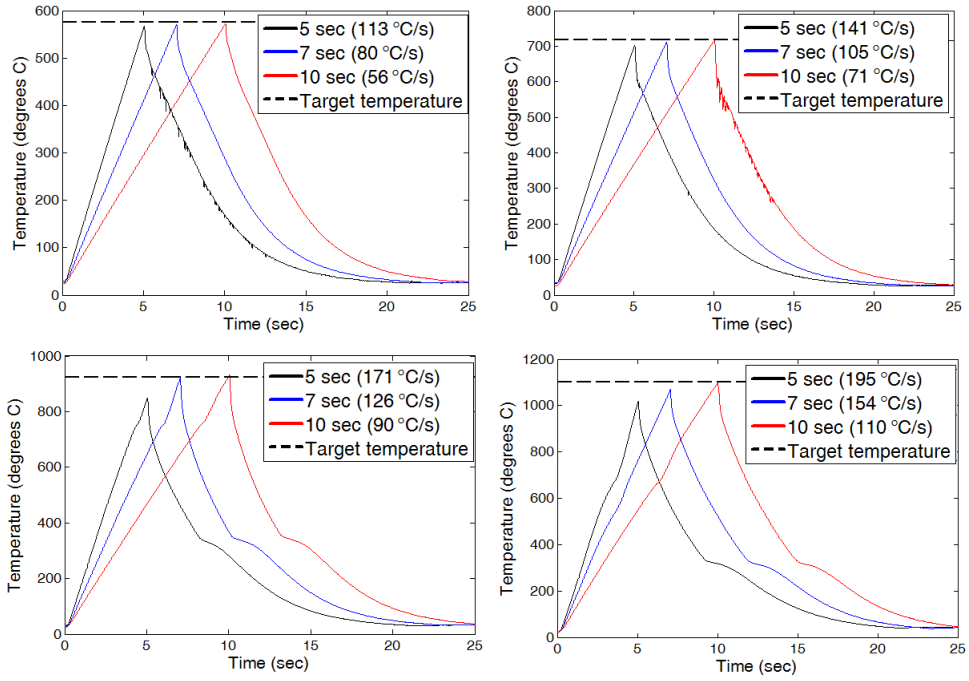

Figure 6.2.12: Effect of varying heating rates on peak temperature for fast heating regime

6.2.6 Effect of different heating rates

Figure 6.2.13 shows the target, slow run and fast run heating regimes. The difference in heating rates between the different regimes is clear, with the fast heating regime being an order of magnitude slower and the slow heating regime being two orders of magnitude slower, with respect to the target heating regime. These heating rates could potentially have different consequences on the final microstructure depending on the peak temperature reached.

To keep the heating rates in context it is important to reiterate a few points. Firstly, the mass and volume of the physical weld HAZ section is an order of magnitude smaller than the rectangular steel sample heated in the Gleeble. This means that the rate of energy input to achieve the same temperature is different for the two systems. The slow heating regime was employed to ensure consistent peak temperatures were achieved, as previous trials indicated that faster heating rates resulted in significant scatter of achieved peak temperatures. The fast heating rate was employed after obtaining satisfactory results from the conservative slow heating regime. Due to the need to obtain a large homogeneous microstructural zone in the sample centre, the stainless steel half-contact grips were employed. These grips do not allow for fast heating rates, therefore the heating rates employed in the fast heating regime are the fastest than can be used whilst achieving consistent peak temperatures between different samples.

In the following discussions, it is important to remember that it was previously stated that Sayles [120] found that the A_{c1} temperature is 733 °C and the A_{c3} temperature is 858 °C.

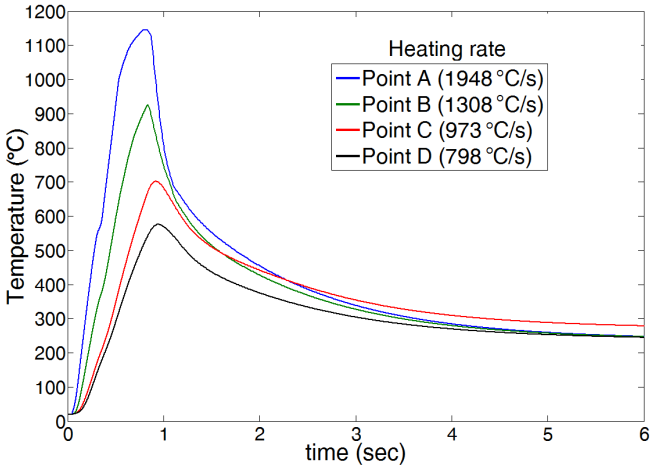

(a) Target temperature-time curves with heating rates

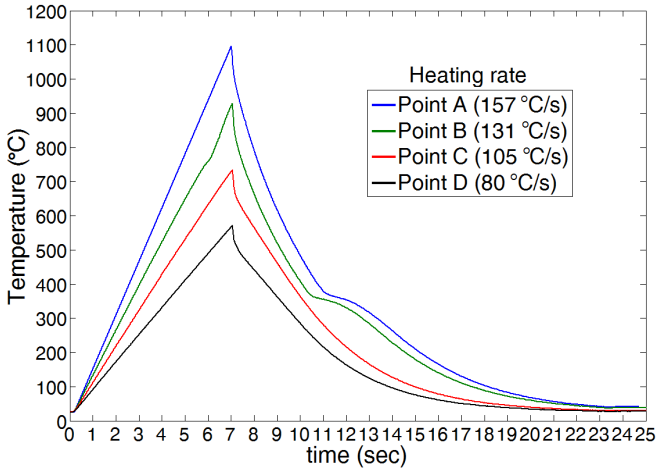

(b) Fast heating regime temperature-time curves with heating rates

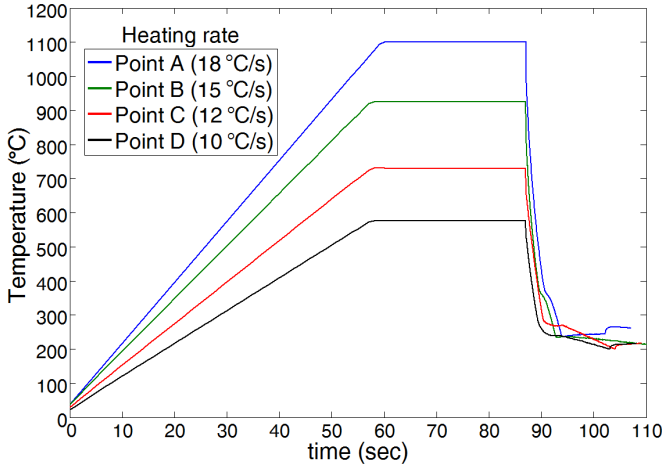

(c) Slow heating regime temperature-time curves with heating rates

Figure 6.2.13: Heating rates for all temperatures regimes for the target simulation, fast and slow heating regimes

6.2.6.1 Peak temperatures below transformation temperature (575 °C and 725 °C)

For the target temperatures below the A_{c1} temperature, the slower heating rates imply that the samples spend more time being tempered at elevated temperatures. Essentially, during tempering, carbon precipitates from martensite, resulting in a two-phase structure of carbide and reduced-carbon martensite [29].

Tempering is usually performed for extended periods at a constant peak temperature, although some research has been performed with short tempering times [124, 125, 126].

It has been reported that martensitic steels exhibit a rapid softening at the early stages of tempering [124, 125, 126]. This rapid softening occurs because martensite is highly unstable, due to being a highly strained lattice structure supersaturated with carbon [127].

Furuhara *et al* [126] performed induction tempering on martensitic steel at three heating rates: 2 °C/s, 100 °C/s and 1000 °C/s. Figure 6.2.14 shows the hardness values of the steel after being heated to a peak temperature of either 550 °C or 650 °C at the previously indicated heating rates and kept at the peak temperature for the indicated amount of time, ranging from 0 seconds to 3600 seconds. The data marker indicated by "As Q" (As Quenched), indicates the initial steel hardness before the tempering procedure. The dashed lines indicate the time spent reaching the peak temperature, after which the samples are held isothermally for the indicated tempering times.

From the figure, it can be seen that the samples heated at 100 °C/s and 1000 °C/s exhibit similar hardness values at zero seconds tempering time. This is especially true for the samples heated to a peak temperature of 550 °C. The samples heated to 650 °C show a difference of approximately 20 kgf/mm^2.

The samples heated by 2 °C/s exhibit significantly lower hardness values than those produced by the higher heating rates, due to spending a longer time at elevated temperatures. The figure also indicates relatively little change in hardness beyond the

initial large decrease in hardness i.e. up to 300 seconds of tempering time. Similar observations were also made by Ahlstrom [125].

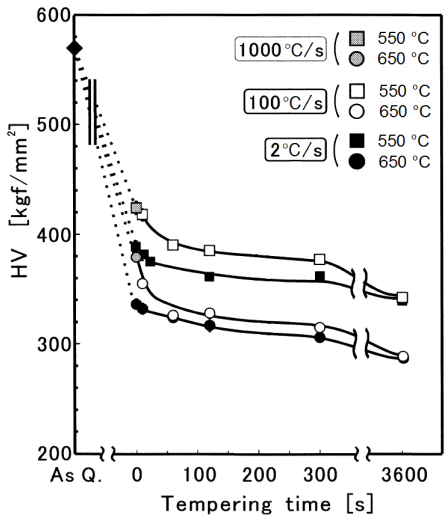

Figure 6.2.14: Vickers hardness of martensitic steel induction tempered for various tempering times, heating rates and peak temperatures. Taken from [126]

From the above considerations, the following conclusions may be made. For the samples heated below the A_{c1} temperature, the majority of tempering occurs in the initial stages. From figure 6.2.14, it seems that the samples produced with the fast heating regime (in the order of 100 °C/s) will correspond well to the target weld zones (produced at heating rates in the order of 1000 °C/s).

A greater degree of variation is to be expected from the samples produced with the slow heating regime. This is due to the samples spending longer times being heated to peak temperatures and are hence tempered to a greater degree. Additionally, the dwell times at peak temperature increases the amount of tempering. It is important to remember that the slow heating regime was a initial experimental attempt, employing conservative experimental heating parameters to ensure consistent peak temperatures and maximised areas of homogeneous microstructure. The previously discussed mass/volume discrepancies between the small target physical weld regions and large physical simulation samples also influenced the decision to employ such conservative heating parameters.

6.2.6.2 Peak temperatures above transformation temperature (925 °C and 1100 °C)

The austenite formation mechanism in martensite has been reported to be diffusion controlled [127]. It has been reported that at temperatures between 790 °C and 870 °C, austenite formed within 2 seconds by rapidly heating thin martensitic steel samples [127].

Austenite grain growth is more sensitive to temperature than time [128, 129, 127]. The rate of increasing austenite formation with increasing temperature is shown in figure 6.2.15 a). This higher sensitivity to temperature is due to increased thermal energy, causing the diffusion rate of carbon atoms to increase, causing austenite to form more rapidly [129].

The effect of dwell time on the austenite grain size at peak temperature is seen in figure 6.2.15 b). From the figure, it can be seen that increasing the dwell time at 1700 °F (930 °C) by a factor of 20 (6 minutes to 120 minutes) only increases the grain size by a factor of 1.9 (94 μm to 174 μm). Increasing the peak temperature for a given dwell time increases the grain size much more dramatically.

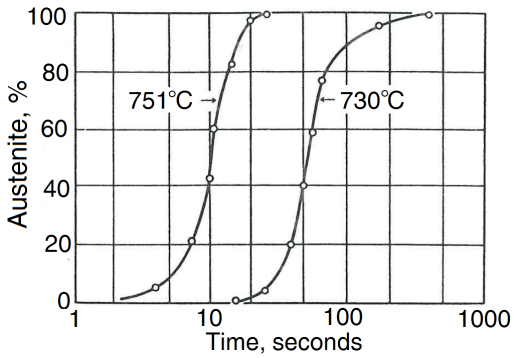

(a) Rate of austenite formation at increasing austenitisation temperatures. Initial microstructure is pearlite in a eutectoid steel. Taken from [127]

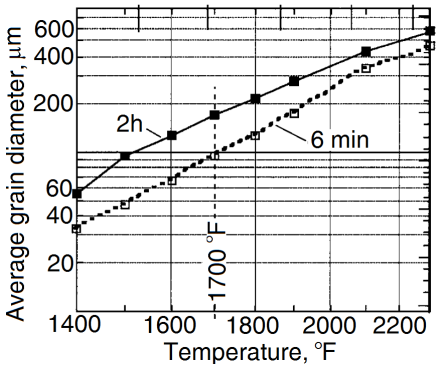

(b) Average grain diameter as a function of austenitisation temperature, held for 6 minutes or 2 hours at peak temperature. Taken from [128]

Figure 6.2.15: Effect of temperature on austenite formation

Heating rate also affects the transformation temperatures. Clarke *et al* [2] performed induction dilatometry on samples consisting of tempered martensite. Heating rates of 0.3 °C/s to 300 °C/s were applied to achieve peak temperatures from 750 °C to 1200 °C, followed immediately by helium gas quenching to room temperature. The effect of heating rate on the A_{c1} and A_{c3} temperatures can be seen in figure 6.2.16, where the transformation temperatures increase with increasing heating rate. In the figure, only the QT (quenched and tempered) points are of interest, and the reader is advised to ignore the other data points. Danon *et al* [130] made similar conclusions to that of Clarke.

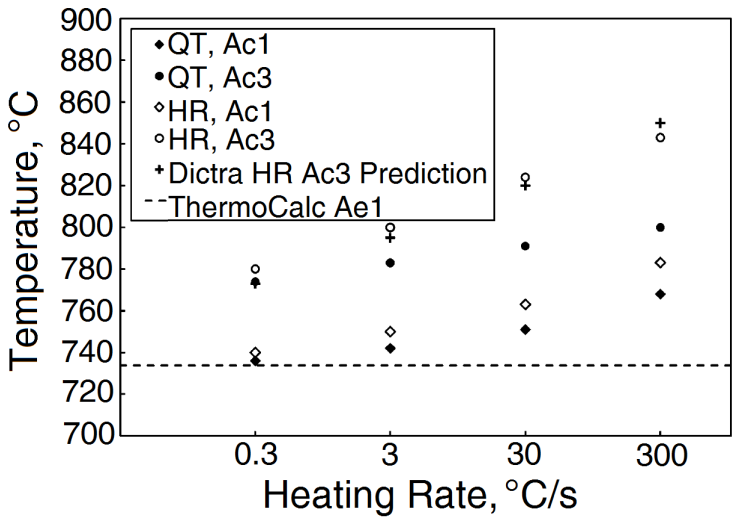

Figure 6.2.16: Transformation temperature as a function of heating rate for steel with tempered martensitic microstructure (QT = quenched and tempered initial steel microstructure). Taken from [2]

From the above considerations, the following conclusions may be made. It is clear that temperature has a greater influence on austenitisation than time. Samples produced with the fast heating rate to 925 °C are likely to form a smaller fraction of austenite than those heated to 1100 °C with the same heating rate. The faster heating rate, however, increases the transformation temperatures. This means the samples produced with the fast heating rate to 925 °C will start to form austenite at higher temperatures and produce an even smaller fraction of austenite. Due to the limitations of the Gleeble setup, the heating rates of the fast regime could not be improved. A higher degree of

austenitisation will be achieved during the slow heating regime, where ample time is given for the austenite grains to grow.

The effects of these heating rates will be seen in the hardness testing section of this chapter.

6.3 Physical simulation trials

6.3.1 Slow heating regime

The heating runs for points A - D are shown in figures 6.3.1 to 6.3.4. As can be seen, there was very little variability between samples, both for the 20 mm wide samples (destined for the plane-strain, dog-bone and uniaxial with central hole geometries) and 25 mm wide samples (destined for the shear geometries). The dwell time was set for 30 seconds, and after completion, the air quench system was automatically activated. In total, 80 physical simulation samples were produced, with 5 repeats for each geometry at each temperature regime.

6.3.2 Fast heating regime

The temperature - time curves for the fast heating regime are presented in figures 6.3.5 to 6.3.8. A high level of consistency can be seen for all samples. The same optimum cooling parameters were employed as in the slow heating regime. Due to time constraints, a total of 48 samples were produced, with 3 repeats for each geometry at each temperature regime.

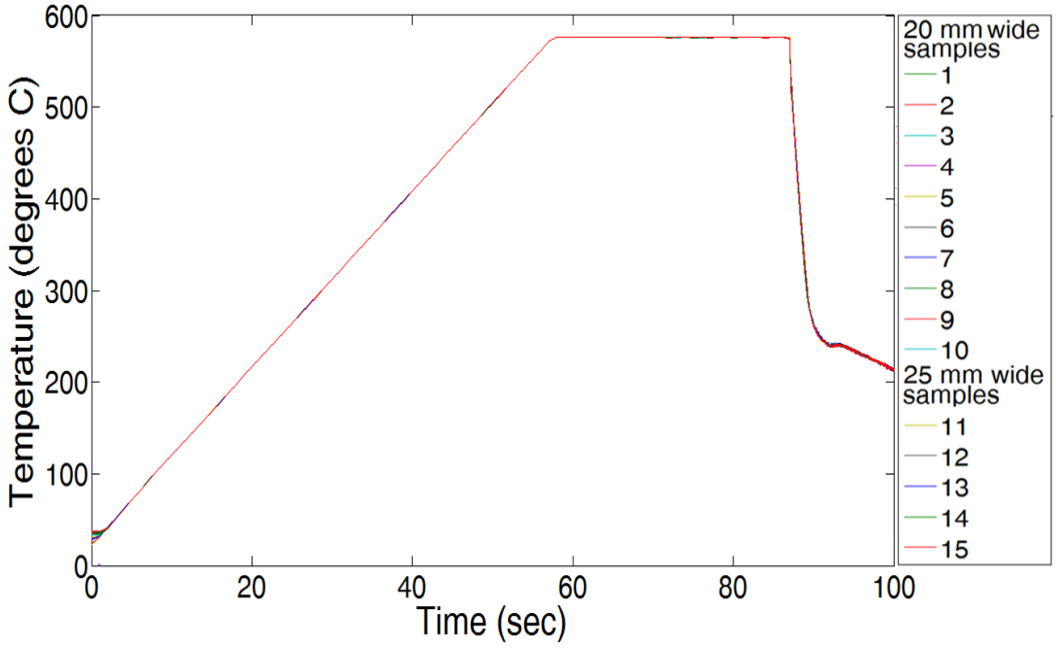

Figure 6.3.1: Temperature - time curve for point D (575 °C peak temperature). Slow heating regime

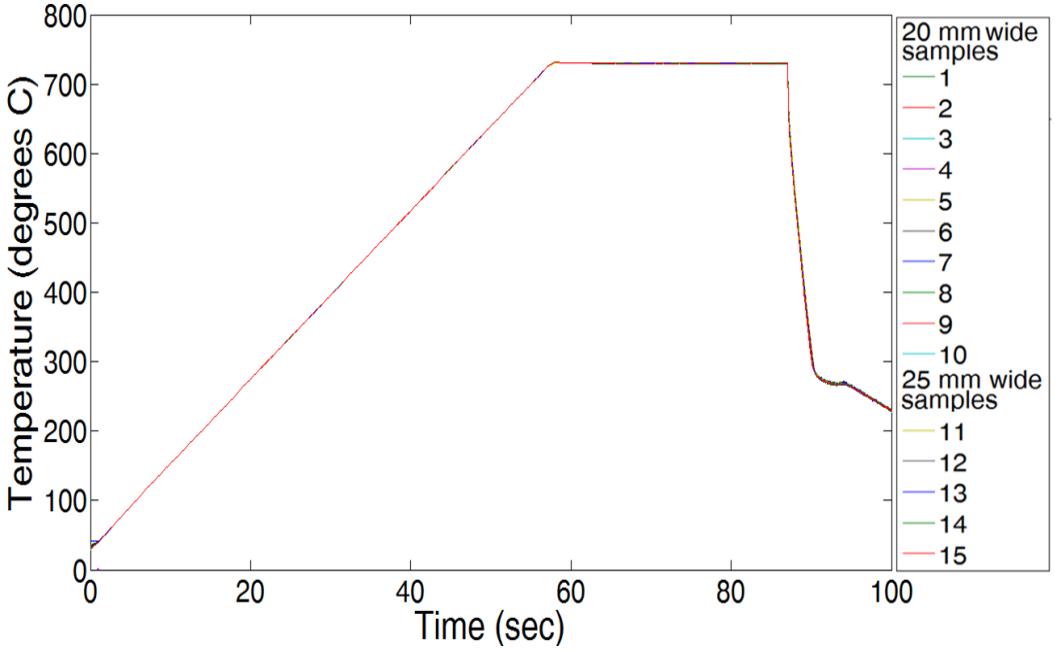

Figure 6.3.2: Temperature - time curve for point C (725 °C peak temperature). Slow heating regime

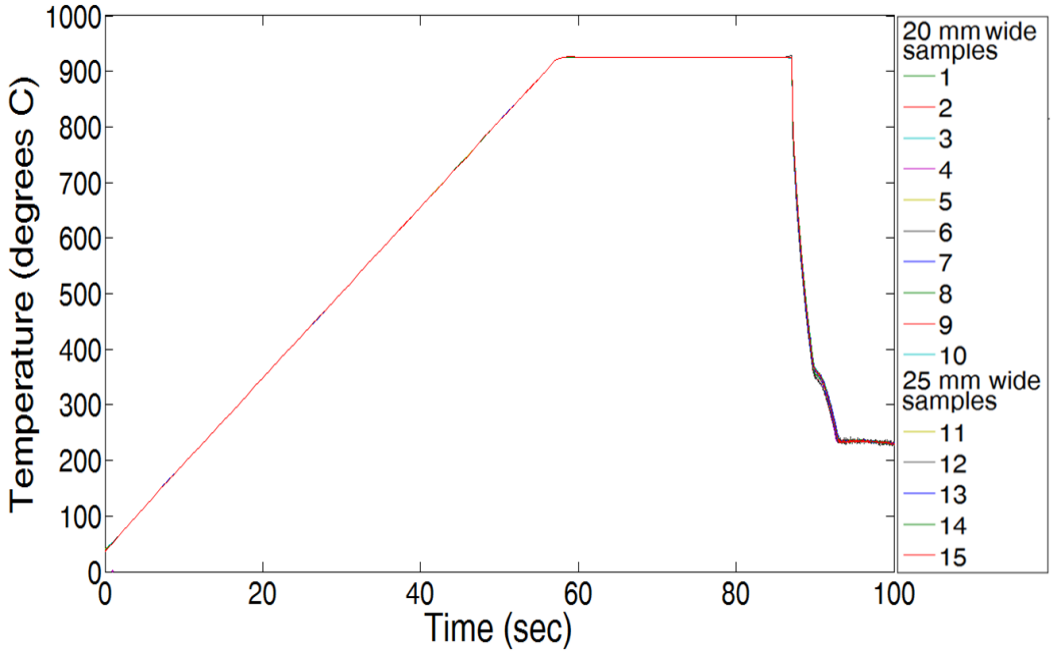

Figure 6.3.3: Temperature - time curve for point B (925 °C peak temperature). Slow heating regime

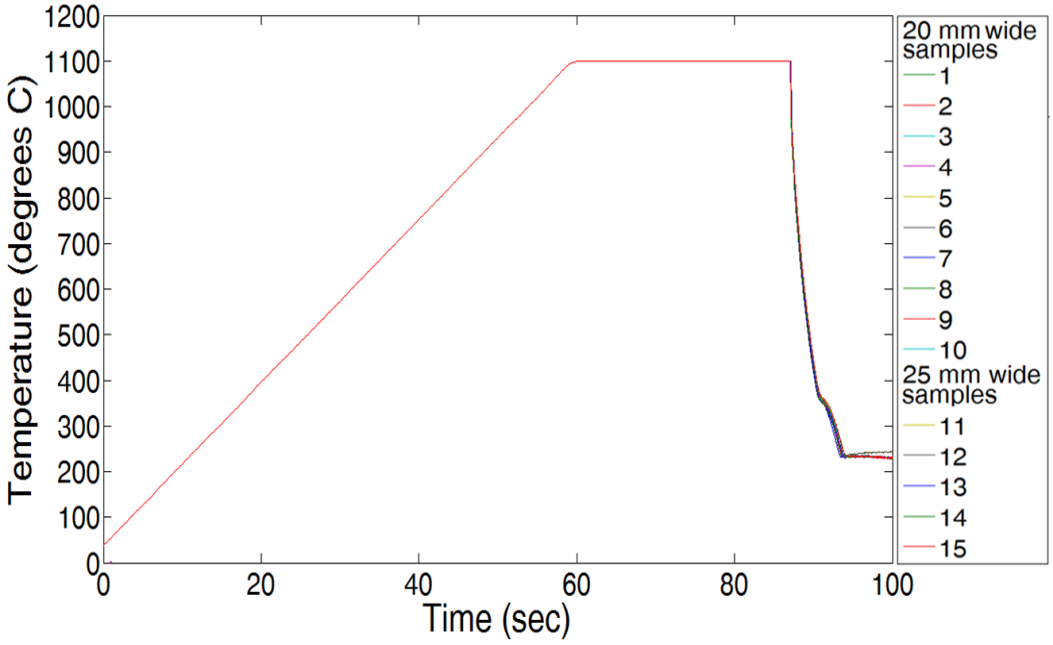

Figure 6.3.4: Temperature - time curve for point A (1100 °C peak temperature). Slow heating regime

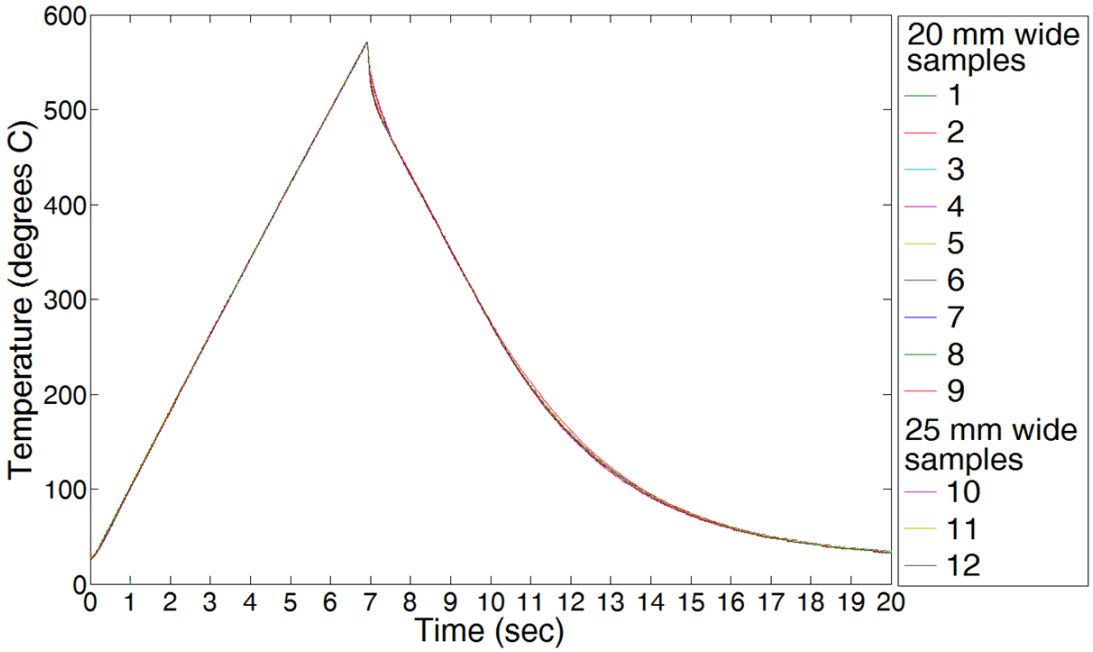

Figure 6.3.5: Temperature - time curve for point D utilising the fast heating rate (575 °C peak temperature). Fast heating regime

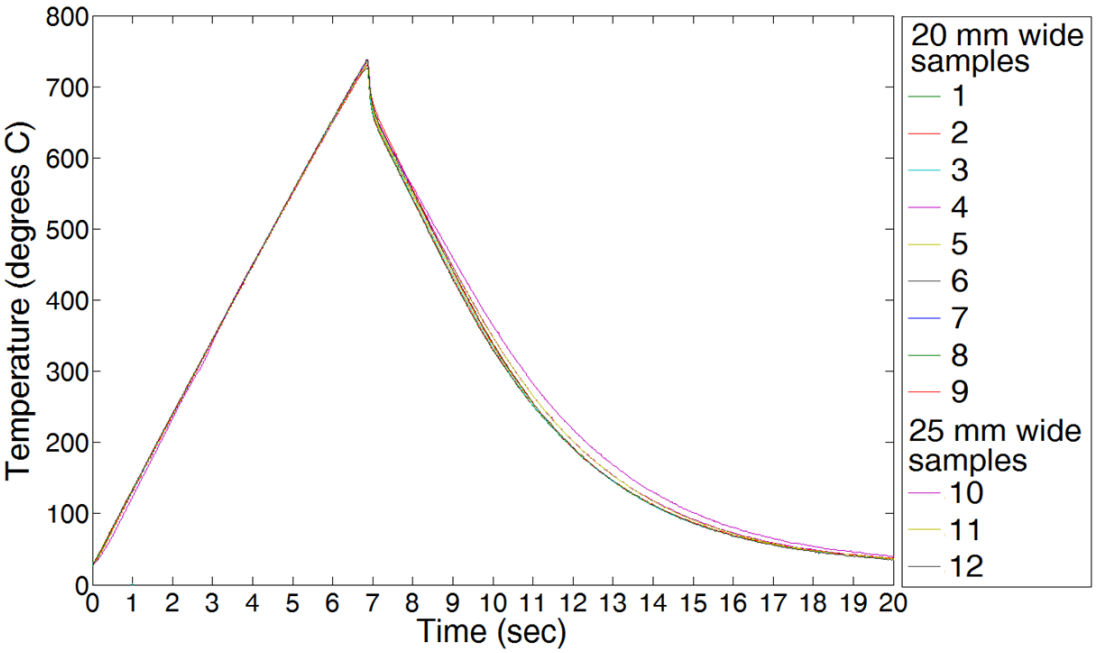

Figure 6.3.6: Temperature - time curve for point C utilising the fast heating rate (725 °C peak temperature). Fast heating regime

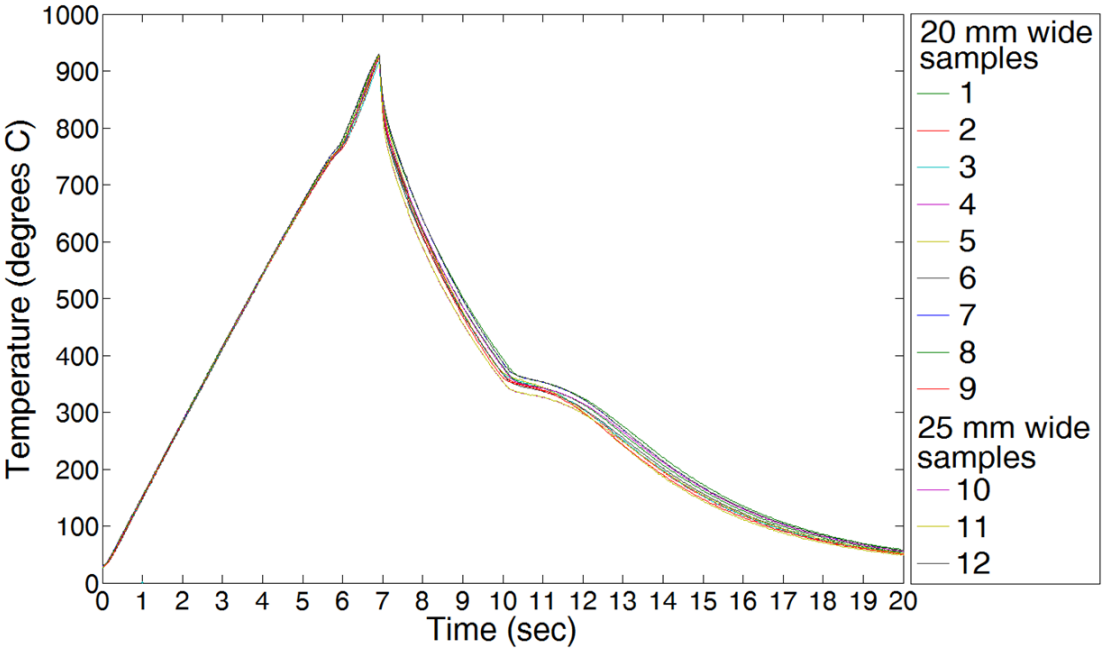

Figure 6.3.7: Temperature - time curve for point B utilising the fast heating rate (925 °C peak temperature). Fast heating regime

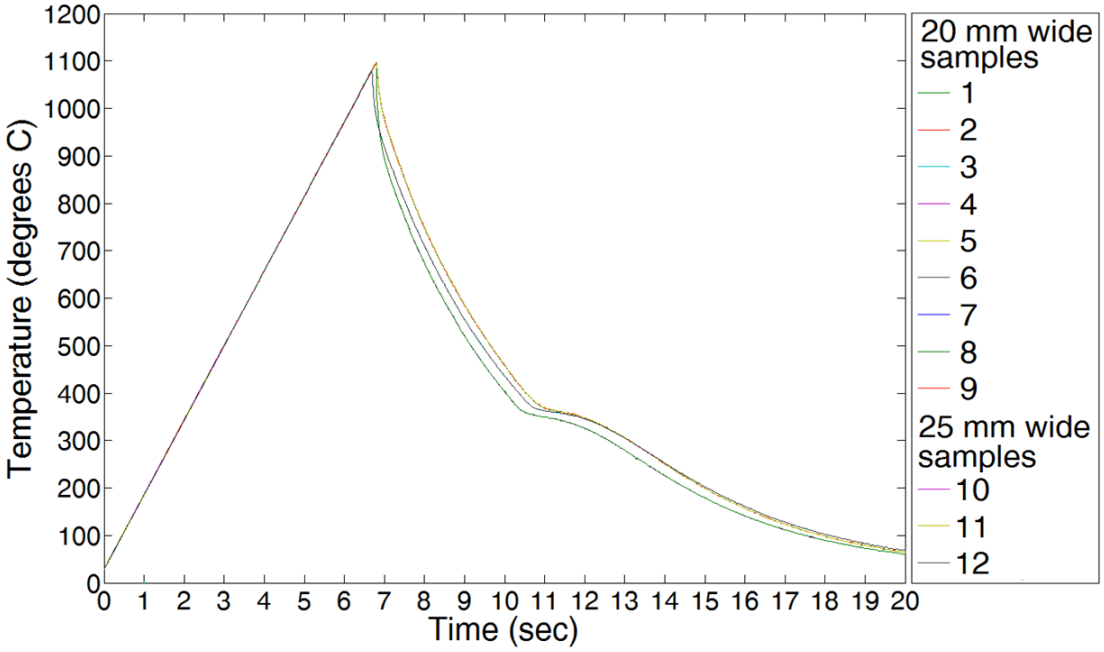

Figure 6.3.8: Temperature - time curve for point A utilising the fast heating rate (1100 °C peak temperature). Fast heating regime

6.3.3 Cooling rates

As all samples in both the slow and fast heating regimes achieved their peak temperatures, and the cooling parameters were unchanged between the slow and fast runs, negligible differences in the cooling curves were seen between both regimes. Therefore, the cooling curves for the slow heating regime as presented, for illustrative purposes.

A close-up view of all the cooling regimes can be seen in figures 6.3.9 to 6.3.12. As previously mentioned, the air quench system was set to the maximum 8.5 MPa pressure setting to achieve the maximum cooling rate. As the peak temperature increases, the actual cooling rates deviate further away from the target cooling rate. For the peak temperatures above the austenitising temperature, an inflection in the curve can be seen towards the end of the cool time. This is most likely due to latent heat release from the martensitic transformation [25, 131].

The fact that the bump occurs at the martensite start temperature strongly suggests this is the case. Nikravesh *et al* [132] performed cooling rate experiments on boron steel in the range of 100 °C/s to 1.5 °C/s. For cooling rates achieved in this work, their findings correspond to martensite start temperatures in the range of 460 - 400 °C and martensite finish temperatures in the range of 270 - 250 °C.

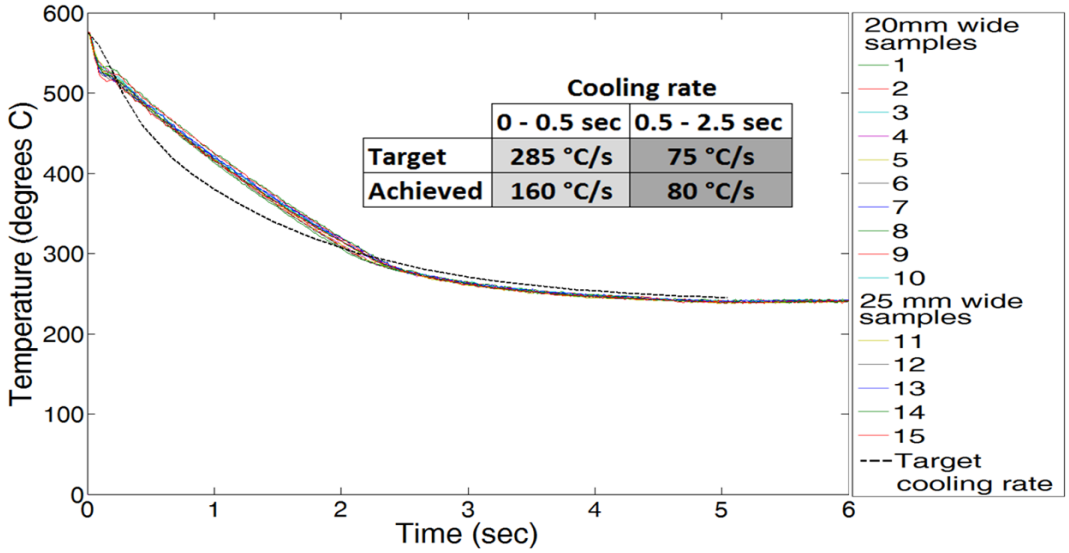

Figure 6.3.9: Cooling curves of point D (575°C peak temperature).

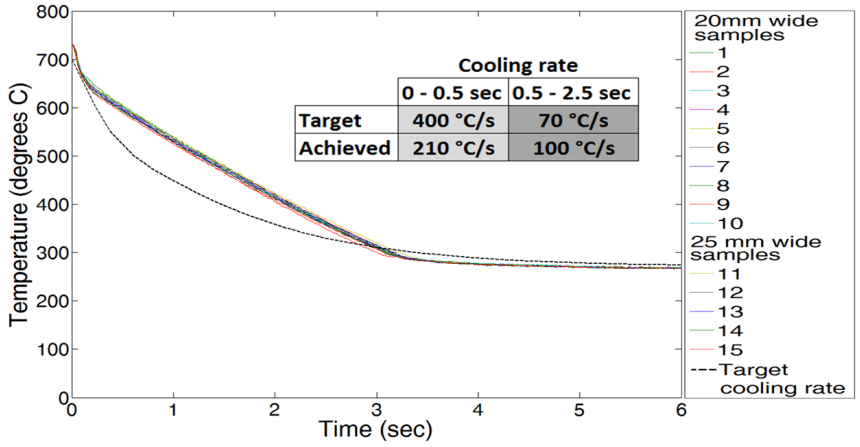

Figure 6.3.10: Cooling curves for point C (725°C peak temperature).

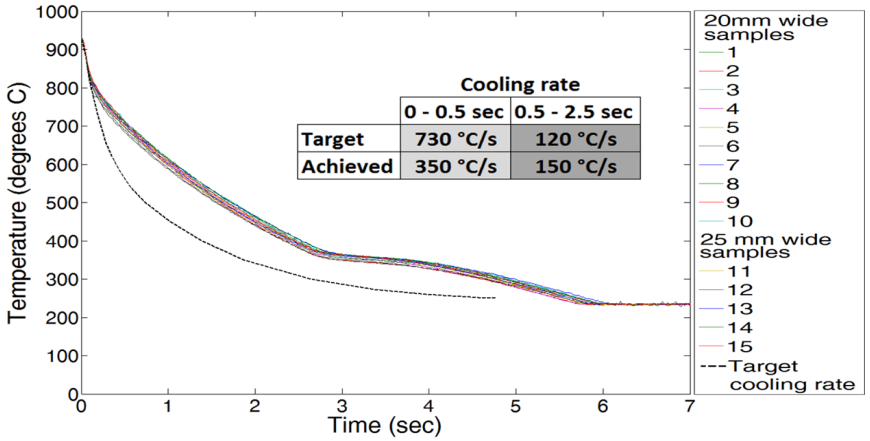

Figure 6.3.11: Cooling curves for point B (925°C peak temperature).

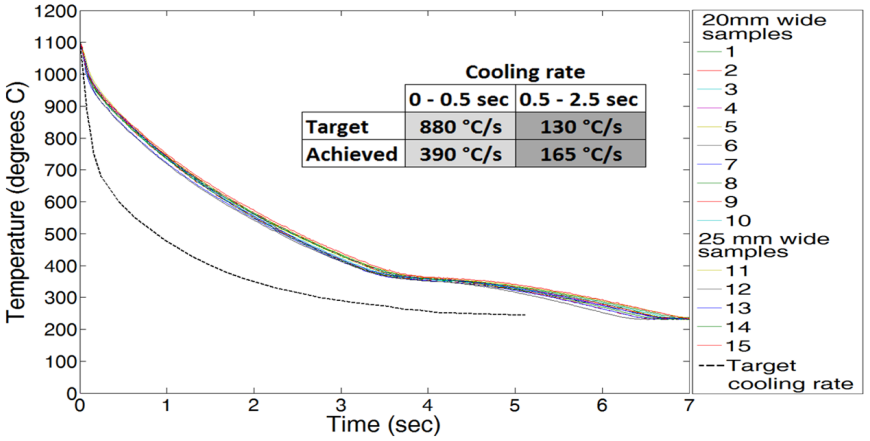

Figure 6.3.12: Cooling curves for point A (1100°C peak temperature).

6.3.4 Thermal gradients across samples

The thermal gradients across the samples were investigated by attaching thermocouples in the centre of the sample and at 10 mm, 15 mm and 20 mm from the centre thermocouple. A final thermocouple was attached at the edge of the sample, midway along the length, as indicated in figure 6.3.13. Three repeats of each peak temperature regime for both the 20 mm and 25 mm wide samples were performed.

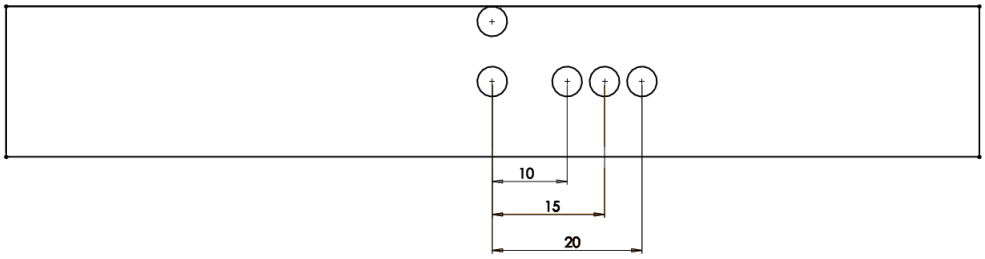

Figure 6.3.13: Thermocouple locations on Gleeble samples. All indicated values are in mm.

Negligible differences were found between the 20 mm and 25 mm wide sample, hence for conciseness, only the results from the 20 mm wide samples are presented in figure 6.3.14. The figure shows the temperature difference between the central sample temperature and the temperature at the indicated distance from the sample centre for both the slow and fast heating regimes.

For all heating regimes and all peak temperature regimes, the difference in peak temperature increases further away from the sample centre. The slow heating regime exhibits the biggest differences. This is most likely due to the slow heating rate allowing time for temperature distributions to form. The fast heating regime exhibits significantly reduced differences in peak temperature along the sample lengths.

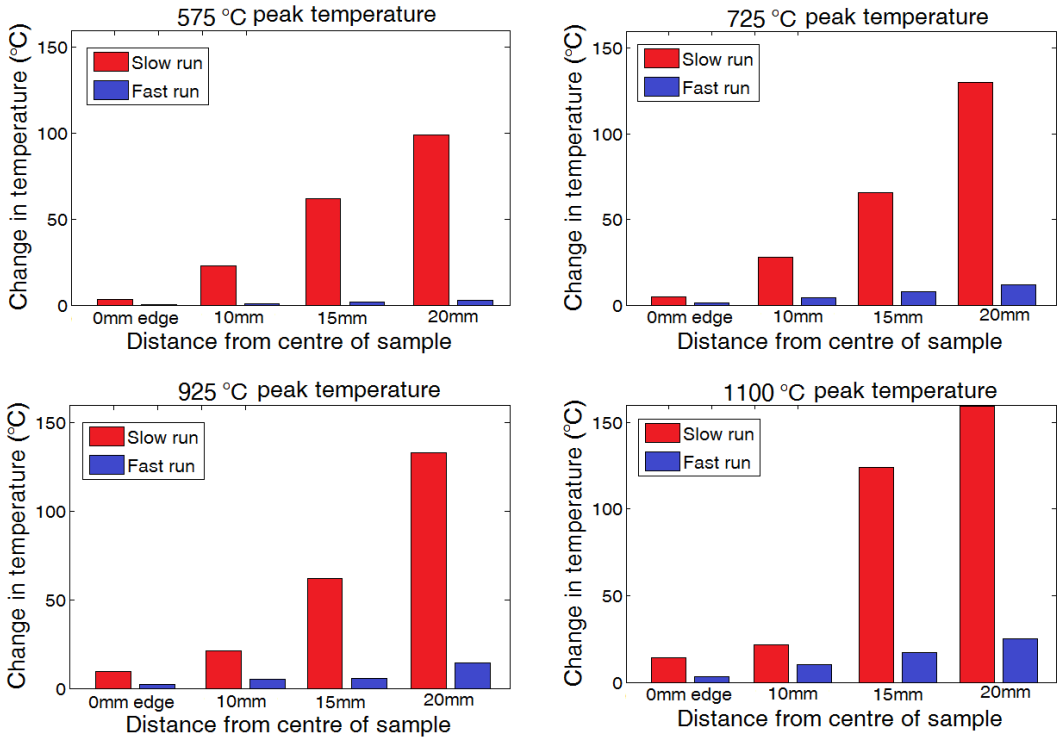

Figure 6.3.14: Differences in peak temperature between central sample location and various locations along sample length for the slow and fast heating regimes (20 mm wide samples)

6.3.5 Hardness distribution across samples

For each of the peak temperature regimes in the fast and slow heating regime, one of the 20 mm wide samples and one of the 25 mm wide samples were measured, with three measurement lines performed across each sample. The indents were performed at 1 mm intervals. Considering that there was minimum variation in the measured temperature-time curves between samples, measuring the hardness of one representative sample is reasonable and efficient. The difference in hardness distribution between the two widths (20 mm and 25 mm) was negligible, hence the results from the two widths were combined to give an average. The results from the slow heating regime are shown in figure 6.3.15.

The dog-bone specimen, which will be cut out from the Gleeble rectangular samples,

has the longest gauge length of all specimens considered, hence the geometry (which is scaled to correlate to the the x-axis of figure 6.3.15) is included in the figure to indicate how the homogenised zone corresponds to the specimen to be cut. For all temperature regimes, it can be seen from figure 6.3.15 that a relatively flat hardness distribution exists between -10 and 10 mm.

The hardness distributions of the samples from the fast heating regime are shown in figure 6.3.16. A more extensive homogeneous hardness distribution can be seen in the sample centres.

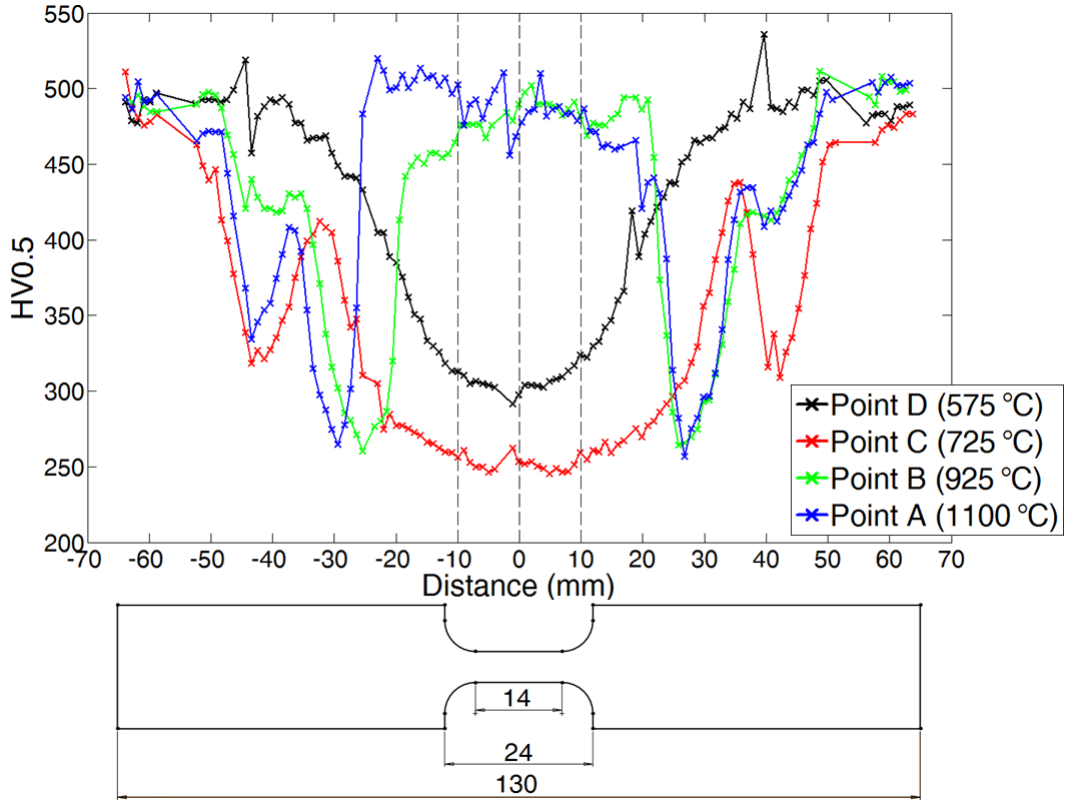

Figure 6.3.15: Hardness profile along Gleeble sample length produced with slow heating regime. Tensile specimen to be cut out at scale of graph.

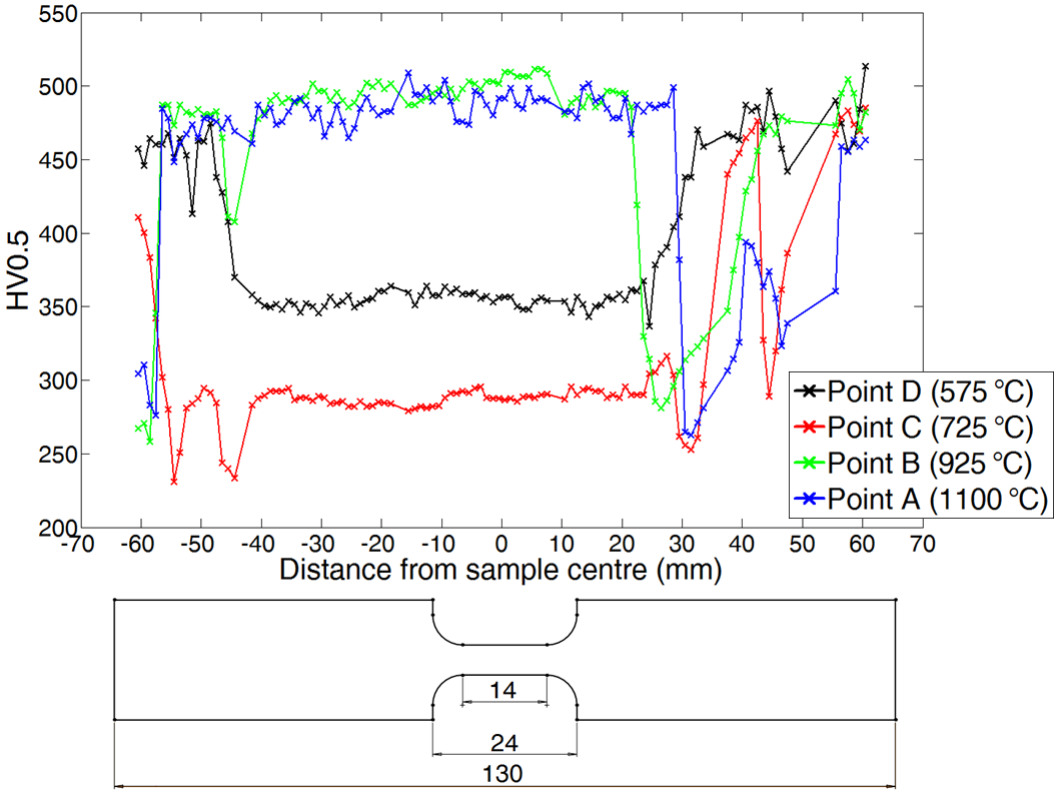

Figure 6.3.16: Hardness distribution across heat treated samples for fast heating rate.

6.4 Discussion of results

The main interest from the thermocouple tests was whether a homogeneous temperature distribution had developed along the sample length. This would lead to a homogeneous microstructure in the gauge length of the destructive samples to be cut out from the rectangular physical simulation samples. The information presented in section 6.3.4 implied that the samples produced from the fast heating regime exhibit a larger area of homogeneous microstructure in the central region than those produced from the slow heating regime. The data also showed that minimal temperature variation occurred from the sample centre towards the edge.

Hardness measurements were performed to verify that a homogeneous microstructural zone had developed. The samples produced with the fast heating regime exhibited a

more extensive homogeneous hardness distribution than those produced from the slow heating regime. It is assumed that the heating rates associated with the slow heating regime combined with extended time at peak temperature has led to a greater variation in temperature across the sample length, giving more variation in the tempered properties.

The striking conclusion is that the slow heating regime is not suitable for physical simulation to create destructive specimens for the creation of a fracture locus. The hardness distribution at the edge regions of the samples will not affect the tensile test results significantly, as they fall well within the grip length. An in-depth discussion of the difference in hardness between the weld and corresponding physically simulated samples is given in the next chapter.

6.5 Final fracture specimen dimensions and production

The hardness distribution was utilised to validate the choice of the fracture specimen designs, to be cut from the rectangular physical simulation samples. The tensile specimens were designed with a gauge length of 10 mm. This means that a homogeneous microstructure exists within the gauge length. The final fracture specimen schematic diagrams are shown in figure 6.6.1.

A clarification on the plane strain specimen is given. Notched round bar specimens are normally used for plane strain testing, where the transverse dimension is sufficiently larger than the axial dimension [118, 119]. For sheet materials, similar geometries as presented in figure 6.6.1 b) have been utilised by many authors to produce near-plane strain tension testing [119, 133, 134, 135, 136]. Such a specimen gives a theoretical triaxiality of $\eta = 0.52$, which lies between uniaxial ($\eta = 0.333$) and plane strain ($\eta = 0.577$) [136]. It can be seen that such a specimen cannot strictly be called a *plane strain* specimen. However, the term has become associated with such a sheet specimen by many authors [119, 133, 134, 135, 136].

The rectangular physical simulation samples were cut via Electrical Discharge Machining (EDM). EDM has been successfully utilised to produce specimens with minimal heat input [137]. An attempt at producing the samples by waterjet cutting resulted in tapered surfaces. These tapered edges might affect the sample response during destructive loading, hence this technique was not used.

6.6 Conclusions

The aim of this chapter was to obtain rectangular steel samples with a sufficiently large area of homogenised microstructure to be able to perform destructive tensile testing. The obtained microstructures should be as close to the target microstructures as possible. This is achieved by reproducing the thermal histories experienced by the target HAZ areas. The Gleeble set-up provides limitations as to how accurately the thermal histories can be reproduced.

Temperature histories of specific points throughout the weld were extracted by simulating the weld schedule in the SOPRAS FEA program. These temperature histories were subsequently used to drive Gleeble physical simulations to recreate the microstructure of the previously defined points. The stainless steel half-contact Gleeble grips were selected so as to maximise the volume of homogeneous microstructure in the sample centres. The target peak temperatures were consistently reached for all samples, however the target heating and cooling rates could not be accurately recreated. This is due to the fact that half-contact grips are not designed for very fast heating rates and the air pressure for the cooling system was at the maximum level and hence the cooling rate could not be increased.

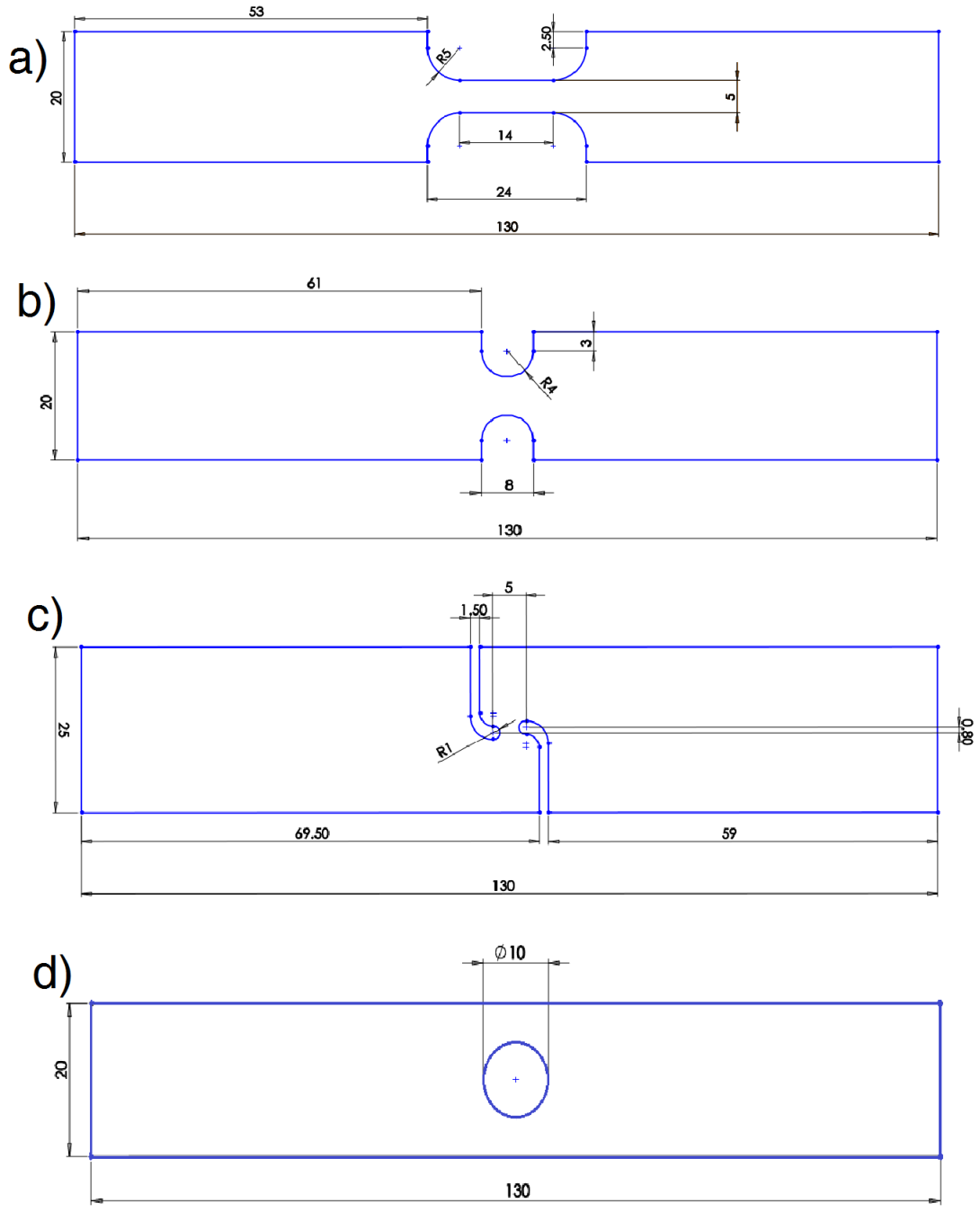

Figure 6.6.1: Final tensile specimen designs. All dimensions shown in mm. a) Tensile dog-bone b) Plane-strain c) Shear d) Uniaxial central-hole

The samples produced through the fast heating regime showed a large area of consistent

hardness values, which were inferred to mean consistent microstructure. The samples produced through the slow heating regime showed steeper hardness gradients along the sample lengths. It was concluded that the initial idea of using a slow heating rate combined with a dwell at peak temperature to ensure homogenisation was incorrect. In fact, a faster heating rate with minimal time at peak temperature resulted in a larger volume of consistent microstructure. This is most likely due to the heat not being able to distribute and form gradients along the sample length. This observation was corroborated by measuring the temperature gradients along the sample lengths. The fast heating regime showed temperature differences between the sample centre and the far-field approximately 5 times lower than the slow heating regime.

Chapter 7

Stress-strain and failure loci extraction

7.1 Introduction

In the previous chapter, two heating regimes were used to physically simulate certain weld microstructures by attempting to reproduce the thermal history experienced by those weld sections. From these samples, tensile destructive geometries were cut, namely dog-bone, shear, plane-strain and central-hole geometries. In this chapter, these samples are destructively tested in a uniaxial tensile testing machine. Through Digital Image Correlation (DIC), material properties such as fracture strain, stress state and stress-strain response will be measured. The measured fracture strain and stress state will be used to construct failure loci. The aim of this chapter is therefore to obtain failure loci and stress-strain curves to be used as input to FE models for modelling weld failure.

7.1.1 Live strain measurement through Digital Image Correlation

DIC is an optical method which employs tracking techniques to measure changes in an image. For strain measurement, the deformation of a small grid is calculated, where the grid typically measures 15 pixels across. To enable the image processing to calculate the strain, there must be random spots of contrasting colour within each grid. To achieve this requirement, the sample is coated with two layers. The first layer is a solid

black coat. The second layer is a random white speckled pattern, normally applied with an airbrush. Samples with the two layers are shown in figure 7.1.1.

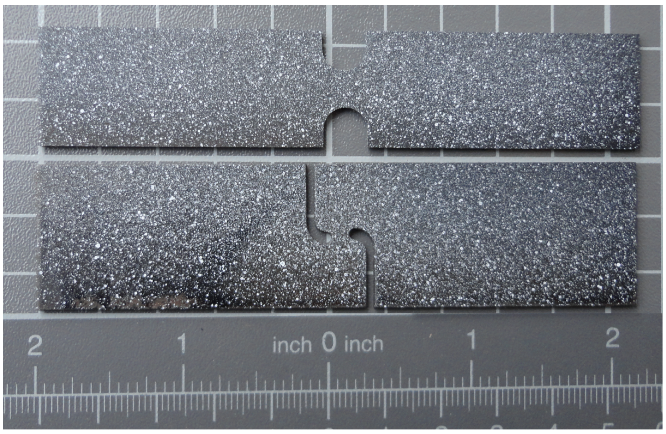

Figure 7.1.1: Plane-strain and shear fracture specimens coated with speckled paint for DIC measurement.

The measurement resolution is determined by the resolution of the camera and lens. Throughout all tests, a Photron SA1.1 high speed camera, with a resolution of 1024 x 1024 pixels was used. To avoid scale effects from one sample to another, a fixed focal length 180 mm macro lens was used, meaning that the same field of view was used in all tests.

The number of pixels used to build a grid in the DIC software may lead to variations in the strain measurement. An investigation on the effect of the number of pixels in a grid was performed by Beaumont [119]. The author looked at grid sizes ranging from 5 to 100 pixels. It was seen that, as the grid size decreased from 100 to 30 pixels, the measured strain increased. Grid sizes of 30 pixels and below showed a convergence in measured strain. The author also found that a significant amount of noise was measured for the smallest grid size of 5 pixels. It was therefore recommended, as a compromise between noise and accuracy, that grid sizes of 15 pixels be used.

Another factor to consider is the location that strain and alpha are measured on the fracture specimen. All fracture specimens have a large area of constant strain levels, with some uncertainty in the precise location of fracture. The choices of measurement

locations are either a point source or an average or maximum of an area. Taking strains from a defined area will be considered first, where the area would encompass the band of consistent strain across the gauge width of the specimen. An advantage of this method is that, even as the pattern distorts at high strain and individual grids are lost by the DIC program, the overall strain would still be detected, however, the fracture strain measured in this manner might not have physical meaning, as it would not be local to the site of fracture initiation.

Measuring from a single point offers the advantage that fracture strain is measured at the point of fracture initiation and is not averaged, which would lead to an underestimation in fracture strain. A disadvantage is that, at high strains, the speckled pattern might become too distorted for the software to perform calculations. It was concluded to take measurements from a single point, as this offers the most physically meaningful strain and alpha measurements.

7.1.1.1 Errors

There are two main error sources associated with two-dimensional DIC measurements. These are related to translations or rotations out of the plane on which the DIC system assumes all images lie. These movements distort the apparent size of a feature and hence introduces an artificial strain. For clarity, this feature would contain a group of pixels making up a grid that corresponds to light and dark speckles.

As a specimen is axially strained, the resulting lateral contraction would cause an out of plane translation. An out of plane rotation would result from the camera not being perfectly aligned to the specimen plane. Figure 7.1.2 a) illustrates the translational movement. In this figure, the line AB describes a feature of length a. The distance from the camera to the feature is l and the translational movement out of the measurement plane is m. As the feature moves further away it will appear smaller, and the DIC system will interpret this as a compressive strain.

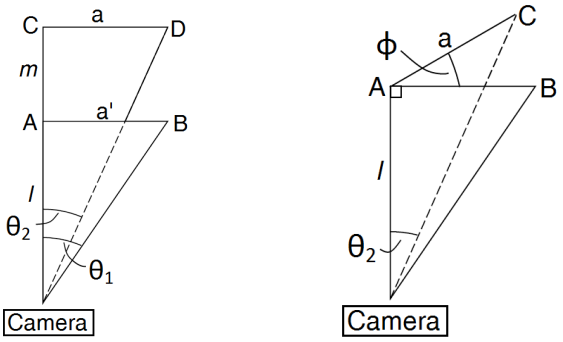

(a) Translational movement of a feature out of the measurement plane

(b) Rotational movement of a feature out of the measurement plane

Figure 7.1.2: Schematic illustrations of translational and rotational sources of error in DIC strain measurement. Taken from [119]

Beaumont presented an equation for an indication of the uncertainty to be expected from DIC measurements resulting from translational movements:

$$e_{trans} = \frac{m}{m+l} \tag{7.1.1}$$

In Beaumont's work, a measuring distance of 0.3 m was assumed, with an out of plane translation of 1.5 mm (corresponding to the sample's thickness), giving an apparent strain of 0.005. This would be a worst case scenario for overestimating the strain. Figure 7.1.2 b) illustrates a feature AB rotated through an angle ϕ. The geometrically derived error calculated by Beaumont is given below:

$$e_{rot} = 1 - \frac{l\cos\phi}{a\sin\phi + l} \tag{7.1.2}$$

Again, assuming a measuring length of 0.3 m, a feature length of 0.1 mm and a rotational error of 5 °, the apparent strain is 0.004. These considerations give the worst case scenario for errors.

7.1.2 Tension testing

The heat treated samples were gripped in a screw driven Instron 5800R tensile test machine with a 100 kN load cell, accurate to ± 25 N. A high speed camera was placed near the specimen, as shown in figure 7.1.3 All samples were loaded at a rate of 1 mm/min. The samples were given an undercoat of black paint and speckle sprayed with white paint as described in section 7.1.1.

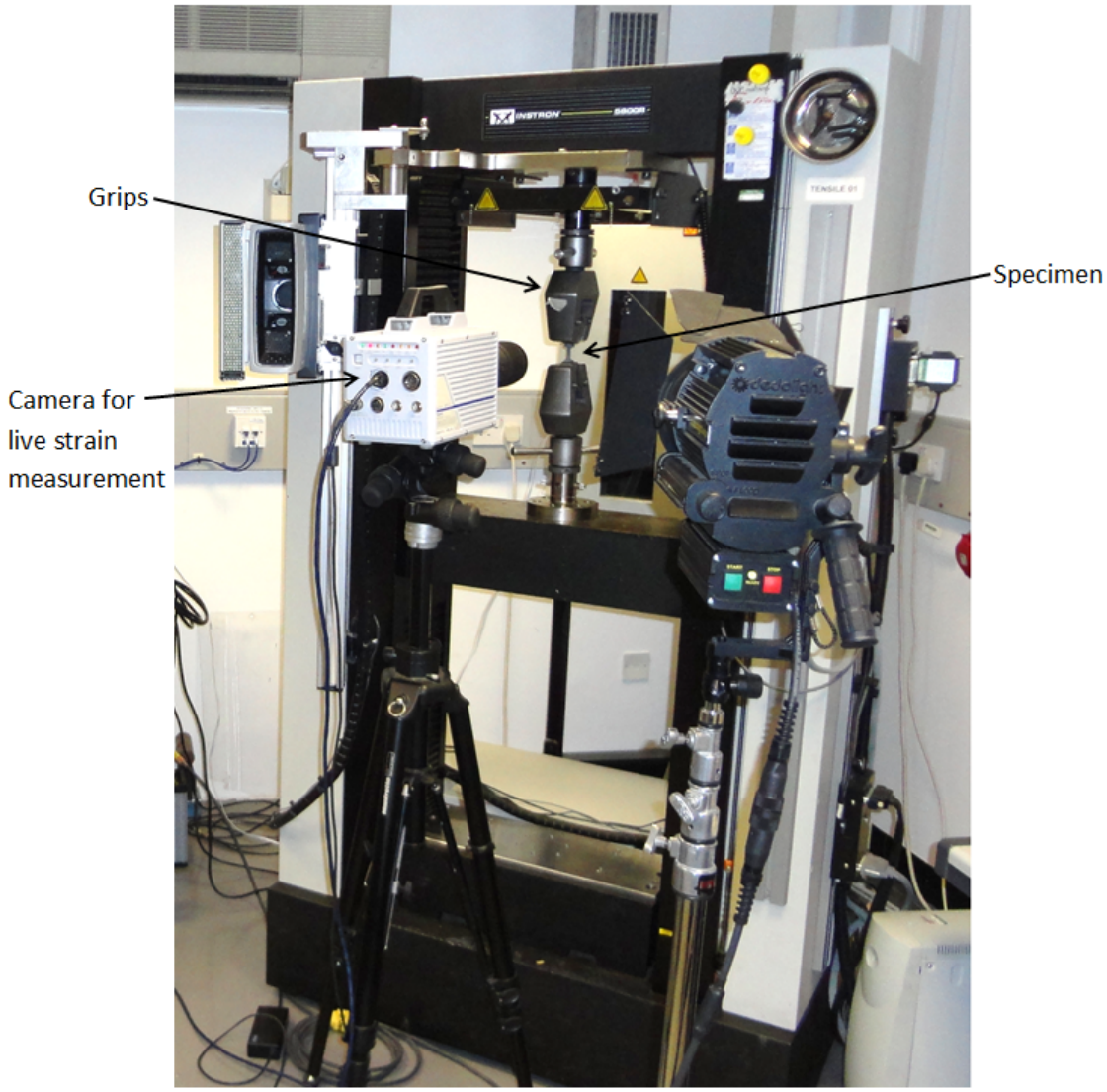

Figure 7.1.3: Instron 5800R with DIC setup.

7.2 Extracting stress-strain curves

For an accurate description of the plastic behaviour of the material in the FE model, measured stress-strain curves can be directly loaded into the material model. Therefore it was deemed appropriate to extract the curves from the Gleeble samples. The tensile samples gauge lengths were too small to be able to attach an extensometer; instead the DIC software was used as a virtual extensometer. Beaumont [119] performed a comparison between strain results from a physical extensometer, a virtual extensometer consisting of 2 points just inside the physical extensometer clips, an average strain across the whole surface inside the extensometer and finally the peak strain taken at the fracture location.

It was found that all 5 strain measurements agree up to the necking point. Beyond that, the effects of local and global measurements become evident. The author found that the virtual extensometer and gauge area (global measurements) exhibited a slightly higher post necking strain than the physical extensometer, due to operating on a shorter gauge length. The locally measured strain reached higher strains than is typical for a tensile test. From these results, it was decided to employ the "area strain" technique, as it compared favourably to a physical extensometer. For all tensile samples, an average true strain was taken within a length of 10 mm.

A total of 20 tensile samples were produced from the slow heating run, with five repeats for each of the four peak temperatures. A total of 12 samples were produced from the fast heating run, with 3 repeats for each of the four peak temperatures.

7.2.1 Results

Figures 7.2.1 and 7.2.2 show the average engineering stress-strain curves extracted from all tests. In the figure, the legends indicate the peak temperature experienced during Gleeble heat treatment.

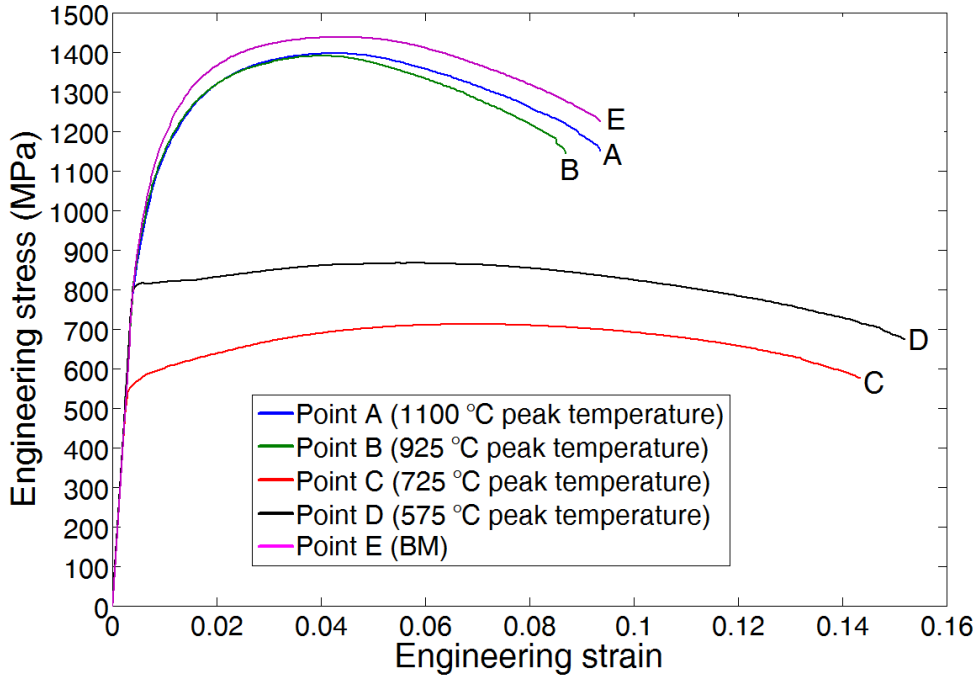

Figure 7.2.1: Engineering stress - strain curves obtained from Gleeble heat treatment runs using slow heating regime.

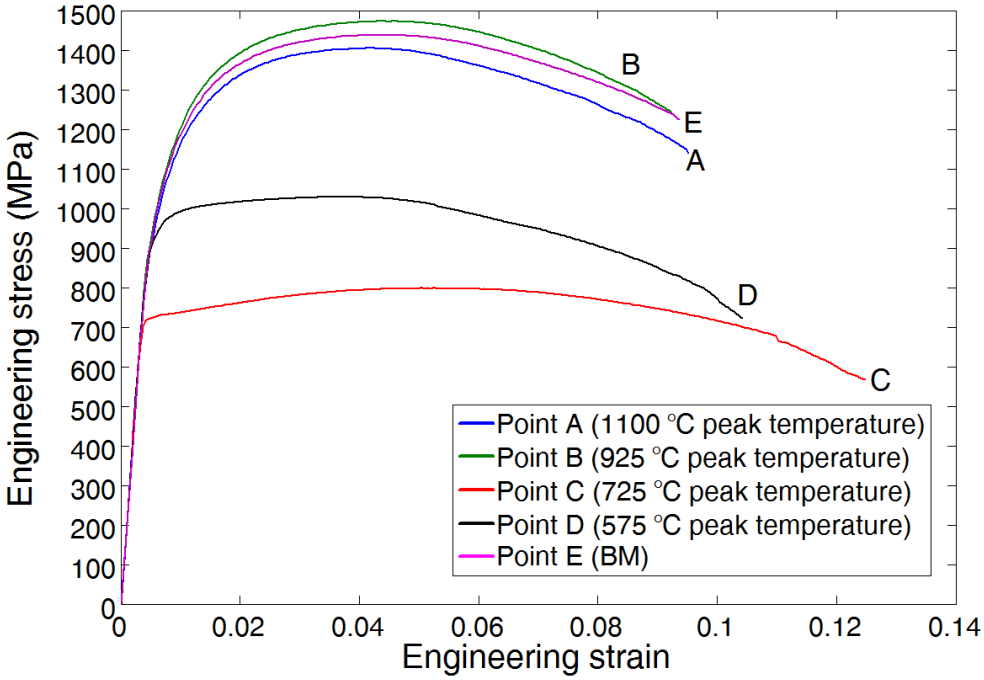

Figure 7.2.2: Engineering stress - strain curves obtained from Gleeble heat treatment runs using fast heating regime.

As can be seen in both figures, all heat treated samples show ductile behaviour. The samples heated beyond the A_{c3} temperature exhibit lower failure strains and higher UTS values than the tempered samples, which were heated to peak temperatures of 575 °C and 725 °C.

7.3 Extracting fracture strain and alpha values

7.3.1 Fracture location

The purpose of this section is to create the $\varepsilon_f - \alpha$ failure loci specific to the previously defined HAZ coordinates. As previously discussed, 3 destructive geometries were utilised; shear, plane-strain and uniaxial with central hole samples. Strain was extracted from the grid at the fracture location. Beaumont [119] performed an investigation, using high speed photography, to establish the fracture locations of the destructive specimens.

For the plane-strain sample, it was found that fracture occurs in the sample centre. For the uniaxial sample, it was found that fracture occurs at the free edge of the hole. It was stated that the crack could initiate at the surface either facing away or towards the camera. However, it was observed that the crack grows much faster through the sheet thickness than the width. From this, it was concluded that measuring fracture strain from the hole edge was appropriate. For the shear sample, the author was not able to observe crack opening or spreading, as could be done in a mode I tensile crack. From this, Beaumont determined the failure mode is a shear in-plane mode II crack. It was therefore recommended to take the failure strain from "the broad central region of even strain" [119]. These locations are shown in figure 7.3.1. The alpha values were extracted from the same points.

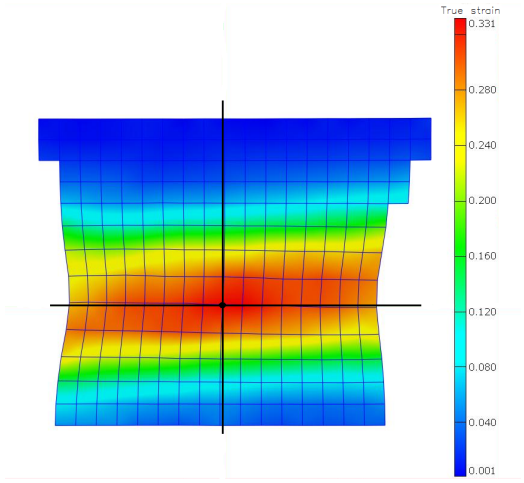

(a) Plane-strain sample

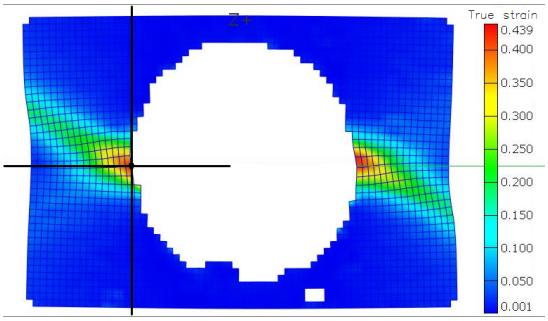

(b) Uniaxial sample

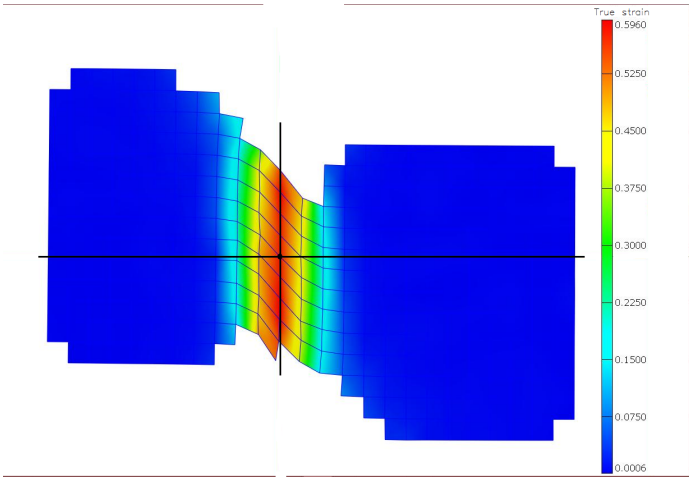

(c) Shear specimen

Figure 7.3.1: True strain distributions of fracture geometries with black crosses indicating fracture strain measuring locations

7.3.2 Alpha values and failure locus construction

Figure 7.3.2 shows the evolution of alpha as the plane-strain specimen is put under tensile load, with large oscillations visible at the start. As $\alpha = \varepsilon_2/\varepsilon_1$, these large oscillations are due to small ε_1 values and associated rounding errors at the beginning of loading. An example is taken from Beaumont [119] to explain this. If the principal strains at fracture are arbitrarily $\varepsilon_1 = 0.33 \pm 0.0015$ and $\varepsilon_2 = -0.021 \pm 0.0015$, then $\alpha = -0.064 \pm 0.0046$. If the uncertainty remains unchanged, but the strains are reduced by two orders of magnitude (associated with the beginning of loading), then $\alpha = 0.064 \pm 0.46$. From this example, it can be seen that large oscillations are present at lower strains and must be removed before calculating the characteristic alpha value.

Additionally, as can be seen from the figure, alpha is not constant with time. Therefore, as proposed by Beaumont [119] and Bao and Wierzbicki [118], a characteristic value is fitted to the recorded data. Another method of obtaining the alpha value is by taking the value at fracture. However, as stated by Beaumont, this final value might not be the most influential, as the majority of damage done to the specimen may have been under a different state. Therefore a mean of the alpha value is used as a representative value. A MatLab script provided by Beaumont was used to perform the fitting.

Figure 7.3.3 shows how the 3 measured points (within the range -1 < α < 0) were used to create a failure locus. As stated previously, it is assumed that the locus can be approximated by a second order polynomial [118]. As there are not enough test points to accurately model the shape of the locus, the procedure outlined by Beaumont [119] is followed. The theoretical stress state of the plane-strain specimen is α = 0 and would give the minimum of the locus. However, the stress state extracted was approximately 0.15 away from the theoretical value. Therefore, to plot a locus with the minimum at the correct stress state, the data for the uniaxial and plane-strain states were mirrored about α = 0 and a parabolic curve fitted through the 4 data points, as shown in the blue line in figure 7.3.3. From this fitted curve, the strain at the theoretical uniaxial stress state (α = 0.5) and the measured shear point were reflected about α = -1, to create the black curve. This procedure was performed for all samples.

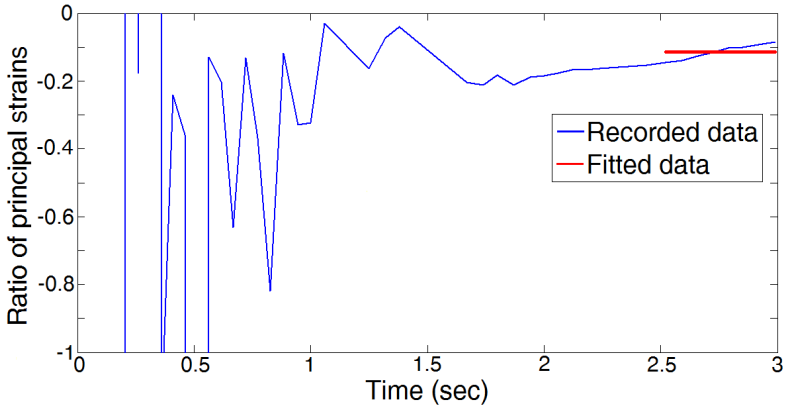

Figure 7.3.2: Alpha against time, showing fitted value

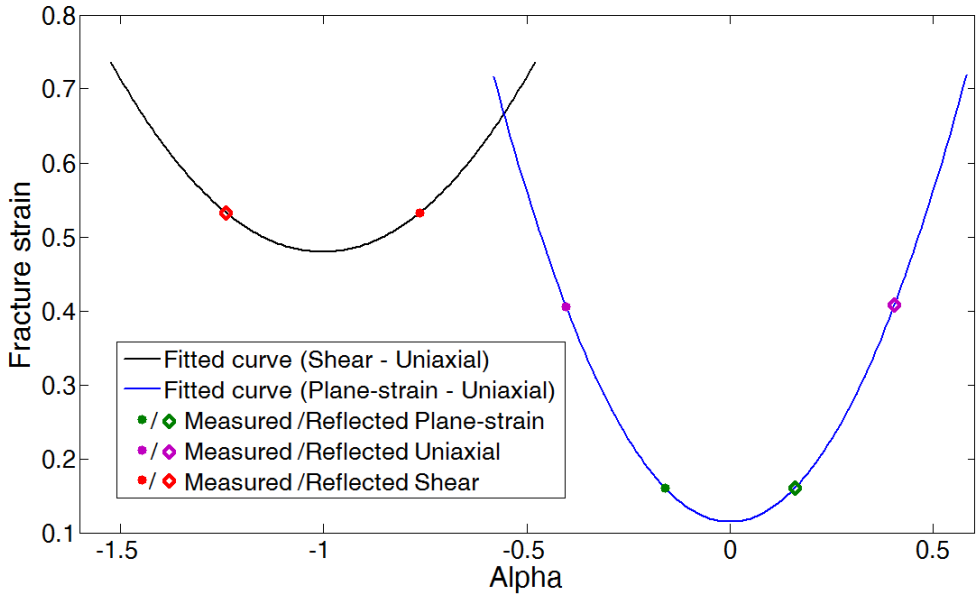

Figure 7.3.3: Example of fitting fracture locus through measured data

Unfortunately, the shear samples from the fast heating Gleeble run were not cut to the specified dimensions, as shown in figure 7.3.4. This was due to a machining error at the EDM cutting facility. This incorrect geometry caused the samples to fail outside the gauge region, giving unusable data. Due to time constraints, it was not possible to repeat the Gleeble runs to obtain fresh shear samples. It was concluded to add the shear results from the slow Gleeble runs to the failure loci of the fast Gleeble runs. This is not ideal, but with the lack of data, this is the closest approximation possible.

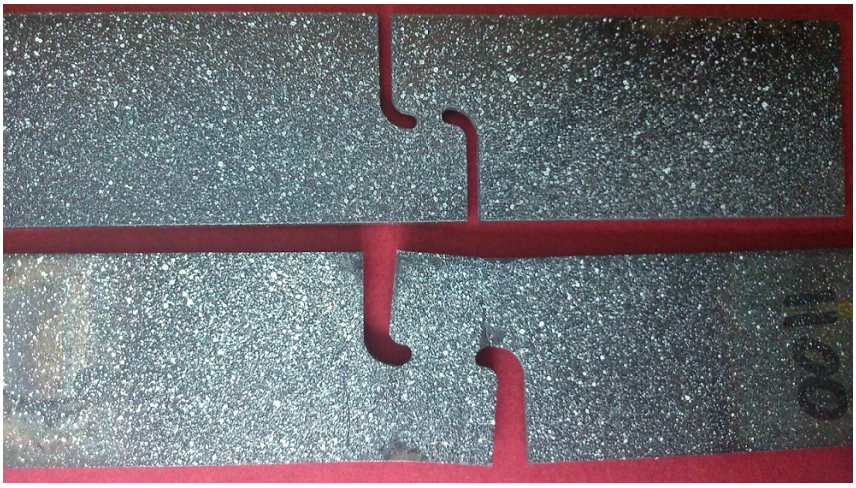

Figure 7.3.4: Incorrect shear specimen (bottom) with correct specimen for reference (top).

7.3.3 Results

Figures 7.3.5 and 7.3.6 show the fitted failure loci of the slow and fast Gleeble runs respectively. The data markers are from the average of 5 and 3 tests for the slow and fast runs respectively. Error bars have been included, showing the standard deviation in measured strain and alpha values. In both figures, the softer samples (575 °C and 725 °C) exhibit larger fracture strains than the harder samples (925 °C and 1100 °C). The near identical curves in the slow run for points A and B is due to extended times spent above the Ac_3 temperature. The same samples in the fast run show a clearer difference in behaviour with respect to each other. Again, this is a consequence of the short time spent at peak temperature, causing the base microstructure to partially transform.

Taking the error bars into account, the tempered samples and austenitised samples are sufficiently separated not to cause concern for overlap of curves. There is, however, potential for some overlap between samples heated to 575 °C and 725 °C. The austenitised curves also exhibit potential for overlap between each other. Hence it should be taken into account that the different weld zones, in reality, may not exhibit as well defined failure loci as presented.

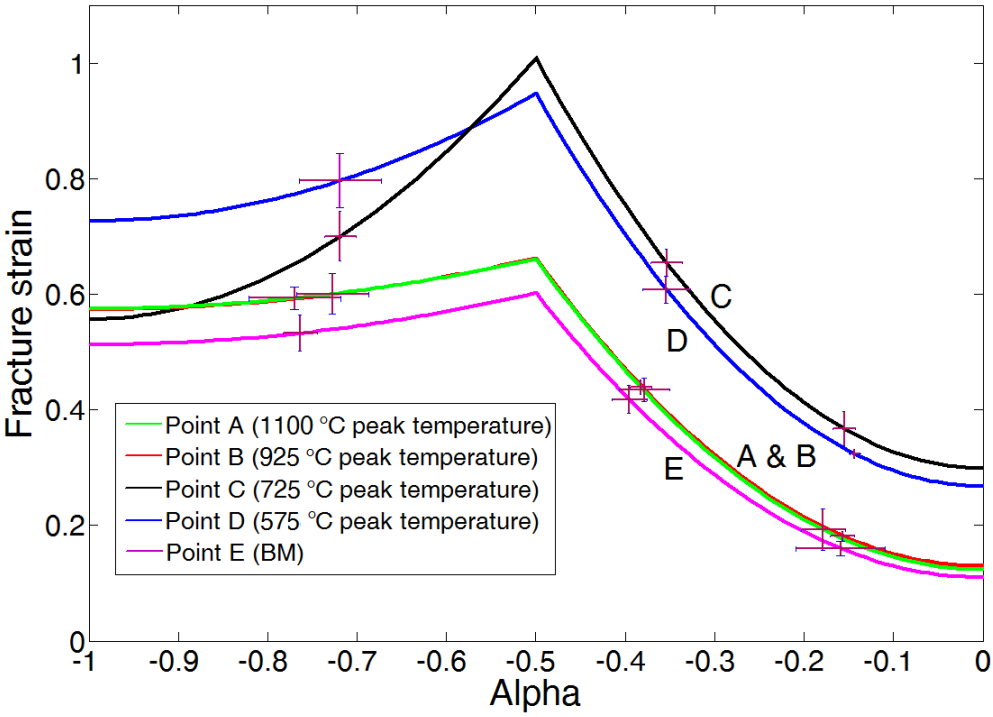

Figure 7.3.5: Failure loci from slow Gleeble runs.

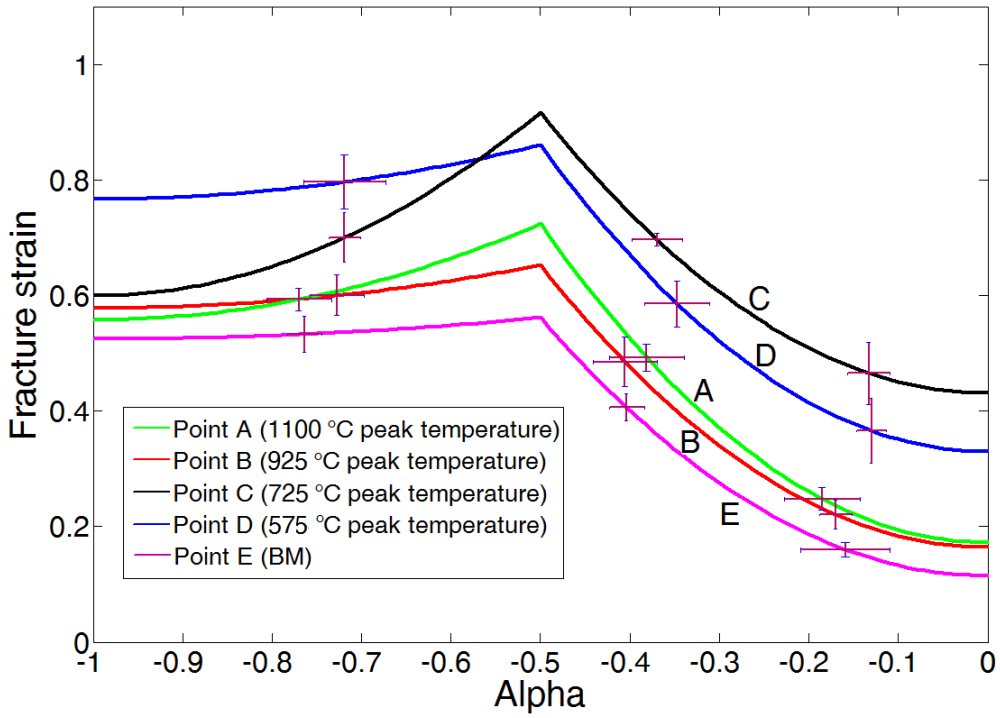

Figure 7.3.6: Failure loci from fast Gleeble runs.

7.4 Comparison of fast and slow heating regimes

The purpose of this section is to establish how accurately the Gleeble samples have been created with respect to their target weld microstructures. From previous sections, it was established that the heating and cooling rates did not match those of the target welding rates, but the extent of this deviation is still not clear.

As mentioned in the introduction chapter, the yield strengths extracted through instrumented indentation will be used as a verification method, along with the weld hardness. After this analysis, a decision will be made as to which Gleeble samples may be disregarded and which samples may be used in the subsequent FE analysis.

7.4.1 Hardness and stress-strain curve evaluation

Figure 7.4.1 a) compares the target weld hardness with the hardness of the physically simulated samples. The hardness values are taken from an average in the range -5 to 5 mm from the sample centre. This length covers the longest gauge length of the four sample geometries, the dog-bone sample. The error bars show the standard deviation within this 10 mm sample length. The error bars for the target weld are the standard deviation from 3 measurements at each location. Figure 7.4.1 b) compares the stress-strain curves of the different heating regimes. These comparisons will help to establish the effects of the different heating regimes in comparison to the target weld regions.

7.4.1.1 Point A

For point A in figure 7.4.1 a), the large error bar for the target value does introduce some uncertainty as to how close the hardness values of the Gleeble samples actually are to the target. However, both the fast and slow heating regime samples exhibit similar *average* hardness values, being approximately 30 HV below the average target value. The corresponding stress-strain curves in figure 7.4.1 b) also exhibit similar

properties. It was previously mentioned that temperature has a greater influence on austenitisation than time. It is clear that, regardless of heating rate or time spent at peak temperature, both samples heated to 1100 °C developed similar stress-strain responses and average hardness values.

7.4.1.2 Point B

Point B in figure 7.4.1 a) shows significant deviations from the target hardness, for both the fast and slow heating regimes. The corresponding stress-strain curves in figure 7.4.1 b) show a greater difference between each other compared to the stress-strain curves of point A.

It was mentioned in the previous chapter that a faster heating rate tends to increase the A_{c1} and A_{c3} temperatures. The effect of this can be seen in the samples associated with point B, which show the greatest deviations from the target hardness. The peak temperature of point B (925 °C) is close to the A_{c3} temperature of 858 °C, so any variation of transformation temperature is likely to have an impact on the amount of austenitisation. From the SORPAS predictions, point B had a target heating rate of 1308 °C/s. This high heating rate is likely to increase the transformation temperatures, leading to less austenite being formed. This can be associated with the lower target weld hardness of approximately 400 HV. The fact that the target weld microstructure also spent much shorter times at elevated temperatures compounds the reduced amount of austenitisation.

The heating rate in the fast heating regime was an order of magnitude slower than the target rate, and the slow heating two orders of magnitude slower. It is possible that these slower heating rates have not affected the transformation temperatures as much, leading to more austenite being formed. This is evidenced by the elevated hardness, resulting from a greater amount of austenite being formed and subsequently being transformed into martensite during cooling. The longer times spent at elevated temperatures also add to the increased amount of austenitisation.

7.4.1.3 Points C and D

The hardness values of points C and D produced by the fast heating regime give better correspondence to the target values than those produced by the slow heating regime. It was shown in the previous chapter, from the work of Furuhara [126], that samples heated at rates of 1000 °C/s and 100 °C/s exhibited similar hardness values. The findings of Furuhara corresponds well with the fast heating regime hardness values of points C and D. The lower hardness values for the slow heating regime samples is due to the samples spending a longer time at elevated temperatures. The lower UTS values and larger failure strains in figure 7.4.1 b) correspond well with a more tempered microstructure.

7.4.1.4 Discussion

It is clear that the samples produced from the fast heating regime give closest correspondence to the target weld hardness values. The samples heated to a peak temperature of 925 °C showed the greatest deviation, for both the fast and slow heating regimes. Sufficient data has been obtained to be able to disregard one of the heating regimes.

The heating rates used in the slow heating regime were two orders of magnitude slower than the target rates. Additionally, a dwell at peak temperature has removed the thermal histories of the samples further away from the target thermal histories. The effect of this is evidenced in the hardness results, which showed the greatest deviation from the target hardness values. Additionally, the hardness distributions along the length of the physically simulated samples, shown in the previous chapter, showed steeper gradients in hardness. The fast heating regime gives the closest correspondence to the target thermal histories, which is evidenced by a closer hardness correspondence to the target hardness values. Additionally, a more extensive area of homogeneous hardness distributions were developed in the samples. For these reasons, the samples produced from the slow heating rate are disregarded in further analysis.

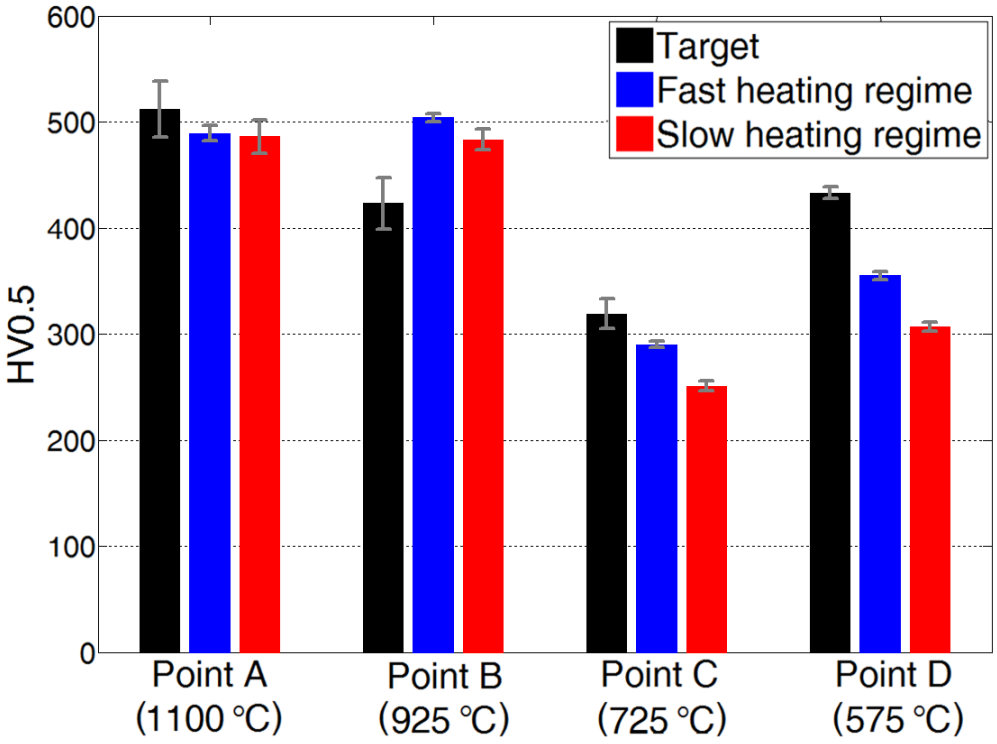

(a) Hardness values of the target weld points and physically simulated samples

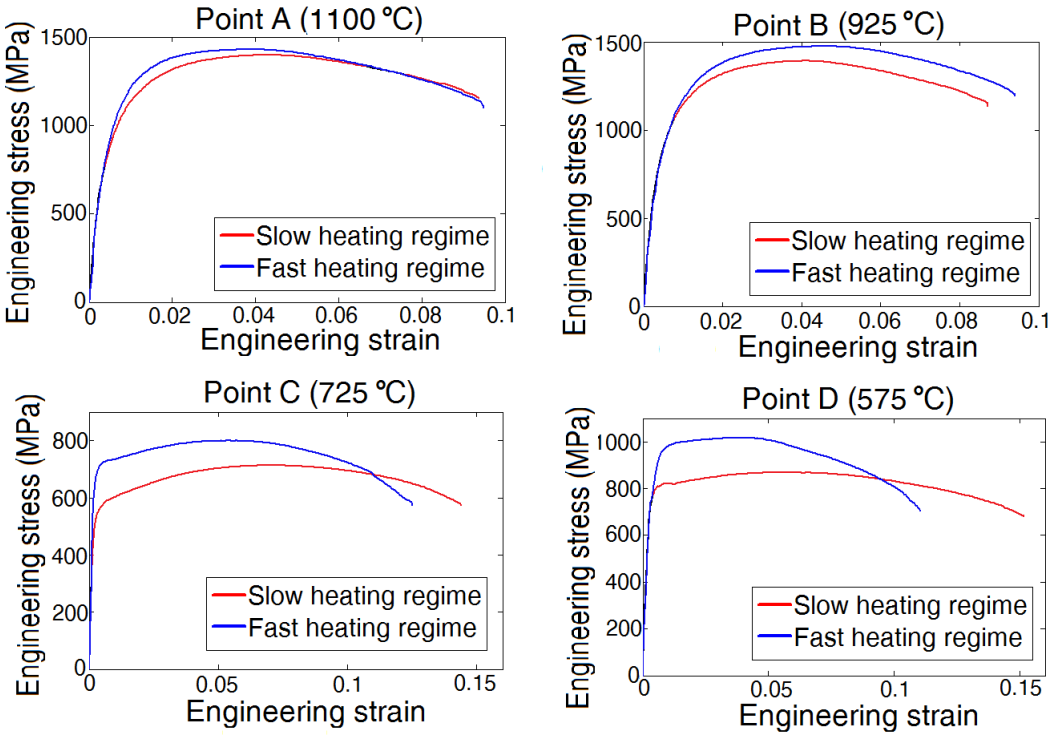

(b) Comparison of engineering stress - strain curves of the slow and fast heating regimes.

Figure 7.4.1: Hardness measurements and stress - strain curves for physically simulated samples produced by the fast and slow heating regimes

7.4.2 Yield strength evaluation

Comparing the yield strengths of the stress-strain curves extracted from the fast heating regime dog-bone samples with the yield strengths extracted directly from the weld using instrumented indentation will add a further verification to whether the HAZ material has been adequately reproduced.

The validity of using the instrumented indentation yield strengths as reference points from which to base the accuracy of the physically simulated samples was established in the results section of the instrumented indentation chapter, where the known boron steel BM yield strength was used as verification. The lower strength and more ductile DP600 results were also used to validate the boron steel soft HAZ indentation results.

Figure 7.4.2 compares the yield strengths calculated from instrumented indentation tests with the yield strengths taken from the Gleeble stress-strain curves for the fast heating regime. In the figure, the black line is the reference from which the deviation of the other lines are measured. As there is no specification in the algorithm [77] used in the instrumented indentation tests as to whether the results correspond to 0% or 0.2% offset yield, both values are presented.

The harder samples (points A and E) at 0.2% offset yield correspond more closely to the indentation results. The softer samples (points C and D) at 0% offset yield correspond more closely to the indentation results. A possible explanation is due to the material behaviour under indentation. For harder materials, an increase in stress has relatively little impact on strain. For softer, more ductile materials, a large change in strain is expected for a relatively small increase in pressure. Considering that all indents were performed under the same pressure, the difference between the more ductile and less ductile behaviour under the same pressure could be a reason for the different yield strength correspondence. Therefore, the 0% offset yield is assumed to correlate well with the softer materials and 0.2% offset yield with the harder materials.

The data points for point B do not correspond well to the instrumented indentation results. Additionally, a large deviation from the target hardness for this point was

shown in figure 7.4.1 a). The hardness and yield strength deviations could be attributed to the effect of heating rate on the A_{c3} temperature and the longer time spent being austenitised. The multiple sets of results that indicate the material of point B was not properly reproduced has reduced confidence in using the material properties extracted from these samples. Thus, the material data extracted from the samples heated to 925 °C has been omitted from further analysis.

Figure 7.4.3 shows the yield comparison with the data of point B omitted. Additionally, the hardness distribution of the physical weld is included to illustrate the gradient of material property variation along the weld. As mentioned previously, the harder samples gave a better correspondence at 0.2 % offset yield and the softer samples a better correspondence at 0% offset yield. The yield strengths of points A and E have thus been taken from the 0.2% offset values and the yield strengths of points C and D from the 0% offset values.

It can be seen that the yield strengths exhibit approximately the same shape as the hardness curve. Point C shows the greatest deviation from the calculated yield strength, with a difference of 120 MPa. This point cannot be disregarded, as it is a critical point in the material distribution through the weld. The other points show much better correlation to the calculated yield strengths. Overall, the reproduced material property distribution seems promising.

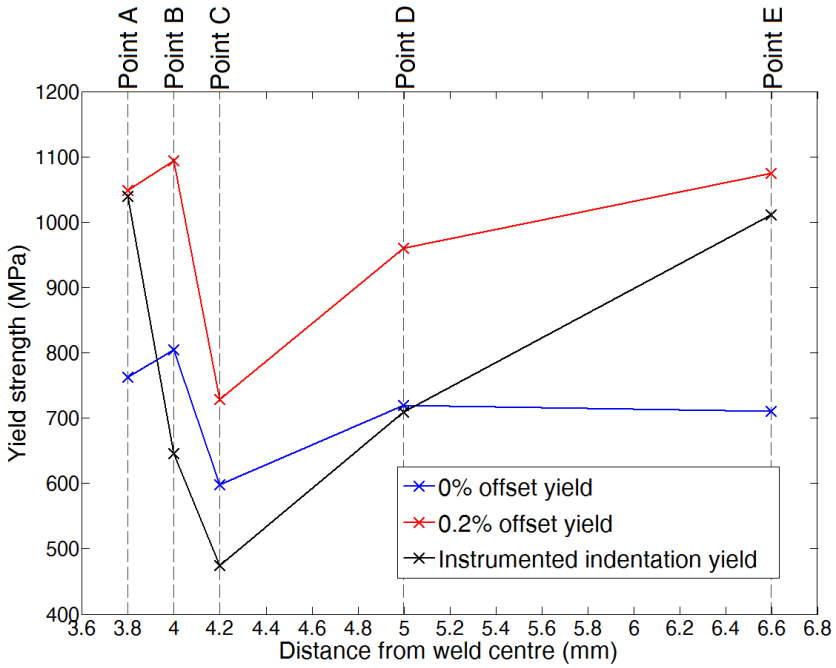

Figure 7.4.2: Comparison of yield strength calculated through instrumented indentation and measured yield strengths of fast heating regime Gleeble samples

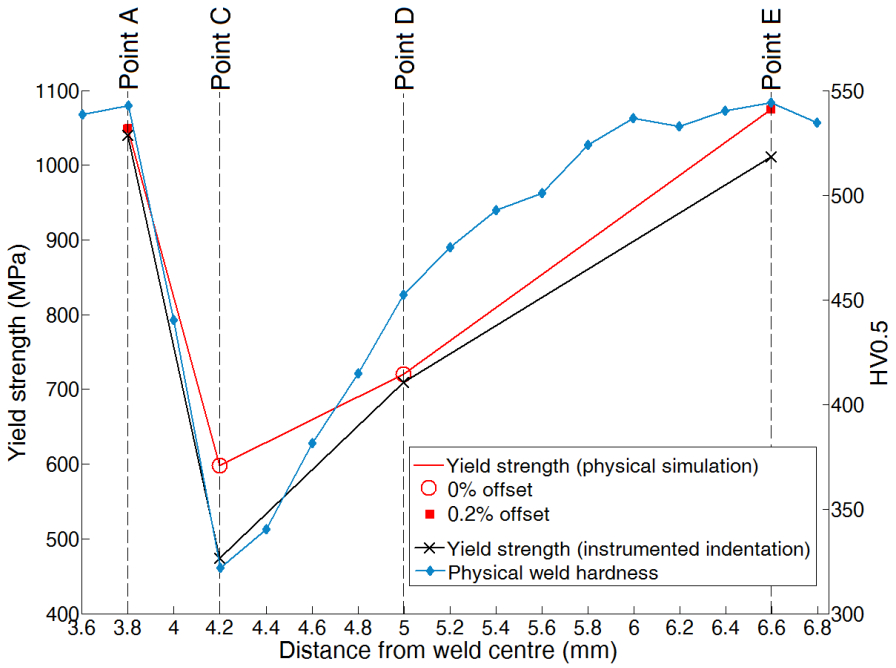

Figure 7.4.3: Yield strength comparison between instrumented indentation and Gleeble runs, with 4 mm data omitted. Physical weld hardness distribution is included to illustrate material property gradients.

7.4.3 Microstructural evaluation

The analysis performed in the preceding sections forms part of a hypothesis that purely quantitative data may be used to verify the accuracy with which the Gleeble samples were reproduced, thus circumventing the need for laborious sample preparation and qualitative microstructural interpretations associated with optical microscopy. This section will verify whether the correct decisions were made in the preceding analysis. Given the overwhelming evidence that samples produced with the slow heating regime experienced either excessive tempering or austenitisation, additional analysis is not required to justify eliminating these samples from the analysis. Therefore, only the weld and fast heating regime samples will be compared.

All samples were prepared for optical microscopy as described in the welding chapter.

7.4.3.1 Peak temperature of point A

A comparison of the microstructure at 3.8 mm from the weld centre and the corresponding Gleeble sample heated to a peak temperature of 1100 °C are given in figure 7.4.4. Image a) shows the hardness indent at 3.8 mm from the weld centre. It is clear that this indent is at the border of two different microstructural zones. The lower left hand corner of image a) shows what appears to be a very fine martensitic microstructure. Martensite is inferred due to the lath-like structure and high hardness value. The physically simulated microstructure in image b) shows a much coarser martensitic microstructure. Due to the longer time spent being austenitised, austenite grain enlargement may have occurred, which led to the coarser martensitic microstructure. Although the microstructures appear visually different, they correspond well in terms of mechanical properties (hardness and yield strength).

7.4.3.2 Peak temperature of point B

The weld microstructure in figure 7.4.5 a) exhibits sharply defined grain boundaries. The microstructure of the Gleeble sample is difficult to distinguish. It is clear that another etchant must be used to investigate the microstructure. From a qualitative comparison of the two images in figure 7.4.5 and the significant difference in hardness previously presented, it must be concluded that the simulated microstructure has severely deviated from the target.

7.4.3.3 Peak temperature of point C

From figure 7.4.6, it is clear that the Gleeble sample produced from the fast heating regime displays a more finely dispersed microstructure than the corresponding weld microstructure, with the weld exhibiting larger ferrite grains (shown in white). Ferrite is inferred due to the low hardness of this region.

From figure 7.4.6 b), it is clear that a large portion of martensite has been transformed into ferrite, with the cementite at the grain boundaries shown in black. The weld does exhibit a coarser microstructure than the Gleeble sample. This could be due to the Gleeble sample spending a longer time at elevated temperatures, leading to more carbon being precipitated out and a finer microstructure being formed.

7.4.3.4 Peak temperature of point D

The white microstructure in both figures 7.4.7 a) and b) is inferred to be ferrite, due to the reduced hardness. The ferrite islands appear to be of comparable size in both images. The Gleeble sample does appear to exhibit a more distinguishable lath microstructure, although the difference between the two images may be due to excessive etching on the Gleeble sample.

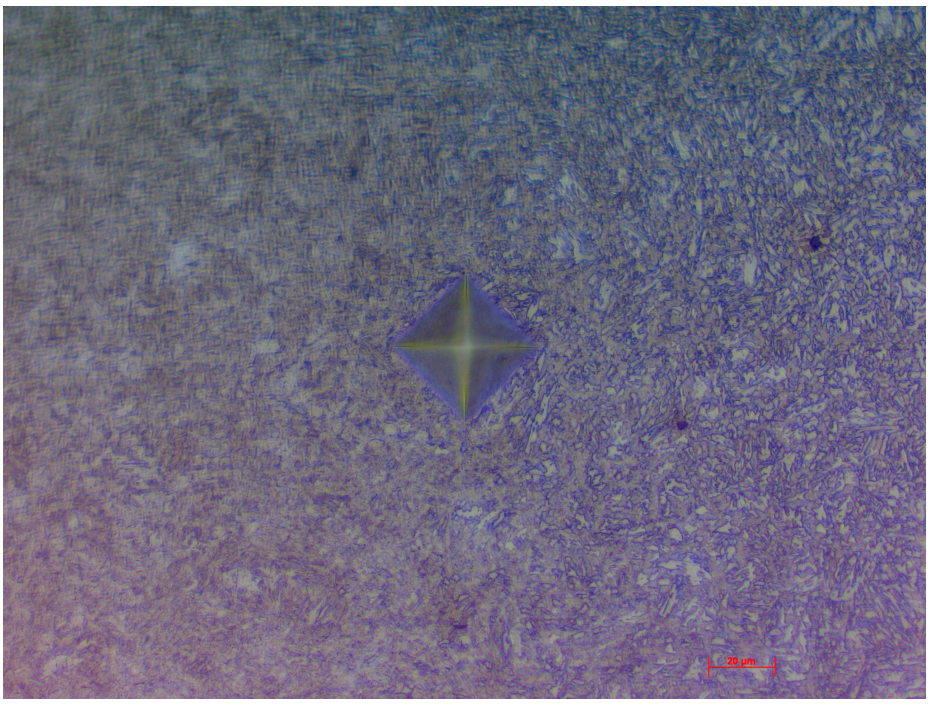

(a) Optical micrograph of commercial boron steel weld at 3.8 mm from weld centre

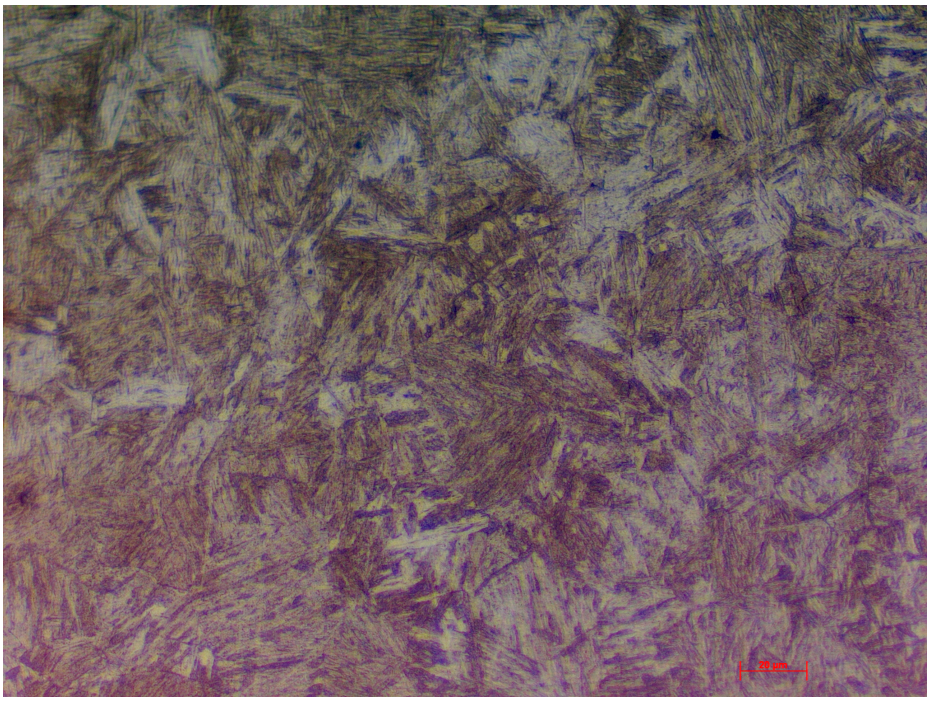

(b) Optical micrograph of Gleeble sample heated to peak temperature of 1100 °C in the fast heating regime

Figure 7.4.4: Point A: Microstructure comparison of weld at 3.8 mm and Gleeble sample heated to peak temperature of 1100 °C

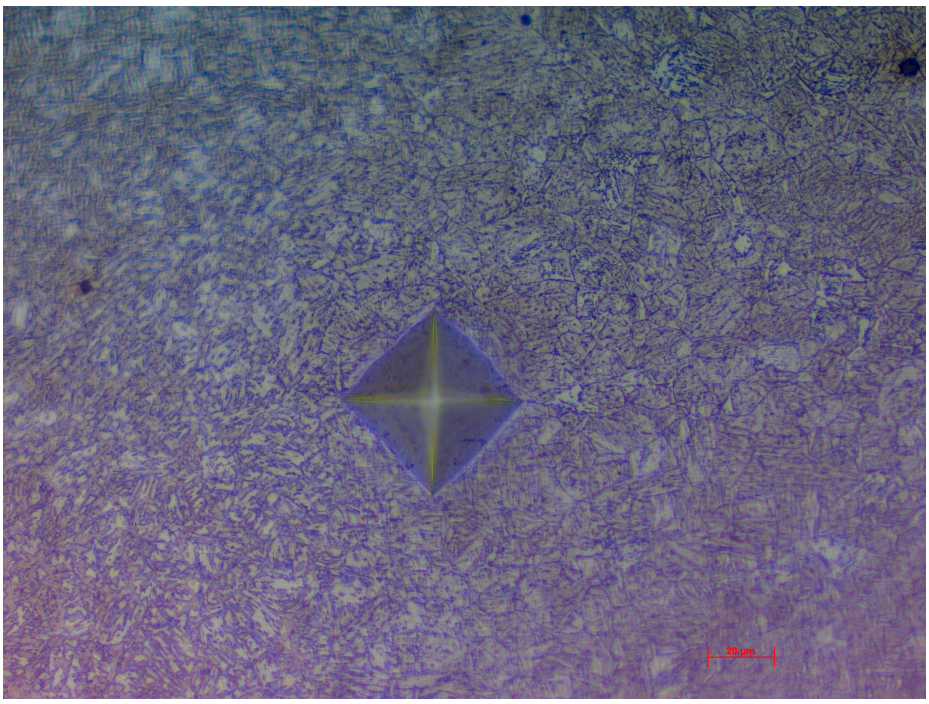

(a) Optical micrograph of commercial boron steel weld at 4.0 mm from weld centre

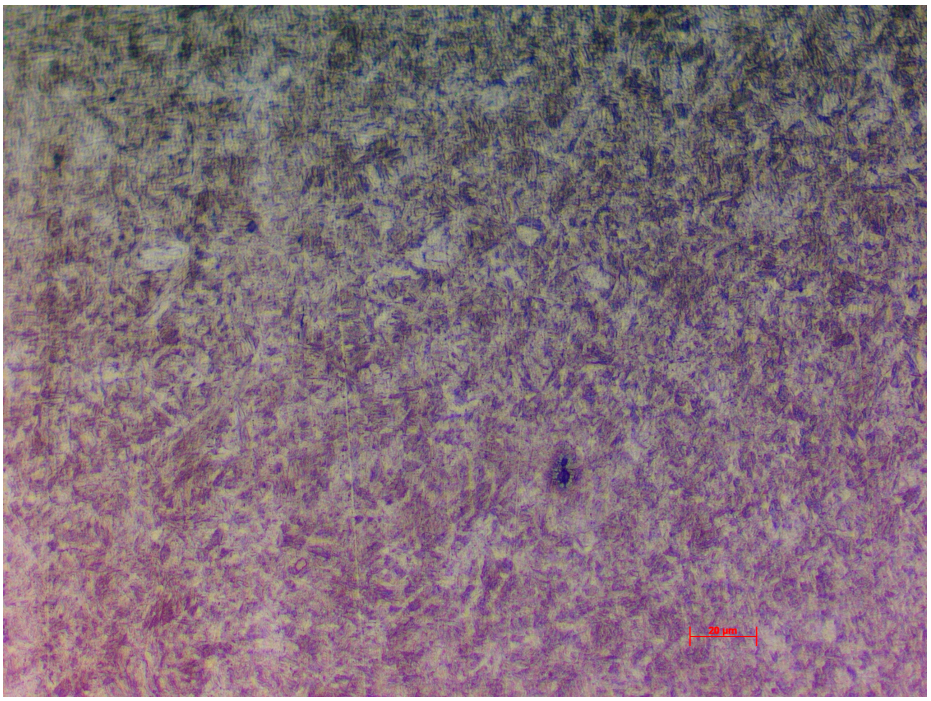

(b) Optical micrograph of Gleeble sample heated to peak temperature of 925 °C in the fast heating regime

Figure 7.4.5: Point B: Microstructure comparison of weld at 4.0 mm and Gleeble sample heated to peak temperature of 925 °C

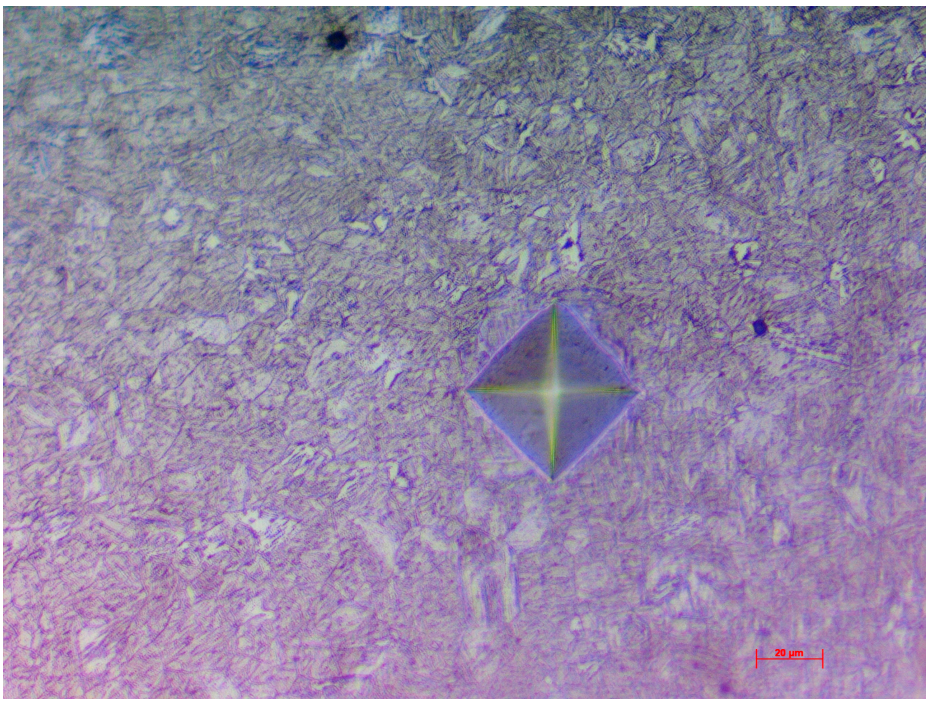

(a) Optical micrograph of commercial boron steel weld at 4.2 mm from weld centre

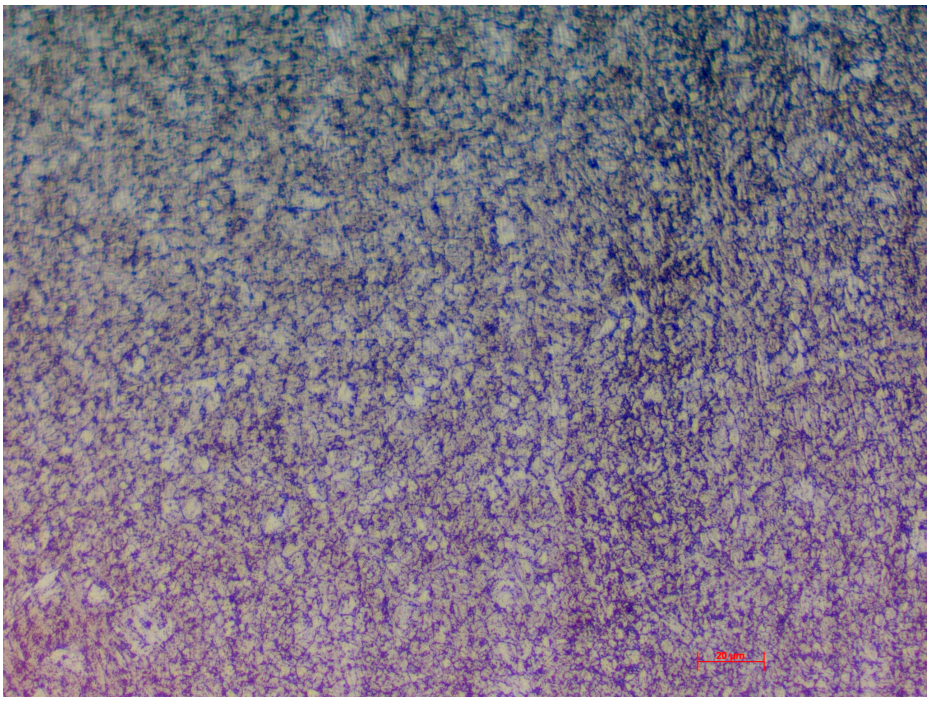

(b) Optical micrograph of Gleeble sample heated to peak temperature of 725 °C in the fast heating regime

Figure 7.4.6: Point C: Microstructure comparison of weld at 4.2 mm and Gleeble sample heated to peak temperature of 725 °C

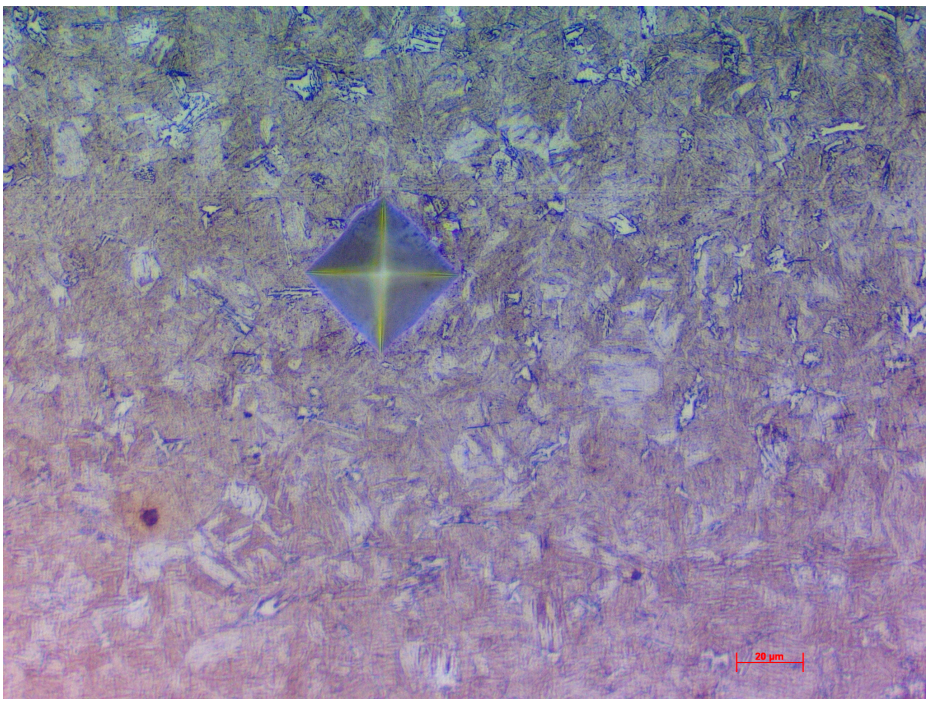

(a) Optical micrograph of commercial boron steel weld at 5.0 mm from weld centre

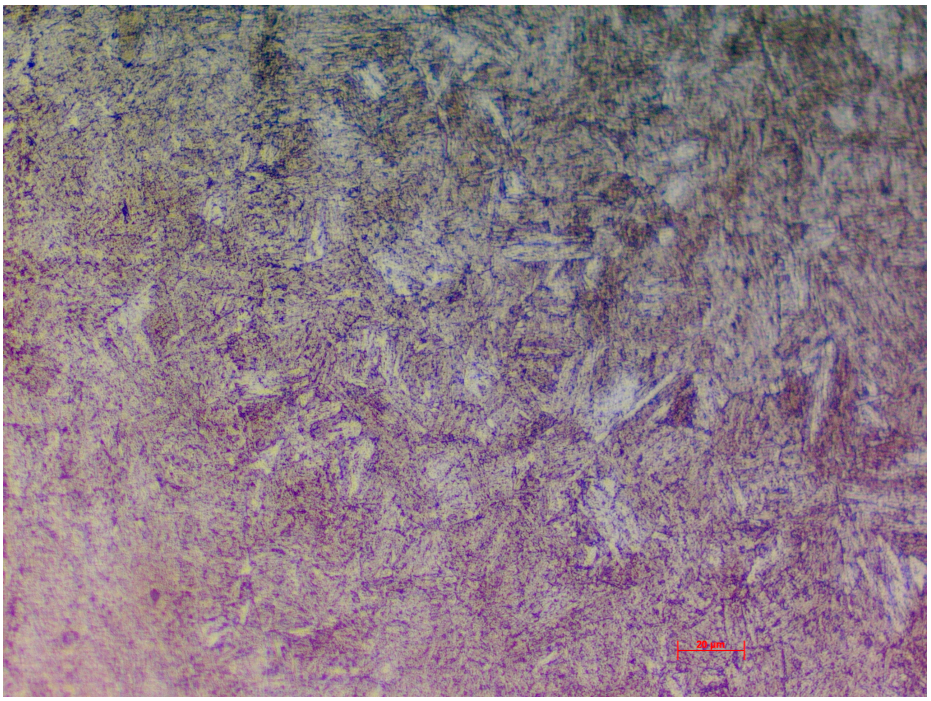

(b) Optical micrograph of Gleeble sample heated to peak temperature of 575 °C in the fast heating regime

Figure 7.4.7: Point D: Microstructure comparison of weld at 5.0 mm and Gleeble sample heated to peak temperature of 575 °C

7.4.3.5 Discussion

It may be concluded that the physically simulated microstructures have deviated from their targets. The sample heated to 1100 °C exhibited a coarser martensitic microstructure compared to the target. Although the microstructure of the sample heated to 925 °C could not be accurately identified, it was clear that significant deviation had occured. Excessive tempering was evident for the samples heated to 725 °C and 575 °C.

For the higher temperature regimes, the steel samples were heated beyond the transformation temperatures and for the lower temperature regimes, the steel samples reached the appropriate tempering temperatures. The main reason for deviations, therefore, seems to be due to the extended time that the samples have been exposed to elevated temperatures. This leads to austenite grain enlargement for the higher temperature regimes or excessive tempering for the lower temperature regimes. An additional parameter which may have led to microstructural deviations is the slower cooling rates achieved. This would particularly affect the samples which have been austenitised. This section has helped to visually interpret the reason for the difference between weld and Gleeble microstructures. The instrumented indentation and hardness results have added value to the investigation by providing quantitative data from which to gauge the accuracy of material reproduction.

7.5 Conclusions

Stress-strain curves and $\varepsilon_f - \alpha$ failure loci were successfully extracted from the heat treated samples using DIC. The points A and E exhibited lower failure strains and higher UTS values than the tempered samples of points C and D.

A method was established to check the accuracy with which the Gleeble samples were reproduced with respect to their target weld microstructures. This method consisted of comparing the physical weld region hardness to that of the corresponding physically

simulated samples. The second verification tool was comparing the calculated yield strengths of the physical weld regions, obtained through instrumented indentation, to the yield strengths taken from stress-strain curves of destructively tested physically simulated samples. To the authors knowledge, instrumented indentation has not previously been used to verify the accuracy of heat treated samples with respect to their target microstructures. Therefore, this work explores a new application of instrumented indentation.

The hardness results indicated that the fast heating regime produced samples with the closest correlation to the target hardness values. The samples corresponding to point B showed the greatest deviation for both the slow and fast heating regimes. This deviation was attributed to the effect of heating rate on the transformation temperatures and time spent at peak temperature. The yield strength comparison of point B confirmed a significant deviation from the target value. This facilitated in the decision to disregard point B from further analysis. It was observed that the austenitised physically simulated samples 0.2% offset yield strengths corresponded more closely to the calculated yield strengths. The tempered samples 0% offset yields corresponded more closely to the calculated yield strengths. Taking this into consideration, the overall yield strength distribution obtained through physical simulation corresponded well to that of the calculated yield strength distribution.

Microstructural analysis indicated that the physically simulated microstructures deviated from their targets. Considering that all samples reached the correct target temperatures, the deviation can be attributed to the extended times spent at elevated temperatures. The use of calculated yield strengths provided an additional parameter from which to gauge the accuracy of material recreation and gave more confidence in utilising the physically simulated samples. Once confidence has been established that the calculated yield strengths are accurate, instrumented indentation can be a valuable tool for gauging the accuracy of recreated microstructures.

Chapter 8

Finite Element Analysis

8.1 Introduction

In the preceding chapters, various material properties were extracted from the weld and BM, in addition to the process induced state of residual stress. In this chapter, these properties are incorporated into FE models to simulate loading of lap-shear and cross-tension destructive specimens. The aim of this chapter is to use FE simulations to predict weld failure, through ultimate load and displacement at failure, and to validate the results with experimentally measured load-displacement curves.

Note that the DP600 steel was used as a verification tool in the residual stress and instrumented indentation experiments, therefore DP600 lap-shear and cross-tension models are not presented.

8.1.1 Elements

An FE model is discretised into many elements; being either solids or shells. Nodes at the boundaries of these elements serve as connectors between 2 or more elements. Shell elements are thin in comparison with their span and are hence more suited to plane-stress conditions [138]. Two dimensional (2D) shell elements are faster to process than three dimensional (3D) solid elements [138] and are routinely used to model the BM in lap-shear and cross-tension simulations [40, 139, 140].

3D solid elements are more accurate in modelling stresses in 3 dimensions and hence give more accurate results that 2D shell elements in the same stress state [119]. However,

3D analyses are at least an order of magnitude more computationally expensive than 2D analyses [141]. If solid elements are to be used to model sheet material, they need to be cubic in shape to avoid numerical instabilities [119]. Furthermore, for accurate modelling of bending in the sheet, multiple layers of solid elements are required through the sheet thickness. These two requirements significantly increase computational time if solid elements are used to model sheet material.

It is therefore more appropriate to use solid elements in the area where significant stress gradients are expected to develop and to use shell elements in the far-field; essentially to transfer the applied force to the solid element structure. This concept has been used by other authors in the field of FE modelling of spot welds [40, 139, 140].

As further justification for using shells, necking in the BM is uncommon for boron steel weld destructive specimens. For more ductile steels, such as DP600, necking is seen in the BM [44]. Therefore, for spot welded steel grades that exhibit failure through necking in the BM, modelling the BM with solid elements might be more appropriate. As BM necking for boron steel was not observed in experimental trials or in the literature, it was deemed appropriate to model the BM sheet with shell elements.

With both solid and shell elements, it is possible to define the number of integration points in each element. These are known as fully- or under-integrated elements. Under-integrated elements have one integration point in the centre of the element. Fully-integrated elements have a higher number of integration points, which are located in a rectangle/diamond shape between the centre of the element and the outer nodes. Under-integrated elements are faster to process, but suffer from “hour-glassing”, which is a zero-energy mode of deformation which produces no stress or strain [142].

Fully-integrated elements do not suffer from hour-glassing, but are more computationally expensive due to the increased number of integration points. Fully integrated elements also have the possibility of producing “negative volumes” under large deformation. This is where the element becomes so distorted that its volume is calculated as negative. This behaviour is more likely for materials that undergo extremely large

deformations, such as soft foams [142]. Fully-integrated elements seem like the logical choice for modelling boron steel, as they are more accurate than under-integrated elements and the constitutive behaviour of boron steel indicates that extreme, foam-like, deformation is unlikely to occur.

8.1.2 Control

There are two methods that are used to solve for a solution in FE analysis: implicit and explicit methods. These methods are used for obtaining solutions to time-dependent ordinary or partial differential equations. Ideally, the momentum and energy transport in the FE model must respond like real life. The model uses discrete sampling locations (at the nodes) at discrete time intervals (timesteps). For a node to see a disturbance, the time resolved location of the disturbance peaks must be less than a nodal distance. Otherwise, the disturbance travels past the node without being registered within that timestep.

Explicit methods calculate the state of the system at a later time from the state of the system at the current time. Implicit methods solve an equation involving the state of the system at both the current and later times. From the fact that implicit methods have two time factors in the calculation, it is clear they are more computationally expensive than explicit methods. However, implicit methods are "unconditionally stable" [143]. That is to say, a large timestep may be used in the calculations while still achieving a stable solution. This will be explained more thoroughly below.

An implicit analysis builds a stiffness matrix for the whole model, with one row/column for each degree of freedom, for each increment in load. The method then calculates the inverse of the matrix and uses this to calculate the deflection from the forces. The calculated reaction forces are then checked against the applied loads and the internal energy checked against externally applied energy and an error is calculated. If this error is above a predefined threshold, a smaller timestep is attempted. Once the error is within the predefined tolerance, the solution converges and proceeds onto the next

load increment. The size of the timestep can be adjusted to how stable the solution is and often it is possible to solve a larger timestep than that used by the explicit method in one iteration.

Explicit methods require a much smaller timestep to ensure numerical stability. This timestep is governed by the Courant-Friedrichs-Lewy (CFL) criterion. As a basic description, if a wave travels across an element and we want to calculate its amplitude in discrete time steps, then the distance travelled by the wave through the element must be less than the length of the element. Hence, for an explicit analysis, a timestep is imposed which is smaller than the time taken for sound to travel through the smallest element. Therefore, as the stress wave perturbation cannot travel further than one element in one timestep, it is possible to calculate a force-displacement balance for each element independently, without needing to take input from any other element's nodes. It is a one-pass calculation for the whole model, without any convergence checks or additional calculations. One is, however, constrained by the small timestep required to allow this method to work.

From these considerations, implicit methods can run with a larger timestep but are more computationally expensive. Explicit methods require a smaller timestep, but are not as computationally expensive. Implicit methods can suffer from non-convergence if the timestep is too large [119]. Therefore, to avoid the possibility of a non-converging solution, simulations were run with explicit solvers.

8.1.3 Material

The FE simulations were performed with LS-Dyna [144], which contains a library of just under 200 material models.

The material card MAT_PIECEWISE_LINEAR_PLASTICITY was chosen. This card describes elasto-plastic behaviour and allows for the experimentally measured stress-strain curves to be directly referenced. An additional MAT_ADD_EROSION

option allows for failure to be modelled. The experimentally derived failure loci can be directly referenced and once an element reaches a critical plastic strain, the element is deleted from the calculation, representing a failed element. This material card has been successfully applied to spot weld models [31].

8.2 Creating the model

8.2.1 Meshing and element selection

The FE models were created in Hypermesh [145], a pre-processor developed by Altair for drawing geometries and applying meshes. The dimensions of the weld model were measured directly from the physical weld using optical microscopy, as shown in figure 8.2.1. The final lap-shear and cross-tension models are shown in figures 8.2.2 and 8.2.3 respectively. In order to reduce computational time, use was made of the geometrical and loading symmetry of the destructive specimens. The lap-shear specimen was presented as a half-model and the cross-tension specimen as a quarter model.

The BM sheets were modelled with shell elements, in order to further reduce computational time. The BM shell sheets are attached to the solid element weld by a shell layer, as shown in figure 8.2.4. This shell layer transfers shell element rotations to the solids elements [146]. To ensure all degrees of freedom are coupled between solid and shell elements, it was necessary to mesh the shell elements over the face adjoining the solid elements. This is in contrast to simply attaching the shells at a single line of nodes on the solid elements. By properly attaching shells to solids, the shell rotations translate into xyz displacements at the attached nodes in the solid elements.

A closer view of the weld mesh is given in figure 8.2.5. The weld and HAZ were modelled with fully integrated, 8-noded solid elements. The solid elements are typically 0.1 mm long in the x-direction.

As a final point, the question of whether the mesh size is adequate for the chosen modeling purpose will be addressed. It is clear that the chosen element sizes are much

greater than microstructural dimensions. If elements of such small scale were used, the computational time would increase dramatically. Instead, the element sizes were chosen as to have a sufficient number of elements crossing the length of nugget and HAZ zones to obtain a gradient of developed strains and hence predict the global ultimate load and displacement at failure. The next question is, would the element size lead to a stress or strain concentration to develop within a single element at the notch tip and hence lead to premature failure?

Whether stress concentration within a single element is of potential concern depends on whether the model is elastic or plastic. In an elastic model, with minimal plasticity and high stress-strain gradients, stress concentration is of concern. In plastic models, such as the one utilised in this work, elements undergo significant amounts of plastic strain before failure. Due to this, the stress-strain curve at these high strains is relatively flat, with stresses being relatively insensitive to increases in strain.. Hence the stresses in the model will be limited by the small slope of the stress-strain curve.

Due to the chosen failure criteria ($\varepsilon - \eta$ loci), failure is not so much stress dependent, but strain dependent. To achieve sufficient plastic strain to fracture requires the whole element to deform. A fully integrated element, with increased number of integration points, will register this deformation to a high degree.

The modeling approach taken in this work is ductile. If deformation occurs to such an extent that significant amounts of plastic straining occurs before the crack at the notch starts to propagate, the error between the model and physical tests in predicting the fracture point will diminish as the threshold of plastic strain required before fracture initiation increases. This will reduce the influence of mesh size in predicting the failure location. Hence, due to the need to deform the elements sufficiently to generate a sufficient plastic strain to reach a failure point, the mesh sensitivity is a less significant factor in the accuracy of the model.

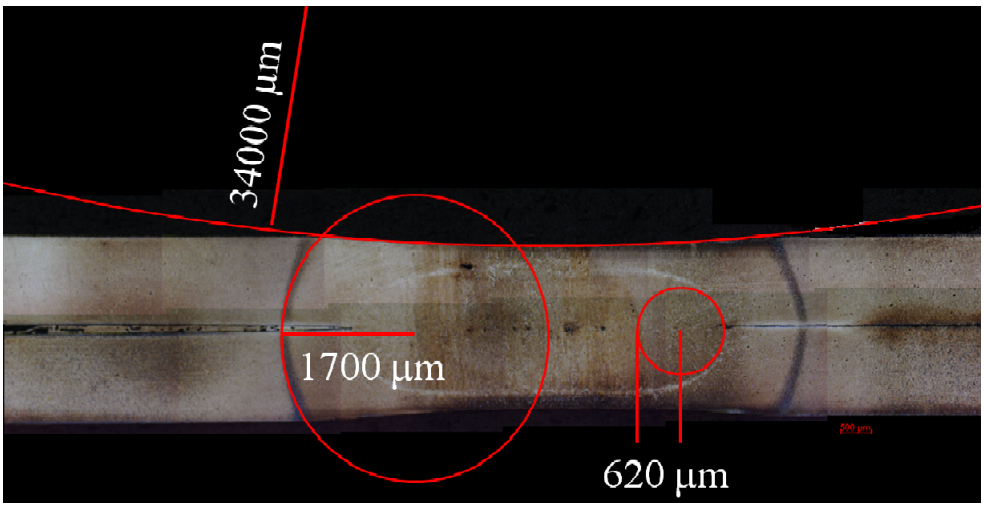

(a) Curvature measurements

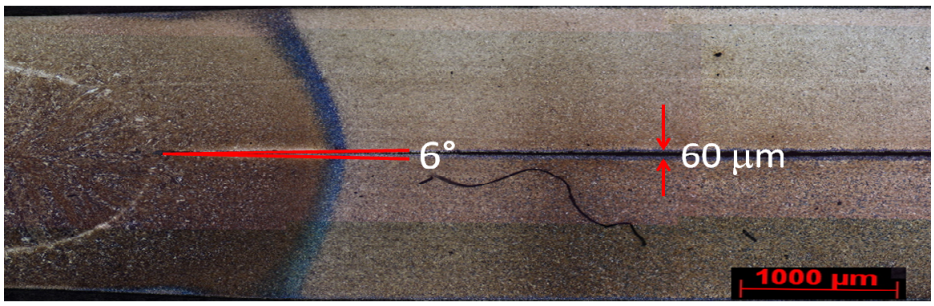

(b) Notch measurements

Figure 8.2.1: Dimensional measurements of boron steel spot weld

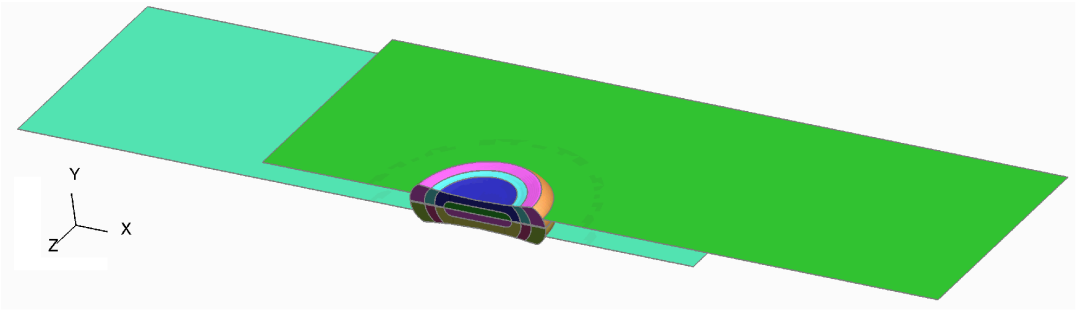

Figure 8.2.2: FE model for lap-shear specimen

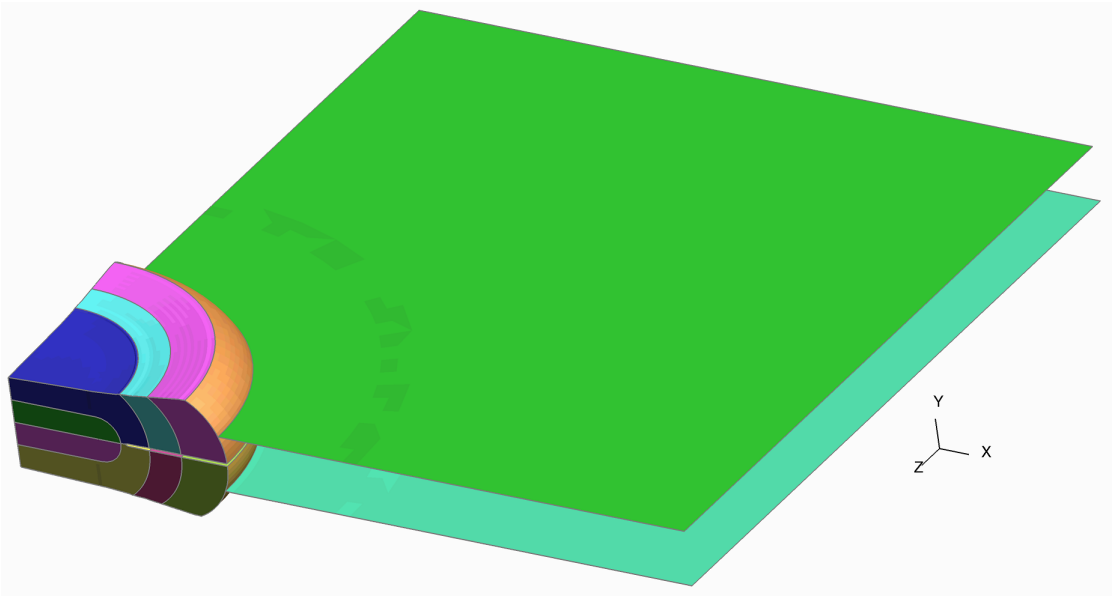

Figure 8.2.3: FE model for cross-tension specimen

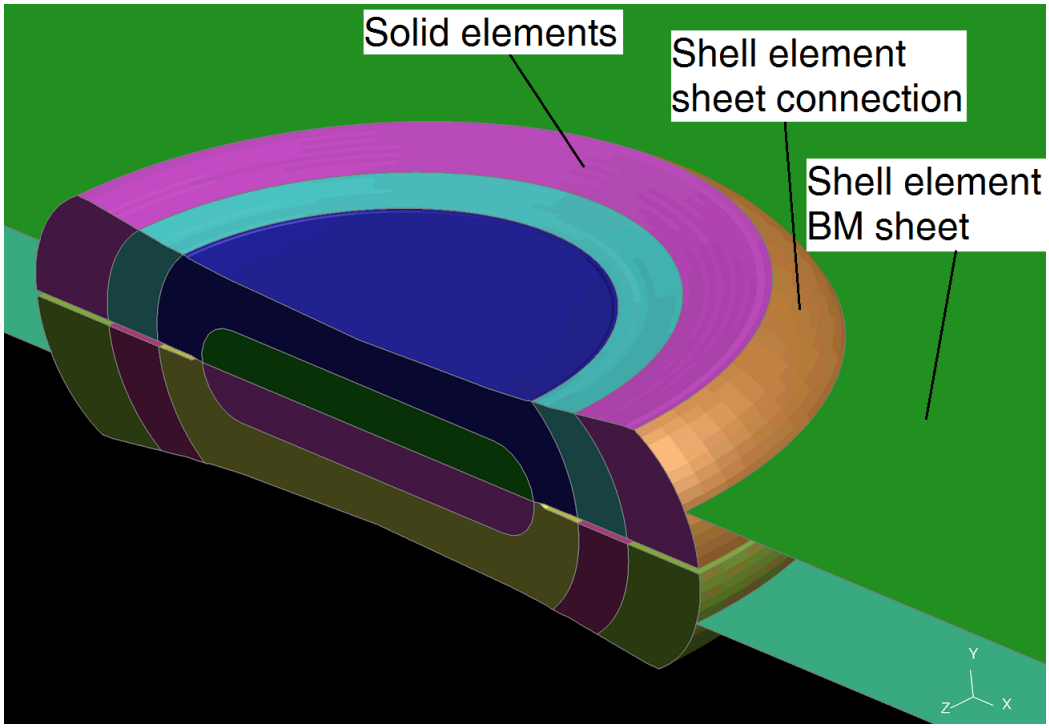

Figure 8.2.4: Connection between solid and shell elements

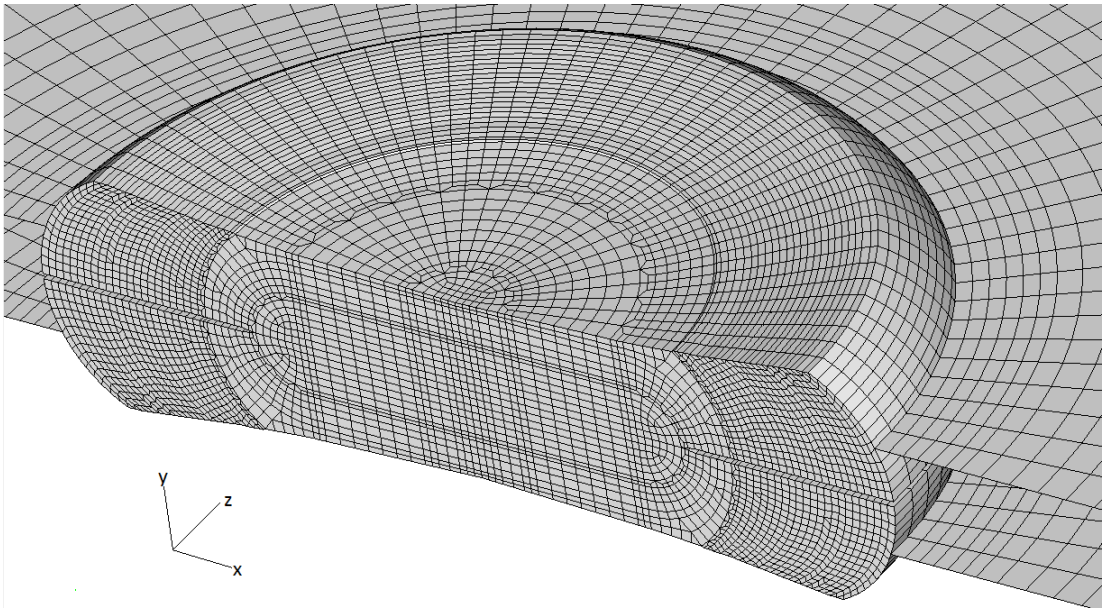

Figure 8.2.5: Mesh of weld

8.2.2 Boundary and loading conditions

In order to simulate the weld destructive specimen's load response while being gripped into the tensile testing machine, appropriate boundary conditions need to be applied.

8.2.2.1 Lap-shear boundary conditions

Boundary conditions were imposed by grouping specified nodes into a "set" and applying restrictions or loads on that set. One end of the lap-shear specimen was fully clamped by restricting translational and rotational degrees of freedom (DOF), as shown on the left-hand side of figure 8.2.6. Loading was applied at the opposite end, with all DOF's restricted except translation in the x-direction.

The symmetry boundary node set is shown in figure 8.2.7. Symmetry boundary conditions require that the out-of-plane displacements are restricted on the symmetry plane, therefore restrictions were applied to translational movement along the z-axis and rotations about the x- and y-axes.

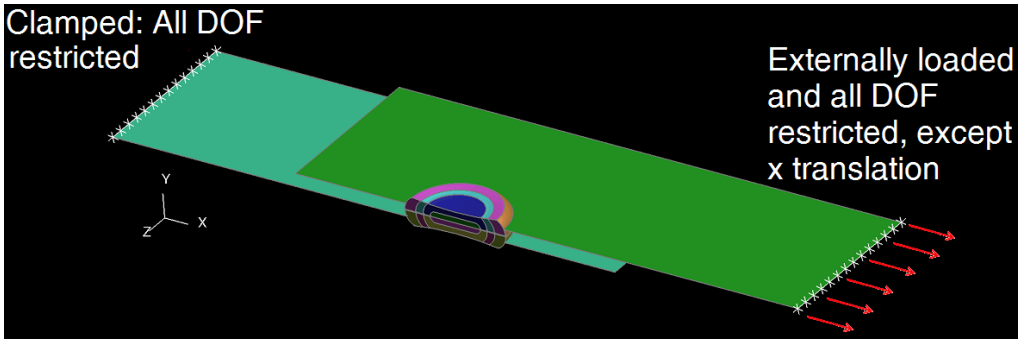

Figure 8.2.6: Lap-shear model, indicating boundary conditions

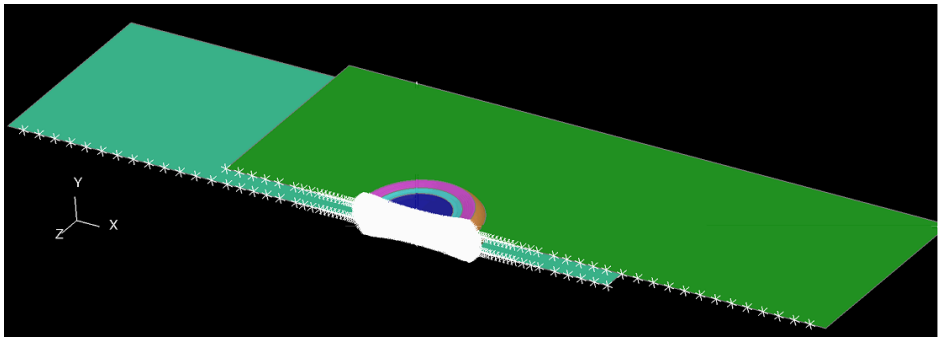

(a) Symmetry boundary node set

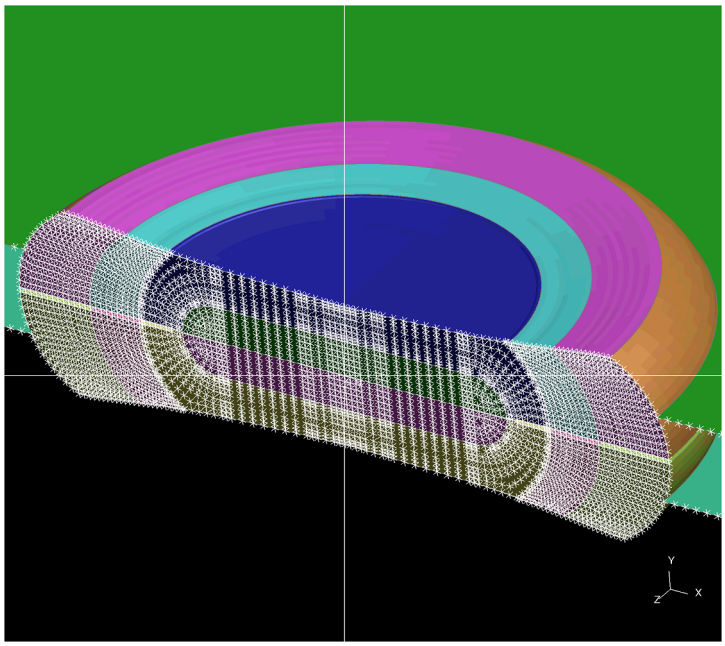

(b) Detail of symmetry boundary nodes

Figure 8.2.7: Symmetry boundary node set of lap-shear sample

8.2.2.2 Cross-tension boundary conditions

Figure 8.2.8 shows the boundary conditions imposed on the cross-tension model bottom sheet, with all DOF's restricted. The symmetry boundary nodes sets are shown in figure 8.2.9. For the node set in the y-z plane, translational restrictions were applied along the x-axis and also rotations about the y- and z-axis. For the node set in the x-y plane, translational restrictions were applied along the z-axis and also rotations about the x- and y-axis. Figure 8.2.10 indicates the boundaries applied to the upper sheet and weld edge. For both node sets, all DOF's are restricted except translation along the y-axis. Additionally, loading was applied to the node set on the top sheet.

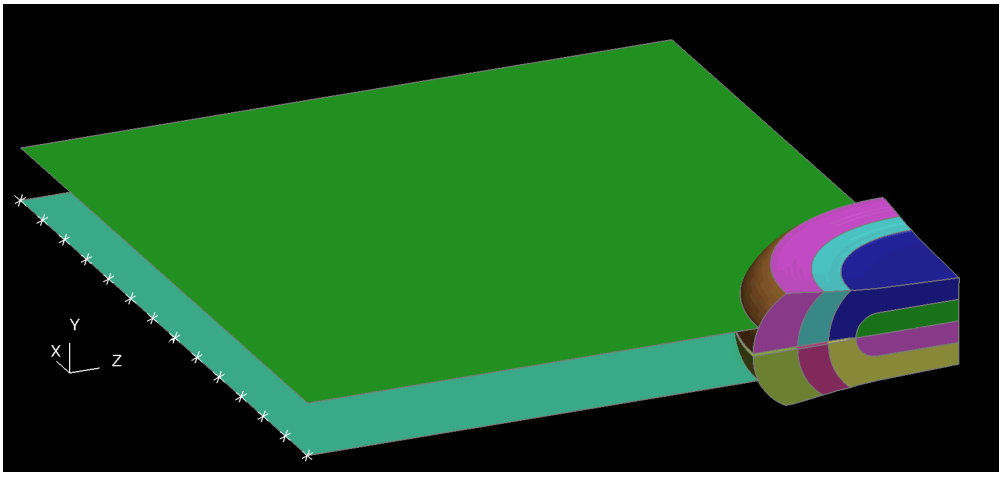

Figure 8.2.8: Cross-tension model, indicating bottom sheet boundary conditions

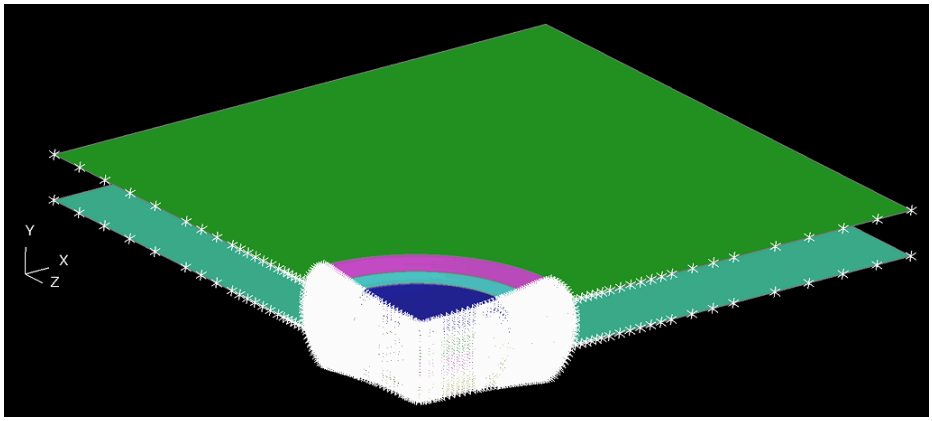

Figure 8.2.9: Cross-tension model, indicating symmetry boundary conditions

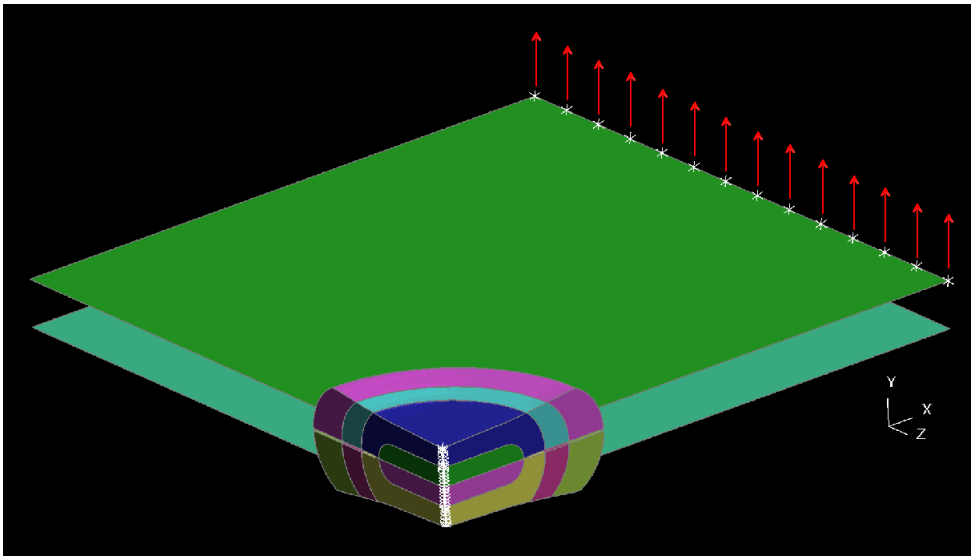

Figure 8.2.10: Cross tension model, indicating loading and weld edge boundary conditions

8.3 Incorporating residual stress distribution data

8.3.1 Overview

The residual stress data was determined experimentally in 1 mm increments, shown as the data labelled “neutron data” in figure 8.3.1. The average solid element size is 0.1 mm. Therefore, in order to assign a specific residual stress value to each element, the residual stress curves were interpolated in steps of 0.1 mm.

Due to time constraints during the neutron diffraction experiments, the measurements did not extend into the far field. The interpolated data was thus smoothed and extrapolated into the far field, where it is assumed that the residual stresses tend to zero, shown in figure 8.3.1 as “interpolated”. The data was fitted using a 7 degree sum of sine function in MatLab, as it provided the closest fit to the original data. As can be seen from the figure, the overall fit is good, with some slight deviations at the peak stress values in the hoop and radial stress directions between 4 mm and 5 mm.

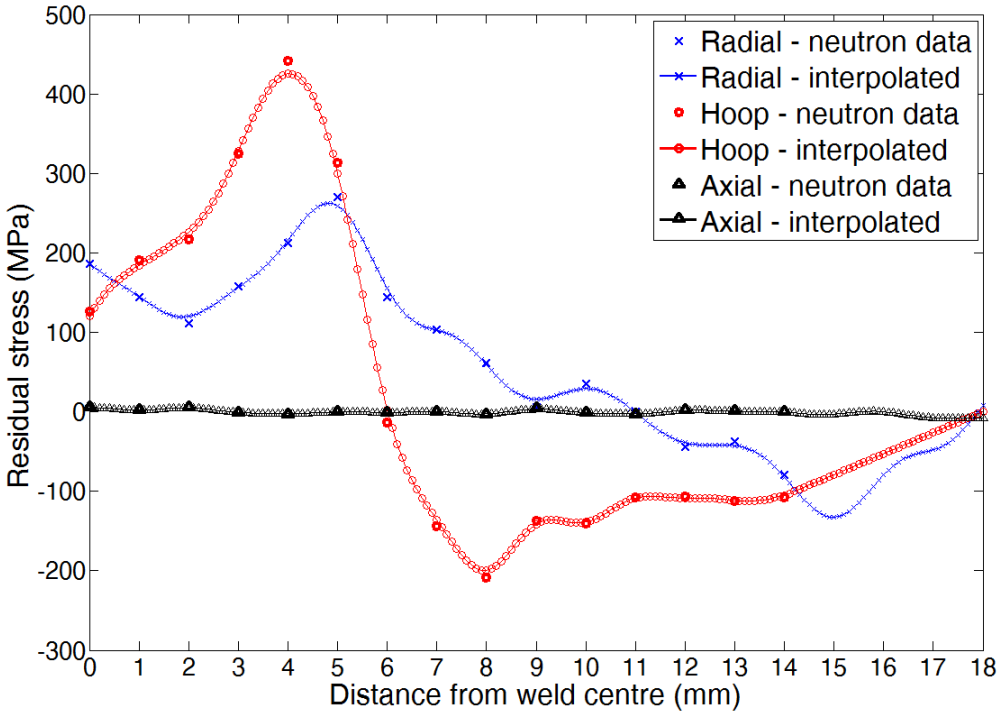

Figure 8.3.1: Interpolating residual stress data and extending into BM

In the next step, the residual stress values at specific distances along the x-axis were assigned to all elements in the x-y symmetry plane at the corresponding x-axis locations in the FE model. That is to say, a simplification assumption was made that there is no variation in material properties along the material thickness in the y-direction. The hardness measurements, taken at intermittent distances along the weld thickness, did not show significant variation. Therefore, this is assumed to be a reasonable assumption.

Once the residual stresses are assigned to the x-y symmetry plane, the values are rotated about the y-axis. In order to perform rotation, it is assumed the weld exhibits symmetrical properties about the weld centre. This is evidenced in the residual stress and hardness measurements. After rotation, all elements at a certain radius from the weld centre are assigned the same residual stress value. The residual stress distributions in the FE model are shown in figure 8.3.2.

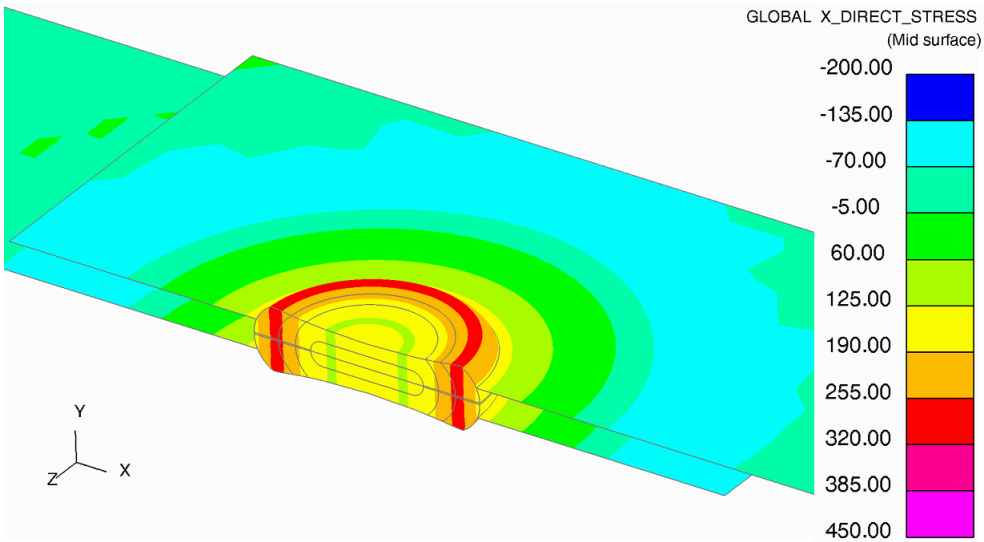

(a) Residual stress in the radial direction

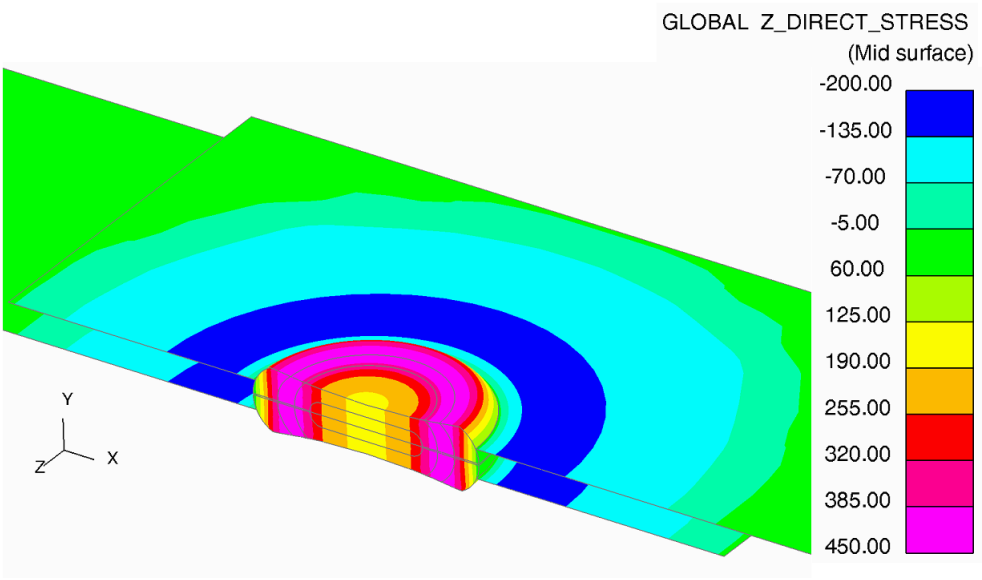

(b) Residual stress in the hoop direction

Figure 8.3.2: Residual stress distributions input into the finite element model. All stress values in MPa

8.3.2 Description of method

A more detailed explanation of the methods of processing and inputting the residual stresses will be given. Solid and shell elements are defined by 8 and 4 nodes respectively,

with each node being defined by an x-, y- and z-coordinate. The node coordinates are the only information for locating a specific element in the model. In order to assign a specific residual stress value to an element at a specific coordinate, it is necessary to know the position of the centre of the element. Otherwise, residual stresses will be assigned to the node coordinates at the edges of the elements and the input residual stress distribution will deviate from the measured distribution.

A program created by Mr David Norman [Tata Steel Automotive Engineering Group, University of Warwick] was used as a tool for finding the coordinates at the centre of the elements. When the FE model is first created, each element and node are assigned an identification number, which will be referred to as "element id" and "node id" from here on. The program reads in the element and node id's and sorts them in ascending order. The program then finds the nodes associated with each element and calculates the centre coordinate of the element by taking the average value. For an 8 noded solid element this would be:

$$x_{average} = (x_1 + \ldots + x_8)/8$$

and so on for the y- and z-coordinates. The element id's and element centre coordinates are then written to a .csv file.

In the next step, a MatLab script, created by the current author, was used to perform the residual stress interpolation described in section 8.3.1. The same MatLab script also reads in the .csv created in the previous step and calculates the radius and angle on the x-z plane for the centre of each element. The radius is centred on the centre of the spot weld model and the angle is with respect to the x-y symmetry plane. Finally, the MatLab script writes out 2 data files; one containing the interpolated residual stress values and associated distances from the weld centre and the other containing the element id, central x-, y- and z-coordinates and the calculated radius and angle values for each element.

The information obtained so far are the locations of the centre of each element and the associated angle and radius of those centres. The interpolated residual stress values

lie on the x-y symmetry plane and are functions of the distance from the weld centre. In the next step, these interpolated stresses are rotated about the y-axis using the previously gathered information about each element. The program developed by Mr David Norman rotates the interpolated stresses using the calculated radii and angles.

After the residual stresses have been input into the model, a "springback" simulation is run. Springback is normally applied to sheet metal forming simulations for calculating springback after cold forming. An output file called a "dynain" file is written, containing the residual stresses after the springback simulation. Performing this simulation has no effect on the originally input residual stresses, except the output dynain file offers a convenient method for moving the residual stresses from model to model.

In the subsequent models, an *INCLUDE option is activated to include the dynain file into the main model. To ensure the residual stresses do not equilibrate whilst the springback simulation is run, all nodes were fixed in translational and rotational directions. The simulation was then run for one timestep.

8.4 Processing material property curves

LS-Dyna accepts failure curves in the form of failure strain (ε_f) versus triaxiality (η), therefore the alpha values were converted into triaxiality. The conversion was performed in accordance with Beaumont [119].

In the previous chapter, yield loci were constructed in terms of strains $\left(\alpha = \frac{\varepsilon_2}{\varepsilon_1}\right)$. This was done because α could be calculated directly from the strain measurements taken through DIC. These measured fracture loci are valid for 2D stress states. The use of thin test geometries (shear, central-hole and plane-strain) makes this a reasonable assumption, where the stress normal to the loading plane is assumed to be zero. For the 3D stress states in the 3D finite element model, η is required.

To convert the measured α values into η, the von Mises yield criterion is assumed, and

the following relation utilised:

$$\eta = \frac{1}{\sqrt{3}} \frac{1+\alpha}{\sqrt{1+\alpha+\alpha^2}}$$

The derivation for this relationship is shown in the appendix. In order to fully account for 3D stresses, information is needed in regards to the lode angle, which is the angle between the origin and the three principal stresses, when the three principal stresses are plotted on a 3D axis set. The experimental time involved in adding the lode angle data to the failure curve was not afforded in this project. Nevertheless, a 2D approximation, as a first attempt to model the failure loci, is a reasonable assumption.

LS-Dyna requires the stress-strain curves to be extended into the large strain domain, as will be explained subsequently. During a tensile test, uniform extension ceases once the material reaches UTS and necking initiates. Once necking initiates, the uniaxial stress state changes to a biaxial state [147] and it is impossible to determine a true uniaxial stress-strain relation. Ling [147] stated that, beyond UTS, the standard tensile test cannot provide sufficient data for modelling. The following procedure was adopted from the work of Ling [147].

The engineering stress-strain values are cut off at UTS and converted to true stress and strain. The curve is then linearly extended into the large strain domain using the true stress-strain gradient at UTS. An example is shown in figure 8.4.1. The procedure is performed again, but with a ln σ - ln ε curve, which is then converted back into a linear curve. The curve loaded into LS-Dyna is then the average of these curves, as shown in figure 8.4.2.

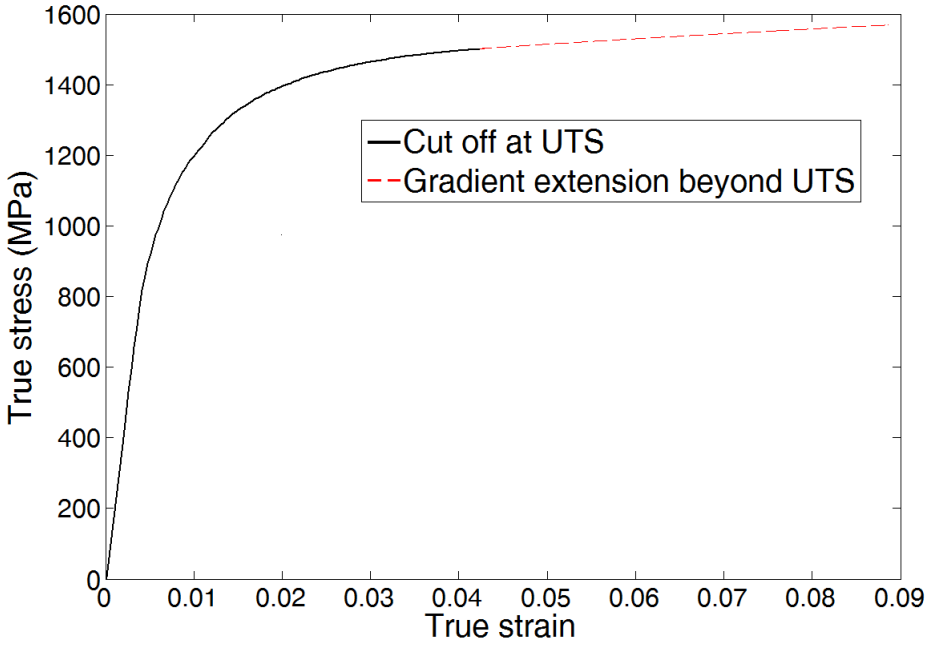

Figure 8.4.1: Extending stress-strain curve into large strain domain

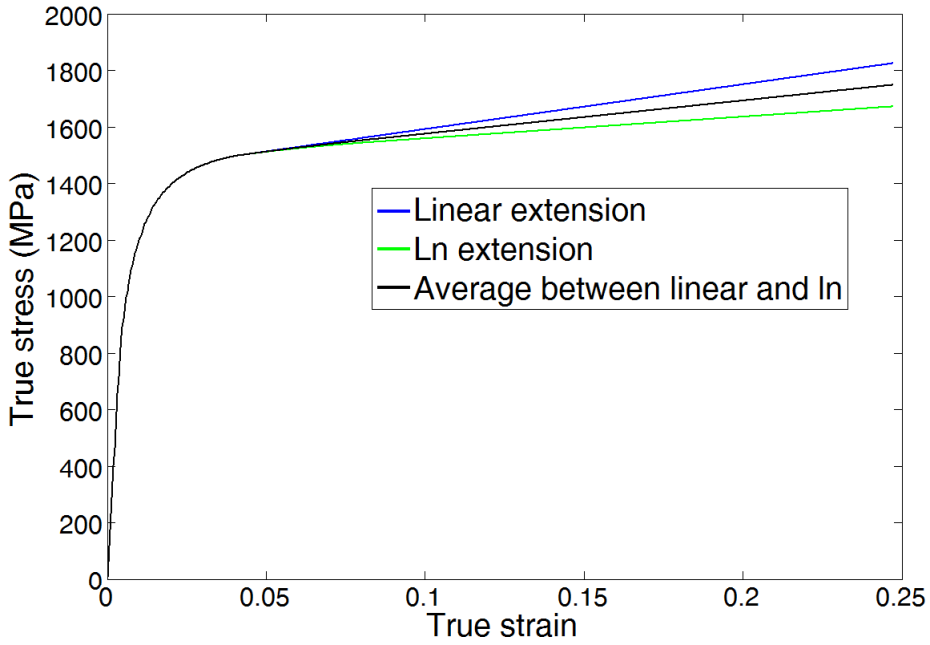

Figure 8.4.2: Stress-strain extrapolation using linear and natural logarithm techniques

8.4.1 Material property curve interpolation

The stress-strain curves and failure loci extracted from the Gleeble experiments are specific to certain distances from the weld centre. Overall, the properties of 5 points were extracted, with one of those points disregarded. As with the residual stress data, the material property curves were interpolated in steps of 0.1 mm. A linear interpolation method was employed, due to the hardness distribution exhibiting linear variation between the Gleeble points. Of course, such linearity could be due to the sampling size. If experiments were performed with finer resolution in terms of distance, perhaps some different variation would be seen. Nonetheless, such assumptions cannot be made with the available data.

An example of the interpolation between the experimentally measured points of 3.8 mm and 4.2 mm is shown in figure 8.4.3. Firstly, the average is taken between the curves at 3.8 mm and 4.2 mm to obtain the curve at 4.0 mm. Then an average between the curves at 3.8 mm and 4.0 mm to obtain the curve at 3.9 mm and so on. A similar procedure was performed for the failure loci. At the end of the interpolation procedure, 29 stress-strain curves and 29 failure loci were obtained spanning a distance from 3.8 mm to 6.6 mm from the weld centre. The material properties at 6.6 mm were assigned to the BM, as this was the nearest point from the weld centre where the hardness values levelled off to a consistent value.

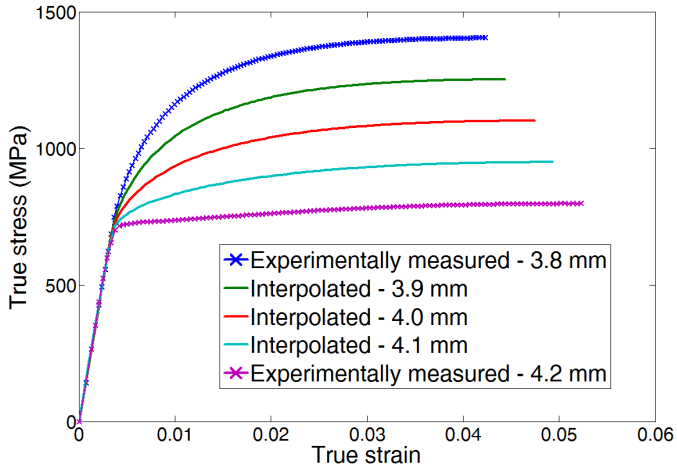

Figure 8.4.3: Linear interpolation of stress-strain curves

8.5 Model discretisation

8.5.1 Roughly discretised models

The weld model was discretised into 5 sections; the nugget, Zone 1, Zone 2, Zone 3 and BM, as shown in figure 8.5.1. The model discretisation is illustrated in figure 8.5.2. The corresponding input material properties assigned to each region are shown in figures 8.5.3 and 8.5.4. As the model is discretised according to the hardness distribution and not microstructure, the HAZ areas are assigned as "zones", as opposed to CGHAZ, SCHAZ etc.

It is worth noting that the material properties extracted for Zone 1 are also assigned to the nugget sections. Due to the Gleeble set-up, the steel samples could not be taken beyond the melting point. Therefore, the Zone 1 physically simulated samples give the closest correspondence to the thermal history which the actual weld nugget experienced, in terms of peak temperature and time at peak temperature. For ease of reference, table 8.5.1 gives the correspondence between the Gleeble physical simulation nomenclature and the simulation nomenclature.

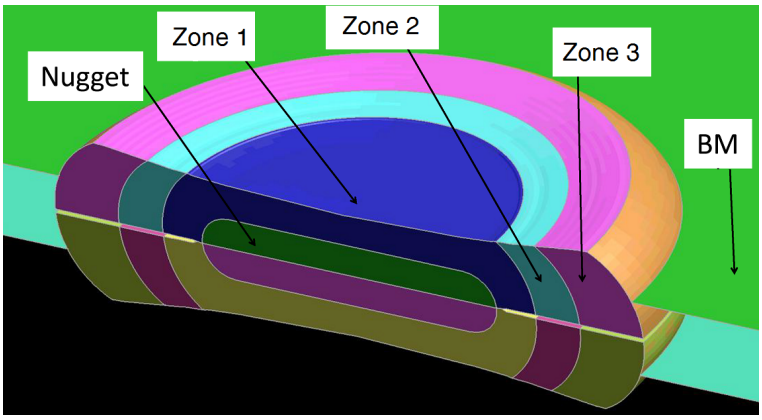

Figure 8.5.1: Part definitions of weld model

FE model	Nugget/Zone 1	Zone 2	Zone 3	BM
Gleeble physical simulation	Point A	Point C	Point D	BM

Table 8.5.1: Correspondence between FE model and Gleeble physical simulation nomenclature

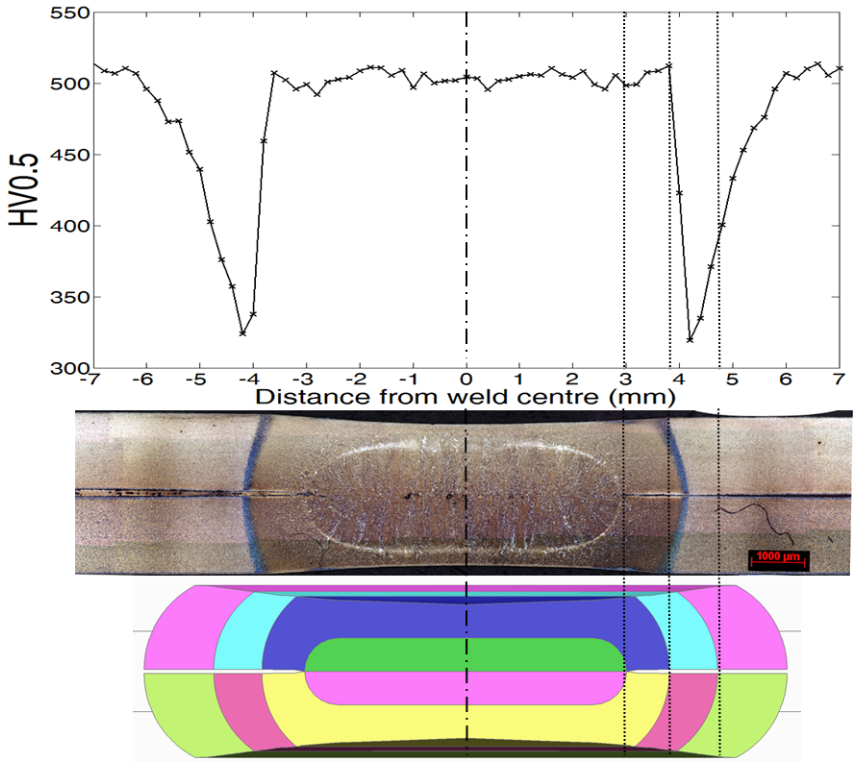

Figure 8.5.2: Weld model discretisation and corresponding hardness levels

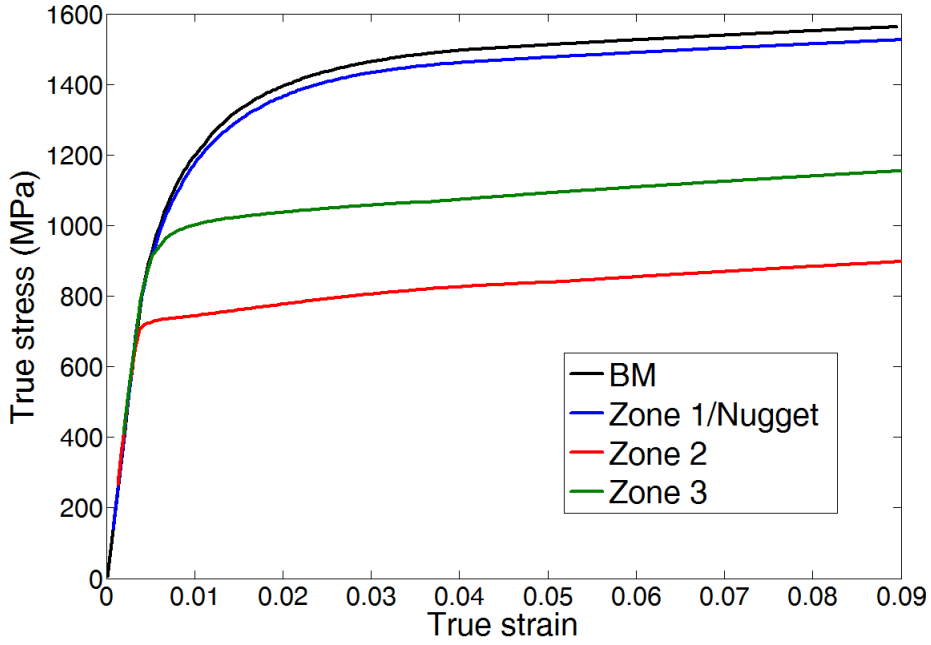

Figure 8.5.3: Input material properties for roughly discretised model: stress-strain curves

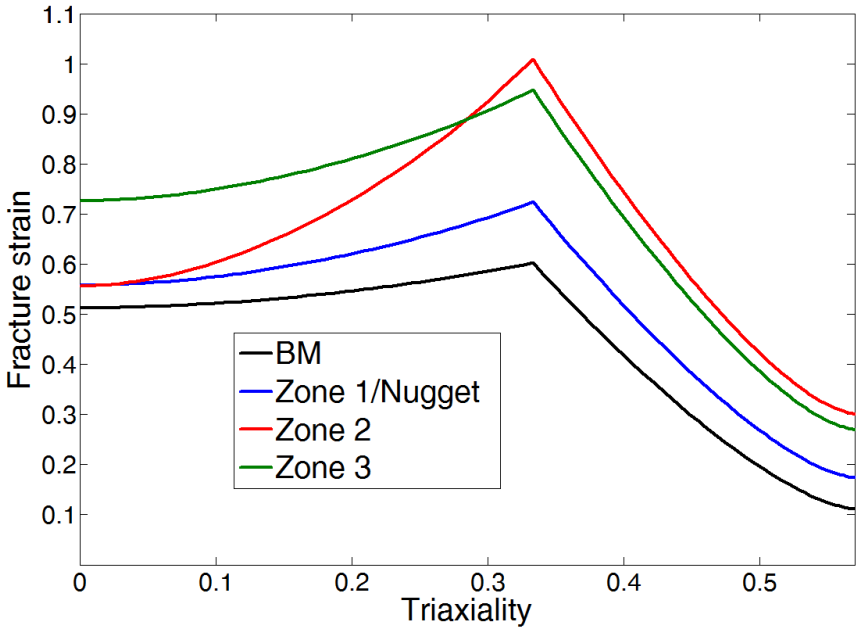

Figure 8.5.4: Input material properties for roughly discretised model: failure loci

8.5.2 Finely discretised model

The model described in section 8.5.1 was discretised during the design stage in Hypermesh, with material properties assigned to each part, leading to a rough discretisation of material properties. In this section, the same weld model is discretised to the level of data interpolation refinement. This method works on exactly the same principles as inputting the residual stress distribution, as described in section 8.3.

As described previously, the stress - strain curves and failure loci were interpolated in steps of 0.1 mm, leading to a total of 29 stress-strain curves and 29 failure loci. LS-Dyna reads in the stress-strain and failure loci and assigns them a "curve id" number. Therefore, in order to assign the material property curves to the correct locations, the curve id's were presented as a function of the distance from the weld centre, as shown in figure 8.5.5. In the figure, each data marker with a unique curve id number contains a specific stress-strain curve or failure locus. The same procedure as outlined in section 8.3 was performed to assign the appropriate curve at the correct radius to each specific element.

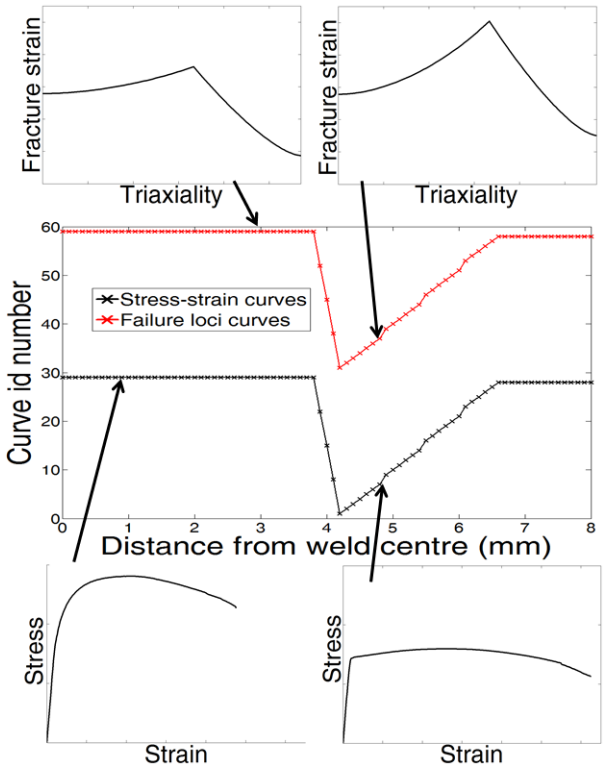

Figure 8.5.5: Material property curve id number distribution

8.6 Lap-shear simulation results

To correlate displacement results with those measured by the 50 mm physical extensometer, displacements at 2 nodes were taken and subtracted from one another, as shown in figure 8.6.1. In order to measure force, a cross-section was placed at the loaded end of the specimen, as shown in the same figure. The resultant forces from the elements assigned to the cross-section are summed to form the section forces [50].

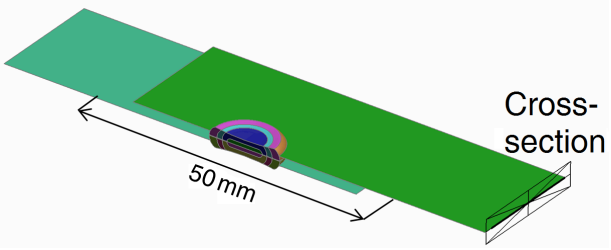

Figure 8.6.1: Simulated extensometer. Nodes are 25 mm from weld centre.

8.6.1 Load - displacement results

The simulated load - displacement curves for the rough and finely discretised models are compared with the 5 experimental lap-shear results, shown in figure 8.6.2. In the figure, the average experimental peak load was 10.13 kN. The simulated peak load for the rough model was 9.55 kN, giving a 0.58 kN underestimation. The simulated peak load for the fine model was 9.15 kN, giving a 0.98 kN underestimation. The average experimental displacement at peak load was 0.40 mm. The simulated displacement at peak load for both models was 0.35 mm, giving a 0.05 mm underestimation.

A comparison of the rough and finely discretised models will be given in the next subsection to establish why the load and displacement were underestimated to a greater degree for the finely discretised model.

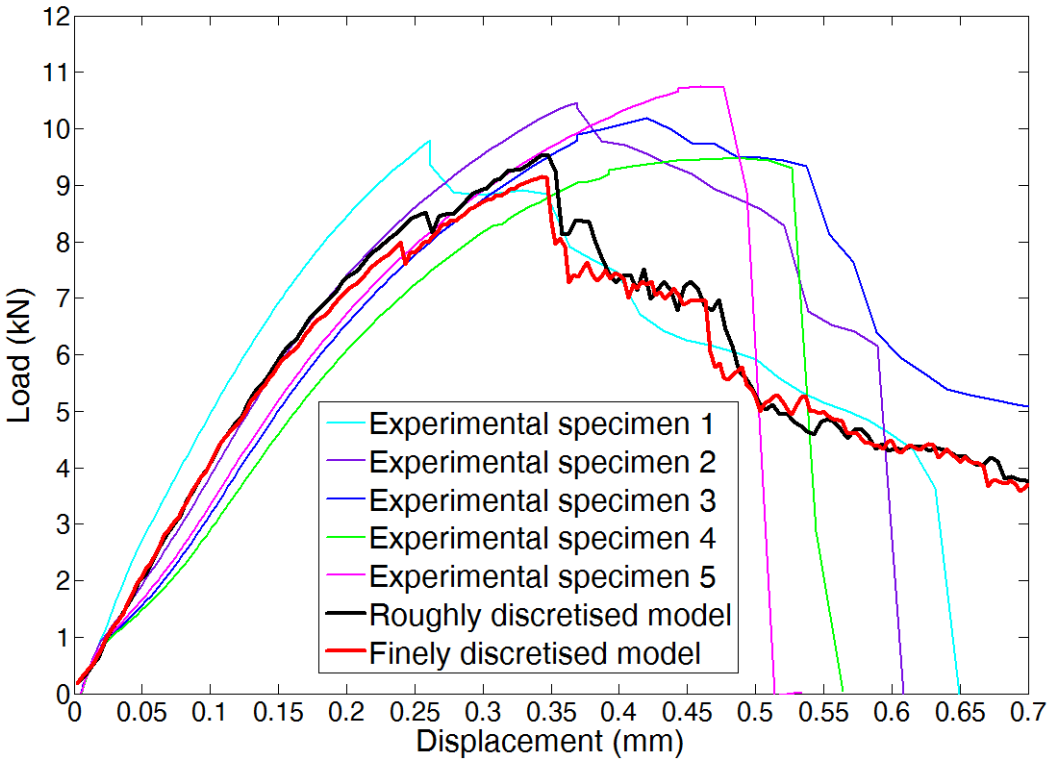

Figure 8.6.2: Load - displacement curves for rough and finely discretised lap-shear models, with experimentally measured curves.

8.6.2 Damage evolution

The rough and finely discretised models show nearly identical damage evolutions, hence only the roughly discretised model is presented in figure 8.6.3, where the figure labels correspond to the indicated labels on the load - displacement curve. At point a), initial failure occurs, with the element just above the notch tip being deleted. The reader is referred to figure 8.6.5 for a detailed view of this failure. The notch tip is at the faying surface, at the border between the nugget and where the sheets are separated. Loading continues until reaching a maximum, whereupon more elements are deleted at the nugget periphery and a significant decrease in load occurs, indicated as point b). A further sudden drop in load occurs at point c), where more elements are deleted. Symmetrical failure occurs on the left and right hand notch tips until point c). From point c) onwards, extensive damage occurs in the bottom half of the nugget on the left hand side. At point d), the crack extends through the thickness of Zone 1 in the bottom half of the weld. From this point, the failure follows a radial path from left to right on the image, tearing Zone 1 further. Button pull-out occurs at point e).

The extent of the radial failure path in the upper half of the weld is shown in figure 8.6.4, with the white marker lines indicating the length of the failed zone. Image a) corresponds with the initial failure at the notch tip, occurring through a 75 ° angle. Image b) shows a cross-section view of the initial failure. It is evident that the upper sheet is no longer attached to the lower sheet at the notch tip within this 75 ° angle.

Image c) corresponds to the point in the loading history where the crack extended through the lower Zone 1 thickness. This is the maximum extent of the radial failure of the upper weld. As can be seen, failure has extended through an angle of 101 °. Image d) shows a cross-section view of the 101 ° damage. It can be seen that significant damage has occurred in the upper Zone 1, with the damage following the border of the nugget in the thickness direction.

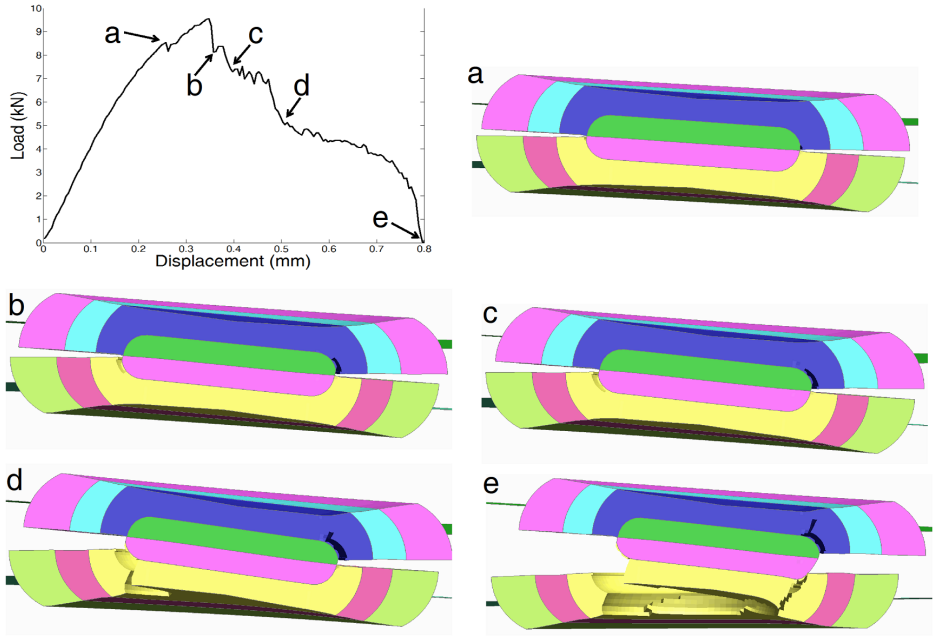

Figure 8.6.3: Damage evolution of roughly discretised lap-shear model

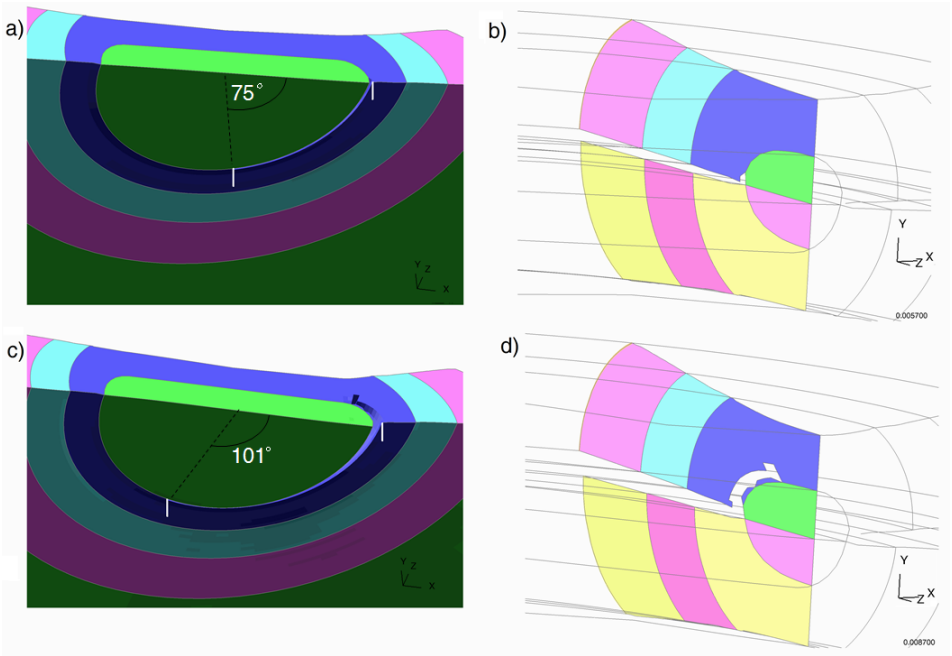

Figure 8.6.4: Radial failure path of roughly discretised lap-shear model. a) Initial failure at notch tip viewed on the faying surface of the upper nugget sheet. b) Cross-section view of initial failure at notch tip. c) Maximum extent of radial failure viewed on faying surface. d) Cross-section view of maximum extent of radial failure.

8.6.3 Comparison of rough and finely discretised lap-shear models

8.6.3.1 Stress and strain contours

In both models, failure initiates at the notch tip, shown in figure 8.6.5. The von Mises stress distributions for the two models are shown in figure 8.6.6. This stress distribution is shown at the last timestep before failure initiates. It can be seen that similar stress contours have developed around the notch tip for both model types.

In the roughly discretised model, abrupt changes in the stress levels can be seen at the interfaces between Zone 1 and Zone 2. This is especially true for the highest stress contour corresponding to approximately 1400 MPa to 1600 MPa. It seems as if the highest stress contour is bounded by the interface between Zone 1 and Zone 2. These abrupt changes may affect the stress concentration around the notch tip. In contrast, no abrupt changes are present in the finely discretised model, with the stress contours changing smoothly through the weld length.

The same stress distributions are presented on the x-z plane in figure 8.6.7. That is, at the faying surface of the upper sheet. Again, similar contours have developed between the two models. The highest stress contours, with values lying between 1440 MPa and 1600 MPa, are slightly more concentrated for the roughly discretised model. This corresponds with the abrupt change in stress seen in the x-y plane in figure 8.6.6 a).

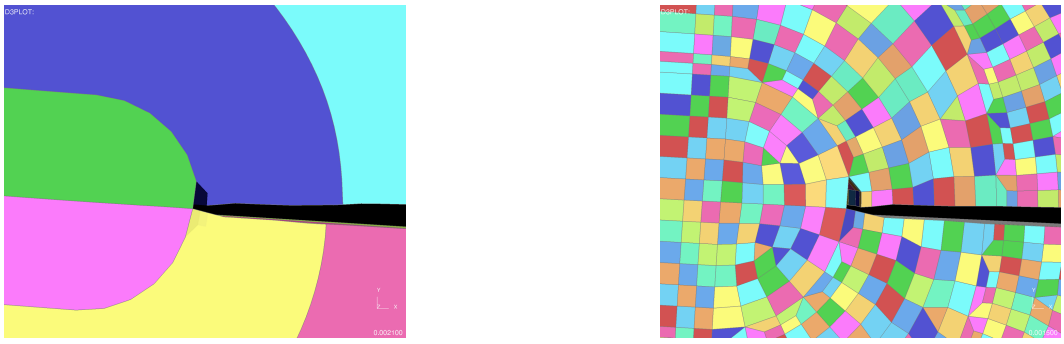

(a) Roughly discretised model

(b) Finely discretised model

Figure 8.6.5: Failure location for lap-shear finely and roughly discretised models

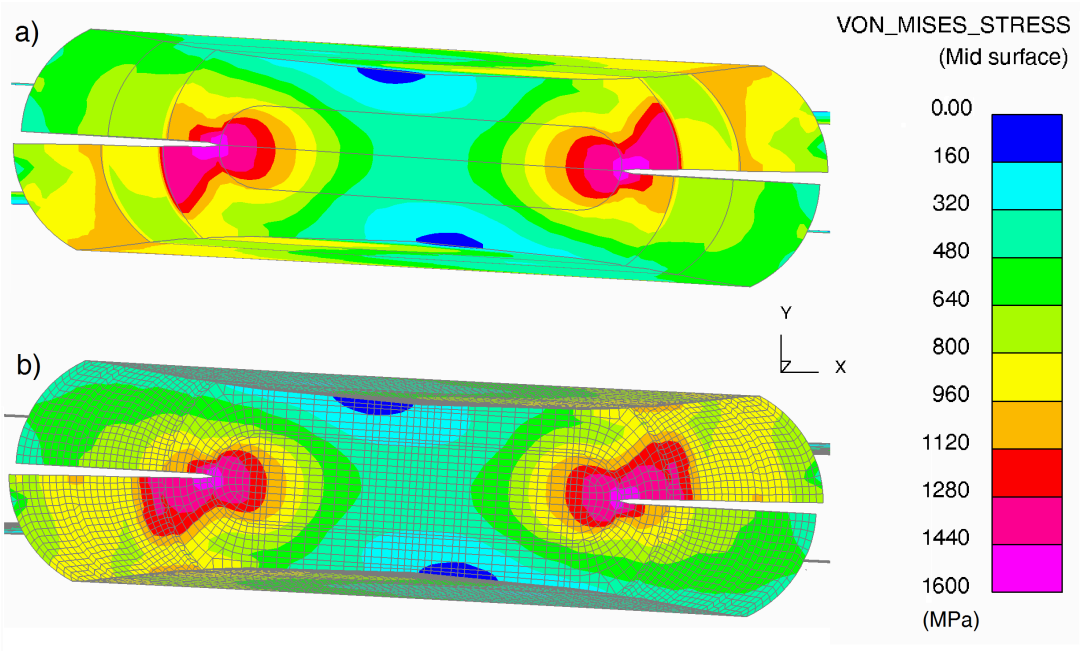

Figure 8.6.6: von Mises stress distributions of a) roughly and b) finely discretised lap-shear models in the x-y plane just before initial failure at the notch tip

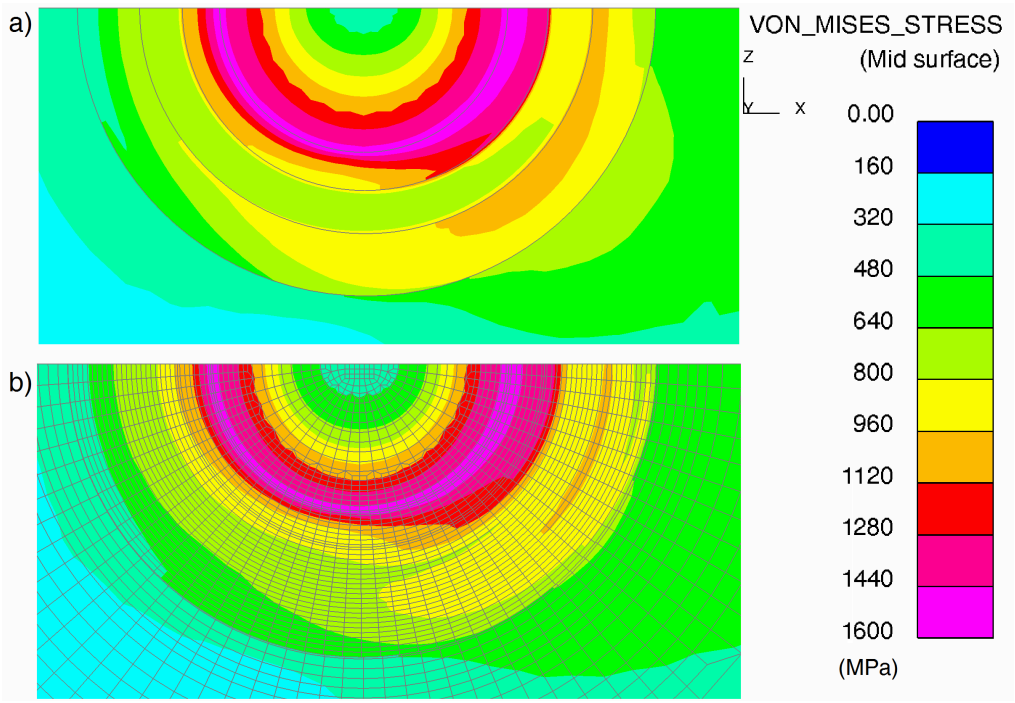

Figure 8.6.7: von Mises stress distributions of a) roughly and b) finely discretised lap-shear models in the x-z plane just before initial failure at the notch tip

The strain distributions, taken just before failure, are shown in figure 8.6.8. Both models show similar strain contours around the notch tip. A secondary high strain contour can be seen for the rough model, at the border between Zone 1 and Zone 2. This strain contour is most likely due to the sudden, significant change in material properties between the two sections. The fine model also shows a secondary high strain contour, with a value of approximately 0.0039. The centre of this secondary strain contour lies exactly at 4.2 mm, where the lowest hardness value is in the physical weld HAZ. This area of reduced mechanical properties is therefore causing this secondary strain development.

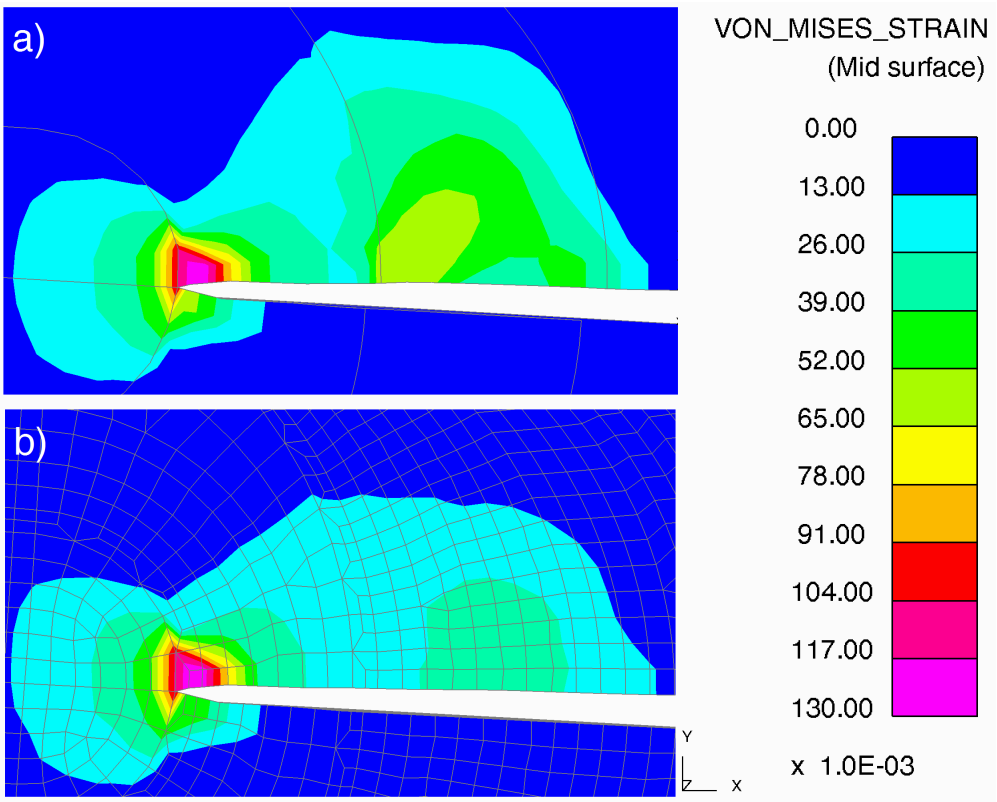

Figure 8.6.8: Strain distributions of a) roughly and b) finely discretised lap-shear models in the x-y plane just before initial failure at the notch tip

8.6.3.2 Strain evolution in HAZ

The loading responses through the HAZ of the rough and finely discretised models are investigated. Figure 8.6.9 a) shows three points of interest on the load-displacement curves. The first point is approximately half of the maximum load. Point 2 is just prior to initial failure and point 3 indicates the maximum load. Image b) shows the selected elements from which the strain data was extracted. The elements run from the notch-tip (3 mm) to the edge of the solid elements (6 mm). This element distribution gives a representative indication of the strain evolution and distribution which occurs in both models during loading.

Figure 8.6.9 c) shows the strain evolution and distribution from the selected elements. At point 1 during loading, both models exhibit similar strain distributions. Slightly higher strains develop at 3.9 mm for the rough model. This is because the Zone 1 and Zone 2 boundaries lie at 3.8 mm. It is therefore the sudden change in material properties at this border which is causing the slight strain increase.

The difference between the two models becomes evident at points 2 and 3 during loading. The rough model exhibits peaks in strain at the zone borders, at 3.9 mm (Zone 1 - Zone 2 border) and 4.7 mm (Zone 2 - Zone 3 border). Significantly higher strains have developed at the border between Zone 1 and Zone 2. The finely discretised model exhibits a strain peak at 4.3 mm, where the area of reduced mechanical properties is situated.

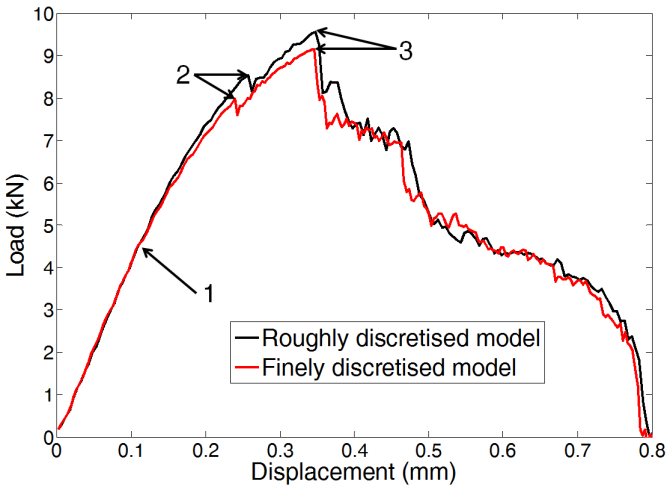

(a) Load-displacement curve for rough and finely discretised lap-shear models indicating points of interest during loading history

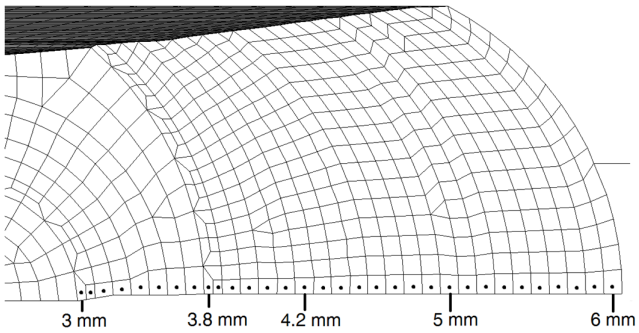

(b) Selected elements from which strains were extracted

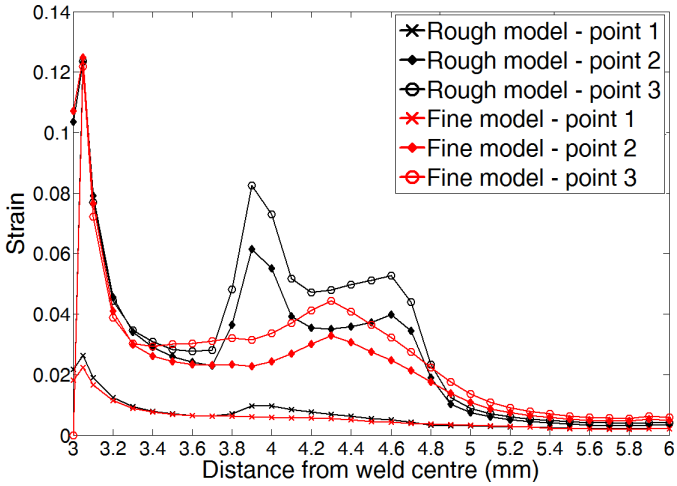

(c) Strain evolution and distribution through HAZ. Points 1 - 3 correspond with those indicated on the load-displacement curve

Figure 8.6.9: Strain evolution and distribution through HAZ of rough and finely discretised lap-shear models

8.6.3.3 Failure in relation to failure loci

The failure criteria for the FE models are based on the strain versus triaxiality curves, where triaxiality is defined as

$$\eta = \frac{\frac{1}{3}(\sigma_1 + \sigma_2 + \sigma_3)}{\sigma_{VM}}$$

where η is the stress triaxiality, $\sigma_{1,2,3}$ are the principal stresses and σ_{VM} is the von Mises stress.

A selection of elements will be used to investigate the strain-triaxiality evolution from initial loading, until severe loss of mechanical integrity, indicated as point 4 on the load-displacement curve in figure 8.6.10. At point 1 on the load-displacement curve, the element labelled 1 fails. The failed element is also indicated on the FE model picture labelled 1. The same labelling principle applies for elements 2, 3 and 4. The strain and triaxialities values were extracted from the indicated solid elements in both the rough and finely discretised models, with the results presented in figure 8.6.11.

Figure 8.6.11 a) shows the failure curve assigned to the elements which failed, along with the strain-triaxiality evolution of each element for the rough and finely discretised model. It is clear that the experimentally measured failure curve does not extend into the large triaxiality range, where the elements have failed.

Figure 8.6.11 b) is a close-up view of the strain-triaxiality evolution of the failed elements. The rough and finely discretised models show very similar strain-triaxiality evolutions. As failure proceeds, the selected elements fail at lower strains. The elements fail over a relatively large triaxiality range, from approximately 0.7 to 1.1. In the absence of a curve in the high triaxiality range, LS Dyna will extrapolate the curve linearly according to the last tangent [P. DuBois, personal communication, Livermore Software Technology Corp.]. In other words, the software has extrapolated the curve using the gradient of the vertex at $\eta = 0.6$.

A conventional failure locus would exhibit a parabola with a positive gradient into the higher triaxiality range. The locus used in the simulation extrapolated the curve using the gradient of the vertex of the parabola, hence the extrapolated part has a gentle negative slope extending into the large triaxiality range. One would therefore expect that, had a wider encompassing failure locus been used, the elements would have failed at a higher strain, due to the positive gradient beyond $\eta = 0.6$. It may be concluded that linear extrapolation is not appropriate, as it deviates severely from the shape of a failure locus. Insufficient data was available to extend the failure locus into the large triaxiality range. The predicted global load at failure and displacement at failure of the simulations do not seem to be affected as they correlate well with the physical lap-shear test results.

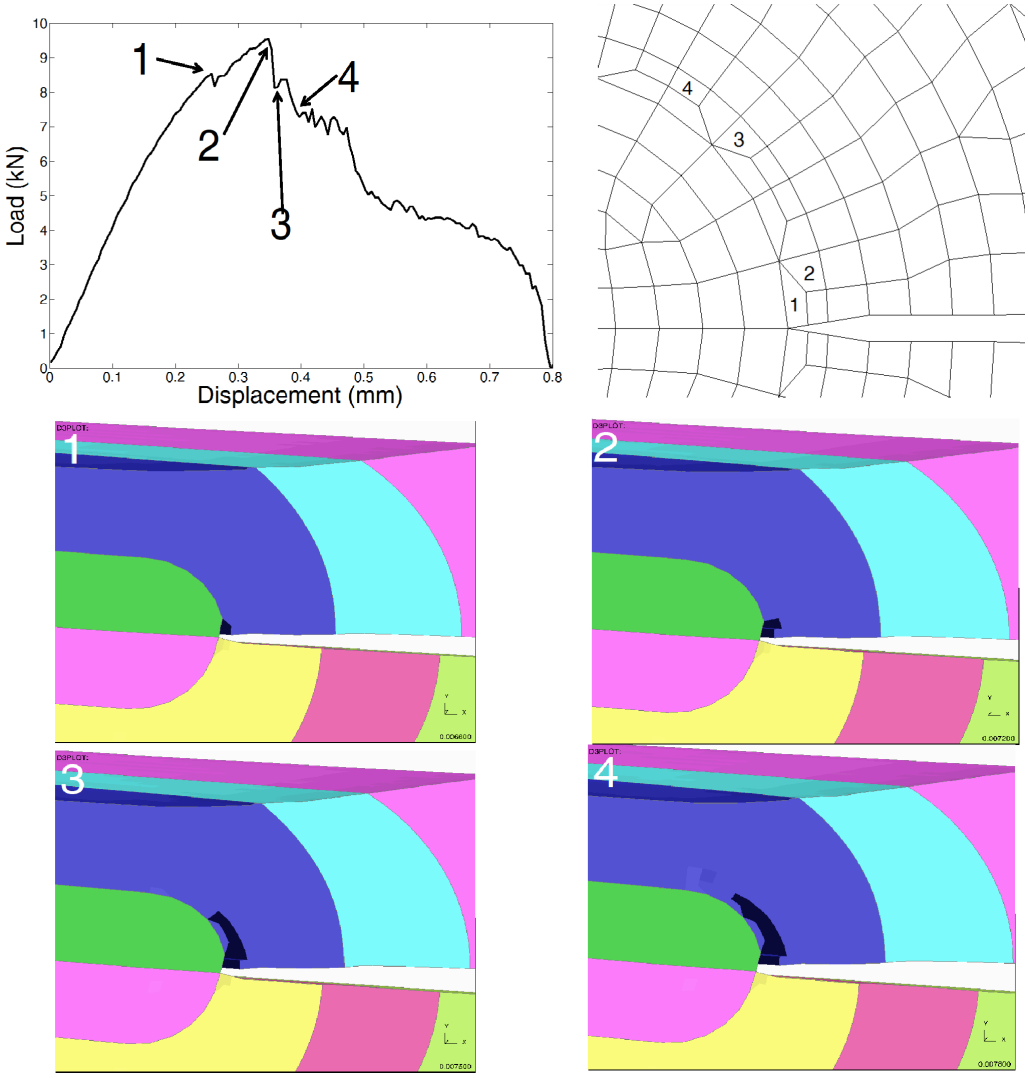

Figure 8.6.10: Selected elements and points on load - displacement graph for investigation into strain-triaxiality evolution during failure of lap-shear model. Element 1 fails at point 1 on the load-displacement graph, with the corresponding model failure labelled as 1.

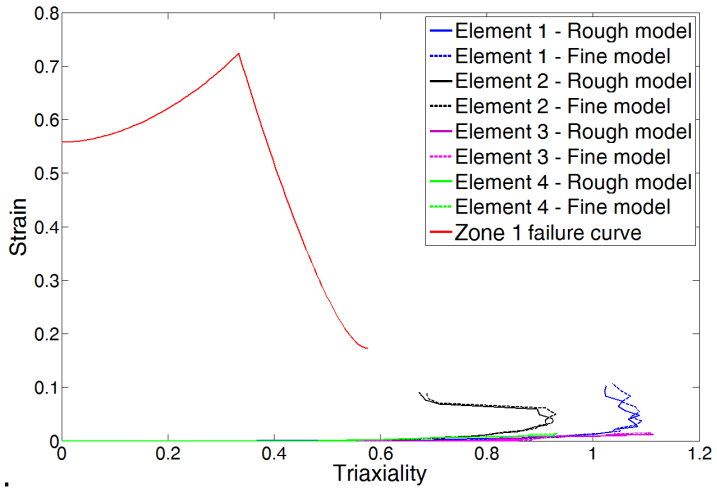

(a) Failure curve of Zone 1 with strain-triaxiality evolution of selected failed elements

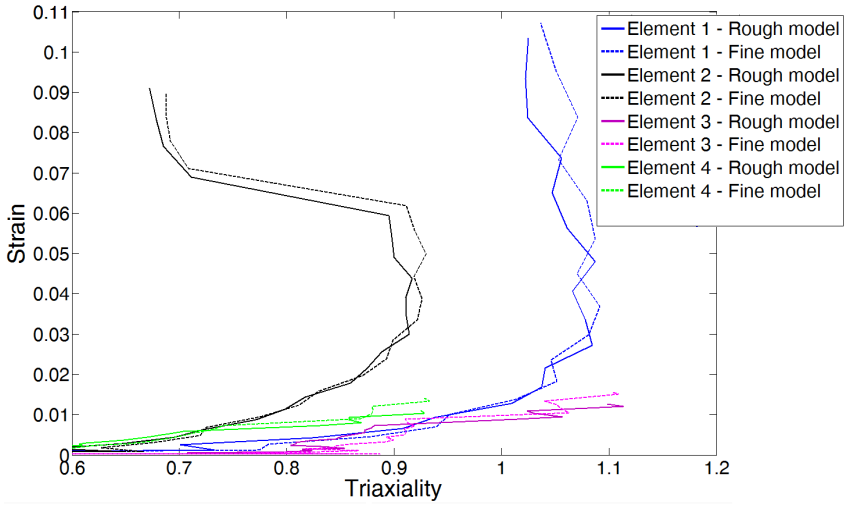

(b) Strain-triaxiality evolution of selected failed elements

Figure 8.6.11: Zone 1 failure curve with strain-triaxiality evolution of selected failed elements for rough and finely discretised lap-shear models

8.6.4 Comparison of lap-shear models with residual stresses

The red lines presented in figures 8.6.12 and 8.6.13 are the direct load - displacement output from the lap-shear models with residual stresses. The reason for the higher noise levels is because the high initial stresses are redistributed as the load is applied. This essentially sets up a vibration in the model which affects the force readings.

A possible method for reducing this noise is by applying global damping to the model for the first few timesteps. This would reduce the stress redistribution while some initial external loading is applied. After a few timesteps, the damping could be switched off and the model would run as normal. This method, however, adds complications. If the model is over-damped, it could freeze in a non-equilibrium position and when damping is switched off, large oscillations could eventually result as the model tries to find equilibrium. Overdamping can be difficult to detect, as the oscillations resulting from when damping is switched off may have small initial velocities and the overall effect may only be detected until later in the simulation [personal communication, D. Norman, Tata Steel].

The critical damping constant (D_{crit}) is related to the lowest natural frequency (ω_{min}) of the system through $D_{crit} = 2\omega_{min}$ [50]. Considering the variation in material properties through the model, in combination with the fact that deflections occur in a number of variations during loading, more than one frequency would be active in the model and hence very difficult to isolate the correct frequency. Trials were performed using damping, with unsatisfactory results. Further work is needed to compensate for the high oscillations that residual stresses introduce. Such work is beyond the scope of this thesis.

Thus, the residual stress FE model data presented in figures 8.6.12 and 8.6.13 do not use damping. It is interesting to note that the finely discretised model does not exhibit as extreme oscillations as the roughly discretised model. The only explanation for this difference is the distribution of material properties, as the rough and fine models are the same in every other respect.

The roughly discretised model with residual stress predicts a peak load of 0.28 kN less than the model without residual stress. The predicted displacement at failure is 0.01 mm less. For the finely discretised models, the difference in peak load is 0.04 kN and displacement at failure is 0.02 mm. From these observations, it may be concluded that including residual stresses have negligible effects on the failure prediction of lap-shear samples. This observation corresponds well to the findings of Ainsworth [67], who

stated that the effects of residual stresses are only noticeable in the elastic regime.

The strain - triaxiality evolutions in the models with residual stresses follow a similar pattern to those presented in figure 8.6.11. The damage evolution and strain distribution evolutions also showed negligible differences compared to the models without residual stresses.

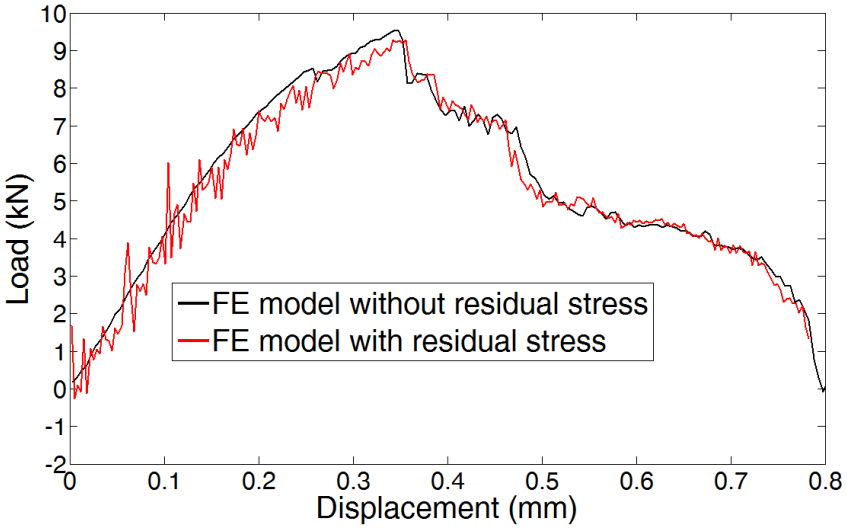

Figure 8.6.12: Load - displacement graphs of roughly discretised lap-shear models with and without residual stress

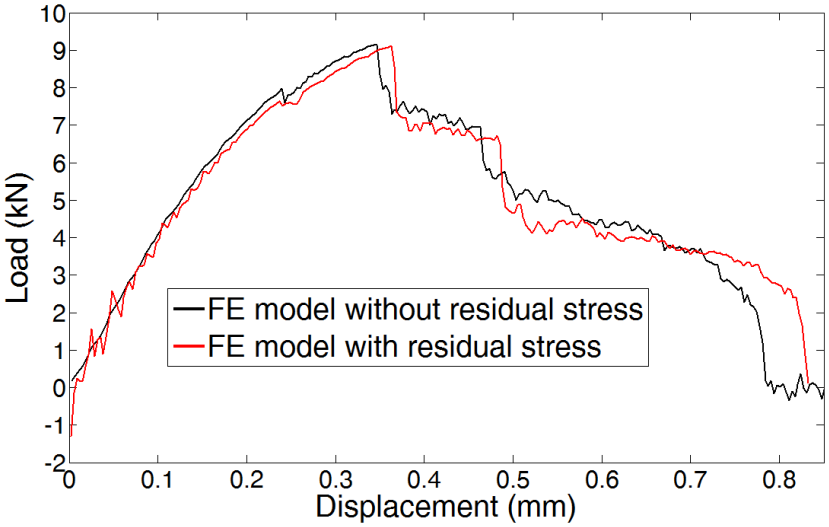

Figure 8.6.13: Load - displacement graphs of finely discretised lap-shear models with and without residual stress

8.7 Cross-tension simulation results

As mentioned previously, an extensometer could not be placed onto the cross-tension testing rig, hence the experimental load-displacement curves contain machine displacement. The FE model does not take machine displacement into account and hence the experimental and FE displacement will not be directly compared. To make comparisons of experimental and simulated peak loads visually easier, the model displacements have been scaled in order to line up the model peak loads with the experimental ones. The load results have not been scaled.

8.7.1 Load - displacement results

The simulated load - displacement curves for the rough and finely discretised models are compared with the 5 experimental cross-tension results, shown in figure 8.7.1. The average experimental peak load is 1.48 kN, where the experimental peaks loads are taken just before the sudden load drop. The load - displacement curve of the roughly discretised model shows some minor drop in load between reaching the peak load and the final sudden load drop. For consistency, the simulated peak load is taken just before the final sudden load drop. Therefore, the simulated peak load is 1.37 kN, giving a conservative 0.11 kN underestimation. The simulated peak load of the finely discretised model is 1.46 kN, giving a 0.02 kN underestimation. It appears that the model exhibits a stiffer loading response than the experimental samples, but this could be due to the displacement scaling.

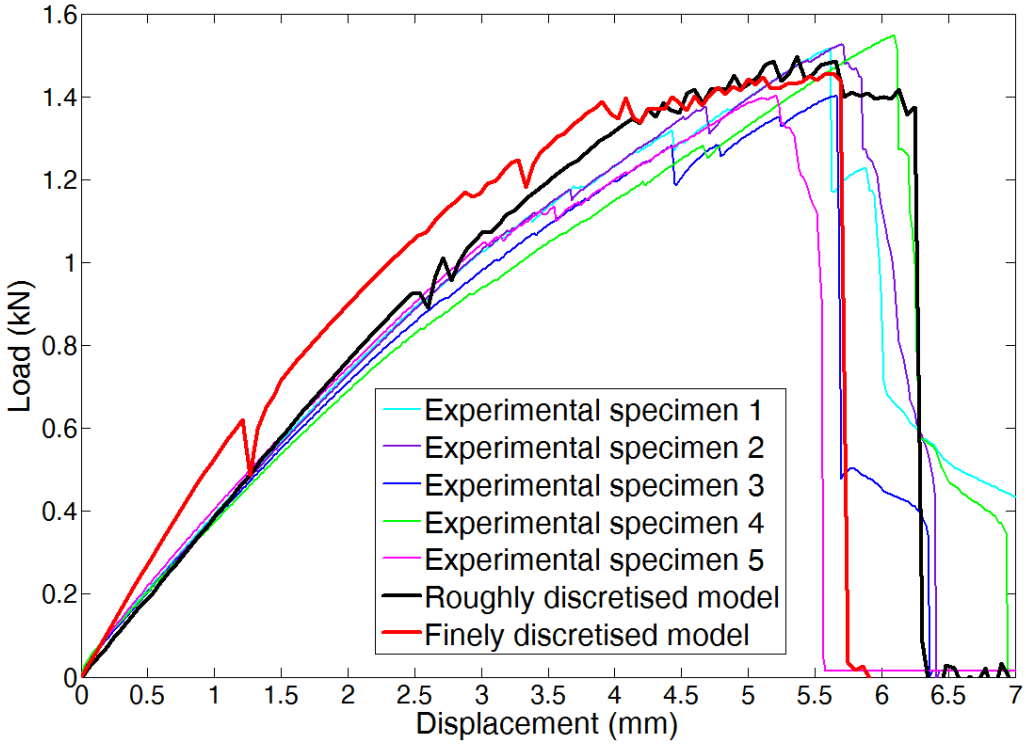

Figure 8.7.1: Load - displacement curves for rough and finely discretised cross-tension models, with experimentally measured curves.

8.7.2 Damage evolution

In contrast to the lap-shear simulations, the rough and fine cross-tension models show noticeable differences in damage evolution. Figure 8.7.2 shows the damage evolution at selected points for both models. The load - displacement curve has not been scaled as in the previous figure, i.e., the displacements have been taken directly from the models.

Damage initiates and grows to a greater degree not at the symmetry faces, as was the case for the lap-shear models, but actually between the symmetry faces. The cross-sectional images presented in figure 8.7.2 are therefore taken at 45 ° to the symmetry faces to give a representative view of the average damage evolution. Damage initiates at points R1 and F1 for the rough and finely discretised models respectively. As can be seen, the damage initiates at the nugget periphery, just to the left of the notch tip.

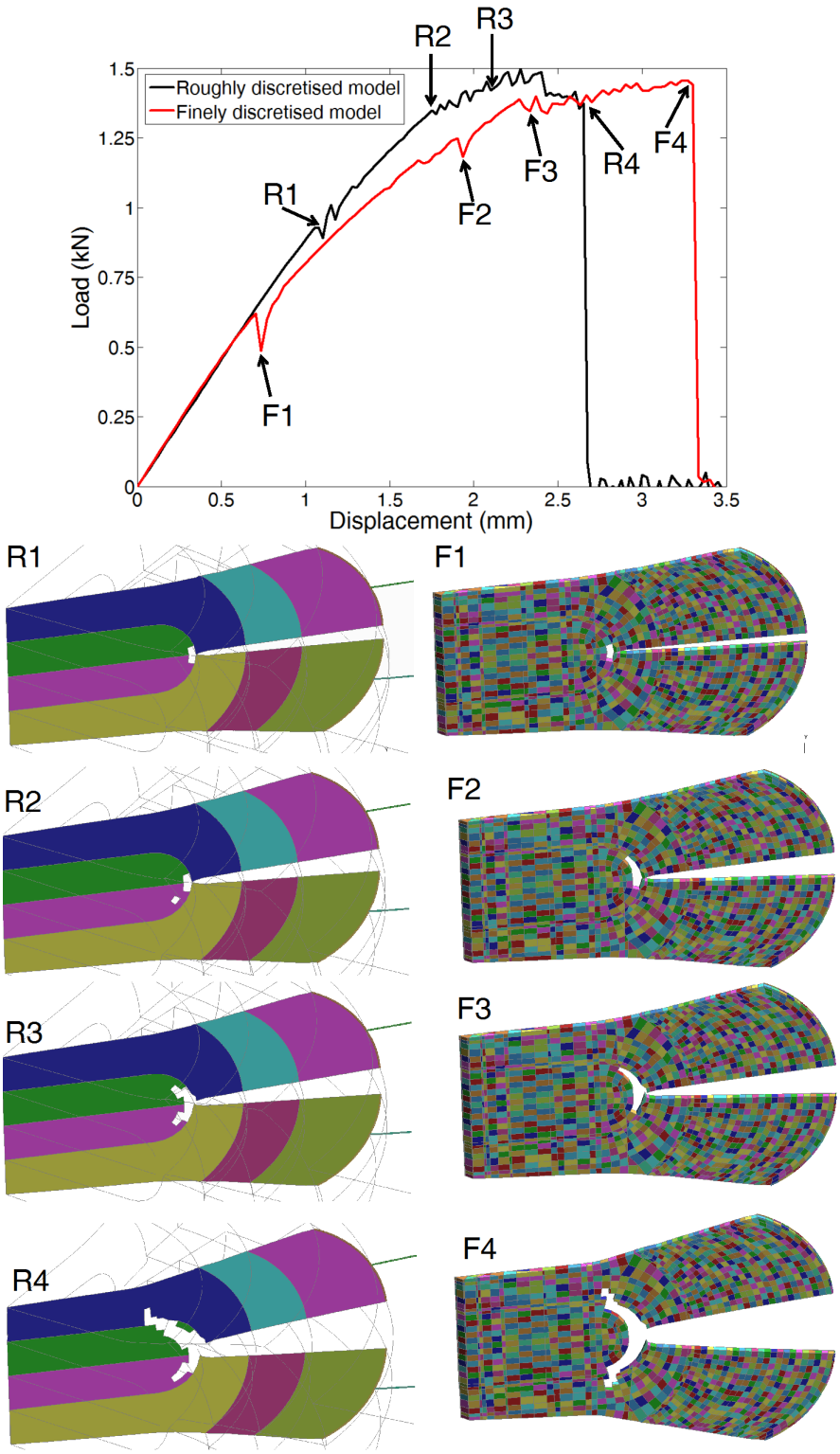

Figure 8.7.2: Damage evolution of roughly discretised cross-tension model

The reason for a greater drop in load for the fine model is shown in figure 8.7.3, where more elements have been deleted in the fine model, indicated by the thick black marker lines. The images show the damage at the bottom sheet faying surface, however, a mirror image of the damage has occurred in the top sheet.

Further damage occurs along the nugget periphery in the weld thickness direction at points R2 and F2. At points R3 and F3, the notch tip separates. At point R3, symmetrical damage has developed around the notch tip. For point F3, however, a greater amount of damage has occurred in the upper half of the weld. The situation has reversed at points R4 and F4, with the finely discretised model exhibiting symmetrical damage. At these points, damage has travelled into Zone 1. Figure 8.7.4 shows the final button pull-out fractures of the models.

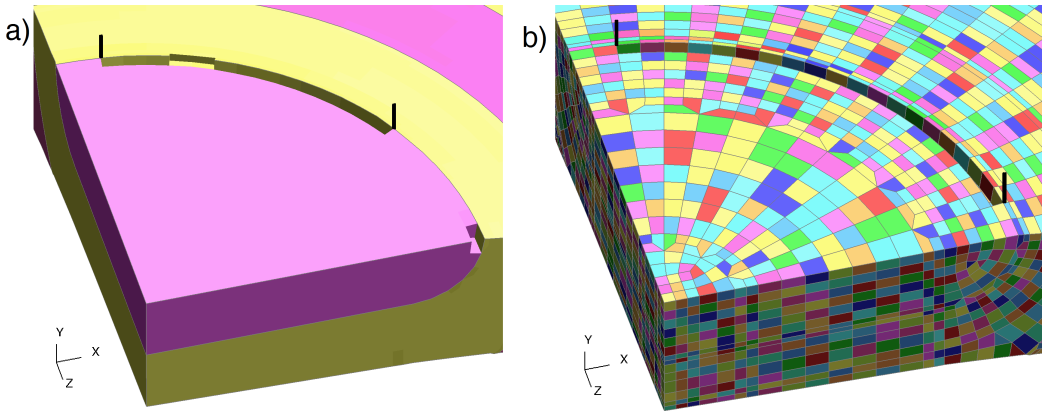

Figure 8.7.3: Initial failure on the bottom sheet faying surface of the a) rough and b) finely discretised cross-tension models

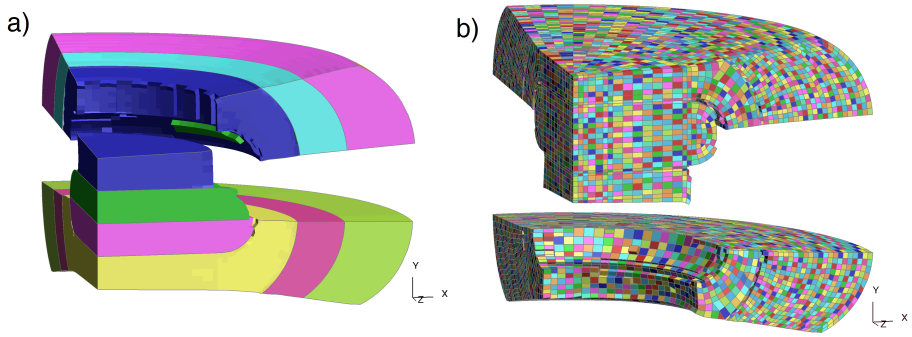

Figure 8.7.4: a) Rough and b) finely discretised cross-tension model final fractures

8.7.3 Comparison of rough and finely discretised cross-tension models

8.7.3.1 Stress and strain contours

The stress distribution, just before initial failure, on the x-y plane is presented for the rough and finely discretised models in figure 8.7.5. Equivalent stress magnitudes have developed at the notch tip for both models. For the roughly discretised model, a circular region of high stress (approximately 1120 MPa) has developed just inside the nugget.

The same stress contours are presented on the x-z plane at the upper sheet faying surface in figure 8.7.6. It is evident that a significantly larger area of high stress has developed in the roughly discretised model. The strain distribution just before initial failure is shown on the upper sheet faying surface in figure 8.7.7. The finely discretised model exhibits approximately half of the maximum strain of the rough model. A more in-depth investigation of the strain evolution through the HAZ will be given in the next section to try and establish the reason for the difference between the two models.

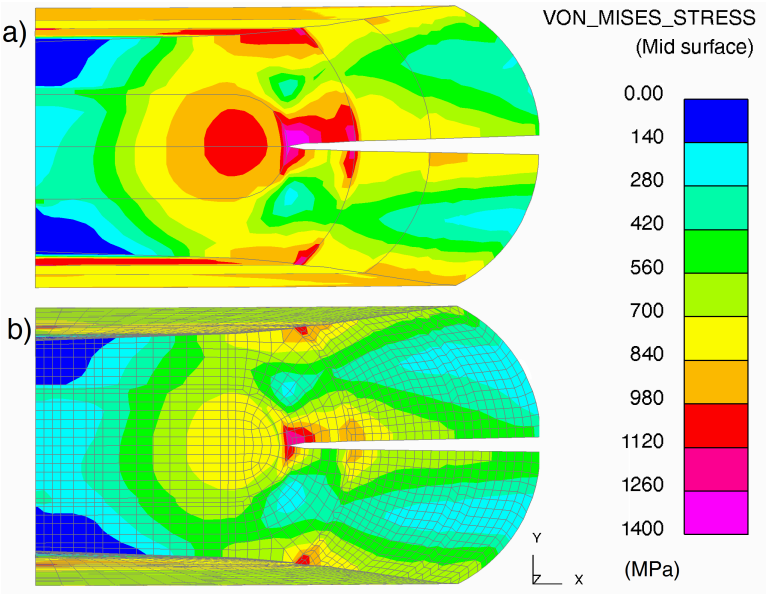

Figure 8.7.5: von Mises stress distributions of a) roughly and b) finely discretised cross-tension models in the x-y plane just before initial failure

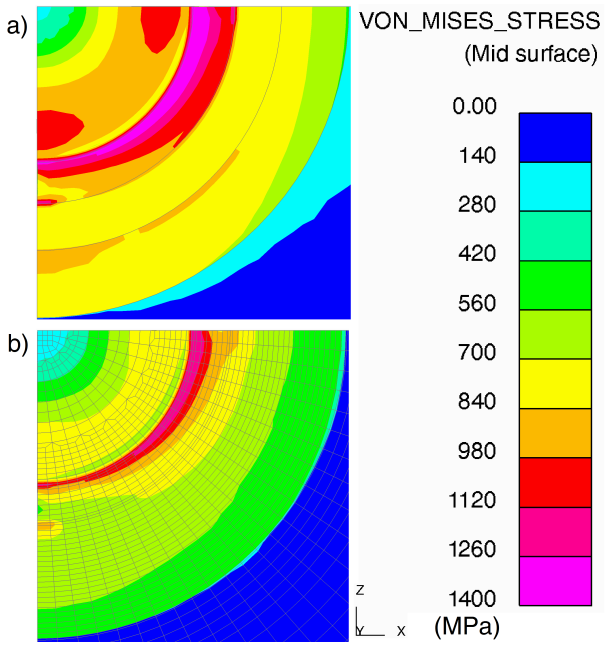

Figure 8.7.6: von Mises stress distributions of a) roughly and b) finely discretised cross-tension models in the x-z plane just before initial failure

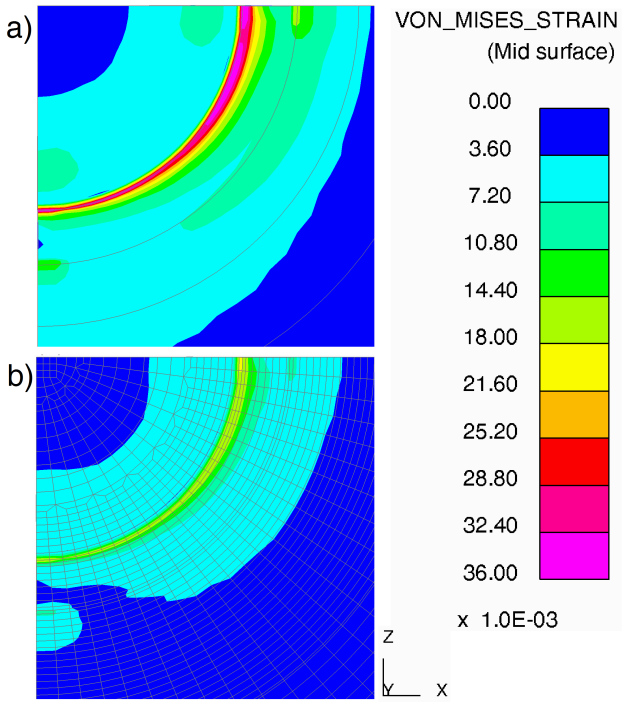

Figure 8.7.7: von Mises strain distributions of a) roughly and b) finely discretised cross-tension models in the x-z plane just before initial failure

8.7.3.2 Strain evolution in HAZ

The strain evolution of the same elements previously indicated in figure 8.6.9 b) are investigated. The selected points of interest on the load - displacement curve are shown in figure 8.7.8 a), with the strain evolutions shown in image b). The effect of the different material properties was evident in the strain distribution evolution presented for the lap-shear models. For the cross-tension models, however, it seems that the effect of geometry has a much greater influence on the strain distribution evolution. Excluding the strain magnitudes, negligible differences can be seen for the rough and finely discretised models, with both exhibiting a strain concentration at 3.8 mm. This concentration is likely caused by the BM sheet bending as it is pulled upward and the thick nugget being restrained. The distribution shown in figure 8.7.8 b) therefore suggests that the geometric effects of bending have a greater effect on the developed strain distributions than the distribution of material properties. The difference in strain magnitudes could be the result of the material property distributions causing greater or lesser bending depending on whether the model is roughly or finely discretised.

8.7.3.3 Failure in relation to failure loci

A selection of elements are used to investigate the strain-triaxiality evolution from initial loading, until severe loss of mechanical integrity, indicated as point 4 on the load-displacement curve in figure 8.7.9. The failure curve assigned to the elements which failed, along with the strain-triaxiality evolution of each element for the rough and finely discretised model are shown in figure 8.7.10 a). As with the lap-shear models, the elements failed at small strains and larger triaxialities than the experimentally extracted failure curve encompasses. Figure 8.7.10 b) shows a close up view of the strain - triaxiality evolutions. Only the final stages of the R1 and F1 elements are shown, as the triaxiality of these elements reached $\eta = 5$, as shown in image a). All elements, except elements R1/F1 fail at approximately $\eta = 1$ and at strains between 0.065 and 0.08.

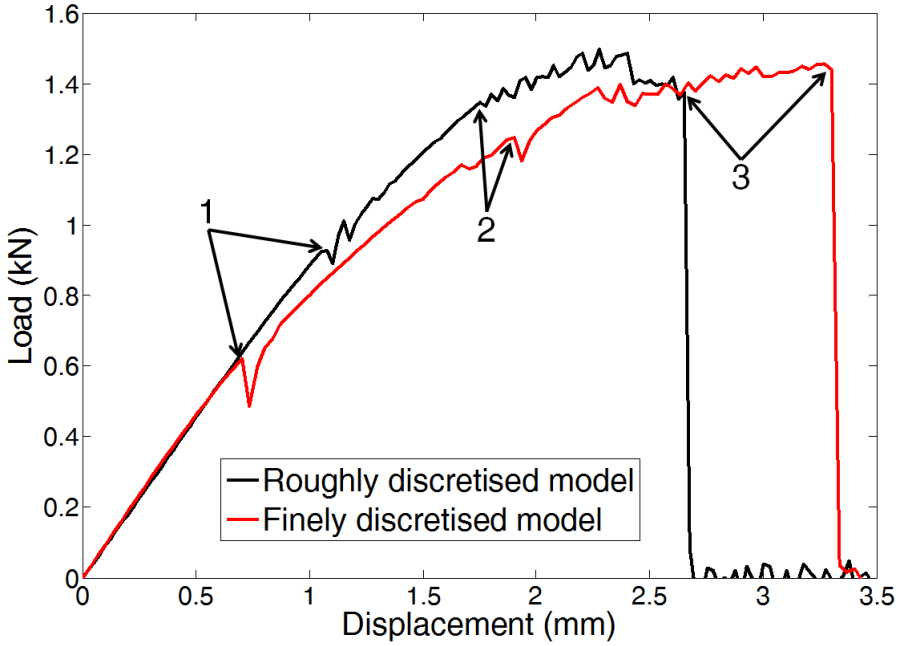

(a) Load-displacement curve for rough and finely discretised cross-tension models indicating points of interest during loading history

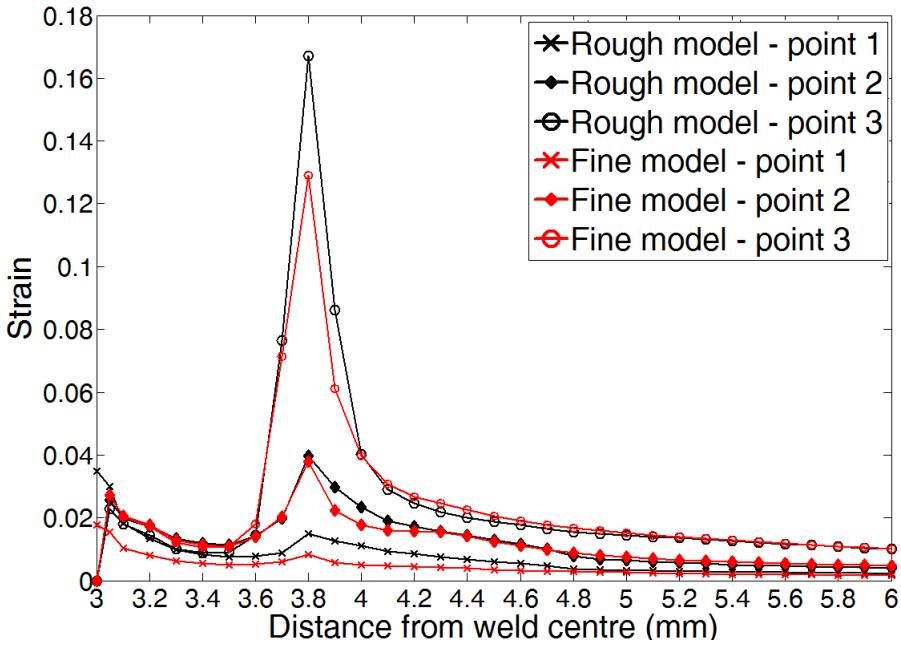

(b) Strain evolution and distribution through HAZ. Points 1 - 3 correspond with those indicated on the load-displacement curve

Figure 8.7.8: Strain evolution and distribution through HAZ of rough and finely discretised cross-tension models

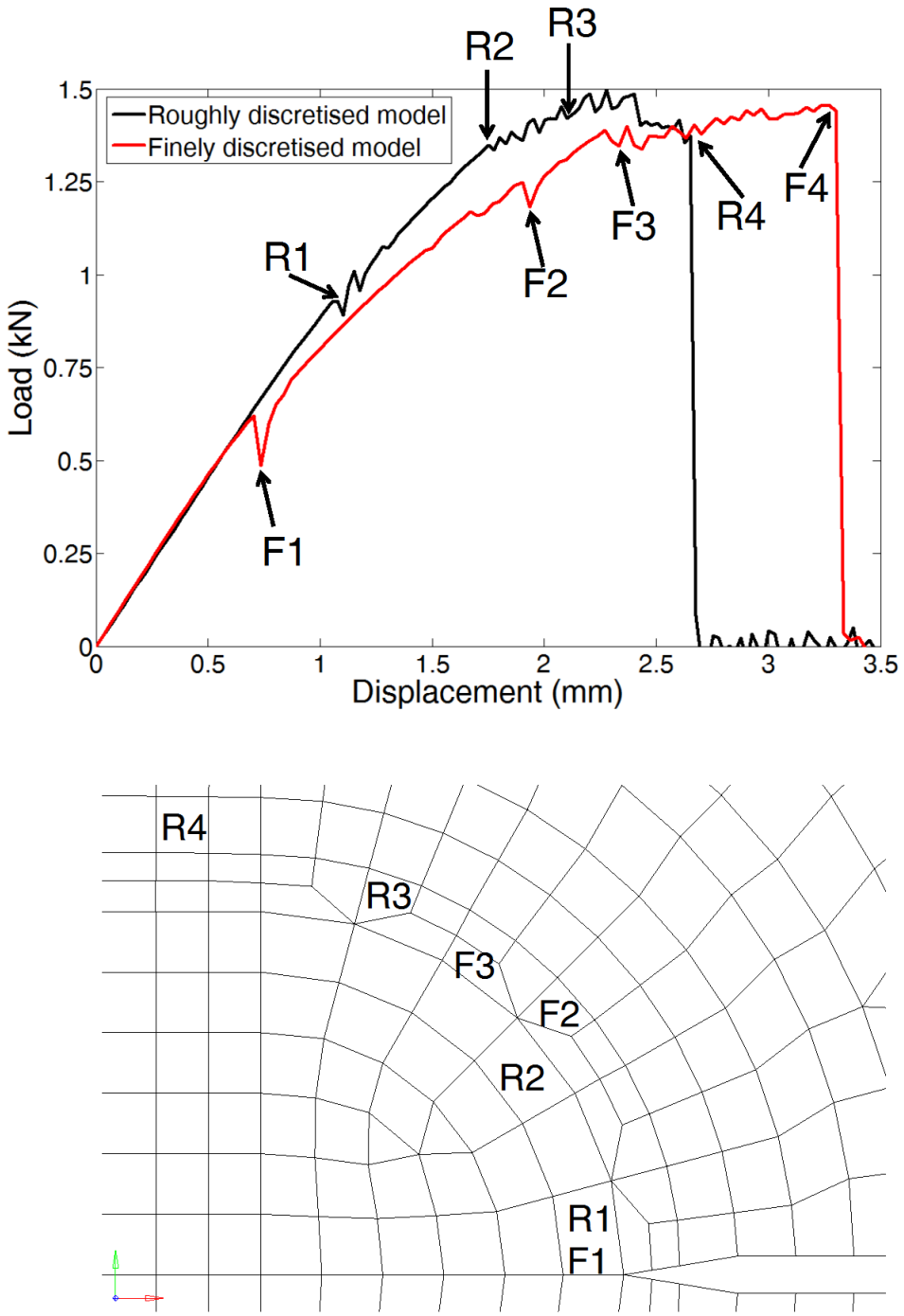

Figure 8.7.9: Selected elements and points on load - displacement graph for investigation into strain-triaxiality evolution during failure of cross-tension models. Element R1/F1 fails at point R1/F1 on the load-displacement graph.

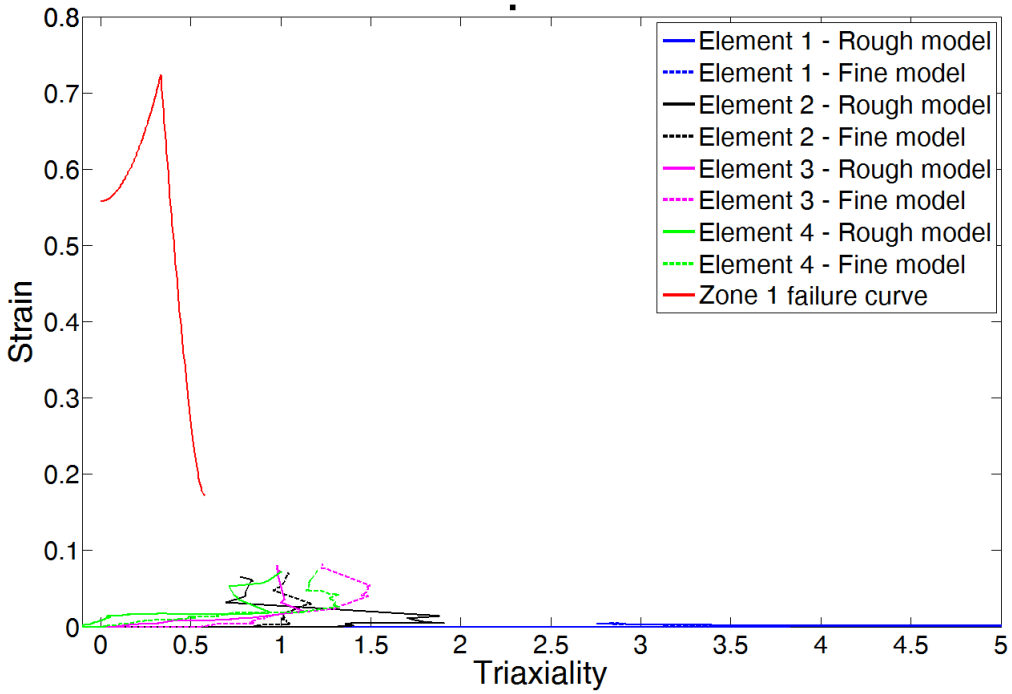

(a) Failure curve of Zone 1/nugget with strain-triaxiality evolution of selected failed elements

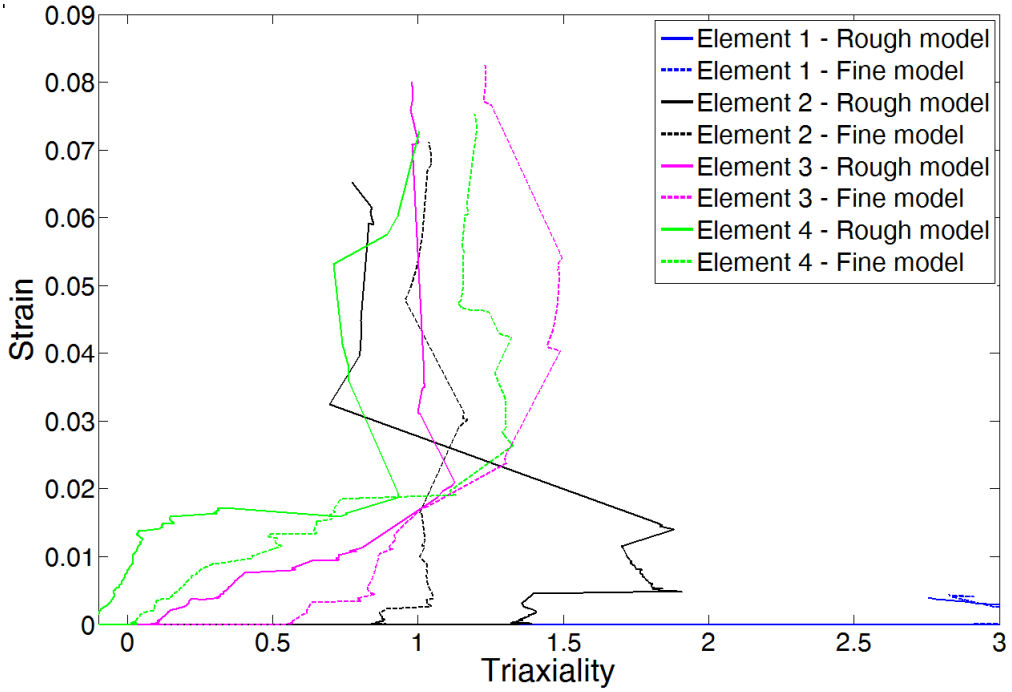

(b) Strain-triaxiality evolution of selected failed elements

Figure 8.7.10: Zone 1/nugget failure curve with strain-triaxiality evolution of selected failed elements for rough and finely discretised cross-tension models

8.7.4 Comparison of cross-tension models with residual stress

Figure 8.7.11 a) compares the load - displacement curves of the roughly discretised cross-tension models with and without residual stress. The load - displacement curves generally follow one another, with a difference of 0.06 kN in peak load and 0.1 mm in displacement at failure between the two models.

Figure 8.7.11 b) compares the finely discretised models with and without residual stress. In this figure, the oscillations resulting from failed elements are easier to see and it can be seen that failure occurs at approximately the same load and displacement as the model without residual stresses. There is a 0.04 kN difference of peak load and and 0.1 mm difference in displacement at failure between the models. As with the lap-shear models, significant noise is present at initial loading and the finely discretised model exhibits superior damping capabilities.

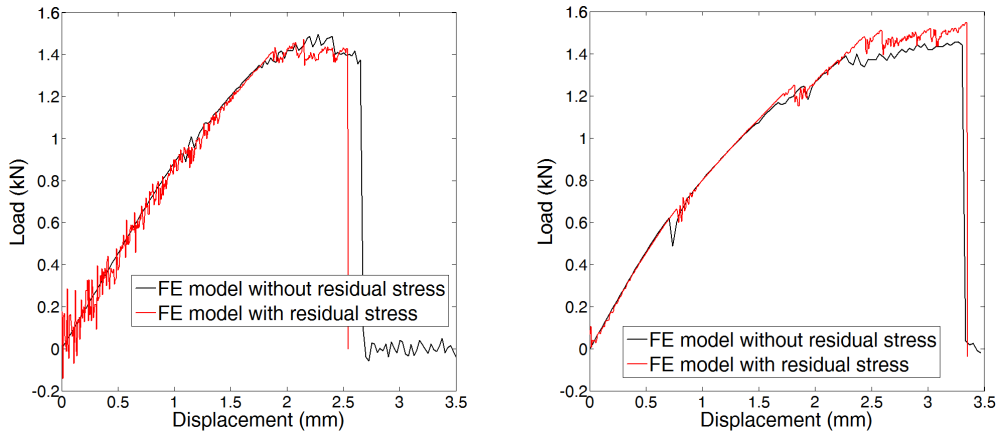

(a) Roughly discretised cross-tension models (b) Finely discretised cross-tension models

Figure 8.7.11: Load - displacement graphs of rough and finely discretised cross-tension models with and without residual stress

8.8 Conclusions

Two model geometries were presented; lap-shear and cross-tension. Four variations of each geometry were investigated. The roughly discretised model had 5 unique stress-

strain and 5 unique failure loci assigned to the weld sections. The finely discretised model had 29 stress-strain and 29 failure loci assigned as a function of the distance from the weld centre. Variants of these models were also presented with experimentally measured residual stresses assigned as a function of the distance from the weld centre.

A novel approach to discretising an FE model was presented. Whereas the rough model was discretised in the mesh design stage, the fine model was discretised using a MatLab script. The element sizes in the meshed model were used to define the level of discretisation. In other words, the elements were approximately 0.1 mm long, and the material properties and process induced states were interpolated in steps of 0.1 mm. Therefore, the fine model was discretised in steps of 0.1 mm.

Use was made of the fact that the FE model could be altered in the form of a text document. Loops were used in the MatLab script to write a document which assigned the interpolated material properties (stress-strain curves, failure loci) and process induced states (residual stresses) to each element in the FE model. Such a technique is not restricted to fine discretisation. For example, if one wishes, the FE models could be discretised in any multiple of 0.1 mm. Such a technique opens up a convenient way to redefine the same model in terms of discretisation. For example, if one has a meshed model of a bolt or an automotive drive shaft, such a model can be refined or coarsened in terms of material property distribution without having to remesh the model. Of course, the technique presented is currently limited to radially symmetric objects.

The results of the lap-shear modelling without residual stresses will be firstly discussed. Good correspondence to the experimentally measured load - displacements curves were seen for the rough and finely discretised models. The rough and fine models underestimated the peak load by 6% and 10%, respectively. This difference in predictive capabilities was due to the material discretisation of the two models. The developed strain distributions through the HAZ showed that artificial strain concentrations occurred at the material boundaries in the roughly discretised model. The finely discretised model exhibited a strain concentration at the point which was previously identified as a location of reduced mechanical properties.

The cross-tension models without residual stress showed good correspondence with the experimental load - displacement curves. The rough and fine models underestimated the peak load by 7% and 1%, respectively. Negligible differences were seen in the developed strain distribution through the HAZ in the two models.

An interesting observation was made by investigating the HAZ strain distributions. The material discretisation had a noticeable effect on the developed strain distributions for the lap-shear models. For the cross-tension models however, the effect of geometry had a much greater influence on the strain distribution evolution, with the effect of bending dominating over any material response.

The elements in the lap-shear and cross-tension models failed within a triaxiality range of 0.7 to 1.5. These values are beyond the scope of the triaxiality measured from the Gleeble physical simulation samples. An improvement to the failure model would be to extend the failure curves into the large triaxiality range. This would be accomplished by destructively testing round bar specimens with various notch radii [118]. As stated previously, boron steel was not available in round bar form at the time of testing.

The final failure mode for all models was button pull-out. The simulated failure type is due to the fact that a ductile failure modelling approach was used. In order to simulate potential brittle interfacial failures, fracture criteria incorporating material fracture toughness or "cohesive zone" models, as described in the Literature Review, would be needed. The brittle fracture limit of a material depends on the material fracture toughness. Materials with low fracture toughness (like glass) fracture in a brittle manner by cracking. For most thin gauge steels, the material fracture toughness is usually sufficiently high for brittle fracture not to be of great concern, with the sheet usually failing as a consequence of ductile fracture.

As shown in the SEM investigations described previously, some areas of brittle failure were observed in lap-shear and cross-tension geometries. This suggests that those regions could have a lower material fracture toughness than one might expect for steel, due to the nature of the extreme heating and cooling combined with the steel chemistry.

The modelling of brittle fracture is a class of problem outside the scope of this thesis. Nevertheless, it seems that the majority of failure occurred by ductile fracture, which accounts for the relatively accurate load - displacement simulations.

The inclusion of residual stresses in the models resulted in unexpected noise in the load - displacement curves resulting from initial stress redistribution. The residual stresses had negligible effects on the load - displacement curves, compared to the equivalent models without residual stresses. For a problem such as destructive tensile testing of welds, the inclusion of residual stresses seems unnecessary. Nevertheless the method of including these stresses opens up exciting possibilities into modelling fatigue problems, where residual stresses are expected to have a greater effect [148]. To this authors knowledge, the incorporation of measured residual stresses into an FE model has not been performed in such detail.

Chapter 9

Conclusions

During spot welding of boron steel, the weld and surrounding material are exposed to a wide range of temperatures, from the melting point at the weld centre to room temperature in the base material. As a consequence, the weld exhibits varying microstructures with corresponding varying material properties, in addition to the distribution of residual stress. It was identified that the material property gradients could potentially have a profound influence on the load bearing capacity and failure strength of the weld as a whole. Additionally, boron steel spot welds exhibit unique hardness profiles. The nugget and base material exhibit high hardness values, with a significant drop in the HAZ. The cause for this sudden drop was established to be due to tempering of the parent martensitic microstructure [41, 42, 43].

It has been stated that the structural differences between the hard BM/nugget and soft HAZ may enhance the stress concentrations around the notch tip [46] and promote strain localisation [45]. Specifically for martensitic steels, the soft HAZ was identified as a critical area with limited deformation capacity [31]. These observations emphasised the need to characterise the HAZ.

The presence and location of the soft HAZ was a major influencing factor in the choice of failure prediction method. Although empirical and analytical methods circumvent the need for significant experimental efforts in extracting material properties, they were deemed unsuitable for application to boron steel welds. This is due to the fact that the majority of these methods make an assumption that the weld can be modelled as a "rigid button" embedded in a ductile sheet. This assumption may be valid for steels such as DP600, where the nugget exhibits significantly higher hardness values than the

BM. However, this assumption cannot be applied to boron steel welds, where the soft HAZ is surrounded by the hard nugget and hard BM. The recommendations by different authors [35, 31] to take HAZ softening into account in performing failure prediction added further justification for pursuing the local extraction of material properties, leading to a more capable failure model.

Dancette [45, 55] and Sommer [31] both recreated HAZ microstructures onto larger tensile specimens, through the use of a Gleeble physical simulator. The weld microstructures were simulated by exposing steel sheet samples to similar thermal histories as those experienced by the corresponding weld regions. Material constitutive behaviour, in the form of stress - strain curves and failure strain versus triaxiality curves (known as failure loci), was subsequently extracted through tensile testing and used as input to FE models for weld failure prediction.

It was recognised that improvements to Sommer's work could be made. Sommer used a standard dog-bone specimen to obtain the uniaxial data point on the $\varepsilon_f - \eta$ locus. It was established that this specimen actually tends towards a plane-strain state during necking [36]. This is especially true for more ductile materials, as might be found in the soft HAZ. The first improvement was thus the use of a tensile sample with a central hole, to ensure a recorded failure strain closer to the uniaxial stress state. In extracting constitutive behaviour from the Gleeble tensile samples, Sommer performed inverse FE simulations, where material properties were incrementally varied to match the simulated force-displacement curves to the experimentally measured ones. Slight deviations from the experimental load-displacement curves were seen, indicating that improvements can be made by directly measuring the tensile samples using Digital Image Correlation (DIC). The second improvement is thus measuring the failure strains and stress states directly from the tensile samples.

Due to the practical limitations of the Gleeble technique, deviations from the target microstructures were expected. It was therefore recognised that a method of verifying that the simulated samples corresponded to the target microstructures was needed. Dancette and Sommer performed validation through optical microscopy. In this project,

it was investigated whether such validation could be performed in a more quantitative manner. The methods chosen to do this were hardness testing and comparing the yield strengths of the Gleeble sample stress - strain curves with the yield strengths extracted directly from the physical weld through instrumented indentation. As instrumented indentation is used as a tool for extracting material properties, an algorithm developed by Dao *et al* [77] was selected as the most complete, usable method.

The weld process inherently produces localised residual strains which also need to be accounted for in the model simulation, together with significant plastic strain redistributions resulting from the mechanical loading of the spot weld to its ultimate failure. Residual stresses have been reported as contributing to spot weld failure [45, 54, 18] and significantly affect the load carrying capacity in the elastic regime [67]. To the authors knowledge, the residual stress distribution of boron steel spot welds have not be measured before. Additionally, such measured residual stresses have not been incorporated into FE models to such a detail as done in this work.

The three experimental arms of this work were thus identified to be:

- Physical simulation of specific weld microstructures, with subsequent material property extraction.
- Extraction of the yield strength distribution of the weld through instrumented indentation.
- Measurement of residual stresses through neutron diffraction.

To be able to perform tests, physical welds had to be produced. As the key purpose of this project was to investigate the mechanical behaviour of welds *currently used in the automotive industry*, a weld schedule obtained from an automotive manufacturer, specifically designed for welding boron steel, was used in this study. Welding trials were performed by varying parameters of the weld schedule. From these trials, the following conclusions were drawn. An increase in current pulse time, from 600 ms to

1000 ms, had a negligible effect on the final nugget diameter. A possible explanation could be that the steel conducted the heat away as fast as it received it. By varying the electrode force, the SORPAS welding simulation results were confirmed, where a lower force resulted in larger nugget diameters. The expulsion limit of the steel was found, where currents above 7.5 kA resulted in a sudden increase in expulsions. From these welding trials, the optimum weld schedule parameters were confirmed and sample welds for material property extraction could be produced with confidence.

Welding trials on DP600 were performed in conjunction with those of boron steel. In this thesis, DP600 is used as a reference material. The DP600 steel is well documented and provides a ready source from which to verify experimental results. For example, the known yield strength of the BM will form one of the validation parameters from which to gauge the accuracy of the instrumented indentation tests. The steel will also provide valuable insight in relation to the neutron diffraction experiments, due to its martensite content and the effect of the ferrite phase.

Weld destructive specimens, in the form of lap-shear and cross-tension geometries, were fabricated with the automotive weld schedule. The main purpose of destructively testing these geometries was to obtain load - displacement curves which were used to validate the subsequent FE models. Extensometers were used to measure the lap-shear specimen elongation. Due to the dimensions of the cross-tension clamps, extensometers could not be used. A total of 5 lap-shear and 5 cross-tension specimens were destructively tested. The lap-shear specimens failed at an average load of 20.26 kN and displacement of 0.40 mm. The cross-tension specimens failed at an average load of 5.91 kN and displacement of 5.66 mm.

Fractography was performed on the lap-shear and cross-tension samples through SEM imaging. It was found that inclusions were prevalent outside the nugget. Large dimples, most likely formed by large inclusions, were observed in an approximately constant radial arc in the corona bond area. This suggests these large inclusions were pushed out during welding. Ductile fracture regions were observed, with small inclusions in the equiaxed dimples, which served as void nucleating sites. The presence of inclusions

are likely to affect the fracture initiation sites and it is therefore likely that they can, in part, explain the scatter in load-displacement curves seen between different weld destructive specimens within the same geometries.

Hardness tests were performed on a sectioned boron steel weld, showing similar hardness levels in the nugget and BM. This is most likely due to significant amounts of martensite present in both areas. A hardness decrease of approximately 180 HV was seen in the HAZ. Little variation in the hardness distributions were seen through the sheet thickness. This is an important result, as this led to an assumption that material properties can be approximated as being constant through the sheet thickness. This meant that priority was given to extracting material data along the length of the work-piece in subsequent experiments.

Hardness tests of the DP600 weld showed a nugget hardness of approximately 100 HV less than the boron steel nugget. The difference in carbon content between the two steel types was identified as a reason for the difference in hardness. This difference was also seen in the yield strengths extracted later through instrumented indentation.

The residual strain distributions of boron steel and DP600 spot welds were measured using the neutron diffraction technique. The measured strains were converted to residual stresses under a plane-stress assumption, which also allows the precise determination of a strain-free lattice parameter across the weld. As stated previously, the residual strain distribution of boron steel spot welds have not been measured before and the results add knowledge about the properties of the weld. Both the DP600 and boron steel welds exhibited tensile stresses in the nugget, due to the molten metal cooling and contracting at the end of the weld cycle. Due to the natural tendency for the work-piece to seek equilibrium, the BM near the HAZ exhibited compressive residual stresses.

A very clear correlation between the residual stress, hardness and strain-free lattice parameter distributions was seen for both welds. Peak tensile stresses of 450 MPa in the hoop direction were observed in the HAZ of the boron steel weld. The reduced

hardness in the HAZ, in conjunction with peaks in residual stress, indicates that this is an area exhibiting extreme properties and will make a significant contribution to the overall loading response of the weld.

The FWHM gave an indication of the microstructural variations through the weld. For the boron steel weld HAZ, a shift in peak breadth away from values associated with martensite corroborated evidence that the microstructure in the HAZ is a softer phase; most likely consisting of tempered martensite. It was previously mentioned that the DP600 weld nugget exhibited a hardness of 100 HV less than the boron steel weld. From the FWHM results, the reduced hardness can be explained in terms of a reduction in tetragonality of the martensite (tending towards a ferritic bcc structure). This is evidenced in the FWHM values, where the DP600 nugget centre showed a FWHM value of 0.27° less than the boron steel weld centre. The reduction in tetragonality stems from the reduced carbon content of DP600 compared to boron steel.

The yield strength distribution of the physical weld was extracted through instrumented indentation. Due to the small size of the different weld zones, cutting tensile test specimens directly from the weld is unachievable. Instrumented indentation offered the opportunity to extract material properties *directly* from the weld. To the authors knowledge, instrumented indentation has not previously been used to verify the accuracy of heat treated samples with respect to their target microstructures. Therefore, this work explores a new application of instrumented indentation. Once an appropriate algorithm has been programmed, instrumented indentation offers a relatively fast method of calculating material properties.

The DP600 and boron steel welds used in the neutron diffraction study were sectioned through the sheet thickness direction and used in the instrumented indentation experiments. An algorithm developed by Dao *et al* [77] was used as a tool to calculate the modulus of elasticity and yield strength distributions of the welds. Three line scans were performed along the sheet length at depths of 0.6 mm, 0.75 mm and 0.9 mm from the sheet-sheet interface, giving three measurement points per unit distance from the weld centre. The individual data points showed some scatter relative to one another at

each unit distance. However, as recommended by Dao, taking an average of the three data points brought the results to acceptable values.

The Young's modulus distributions showed some scatter for both welds, but centred around commonly accepted values for steel of 205 GPa. After taking an average of the individual data points at each unit distance, the yield strength of the boron steel weld nugget showed a consistently high level at 1040 MPa. The calculated BM yield strength was 1011 MPa. A comparison of this value to the yield strength extracted from stress - strain curves of boron steel BM showed an underestimation of 36 MPa. In comparing the DP600 BM yield strength to those from the BM stress - strain curves, the instrumented indentation results showed an underestimation of 25 MPa.

Comparing the calculated BM and nugget yield strengths from instrumented indentation to those of measured stress - strain curves validated the accuracy of the method for the high strength materials. However, it was suggested that these high strength areas of the weld are likely to exhibit different responses to indentation than the softer HAZ areas. An interesting observation was made that the calculated yield strength of the higher strength boron steel BM correlated well with the 0.2% offset yield of the corresponding stress - strain curve. The calculated yield strength of the DP600 BM corresponded well to the 0% offset yield of the corresponding stress - strain curve. An explanation was offered, in that these two different materials have different responses to indentation. For harder, higher strength materials, an increase in stress has relatively little impact on strain. For softer materials, a large change in strain is expected for a relatively small increase in pressure. Considering that all indents were performed under the same pressure, the difference between harder and softer behaviour under the same pressure could be a reason for the different yield strength correspondence.

As mentioned, the calculated yield strengths of the high strength materials were validated. Validation of the calculated yield strengths for the softer, more ductile boron steel HAZ was needed. The results from the DP600 BM were therefore used as verification that the algorithm works for softer, more ductile metals, where the calculated BM yield strength corresponded well to the yield strength taken from the stress - strain

curve.

The Gleeble physical simulation experiments provided the main material properties which were used for FE simulations of failure performance. These properties were the stress - strain responses of different weld sections and the corresponding $\varepsilon_f - \eta$ failure loci. As mentioned previously, due to the small size of the weld, cutting test specimens directly from the weld is unachievable. To overcome this problem, specific weld and HAZ microstructures were recreated onto practical tensile specimens by subjecting these specimens to the same thermal histories as the target weld zones.

In total, four different geometries with five different microstructures each were created. Standard tensile dog-bone specimens provided the stress - strain response of the materials. Shear, central-hole and plane-strain specimens provided failure strains at specific stress states, which were used to construct the $\varepsilon_f - \eta$ failure loci. This technique took its lead from the work of Dancette and Sommer, with the previously mentioned improvements applied.

An additional improvement was the discretisation of physically simulated HAZ materials. Sommer characterised three weld regions for boron steel welds, namely the nugget, HAZ and BM. The HAZ material of Sommer corresponded to the point of lowest hardness. A potential problem with such characterisation would be that the interplay of material gradients would be lost and have significant effects on the FE results. Therefore, the final improvement on Sommer's work was to characterise the HAZ in a more finely discretised manner. Five points around the HAZ were selected for physical simulation. These five points were chosen to enable data interpolation be made between them, thus further improving the level of material discretisation in the weld FE models. The BM properties were also characterised.

Temperature histories of the chosen points, for physical simulation campaigns, were extracted from the SORPAS finite element welding simulation programme using the appropriate automotive weld schedule. These temperature - time curves were subsequently used to guide the Gleeble physical simulations. The peak target temperat-

ures were 1100 °C, 925 °C, 725 °C and 575 °C, which were denoted as points A, B, C and D respectively.

During the Gleeble physical simulations, it was important to maximise the area of homogeneous microstructure in the samples and stainless steel half-contact grips were recommended to achieve this. These grips do not, however, allow for very fast heating rates. This led to problems in accurately recreating the heating rates experienced by the physical weld regions. Nevertheless, it was concluded that achieving a homogeneous microstructure was more important, because the interplay of microstructural gradients in the sample gauge lengths would invalidate any measured data. The actual achieved thermal histories were recorded through thermocouples attached to the samples and used to gauge the deviation from the target thermal histories.

Two heating regimes were utilised; a conservative "slow heating" regime and a more ambitious "fast heating" regime. The effect of these different heating regimes on the developed microstructure distributions were investigated by measuring the thermal gradients and hardness distributions along the sample lengths. The samples produced with the slow heating regime exhibited significant thermal and hardness gradients along the sample length. The samples produced with the fast heating regime exhibited significantly smaller thermal gradients and thus displayed a larger area of even hardness.

It was inferred that the dwell period in the "slow heating" regime allowed greater temperature distributions to develop, thus leading to significant hardness gradients along the sample lengths. The use of the stainless steel half-contact grips was sufficient in itself to achieve a homogeneous hardness distribution without the addition of a dwell period. The measured hardness distributions also aided in finalising the tensile sample geometries so that homogeneous material was present in the sample gauge lengths. From these physical simulations, tensile geometries were machined out for subsequent testing and extraction of material constitutive behaviour.

The stress - strain curves and failure loci were successfully extracted from the physically simulated samples through tensile testing. A DIC measuring system was used to extract

the strain evolution for constructing the true stress - true strain curves and the failure strain values for constructing the failure loci. Additionally, the DIC system provided a means to measure the stress state of the samples. The failure loci were constructed by fitting second order polynomials to the three measured stress state points (shear, uniaxial and plane-strain), as recommended by Beaumont [119] and Bao and Wierzbicki [118]. The tempered samples which were heated to peak temperatures of 575 °C and 725 °C exhibited larger failure strains than the harder samples heated to 925 °C and 1100 °C.

To establish how accurately the physically simulated samples were created with respect to their target weld microstructures, hardness comparisons were used as an initial evaluation method. The samples produced from the fast heating regime exhibited the closest correlation to the target weld hardness values. The samples produced from the 925 °C peak temperature runs, for both the slow and fast heating regimes, exhibited significantly higher hardness values compared to the target. This was attributed to the fact that these samples were austenitised for a longer time than the corresponding point on the physical weld. Additionally, the higher heating rates experienced by the weld may have increased the transformation temperatures, meaning that the target weld section experienced even less austenitisation than the physically simulated samples.

At this point in the analysis, the slow heating regime samples were omitted from further analysis. The samples produced from the fast heating regimes exhibited closer correspondence to the target weld sections, both in terms of hardness and thermal histories. The hardness distribution of these samples also showed a larger area of homogeneous hardness, thus reducing the possibility of microstructural gradients affecting the loading response of the tensile samples.

Further verification of the accuracy of material property recreation was performed by comparing the yield strengths of the stress-strain curves extracted from the fast heating regime tensile samples with the yield strengths extracted directly from the weld using instrumented indentation. It was observed that the 0.2% offset yields of the harder samples (heated to 925 °C and 1100 °C) correlated better with the instrumented in-

dentation yield strengths. The 0% offset yields of the softer, tempered samples (heated to 575 °C and 725 °C) correlated better with the instrumented indentation yields. This observation was also made in the instrumented indentation experiments with both the harder boron steel BM and softer DP600 BM.

Optical microscopy was used to verify that the correct decisions, in regards to material reproduction and material omissions, were made with the use of purely quantitative data. The optical microscopy revealed that that the physically simulated microstructures deviated from their targets. Considering that all samples reached the correct target temperatures, the deviation can be attributed to the extended times spent at elevated temperatures.

The data obtained from the physical simulation trials formed the main input to the FE models. Two model geometries were studied; lap-shear and cross-tension. There were also four variations of each geometry; roughly discretised, finely discretised, roughly discretised with residual stress and finely discretised with residual stress. The roughly discretised model had 5 unique stress - strain curves and 5 unique failure loci assigned to the weld model sections.Through linear interpolation between these 5 unique material properties, 29 stress - strain and 29 failure loci were obtained and subsequently input into the finely discretised models.

A novel approach to discretising an FE model was presented. Whereas the rough model was discretised in the mesh design stage, the fine model was discretised using a MatLab script, where the element sizes were used to define the level of discretisation. Use was made of the fact that the FE model could be altered in the form of a text document. MatLab scripts were created to write a document which assigned the interpolated material properties (stress-strain curves, failure loci) and process induced states (residual stresses) to each element in the FE model.

Both the rough and finely discretised lap-shear models, without residual stress, showed good correspondence to the experimentally measured load - displacement curves, with an underestimation in peak load of 6% and 10% respectively. The effect of material

discretisation was evident in the developed strain distributions of both models. The developed strain distributions through the HAZ showed that artificial strain concentrations occurred at the material boundaries in the roughly discretised model. The finely discretised model exhibited a strain concentration at the point which was previously identified as a location of reduced mechanical properties.

The cross-tension models without residual stresses also showed good correspondence to the experimental load - displacement curves, with an underestimation in peak load of 7% and 1% respectively. Negligible differences were seen in the developed strain distribution through the HAZ in the two models.

An interesting observation was made on the effect of material discretisation on the strain distribution evolution through the HAZ of the two different geometries. Noticeable differences were seen in the developed strain distributions for the rough and finely discretised lap-shear models. For the cross-tension models however, the effect of geometry had a much greater influence on the strain distribution evolution, with the effect of bending dominating over any material response.

As mentioned previously, the $\varepsilon_f - \eta$ failure loci were used to define the conditions of failure. It was observed that elements in the lap-shear and cross-tension models failed within the triaxiality range of 0.7 to 1.5. These values are beyond the scope of the triaxiality measured from the Gleeble physical simulation samples. An improvement to the failure model would be to extend the failure loci into the large triaxiality range. This would be accomplished by destructively testing round bar specimens with various notch radii [118]. Boron steel was not available in round bar form at the time of testing.

The inclusion of the experimentally measured residual stress distributions had little effect on the simulated load - displacement curves, with respect to the models without residual stresses. From literature, it was stated that residual stresses do significantly affect the load carrying capacity, although the effects are reduced with increasing plasticity [67]. Nevertheless the method of including these stresses opens up exciting possibilities into modelling fatigue problems, where residual stresses are expected to have a

greater effect [148]. To this authors knowledge, the incorporation of measured residual stresses into an FE model has not been performed in such detail as done in this work.

The failure mode in all simulations was that of button pull-out. This failure simulation was attributed to the ductile failure modelling approach used in this work. Ductile fracture models often use a maximum plastic strain limit to determine the fracture point, as was done in this work. From the SEM investigations of the physical lap-shear and cross-tension samples, it was observed that the majority of failure occurred by ductile fracture. Some areas of brittle fracture were also observed. These areas of brittle fracture suggest the presence of material with low fracture toughness, which may have occurred due to the nature of the extreme heating and cooling during welding. For most thin gauge steels, material fracture toughness is usually sufficiently high for brittle fracture not to be of great concern. The modelling of brittle fracture is a class of problem outside the scope of this thesis and requires a different experimental approach.

In conclusion, the following main points may be stated about this thesis:

- Residual strain distributions of boron steel spot welds, which have not been measured before, were presented. Clear correlations between hardness and residual stress distributions were seen.
- A new application of instrumented indentation was attempted by verifying the accuracy of heat treated samples with respect to their target microstructures by comparing yield strengths.
- The boron steel HAZ was characterised in a finer level of detail than seen in other literature works.
- Through physical simulation, stress - strain and failure loci corresponding to certain HAZ areas were successfully extracted and used to model weld failure.
- A new method of finite element model discretisation was presented, where material properties and residual stresses may be input as a relatively smooth function through the length of the model.

9.1 Recommendations for further work

All boron steel spot welds that were investigated stemmed from a single optimised automotive industry weld schedule. Different weld schedules are likely to produce welds with different material property distributions. Investigating the properties from welds produced by adaptively controlled welding would be very interesting. During adaptive welding, the current is continuously adjusted. This could potentially lead to different microstructural gradients in the HAZ. Preliminary tests were performed with an adaptive weld schedule. The measured hardness distribution of the produced weld exhibited a remarkably different shape compared to the automotive schedule weld. Attempting to recreate an adaptive weld schedule on a Gleeble machine would present a considerable challenge.

A significant improvement for the instrumented indentation and Gleeble verification method would be to extract the yield strengths of the physically simulated samples and compare these calculated yield strengths with the measured yield strengths obtained through tensile testing. This was, however, not possible in the timescale of the project. Such a technique would lend further verification of the material recreation accuracy.

Due to the limited allocated time on the Gleeble machine, the range of experimental parameters were limited. Perhaps the most obvious improvement to the work presented would be to investigate physical simulation using different grips. As mentioned previously, copper grips allow for very fast heating rates, however, the zone of heated material is small. It would be interesting to investigate whether the tensile specimen geometries may be adjusted to compensate for this smaller heat treated zone. An investigation may also be performed to develop special grips to find a compromise between faster heating rates and obtaining large areas of homogenised microstructure. Additionally, performing physical simulation trials with finer intervals around the transformation temperatures may have improved the accuracy of the recreated microstructures with respect to their targets.

In obtaining load - displacement curves for the cross-tension samples, the displacements

could not be measured accurately. An improvement may be to spray a speckled pattern on the cross-tension grips and use DIC to measure displacements.

Through FE modelling, it was observed that the elements tended to fail in the large triaxiality range. To account for this in the failure loci, additional physically simulated test geometries would need to be created. This would be accomplished by destructively testing round bar specimens with various notch radii [118]. As stated previously, boron steel was not available in round bar form at the time of testing, however, it may be possible to have such bars custom made. Heat treating such bars would require additional trials on the Gleeble machine, as the mass and volume would be different to the thin sheet geometries used in this work.

It was mentioned that an innovative technique was used to input experimentally measured residual stresses into FE models. However, the effect of residual stresses on the load response during simulated destructive testing was negligible. Residual stresses are expected to play a more significant role in fatigue loading simulations and may provide interesting insights into how the residual stresses redistribute during loading.

A ductile failure model was presented. It is possible to extend the model to incorporate brittle failure by using similar experimental methods as used in this work. For example, to obtain the fracture toughness of the HAZ, the physically simulated samples may have a notch machined in the gauge length and subjected to mode 1 loading. A cohesive modelling approach may also be undertaken to simulate interfacial failure.

References

[1] R.W.K. Honeycombe and H.K.D.H. Bhadeshia. *Steels Microstructure and Properties*. Edward Arnold, 1995.

[2] K.D. Clarke, C.J. VanTyne, C.J. Vigil, and R.E. Hackenberg. Induction hardening 5150 steel: effects of initial microstructure and heating rate. *Journal of materials engineering and performance*, 20(2), 2011.

[3] D. Tabor. A simple theory of static and dynamic hardness. *Proceedings of the Royal Society of London*, Series A: Mathematical and Physical Sciences, 1947.

[4] A. Bardelcik, M.J. Worswick, S. Winkler, and M.A. Wells. A strain rate sensitive constitutive model for quenched boron steel with tailored properties. *International Journal of Impact Engineering*, 50, 2012.

[5] D. Mohr and F. Ebnoether. Plasticity and fracture of martensitic boron steel under plane stress conditions. *International Journal of Solids and Structures*, 46:3535–3547, 2009.

[6] M. Naderi, L. Durrenberger, A. Molinari, and W. Bleck. Constitutive relationships for 22mnb5 boron steel deformed isothermally at high temperatures. *Materials Science and Engineering A*, 478(1), 2007.

[7] M. Naderi, A. Saeed-Akbari, and W. Bleck. The effects of non-isothermal deformation on martensitic transformation in 22mnb5 steel. *Materials Science and Engineering A*, 487, 2007.

[8] M. Merklein and J. Lechler. Investigation of the thermo-mechanical properties of hot stamping steels. *Journal of Materials Processing Technology*, 177(1), 2006.

[9] R. Mohan Iyengar, B. Fedewa, Y.W. Wang, D.F. Maatz Jr, and R.L. Hughes. Implications of hot stamped boron steel components in automotive structures. *SAE Technical Paper*, 2008-01-0857, 2008.

[10] H. Karbasian and A.E. Tekkaya. A review of hot stamping. *Journal of Materials Processing Technology*, 210(15), 2010.

[11] Key to Metals. Boron in steel part 2. http://www.keytometals.com/page.aspx?ID=CheckArticlesite=ktsNM=214 [Accessed December 2013].

[12] A. Bardelcik, C.P. Salisbury, S. Winkler, M.A. Wells, and M.J. Worswick. Effect of cooling rate on the high strain rate properties of boron steel. *International Journal of Impact Engineering*, 37(6), 2010.

[13] W.F. Brown, B.C. Dolphin, J.F. Cantalin, A.W. Schueler, and F.J. Wallace. *AWS Welding Handbook Section 2*. Americal Welding Society, 1964.

[14] L.M. Gourd. *Principles of welding technology*. Edward Arnold, 3rd ed. edition, 1995.

[15] H. Zhang and J. Senkara. *Resistance welding: fundamentals and applications*. CRC Press, 2012.

[16] G.S. Jung, K.Y. Lee, H.K.D.H. Bhadeshia, and D.W. Suh. Spot weldability of trip assisted steels with high carbon and aluminium contents. *Science and Technology of Welding and Joining*, 17(2), 2012.

[17] N. Harlin, T.B. Jones, and J.D. Parker. Weld growth mechanism of resistance spot welds in zinc coated steel. *Journal of Materials Processing Technology*, 143 - 144, 2003.

[18] Y.J. Chao. Ultimate strength and failure mechanism of resistance spot weld subjected to tensile, shear, or combined tensile/shear loads. *Journal of Engineering Materials and Technology*, 125(2), 2003.

[19] Sunstone Engineering. Capacitive discharge, fine-spot resistance welder instruction pamphlet. http://www.sunstoneengineering.com/site/pages/dpInstructions [Accessed December 2013].

[20] A.C. Reardon. *Metallurgy for the non-metallurgist*. ASM International, 2011.

[21] R.E. Smallman and R.J. Bishop. *Modern physical metallurgy and materials engineering*. Butterworth Heinemann, 6th edition, 1999.

[22] ASM Handbook. *Volume9 Metallography and Microstructures*. ASM International, 1985.

[23] H.K.D.H Bhadeshia. Diffusional formation of ferrite in iron and its alloys. *Progress in Materials Science*, 29(4), 1985.

[24] D.A. Porter and K.E. Easterling. *Phase Transformations in Metals and Alloys*. Van Nostrand Reinhold, 1981.

[25] P. Akerstrom and M. Oldenburg. Austenite decomposition during press hardening of a boron steel - computer simulation and test. *Journal of Materials Processing Technology*, 174(1), 2006.

[26] H.K.D.H Bhadeshia. *Bainite in steels*. Institute of Materials, 2nd edition edition, 2001.

[27] B.P.J. Sandvik and C.M. Wayman. Crystallography and substructure of lath martensite formed in carbon steels. *Metallography*, 16(2), 1983.

[28] P. Haasen. *Physical metallurgy*. Cambridge University Press, 3rd edition, 1996.

[29] R.E. Reed Hill. *Physical metallurgy principles*. Van Nostrand, 1973.

[30] R. Blondeau. *Metallurgy and mechanics of welding*. Wiley, 2013.

[31] S. Sommer. Characterization and modeling of fracture behaviour of spot welded joints in hot-stamped ultra-high strength steels. *LS Dyna forum, Ulm*, 1, 2010.

[32] Dynamic Systems Inc. Gleeble. http://www.gleeble.com [Accessed August 2014].

[33] G. Avramovic-Cingara, Y. Ososkov, M.K. Jain, and D.S. Wilkinson. Effect of martensite distribution on damage behaviour in dp600 dual phase steels. *Materials Science and Engineering*, 516(1), 2009.

[34] M. Matya and X.Q. Gayden. Development of requirements for resistance spot welding dual-phase (dp600) steels part 1 - the causes of interfacial fracture. *Welding Journal*, 84(11), 2005.

[35] K. Yamazaki, K. Sato, and Y. Tokunaga. Static and fatigue strength of spot welded joints in ultra-high-strength, cold-rolled steel sheets. *Welding International*, 14(7), 2000.

[36] H. Lanzerath, A. Bach, G. Oberhofer, and H. Gese. Failure prediction of boron steels in crash. *SAE International*, 2007.

[37] V.H.B. Hernandez, S.K. Panda, Y. Okita, and N.Y. Zhou. A study on heat affected zone softening in resistance spot welded dual phase steel by nanoindentation. *Journal of Materials Science*, 45(6), 1979.

[38] K.H. Chung, W. Lee, J.H. Kim, C. Kim, S.H. Park, D. Kwon, and K. Chung. Characterization of mechanical properties by indentation tests and fe analysis-validation by application to a weld zone of dp590 steel. *International Journal of Solids and Structures*, 46(2), 2009.

[39] C. Ullner, S. Brauser, A. Subaric-Leitis, G. Weber, and M. Rethmeier. Determination of local stress-strain properties of resistance spot-welded joints of advanced high-strength steels using the instrumented indentation test. *J Mater Sci*, 47:1504–1513, 2011.

[40] S. Dancette, D. Fabregue, R. Estevez, V. Massardier-Jourdan, T. Dupuy, and M. Bouzekri. A finite element model for the prediction of advanced high strength steel spot welds fracture. *Engineering Fracture Mechanics*, 87:48–61, 2012.

[41] Y. Yu, C. Wang, S. Chen, and Z. Lu. Study on intermediate frequency spot welding process of hot stamping high strengh steel. *Advanced Materials Research*, 339:375–378, 2011.

[42] H.S. Choi, G.H. Park, W.S. Lim, and B.M. Kim. Evaluation of weldability for resistance spot welded single-lap joint between ga780dp and hot stamped 22mnb5 steel sheets. *Journal of Mechanical Science and Technology*, 25:1543–1550, 2011.

[43] J.P. Kong, T.K. Han, K.G. Chin, B.G. Park, and C.Y. Kang. Effect of boron content and welding current on the mechanical properties of electrical resistance spot welds in complex phase steels. *Materials and Design*, 54, 2013.

[44] S. Sommer. Modeling of the fracture behaviour of spot welds using advanced micro-mechanical damage models. *IOP Conf. Series: Materials Science and Engineering*, 10, 2010.

[45] S. Dancette, D. Fabregue, V. Massardier-Jourdan, J. Merlin, T. Dupuy, and M. Bouzekri. Experimental and modeling investigation of the failure resistance of advanced high strength steels spot welds. *Engineering Fracture Mechanics*, 78:2259–2272, 2011.

[46] ASM Handbook. *Volume6A Welding Fundamentals and Processes*. ASM International, 2011.

[47] Y.J. Chao. Failure mode of spot welds: interfacial versus pullout. *Science and Technology of Welding and Joining*, 8(2):133 – 137, 2003.

[48] S.H. Lin, J. Pan, T. Tyan, and P. Prasad. A general failure criterion for spot welds under combined loading conditions. *International Journal of Solids and Structures*, 20, 2003.

[49] S. Zhang. Fracture mechanics solutions to spot welds. *International Journal of Fracture*, 112(3), 2001.

[50] LS DYNA. Keyword user's manual version 971. 2010.

[51] A.L. Gurson. Continuum theory of ductile rupture by void nucleation and growth: Part i - yield criteria and flow rules for porous ductile media. *Journal of Engineering Materials and Technology*, 99(1), 1965.

[52] P.F. Thomason. *Ductile Fracture of Metals*. Oxford Pergamon Press, 1990.

[53] L.M. Brown and J.D. Embury. The microstructure and design of alloys. *London Institute of Metals. Proc. 3rd International Conference on Strength of Metals and Alloys*, 1(1), 1973.

[54] X. Kong, Q. Yang, B. Li, G. Rothwell, R. English, and X.J. Ren. Numerical study of strengths of spot-welded joints in steel. *Materials and Design*, 29:1554–1561, 2008.

[55] S. Dancette, V. Massardier-Jourdan, D. Fabregue, J. Merlin, T. Dupuy, and M. Bouzekri. Haz microstructures and local mechanical properties of high strength steels resistance spot welds. *ISIJ International*, 51:pp. 99–107, 2010.

[56] P.J. Withers and H.K.D.H Bhadeshia. Residual stress part 1 - measurement techniques. *Materials Science and Technology*, 17(4), 2001.

[57] VECTER. Deep hole drilling. http://www.veqter.co.uk/residual-stress-measurement/deep-hole-drilling [Accessed August 2014].

[58] R.H. Leggatt, D.J. Smith, S.D. Smith, and F. Faure. Development and experimental validation of the deep hole method for residual stress measurement. *The Journal of Strain Analysis for Engineering Design*, 31(3), 1996.

[59] P.J. Withers and H.K.D.H Bhadeshia. Residual stress part 2 - nature and origins. *Materials Science and Technology*, 17(4), 2001.

[60] M.T. Hutchings, P.J. Withers, T.M. Holden, and T. Lorentzen. *Introduction to the characterization of residual stress by neutron diffraction.* CRC Press, 2005.

[61] J. Altenkirch. Stress engineering of friction stir welding: Measurement and control of welding residual stress. *Ph.D. Thesis, University of Manchester*, 2009.

[62] Geneva Switzerland: ISO. Polycrystalline materials - determination of residual stresses by neutron diffraction iso/tta 3:2001(e). 2001.

[63] H.F. Poulsen. *Three-Dimensional X-Ray Diffraction Microscopy: Mapping Polycrystals and their Dynamics*, volume 205 of *Springer Tracts in Modern Physics.* Springer, 2004.

[64] P. Martinson, S. Daneshpour, M. Kocak, S. Riekehr, and P. Staron. Residual stress analysis of laser spot welding of steel sheets. *Materials and Design*, 30(9), 2009.

[65] M. Anastassiou, M. Babbit, and J.L. Lebrun. Residual stresses and microstructure distribution in spot-welded steel sheets: relation with fatigue behaviour. *Materials Science and Engineering: A*, 125(2), 1990.

[66] J.W.L. Pang, M. Preuss, P.J. Withers, G.J. Baxter, and C. Small. Effects of tooling on the residual stress distribution in an inertia weld. *Materials Science and Engineering: A*, 356(1), 2003.

[67] R.A. Ainsworth, J.K. Sharples, and S.D. Smith. Effects of residual stresses on fracture behaviour - experimental results and assessment methods. *The Journal of Strain Analysis for engineering Design*, 35(4), 2000.

[68] S.I. Bulychev, V.P. Alekhin, M.Kh. Shorshorov, and A.P. Ternovskii. Mechanical properties of materials studied from kinetic diagrams of load versus depth of impression during microimpression. *Strength of Materials*, 8(9), 1976.

[69] W.C. Oliver and G.M. Pharr. An improved technique for determining hardness and elastic modulus using load and displacement sensing indentation experiments. *J. Mater. Res.*, 7(6), 1992.

[70] M.F. Doerner and W.D. Nix. A method for interpreting the data from depth-sensing indentation instruments. *J Mater Res*, 1(4), 1986.

[71] I.N. Sneddon. The relation between load and penetration in the axisymmetric boussinesq problem for a punch of arbitrary profile. *International Journal of Engineering Science*, 3(1), 1965.

[72] E.J. Pavlina and C.J. Van Tyne. Correlation of yield strength and tensile strength with hardness for steels. *Journal of Materials Engineering and Performance*, 17(6), 2008.

[73] A.E. Giannakopoulos and S. Suresh. Determination of elastoplastic properties by instrumented sharp indentation. *Scripta Materialia*, 40(10), 1999.

[74] A.C. Fischer-Cripps. Nanoindentation, 2011.

[75] W.C. Oliver and G.M. Pharr. Measurement of hardness and elastic modulus by instrumented indentation: Advances in understanding and refinements to methodology. *Journal of Materials Research*, 19(1), 2004.

[76] A. Bolshakov and G.M. Pharr. Influence of pileup on the measurement of mechanical properties by load and depth sensing indentation techniques. *Journal of Materials Research*, 13(4), 1998.

[77] M. Dao, N. Chollacoop, K.J. van Vliet, T.A. Venkatesh, and S. Suresh. Computational modeling of the forward and reverse problems in instrumented sharp indentation. *Acta Materialia*, 49(19), 2001.

[78] A.E. Giannakopoulos, P.L. Larsson, and R. Vestergaard. Analysis of vickers indentation. *International Journal of Solids and Structures*, 31(19), 1994.

[79] P.L. Larsson, A.E. Giannakopoulos, E. Sonderlund, D.J. Rowcliffe, and R. Vestergaard. Analysis of berkovich indentation. *International Journal of Solids and Structures*, 33(2), 1995.

[80] A. Bardelcik, M.J. Worswick, and M.A. Wells. The influence of martensite, bainite and ferrite on the as-quenched constitutive response of simultaneously quenched and deformed boron steel - experiments and model. *Materials and Design*, 55(1), 2014.

[81] Y-T. Cheng and C-M. Chen. Can stress-strain relationships be obtained from indentation curves using conical and pyramidal indenters? *Journal of Materials Research*, 14(9), 1999.

[82] S. Basu, A. Moseson, and M.W. Barsoum. On the determination of spherical nanoindentation stress-strain curves. *Journal of Materials Research*, 21(10), 2006.

[83] N. den Uijl, T. Okada, T. Moolevliet, A. Mennes, E. van den Aa, M. Uchihara, S. Smith, H. Nishibata, T. van der Veldt, and K. Fukui. Performance of resistance spot-welded joints in advanced high-strength steel in static and dynamic tensile tests. *Welding in the World*, 56(8), 2012.

[84] International Standards Organisation. En iso 18278-2:2002. *ISO*, 2002.

[85] British Standard Institute. Bs en iso 18278-2:2004 alternative procedures for the assessment of sheet steels for spot welding. *British Standards*, 2004.

[86] British Standard Institute. Bs en iso 14373:2007 resistance welding - procedure for spot welding of coated and uncoated low carbon steels. *British Standards*, 2007.

[87] SORPAS Version 2. Swantec software and engineering aps. World Headquarters,Diplomvej 373,2800 Kongens Lyngby,Denmark,.

[88] British Standard Institute. Bs en iso 10447:2007 resistance welding - peel and chisel testing of resistance spot and projection welds. *British Standards*, 2007.

[89] D.J. Radakovic and M. Tumuluru. An evaluation of the cross-tension test of resistance spot welds in high-strength dual-phase steels. *Welding Journal*, 2012.

[90] British Standard Institute. Bs en iso 14272:2002 specimen dimensions and procedure for cross tension testing resistance spot and embossed projection welds. *British Standards*, 2001.

[91] British Standards Institute. Bs en iso 14273:2001 specimen dimensions and procedure for shear testing resistance spot, seam and embossed projection welds. *British Standards*, 2001.

[92] L. Han, M. Thornton, and M. Shergold. A comparative study between self-piercing riveting and resistance spot welding of aluminium sheets for the automotive industry. *Materials and Design*, 31(3), 2010.

[93] British Standard Institute. Bs en iso 14323:2006 resistance spot welding and projection welds - destructive testing of welds - specimen dimensions and procedure for impact shear test and cross-tension testing. *British Standards*, 2006.

[94] ASM Handbook. *Volume12 Fractography.* ASM International, 1987.

[95] G.F. Vander Voort. *Metallography Principles and Practice*. ASM International, 1984.

[96] British Standards Institute. Bs en iso 6507-1:1998 metallic materials - vickers hardness test. *British Standards*, 1998.

[97] C. Ma, D.L. Chen, S.D. Bhole, G. Boudreau, A. Lee, and E. Biro. Microstructure and fracture characteristics of spot-welded dp600 steel. *Materials Science and Engineering A*, 485(1), 2008.

[98] G. Krauss. Martensite in steel: strength and structure. *Materials Science and Engineering A*, 273(1), 1999.

[99] R. Filippone, J. Root, P. Jacques, and S. Yue. The influence of martensite on line broadening in neutron diffraction spectra of a dp steel. *ISIJ International*, 42(3):304–309, 2002.

[100] D.J. Hughes, G. Bruno, T. Pirling, and P.J. Withers. First impressions of salsa: The new engineering instrument at ill. *Neutron News*, 17(3):28–32, 2006.

[101] T. Pirling, G. Bruno, and P.J. Withers. Salsa - a new instrument for strain imaging in engineering materials and components. *Materials Science and Engineering A*, 437(1), 2006.

[102] D.J. Hughes, E. Koukovini-Platia, and E.L. Heeley. Residual stress in a laser welded eurofer blanket module assembly using non-destructive neutron diffraction techniques. *Fusion Engineering and Design*, 89(1), 2014.

[103] P. Staron, M. Kocak, S. Williams, and A. Wescott. Residual stress in friction stir-welded al sheets. *Physica B: Condensed Matter*, 350(1), 2004.

[104] A.J. Allen, M.T. Hutchings, C.G. Windsor, and C. Andeani. Neutron diffraction methods for the study of residual stress fields. *Advances in Physics*, 34(4), 1985.

[105] R.S. Florea, C.R. Hubbard, K.N. Solanki, D.J. Bammann, W.R. Whittington, and E.B. Marin. Quantifying residual stresses in resistance spot welding of 6061-

t6 aluminium alloy sheets via neutron diffraction measurements. *Journal of Materials Processing Technology*, 212(11), 2012.

[106] British Standard Institute. Iso/ts 21432:2005 non-destructive testing - standard test method for determining residual stresses by neutron diffraction. *British Standards*, 2005.

[107] A. Paradowska, J.W. Price, R. Ibrahim, and T. Finlayson.

[108] M.N. James, P.J. Webster, D.J. Hughes, Z. Chen, N. Ratel, S.P. Ting, and A. Steuwer.

[109] International Organization for Standardization. Iso tta 3:2001(e), 2001.

[110] LAMP. Large array manipulation program. http://www.ill.eu/data-treat/lamp/the-lamp-book[Accessed August 2014].

[111] W. Woo, V.T. Em, E.Y. Kim, S.H. Han, Y.S. Han, and S.H. Choi. Stress-strain relationship between ferrite and martensite in a dual-phase steel studied by in situ neutron diffraction and crystal plasticity theories. *Acta Materialia*, 60(20), 2012.

[112] D.T. Llewellyn and R.C. Hudd. *Steels metallurgy and applications*. Butterworth Heinemann, 3rd edition, 1998.

[113] N.A. Stilwell and D. Tabor. Elastic recovery of conical indentations. *Proceedings of the Physical Society*, 78(2), 1961.

[114] S. Jayaraman, G.T. Hahn, W.C. Oliver, C.A. Rubin, and P.C. Bastias. Determination of monotonic stress-strain curve of hard materials from ultra-low-load indentation tests. *International Journal of Solids and Structures*, 35(5), 1998.

[115] K.L. Johnson. *Contact mechanics*. Cambridge University Press, 1992.

[116] Y.T. Cheng and C.M. Cheng. Scaling, dimensional analysis and indentation measurements. *Materials Science and Engineering R: Reports*, 44(4), 2004.

[117] British Standards Institute. Bs en iso 14577-1:2002 metallic materials - instrumented indentation test for hardness and materials parameters. *British Standards*, 2002.

[118] Y. Bao and T. Wierzbicki. On fracture locus in the equivalent strain and stress triaxiality space. *International Journal of Mechanical Sciences*, 46(1), 2004.

[119] R.A. Beaumont. Determining the effect of strain rate on the fracture of sheet steel. *Ph.D. Thesis, University of Warwick*, 2012.

[120] A. Sayles. Tata steel test report number 11kt1037. Technical report, 2011.

[121] British Standards Institute. Bs en iso 6892-1:2009 metallic materials - tensile testing part 1: Method of test at ambient temperature. *British Standards*, 2009.

[122] H. Ebelsheiser, M. Feucht, and F. Neukamm. On calibrating advanced damage models using sheet metal coupon tests. *LS-DYNA Anwenderforum Bamberg*, 2008.

[123] J. Peirs, P. Verleysen, W. Van Paepegem, and J. Degrieck. Novel pure shear sheet specimen geometry for dynamic material characterisation. *9th International Conference on Mechanical and Physical Behaviour of Materials under Dynamic Loading*, 2009.

[124] R.N. Caron and G. Krauss. The tempering of fe-c lath martensite. *Metallurgical Transactions*, 3(9), 1972.

[125] J. Ahlstrom, K. Cvetkovski, B. Karlsson, and I. Siller. Short-time tempering kinetics of quench hardened pearlitic steels. *Conference Proceedings ICTPMCS-2010 Shanghai China*, 1(1), 2010.

[126] T. Furuhara, K. Kobayashi, and T. Maki. Control of cementite precipitation in lath martensite by rapid heating and tempering. *ISIJ International*, 44(11), 2004.

[127] G. Krauss, M.A. Grossmann, and E.C. Bain. *Principles of heat treatment of steel.* American Society for Metals, 1980.

[128] O.O. Miller. Influence of austenitizing time and temperature on austenite grain size of steel. *Transactions of the American Society for Metals*, 43(1), 1951.

[129] G.E. Totten and M.A. Howes. *Steel heat treatment handbook*. CRC Press, 1997.

[130] A. Danon, C. Servant, A. Alamo, and J.C. Brachet. Heterogeneous austenite grain growth in 9cr martensitic steels: influence of the heating rate and the austenitization temperature. *Materials Science and Engineering: A*, 348(1), 2003.

[131] S.J. Lee and Y.K. Lee. Latent heat of martensitic transformation in a medium-carbon low-alloy steel. *Scripta Materialia*, 60(1), 2009.

[132] M. Nikravesh, M. Naderi, and G.H. Akbari. Influence of hot plastic deformation and cooling rate on martensite and bainite start temperatures in 22mnb5 steel. *Materials Science and Engineering:A*, 540(1), 2012.

[133] T. Kuwabara. Advances in experiments on metal sheets and tubes in support of constitutive modeling and forming simulations. *International Journal of Plasticity*, 23(3), 2007.

[134] Y. Li and T. Wierzbicki. Prediction of plane strain fracture of ahss sheets with post-initiation softening. *International Journal of Solids and Structures*, 47(17), 2010.

[135] R.H. Wagoner and N.M. Wang. An experimental and analytical investigation of in-plane deformation of 2036-t4 aluminum sheet. *International Journal of Mechanical Sciences*, 21(5), 1979.

[136] A.M. Beese, M. Luo, Y. Li, Y. Bai, and T. Wierzbicki. Partially coupled anisotropic fracture model for aluminum sheets. *Engineering Fracture Mechanics*, 77(7), 2010.

[137] M.B. Prime, T. Gnaupel-Herold, J.A. Baumann, R.J. Lederich, D.M. Bowden, and R.J. Sebring. Residual stress measurements in a thick, dissimilar aluminium alloy friction stir weld. *Acta Materialia*, 54(15), 2006.

[138] R.D. Cook. *Finite element modeling for stress analysis*. Wiley, 1994.

[139] D. Radaj, Z. Zhaoyun, and W. Mohrmann. Local stress parameters at the weld spot of various specimens. *Engineering Fracture Mechanics*, 37(5), 1990.

[140] P. Salvini, F. Vivio, and V. Vullo. A spot weld finite element for structural modelling. *International Journal of Fatigue*, 22(1), 2000.

[141] J.T. Mottram and C.T. Shaw. *Using finite elements in mechanical design*. McGraw-Hill, 1996.

[142] J.O. Hallquist. *LS-Dyna Theory Manual*. Livermore Software Technology Corporation, 2006.

[143] T.J.R. Hughes, K.S. Pister, and R.L. Taylor. Implicit-explicit finite elements in nonlinear transient analysis. *Computer Methods in Applied Mechanics and Engineering*, 17(1), 1979.

[144] LS-Dyna Version 9.4. Livermore software technology corporation. World Headquarters, 7374 Las Positas Road, Livermore, CA 94551,USA,.

[145] Hypermesh Version 11. Altair engineering inc. World Headquarters,1820 East Big Beaver Rd,Troy, MI 48083,USA,.

[146] D. Norman. Modelling spotweld fracture using using crachfem. *9th European LS-DYNA Conference*, 1(1), 2013.

[147] Y. Ling. Uniaxial true stress-strain after necking. *AMP Journal of Technology*, 5(1), 1996.

[148] G. Bussu and P.E. Irving. The role of residual stress and heat affected zone properties on fatigue crack propagation in friction stir welded 2024-t351 aluminium joints. *International Journal of Fatigue*, 25(1), 2003.

Appendix A

Establish relationship between α and β

The von Mises yield criterion is defined as:

$$\sigma_{vm} = \frac{1}{\sqrt{2}}\sqrt{(\sigma_1 - \sigma_2)^2 + (\sigma_2 - \sigma_3)^2 + (\sigma_3 - \sigma_1)^2}$$

For a two-dimensional stress state, the von Mises yield criterion reduces to

$$\sigma_{vm} = \sqrt{\sigma_1^2 - \sigma_1\sigma_2 + \sigma_2^2}$$

Differetiate the von Mises yield locus to establish the relationship between α and β, where $\alpha = \frac{\varepsilon_2}{\varepsilon_1}$ and $\beta = \frac{\sigma_2}{\sigma_1}$.

$$2\sigma_1\frac{d\sigma_1}{d\sigma_2} - \left(\sigma_1 + \sigma_2\frac{d\sigma_1}{d\sigma_2}\right) + 2\sigma_2 = 0$$

Rearrange to obtain

$$\frac{d\sigma_1}{d\sigma_2} = -\frac{2\sigma_2 - \sigma_1}{2\sigma_1 - \sigma_2}$$

We consider that the strains are orthogonal to the yield locus $\therefore \frac{d\varepsilon_2}{d\varepsilon_1} = -\frac{d\sigma_1}{d\sigma_2}$

Therefore:

$$\alpha = \frac{d\varepsilon_2}{d\varepsilon_1} = -\frac{d\sigma_1}{d\sigma_2} = \frac{2\sigma_2 - \sigma_1}{2\sigma_1 - \sigma_2}$$

Substitute the definition of β $\left(= \frac{\sigma_2}{\sigma_1}\right)$ into the above equation to obtain

$$\alpha = \frac{2\beta - 1}{2 - \beta}$$

A.1 Convert α to η

For a two-dimensional stress state, the definition of η is

$$\eta = \frac{\sigma_m}{\sigma_{vm}} = \frac{\frac{1}{3}(\sigma_1+\sigma_2)}{\sqrt{\sigma_1^2+\sigma_1\sigma_2+\sigma_2^2}}$$

Substitute the definition of β into the above equation to obtain

$$\eta = \frac{\frac{1}{3}(1+\beta)}{\sqrt{1-\beta+\beta^2}}$$

From the previous section, we have estbalished that $\alpha = \frac{2\beta-1}{2-\beta}$, and we now substitute this derived relationship into the above equation to obtain:

$$\eta = \frac{1}{\sqrt{3}}\frac{1+\alpha}{\sqrt{1+\alpha+\alpha^2}}$$

Substitute the definition of α $\left(= \frac{\varepsilon_2}{\varepsilon_1}\right)$ into the above equation to obtain

$$\eta = \frac{1}{\sqrt{3}}\frac{\varepsilon_1+\varepsilon_2}{\sqrt{\varepsilon_1^2+\varepsilon_1\varepsilon_2+\varepsilon_2^2}}$$

Finally, we take the definition of plastic strain (ε_{pl}) , defined as:

$$\varepsilon_{pl} = \frac{2}{\sqrt{3}}\sqrt{\varepsilon_1^2 + \varepsilon_1\varepsilon_2 + \varepsilon_2^2}$$

and substitute it into the equation for η, to obtain:

$$\eta = \frac{2(\varepsilon_1+\varepsilon_2)}{3\varepsilon_{pl}}$$